SCUOLA DI DOTTORATO
UNIVERSITÀ DEGLI STUDI DI MILANO-BICOCCA

Dipartimento di / Department of

Scienza dei Materiali

Dottorato di Ricerca in / PhD program Scienza e Nanotecnologia dei Materiali
Ciclo / Cycle XXXI

Curriculum in (se presente / if it is) .....

Design of Functional Porous Materials with Stimuli-Responsive Mobile Elements

Cognome / Surname Castiglioni Nome / Name Fabio

Matricola / Registration number 725950

Tutore / Tutor: Prof. Piero Sozzani

Cotutore / Co-tutor:
(se presente / if there is one)

Supervisor:
(se presente / if there is one)

Coordinatore / Coordinator: Prof. Marco Bernasconi

ANNO ACCADEMICO / ACADEMIC YEAR 2017/2018

Summary

1. Chapter 1

Introduction

Nature is the everlasting muse of scientist. Science itself is defined as "the intellectual and practical activity encompassing the systematic study of the structure and behaviour of the physical and natural world through observation and experiment"[1]. Every discovery made by humankind was somehow inspired by Nature and porous materials make no exception: animal bone tissue, plant leaves, wood and coral (**Figure 1.1**)[2–5] are just a few examples of naturally occurring porous materials. In these examples, the main function of the network is structural (i.e., to sustain the organism) and pores are filled with everything that might be needed to keep the tissue alive, healthy and operative (blood vessels or lymphatic vessels, marrow or sap, nerves, etc.).

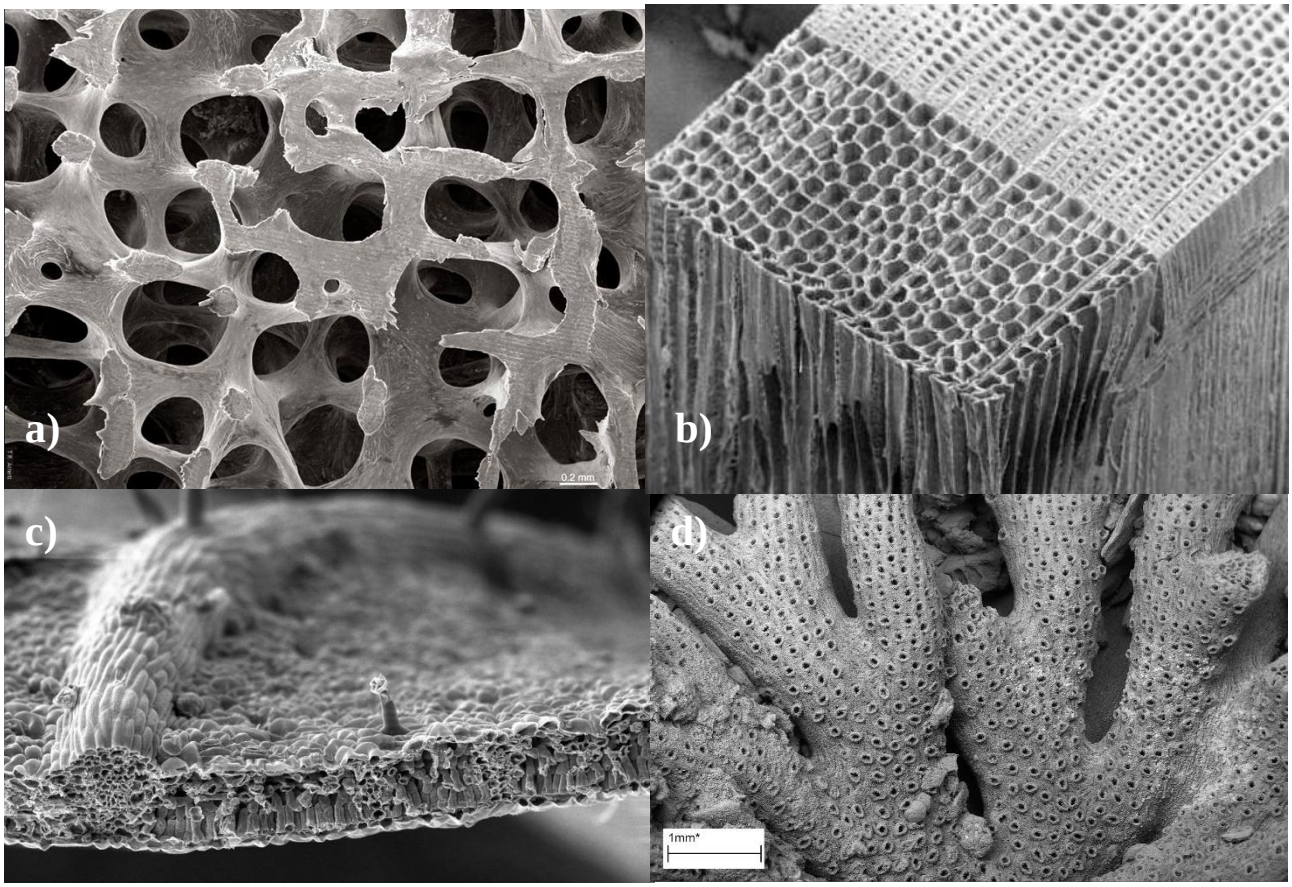

***Figure 1.1**. **a)** Low-power scanning electron microscopy of a normal bone architecture in the 3rd lumbar vertebra of a 30-year-old woman. Marrow and other cells removed to reveal thick, interconnected plates of bone. **b)** Scanning electron micrograph of Pinus wood. **c)** Scanning electron microscope image of a leaf from a Black Walnut tree. **d)** Scanning electron micrography of coral Hornera Striata.*

However, in most applications that has been envisaged for materials with accessible voids, the framework is used functionally: we exploit the open volume and the high surface area of porous materials. To do so, pores require to be permanent and accessible. In other words, guest species contained in the porous structure (as synthesized porous materials usually contain residual solvent molecules or gases) must be removeable and replaceable many times without provoking the collapse of the structure. Nature did not fail in providing a few examples of naturally occurring materials with permanent and accessible porosity, such as charcoal and clay. Their use as sorbent was already known to ancient Egyptians, Greeks and Romans[6], who used them for

desalination of water, clarification of fat and oil and for the treatment of numerous diseases. However, we must wait several centuries before a proper science of porous materials -i.e., a systematic study of their structure and properties- began. The starting point might be considered the work of the Swedish mineralogist Axel Fredrik Cronstedt who, in 1756, observed that, upon heating a particular type of mineral, it hissed and bubbled as it was boiling and thus named it *zeolite* from the Greek words *zeo*, to boil, and *lithos*, stone. Afterwards it was understood that zeolites[7] are porous crystalline aluminosilicates with general formula $M_{x/n}[(AlO_2)_x(SiO_2)_y]m\cdot H_2O$ (where M is a metal cation of valence *n* required to neutralize the negative charges *x* of the aluminosilicate framework) and the bubbling is produced by water molecules adsorbed in the pores that are released upon heating. The process is completely reversible. Nowadays, 40 different naturally occurring zeolites are known and two of them (clinoptilolite[8] and mordenite[9]) find extensive use for ion-exchange (radioactive) agricultural uses and as sorbents. The strong industrial interest around zeolites promoted an intense research activity aimed at the synthesis of new structures with tailored properties that resulted in the discovery of a total of 232 zeolite structures, both natural and synthetic, according to the Database of the International Zeolite Association (IZA)[10]. This interest is mainly powered by economic reasons as zeolites found applications in many industrially relevant fields, such as sorbent of small polar or polarizable molecules and bulk separations based on molecular sieving processes, catalyst for hydrocarbon transformation promoted by the strong acidity of certain type of zeolites, support for other catalytic systems, ion-exchange agents for water softening and even health-related applications[7]. This great variety of different applications arises from the fine tunability of frameworks composition and pore dimensions that can be controlled by the synthetic conditions. In other words, the properties of the final material can be foreseen and controlled by the preparative conditions. These last characteristics explain why zeolite triggered an enormous interest from the scientific point of view as well. Nowadays zeolites still constitute the industrially and economically most important porous material with its global market worth 29.08 billion of dollars in 2016[11].

1.1. The family of porous materials: from the inorganic crystalline zeolites to the organic amorphous covalent organic frameworks

As mentioned in the previous paragraph, zeolites are industrially and economically the most important porous material, but they constitute just one relative of the big family of materials with open porosity. During the course of the last 70 years, scientists developed more and more strategies to assemble porous solid structures, exploiting a variety of interactions, both covalent and non-covalent. The first level of these materials classification might be according to their nature: inorganic, hybrid or fully organic. Zeolites belongs to the class of inorganic porous materials, along with activated carbon[12,13] (another heavyweight champion between porous material with its USA market worth 759 million of dollars in 2015[14]), porous metals[15] and porous ceramics[15]. Among the hybrid organic-inorganic materials we find Periodic Mesoporous Organosilicas (PMOs)[16] and Metal-Organic Frameworks (MOFs)[17], while organic porous materials are represented by Porous

Organic Frameworks (POFs)[18] ad Porous Molecular Crystals (PMCs)[18]. All these macro-categories can be further divided in many subgenres. For example, hyper-cross-linked polymers (HCPs)[19], polymers of intrinsic microporosity (PIMs)[20], covalent organic frameworks (COFs)[21], conjugated microporous polymers (CMPs), covalent triazine frameworks (CTFs) and porous aromatic frameworks (PAFs)[22] all belong to the POFs class and differ from each other on the basis of the preparative methodology and the chemical nature of the monomers used in their synthesis.

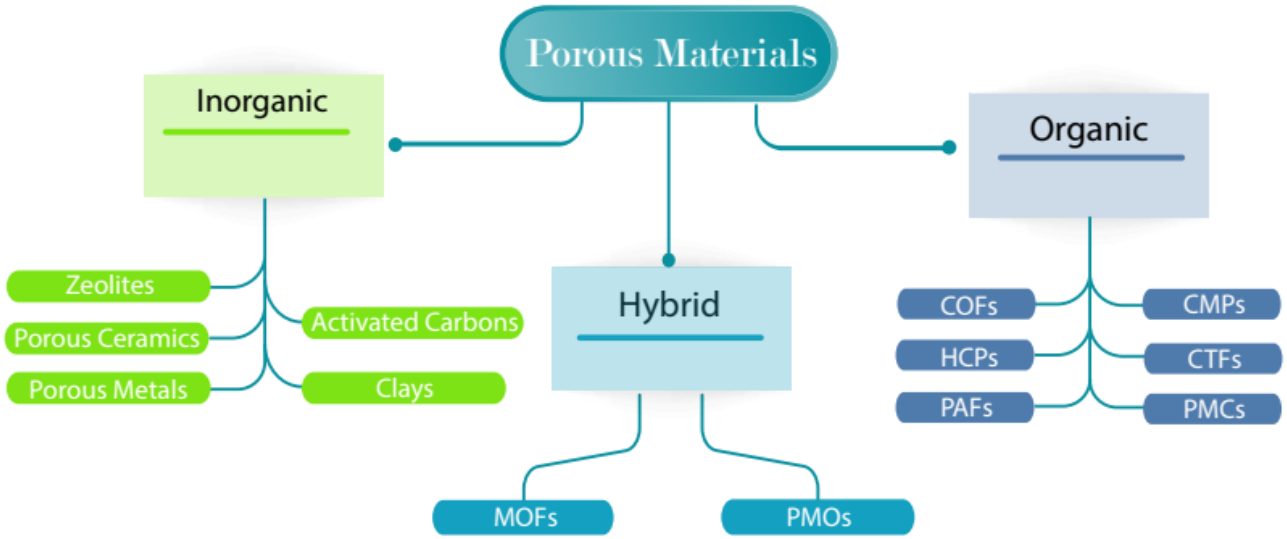

Figure 1.2. Diagram of the most common class of porous materials categorized according to their chemical nature.

It would be impossible to adequately cover such a great variety of different materials in the introduction of this thesis. Moreover, reviewing the entire literature of porous materials is beyond the scope of this work. For further information about each class of materials, the reader might refer to the cited literature. In the following, a brief overview about MOFs, CMPs and PAFs will be given, as the new materials presented in this thesis belong to the aforementioned classes of porous materials.

1.2. Basic concepts of porous materials characterization and adsorption phenomena

Before venturing deeper into the jungle of porous materials, it is opinion of the author that an outline of the basic concepts used in their characterization is needed. Further information can be retrieved from the books reported in the bibliography[6,15,23,24]. An exhaustive mathematical treatment of adsorption phenomena is given in Appendix 1.

IUPAC[23] defines a porous material as a solid with cavities, channels or interstices that are deeper than they are wide. According to this definition, however, every solid material, in principle, could be regarded as a porous

material, even when pores are occurring as defects that are detrimental for the material's properties. Thus, in describing a porous solid, care must be exercised in the choice of terminology in order to avoid ambiguity. Then, in defining a porous material, we may add that porosity must be produced on purpose. With the help of **Figure 1.3**, we can classify pores according to their availability to an external fluid. From this viewpoint, a first category of pores regards those totally isolated from their neighbours, as in region (a), which are described as *closed pores*. They influence macroscopic properties such as bulk density, mechanical strength and thermal conductivity, but are inactive in processes like fluid flow and adsorption of gases. In this thesis, the characterization of the porous material will rely entirely on gas adsorption techniques and, because of that, we are not going to consider closed pores as actual pores. On the other hand, pores which have a continuous channel of communication with the external surface of the body, like (b) (c) (d) (e) and (f), are described as *open pores*. Some may be open only at one end (like b) and (f); they are then described as *blind pores*. Others may be open at two ends (*through pores*), like around (e). Pores may also be classified according to their shape: they may be *cylindrical* (either open (c) or *blind* (f)), *ink-bottle shaped* (b), *funnel shaped* (d) or *slit-shaped.*

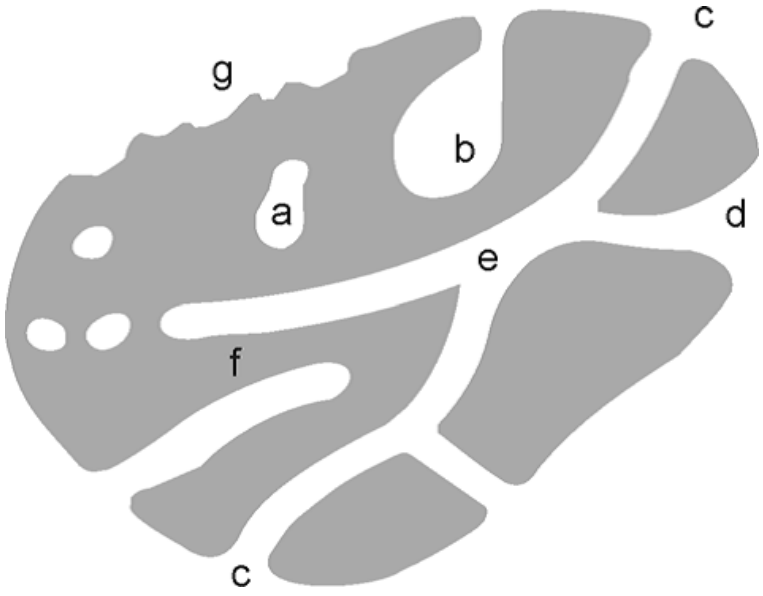

Figure 1.3. Schematic cross-section of a porous solid. Image reproduced from Rouquerol F., Rouquerol J., Sing K. S. W., Llewellyn P., Maurin G., Adsorption by Powders and Porous Solids, Elsevier, 2014, p. 10.

Close to, but different from porosity is the *roughness* of the external surface, represented around (g). To make the distinction, a convenient and simple convention is to consider that a rough surface is not porous unless it has irregularities that are deeper than they are wide.

Since some pores are not detectable by certain characterization techniques, it is important, when reporting porosity data, to describe the method used, as well. For example, the "*specific surface area*" is defined as the accessible (or detectable) area of solid surface per unit mass of material and it is strongly dependent on the method and experimental conditions employed, and on the size of the probe used (e.g. adsorbate molecular

size). In the literature of porous materials, it is common practice to calculate specific surface areas from N_2 adsorption isotherms at 77K adopting the BET model (see further for additional information about the BET model). Similarly, the *pore volume*, defined as the volume occupied by voids only, is heavily dependent from the method used to asses it, especially regarding the model used to describe to pores (slit, cylindrical, etc.).

Another very important parameter in porous solids characterization is the *pore size*, because many practical applications of porous materials rely on pores dimension, but it is even harder to give a precise definition for it. The problems already mentioned for the specific surface area are complicated by the fact that the pore shape is usually highly irregular and variable, leading to a variety of definitions of "size". Moreover, pore systems usually consist of interconnected networks, and the recorded results will often depend on the sequence in which pores are encountered within the method used (e.g. mercury intrusion). For these reasons, quantitative descriptions of pore structure are often based on model systems. For the sake of simplicity, the shape of pores, when known or assumed, is preferably described in terms of *cylinder*, *prisms*, *cavities* and *windows*, *slits*, or *spheres*. The real description many real porous solids is complicated by the existence of *different shapes* of pores inside the same material, *connections* between pores which may vary in size, shape and location and a *distribution in pores size*.

In most uses of porous solids, the *size of pores* is a major parameter: hence the development of a number of methods whose aim is to carry out a "pore size analysis". Pore size has a precise meaning when the geometrical shape of the pores is well defined and known (e.g. cylindrical, slit-shaped etc ...). Nevertheless, the limiting size of a pore is that of its *smallest dimension* which, in the absence of any further precision, is referred to as the width of the pore (i.e. the wall-to-wall distance of a slit-shaped pore, the diameter of a cylindrical pore). To avoid a misleading change in scale when comparing cylindrical and slit-shaped pores, *one should use the diameter of a cylindrical pore (rather than its radius) as its "pore-width "*

According to their size, IUPAC[24] suggested the following classification for pores:

- *Micropores* have widths smaller than 2 nm;
- Mesopores have widths between 2 and 50 nm;
- *Macropores* have widths larger than 50 nm.

Every method used in porous materials characterization rely on the same basic concept: a probe is infiltrated into the open framework and information concerning available pore volume, specific surface area and pore size are extrapolated knowing the amount of probe used, its size and how it is adsorbed (for example, pore size influences isotherms shape). Depending on the choice of the probe, the methodology is different: mercury porosimetry[25] use liquid mercury to determine total pore volumes, helium pycnometry makes use of helium to measure the density of a material, gas adsorption employs various gaseous probes to evaluate the porosity of the material. The latter technique is the most commonly employed in porous materials research and throughout this thesis materials characterization will rely on the phenomenon of *surface adsorption*, which it is defined as

the enrichment of material or increase in the density of the fluid in the vicinity of an interface. For our purposes, the fluid in the vicinity of the material will always be a gas (the *adsorptive)*. During the adsorption, molecules of the gas phase stick on the surface of the material (the *adsorbent*), forming an *adsorbate phase*. Adsorbed molecules can also *desorb* from the surface, returning to the gas phase. Often one can observe dynamic equilibrium between the number of molecules adsorbed and those desorbed in a certain time interval. Such a situation is called *adsorption equilibrium*. If these molecular flows to and from the surface do not match, we have either an *adsorption process* or a *desorption process.* The relation, at constant temperature, between the amount adsorbed and the equilibrium pressure, or concentration, is known as the *adsorption isotherm*.

Adsorption phenomena can be differentiated between *physisorption and chemisorption*. In physisorption, interactions between adsorbent and adsorbate are weak (van der Waals and/or dispersion interactions) and both the adsorbent and the adsorbate retain their identity (no chemical reaction). Physisorption is always reversible and adsorbed molecule can desorb lowering the adsorptive gas pressure or increasing the temperature. *Chemisorption* occurs whenever there is a chemical reaction between adsorptive and adsorbent that results in chemical bond formation. The process is not reversible as the starting materials (adsorptive and adsorbent) cannot be retrieved in their initial states. All the adsorption processes described in this thesis are physisorption processes.

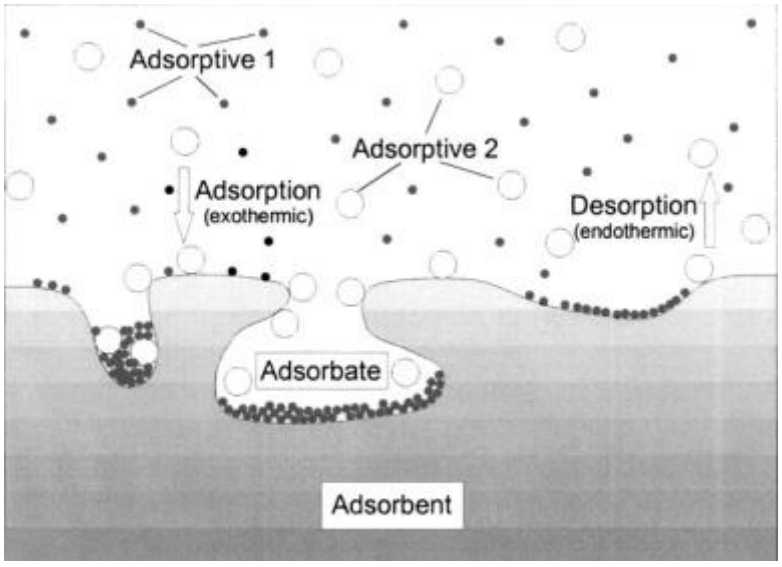

Figure 1.4. Adsorption system consisting of a two-component adsorptive gas (Adsorptive 1, Adsorptive 2), adsorbed phase or adsorbate (Adsorbate) including also the 2 components (1, 2) showing however different concentrations than in the gas phase due to their different interaction with the sorbent atoms, and a solid sorbent phase (Adsorbent). Adsorption is the transfer of molecules from the gas or liquid phase to the surface of the solid phase, normally an exothermic process. Desorption is the transfer of molecules sticking to the surface of the solid back to the gas or liquid phase, normally an endothermic process. Image reproduced from Keller J., Staudt R., Gas Adsorption Equilibra, Springer, 2005, p. 19.

Adsorption, both physisorption and chemisorption, occurs because the adsorbate has a lower chemical potential then the gas phase, i.e. the interactions between the adsorbent surface and the gas molecules lower the overall energy of the system. Thus, adsorption is a spontaneous exothermic process. Usually, the strength of the adsorbent-adsorptive interactions is measured in terms of the (molar) *enthalpy of adsorption*, ΔH_m. Since adsorption is exothermic, ΔH_m is always negative. Typical ΔH_m values range from 10-50 kJ/mol for physisorption and 70-200 kJ/mol for chemisorption.

The amount of gas adsorbed, n^a, by the mass, m^s, of solid is dependent on the equilibrium pressure, p, the temperature, T, and the nature of the gas–solid system. For a given gas adsorbed on a particular solid at a constant temperature we may write (if the pressure p of the gas is below its critical temperature p^O):

$$n^a/m^s = f(p/p^O)T \qquad [1.1]$$

where p^O is the saturation pressure of the adsorptive at temperature T. Equation [1.1] represents the adsorption isotherm which is the relationship between the amount adsorbed by unit mass of solid and the equilibrium pressure (or relative pressure), at a known temperature. Experimental adsorption isotherms recorded in the literature for many different gas–solid systems have various characteristic shapes. These shapes are important since they provide useful preliminary information about the pore structure of the adsorbent. The majority of vapour isotherms (i.e. at sub-critical temperatures) may be divided into nine groups in an extended IUPAC classification[24] (see **Figure 1.5**). Other shapes are sometimes found, and these can usually be explained as a combination of two (or more) of the nine shapes proposed and such an isotherm is then said to be *composite.*

The Type I(a) and I(b) isotherms are reversible and concave to the relative pressure (p/p^o) axis. They rise steeply at low relative pressures and reach a plateau: the amount adsorbed by the unit mass of solid, n^a/m^s approaches a limiting value, as $p/p^o \rightarrow 1$. They are obtained with microporous adsorbents. Enhanced adsorbent–adsorbate interactions occur in micropores of molecular dimensions. A decrease in the micropore width results in both an increase in the adsorption energy and a decrease in the relative pressure at which the micropore-filling occurs. The narrow range of relative pressure necessary to attain the plateau is an indication of a limited range of pore size and the appearance of a nearly horizontal plateau indicates a very small external surface area. Type I(a) corresponds to the filling of narrow micropores, whereas Type I(b) indicates the presence of wider micropores. With all Type I isotherms, the limiting adsorption is dependent on the available micropore volume. The Type II isotherm is concave to the p/p^O axis, then almost linear and finally convex to the p/p^O axis. This shape is obtained with a non-porous or a macroporous adsorbent, which allows unrestricted multimolecular adsorption to occur at high p/p^O. When the equilibrium pressure equals the saturation vapour pressure, the adsorbed layer becomes a bulk liquid or solid.

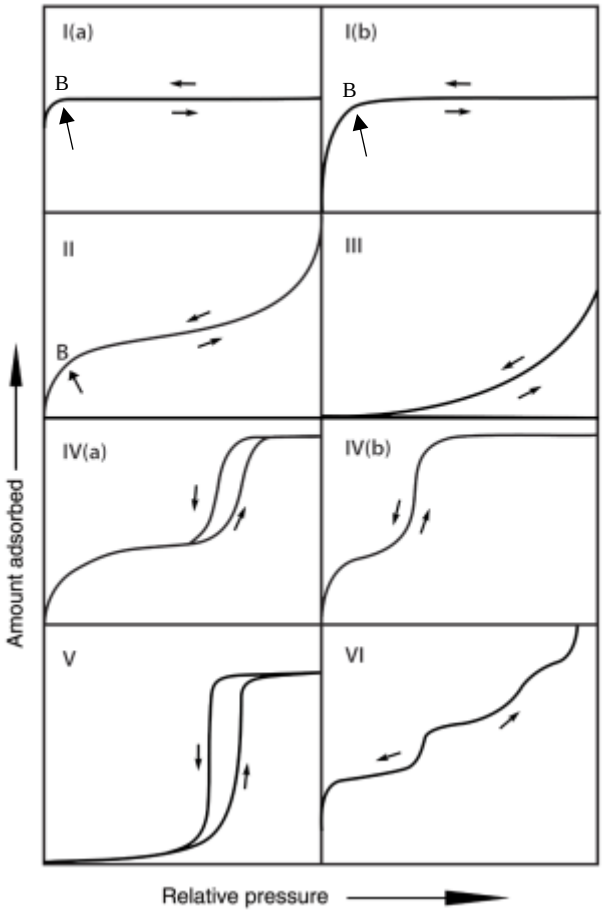

Figure 1.5. Classification of vapour adsorption/desorption isotherms according to IUPAC. Image reproduced from IUPAC technical report, M. Thommes et al., Physisorption of gases, with special reference to the evaluation of surface area and pore size distribution, 2015.

If the knee of the isotherm is sharp, the uptake at Point B – the beginning of the middle quasi-linear section – is usually considered to represent the completion of the monomolecular layer (the monolayer) and the beginning of the formation of the multimolecular layer (the multilayer). The ordinate of Point B gives an estimation of the amount of adsorbate required to cover the unit mass of solid surface with a complete monolayer (i.e. the monolayer capacity). A number of powders or aggregates (e.g. clays, pigments, cements) give Type II(b) isotherms. Here, the narrow hysteresis loop is the result of inter-particle capillary condensation. A Type III isotherm is convex to the p/p^O axis over the complete range and therefore has no Point B. This shape is indicative of weak adsorbent–adsorbate interactions on a non-porous or macroporous adsorbent. True Type III isotherms are not common. The Type IV(a) and IV(b) isotherms, whose initial region is closely related to Type II isotherms, level off at high relative pressures with a characteristic saturation plateau, although this may be short and reduced to an inflexion point. They are obtained with mesoporous adsorbents. Type IV(a) isotherms, which are much more common than Type IV(b), exhibit hysteresis loops: the lower (adsorption) branch is obtained by the progressive addition of gas and the upper (desorption) branch by the progressive withdrawal. The hysteresis loop is associated with the filling and emptying of the mesopores by capillary condensation. The Type V isotherm is initially convex to the p/p^O axis and also levels off at high relative pressures. As in the case of the Type III isotherm, this is indicative of weak adsorbent–adsorbate interactions,

but here on a microporous or mesoporous solid. A Type V isotherm usually exhibits a hysteresis loop which is associated with pore filling and emptying. Such isotherms are relatively rare. The Type VI isotherm, or stepwise isotherm, is also relatively rare and is associated with layer-by-layer adsorption on a highly uniform surface such as graphitised carbon. The sharpness of the steps is dependent on the system and the temperature. The above classification is necessarily somewhat idealised since, as already pointed out, many experimental physisorption isotherms have a composite nature and others are more complex than was formerly thought.

As stated above, gas adsorption isotherms can be used to derive some important parameters for porous materials characterization, such as specific surface area, total pore volume and pore size. The most important theory of gas adsorption on solid surfaces is the Langmuir model, while the Brunauer-Emmet-Teller (BET) model can be though as an improvement and a generalisation of the former model. These two theories are currently used in porous materials literature for gas adsorption data treatment and for the calculation of the aforementioned parameters. The detailed mathematical description of the two models along with the calculations performed to derive porosity parameters are reported in Appendix 1.

In brief, the two models calculate the surface area of a material from the adsorbed quantity of a probe gas. Each adsorbed molecule accounts for a certain occupied area that depends on its molecular cross-sectional area. The two models differ in the way they picture the adsorbent surface and about the possibility of multilayer adsorption (i.e., the adsorption of gas molecule over a layer of adsorbate). Even though both theories were developed for adsorption over a flat solid surface, they are commonly used for the data treatment of porous material, in particular of microporous material.

1.3. Metal-Organic Frameworks: porous materials on-demand

In chapters 2 and 3 of this thesis, a total of three new MOFs structures employing nitrogen-based ligands are reported. In this paragraph, a brief overview about Metal-Organic Frameworks chemistry and their possible applications will be given.

Metal-Organic Frameworks (MOFs) are a class of Coordination Polymers (CP). Coordination Polymer is a term used for the first time by J. C. Bailar in 1964[26] to identify all those compounds in which a polydentate linker, usually organic, is bound to a metal center either of the transition series or of the main groups. The linker and the metal centre are called *building blocks*. If the conditions are favorable, the synthesis of a CP will proceed through self-assembly (**Figure 1.6**) and eventually the pure final product will be isolated. CP properties are mainly determined by the characteristics of the building blocks. Among the numerous properties of CP's, porosity is one of the most studied. Coordination polymers that show intrinsic porosity are called Porous Coordination Polymers (PCP)[27]. MOFs can be listed in the PCP group.

MOFs research started in the 1990s with the pioneering work of Omar Yaghi, who first reported the synthesis of a stable MOF with permanent porosity, the so called MOF-5[28]: During the last 30 years, interest around MOFs never faltered. The never-ending attention on these materials is fuelled by the great versatility with which new MOFs structures can be designed.

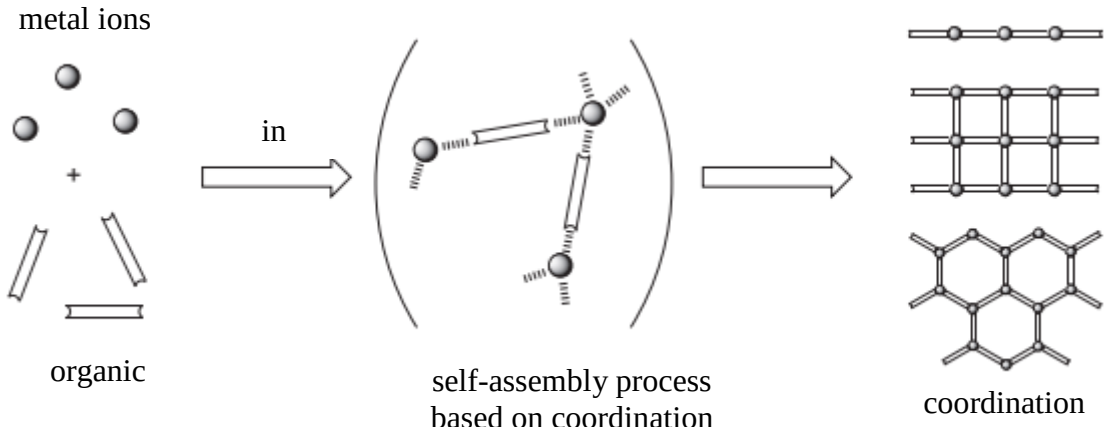

Figure 1.6. Schematic representation of the synthesis guided by self-assembly of a coordination polymer.

As previously stated, MOFs are constructed by joining an organic linker with a metal centre. As long as the linker has at least two suitable binding sites for the metal ion, any molecule can in principle be used in MOFs synthesis. This means that a tailored organic linker can be design for a precise application, synthesized utilizing standard organic chemistry protocols and used to build a MOF with a precise spatial geometry. The numerous metal ion that have been proven adapt for MOFs preparation add even more variety to the possible structures. This led to the synthesis of tenths of thousands of different MOFs structures: the Cambridge Crystallographic Data Centre contains 75 600 entries for MOFs (research based on 5.38 CDS version)[29]. When such a great number of possibilities is thrown into the bowl, scientists always feel the urge to rationalize the process and find a way to foresee at least to some extent the result of an action. The principles that govern MOFs formation have been identified by Yaghi, Eddaudi and O'Keeffe in what today is known as *reticular synthesis*[30], which can be defined as the process of assembling judiciously designed rigid molecular building blocks into predetermined ordered structures (networks), which are held together by strong bonding (**Figure 1.7**).[31]

This approach is different from retrosynthesis of organic compounds because the structural integrity and rigidity of the building blocks in reticular synthesis remain unaltered throughout the construction process—an important aspect that could help to realize fully the benefits of design in crystalline solid-state frameworks. Similarly, reticular synthesis should be distinguished from supramolecular assembly because, in the former, building blocks are linked by strong bonds throughout the crystal. Following the principle of reticular synthesis, scientist can foresee the crystal structure of a MOF, its pore dimension and its properties with a satisfactory reliability.

In early days of MOFs research the main objective was creating porous structures with the highest possible surface area. Today, the world record is held by NU-110[32], a Cu(II)-based MOF synthesized by Omar Farha in 2012 showing a BET surface area of 7000 m^2/g.

However, thanks to their easily tunable and predicatable properties, researcher envisaged more sophisticated properties for MOFs and they found possible applications in a plethora of different fields that includes gas storage and separation[33], catalysis[34], drug-delivery[35], bio-imaging[36], proton, electron and ion conduction[37], optoelectronic applications[38] and more.

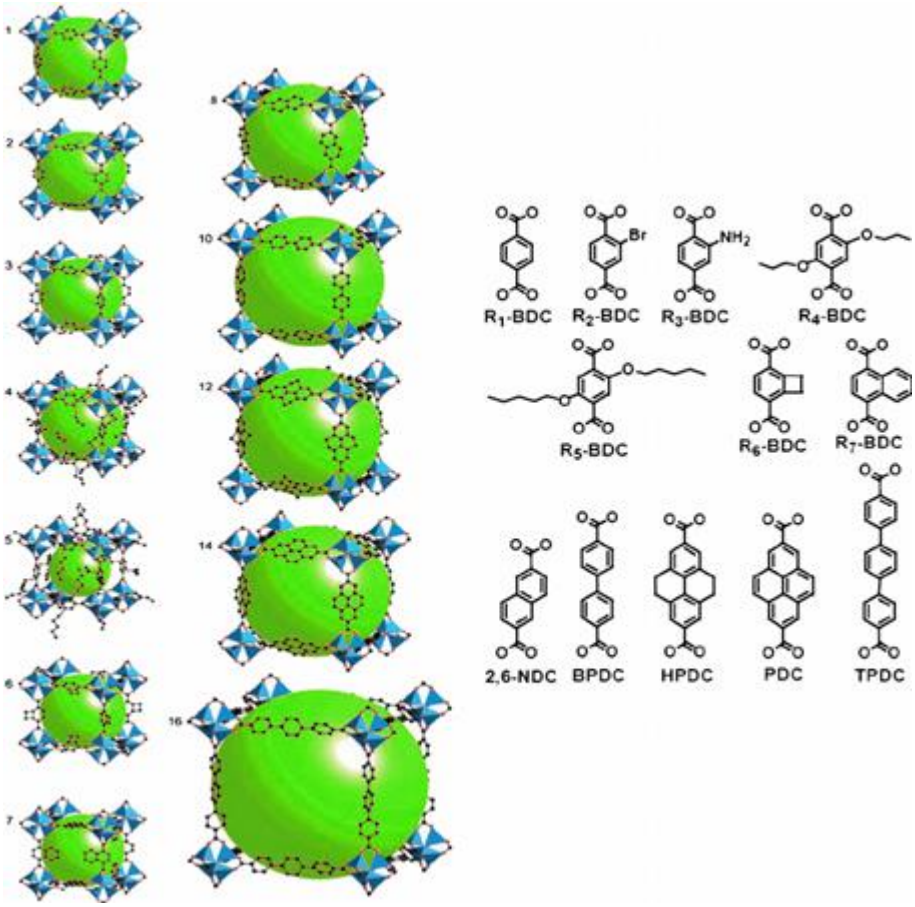

Figure 1.7. Application of the reticular synthesis *principles for the preparation of the IRMOF family by Eddaoudi et al. In this work, a series of rod-like bidentate ligands with different length and functionalities was reacted with a Zn(II) salt to prepare a family of isoreticular MOFs. The green spheres represent voids of each framework. Image reproduced from* Science*, 2016, 295, 5554, 469.*

Although MOFs synthesis might look easy, especially if you are employing commercially available ligands, this is not really the whole story. It is true that MOFs structure and properties are largely predictable. Still, at some point, someone must go in the lab and synthesize them. As a synthetic material scientist, I dare to say that MOFs synthesis and chemical synthesis in general are 80% science and 20% art, as without the proper lab

experience and a pinch of experimental attitude, no matter how many procedures you read, you will end up with some undefined yellow-to-brown substance in your flask.

As previously stated, to be eligible for MOFs synthesis, an organic linker must have at least two suitable binding sites for the metal ions. The most common functional group used in this regard is the carboxylate group. Carboxylates are widely used because of their simple synthesis, well known coordination chemistry and chemical and thermal stability. However, carboxylate-metal bond is often very sensible to chemical aggression, for example from moisture. The new MOFs presented in this thesis all employ nitrogen-based ligand. Polyazolate[39] systems offer a closely related stereochemistry to carboxylate and, at the same time, a higher basicity, possibly guaranteeing more robust coordinative bonds and, consequently, more stable structures. Among the N-based ligands, pyrazole constitutes an excellent candidate as metal-coordinating group because its chemistry is well known and, when in anionic form, can firmly bind various type of azophilic transition metals. Over twenty different coordination modes have been observed for pyrazolate anion, but the most common are *mono*-dentate, *endo*-dentate and *exo*-bidentate[40].

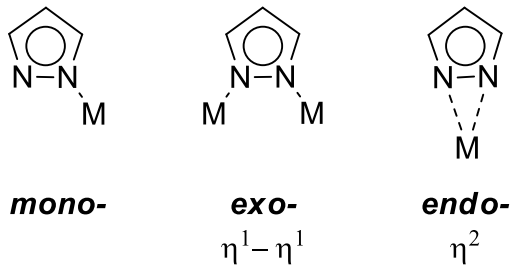

Figure 1.8. The three most common coordination modes for the pyrazolate anion

The *exo*-bidentate mode allows the binding of multiple metal centres per ligand unit, thus creating 1-D metal-organic polymers chains. Three different modes are known for this coordination, with metal centers bridged to one, two or three units of pyrazolate.

During the course of the years, many synthetic protocols for the functionalization of pyrazoles have been reported and know they can be exploited to prepare organic ligands suitable for MOFs synthesis (**Figure 1.10**). For example, Yin and Kitagawa synthesized the ligand 3,3',5,5'-tetramethyl-4,4'-bipyrazole (H_2Me_4BPZ) and they used it to prepare [$Cu(Me_4BPZ)$][41] and [$Ag_2(Me_4BPZ)$][42], respectively. Later, Long synthesized 1,4-benzenedi(4′-pyrazolyl) (H_2BDP), a ligand that can be viewed as an extension of H_2Me_4BPZ, and used it to build MOF [Co(BDP)][43]. This material shows very unusual five-step N_2 sorption and broadly hysteretic H_2 sorption at 77 K, which were ascribed to the scissor-like breathing of the framework. Using the same ligand, Galli et al. prepared [Ni(BDP)][44] which showed a framework flexibility similar to [Co(BDP)].

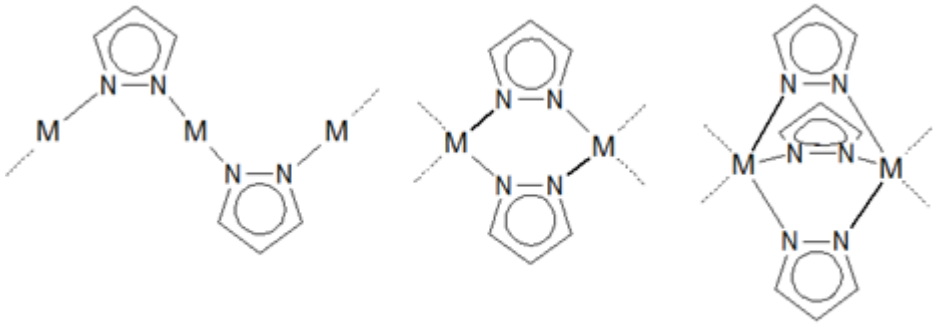

*Figure 1.9. Schematic representation of the three **exo**-bidentate pyrazolate-metal coordination modes.*

The strategy of extending the length of the organic ligand while keeping the same metal ion to prepare new structures with larger pores is very common in MOFs research and it is based on the *isoreticular principle*[31] (**Figure 1.7**). According to this principle, the topology of the final structure depends on the geometry of the organic linker and on the coordination geometry of the metal nodes. Thus, extending the length of the linker, i.e. moving the coordination sites further apart, and keeping the same metal ion, should give a series of isoreticular structures with pore dimensions proportional to the organic linker length.

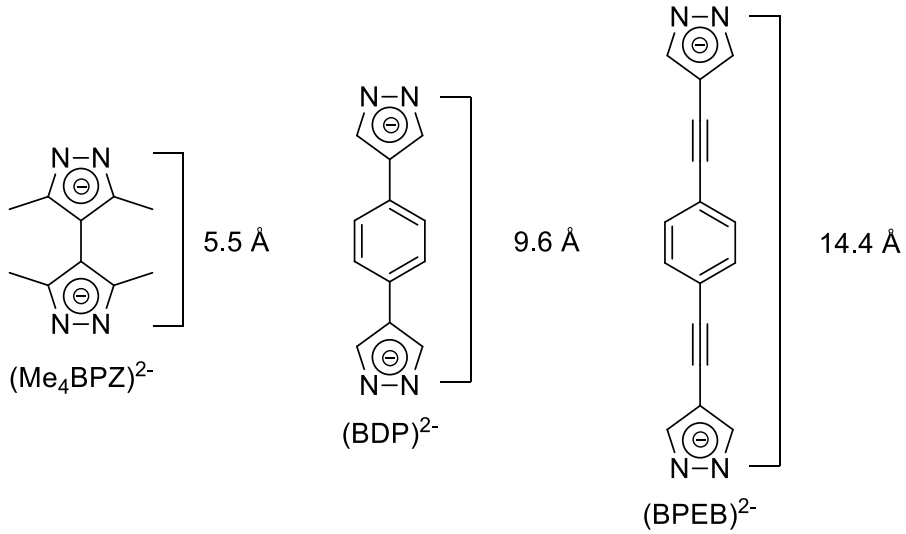

Figure 1.10. Chemical structure of some bis-pyrazolate used in MOFs preparation

Although with some limitations, this principle has been successfully applied many times and it was followed by Long to design H_2BDP and again by Masciocchi et al. when they synthesized 1,4-bis(1H-pyrazol-4-ylethynyl)benzene (H_2BPEB) (**Figure 1.10**). H_2BPEB was then employed to prepare [Zn(BPEB)], [Ni(BPEB)] and $[Fe_2(BPEB)_3]$[45], which all showed very good surface areas and gas adsorption capacities. The addition of triple bonds on the *para* positions of the central aromatic ring did not only elongate the ligand, but possibly made it a *molecular rotor*. The *para*-phenylene ring of H_2BPEB is expected to show fast rotational dynamics

around its 1,4-axis thanks to the low energy barrier for rotation around C-C *sp*-*sp*^{2} bods and the free volume surroundings rotors guaranteed by the porous structure of the MOFs. This is what gave birth to chapters 2 and 3 of this thesis where the synthesis of new MOFs employing two derivatives of H_2BPEB (H_2BPEB-d_4 and H_2BPEFB) and of the characterization of the dynamics in solid-state of the central *p*-phenylene ring are described. In Paragraph 1.5 a brief overview about molecular motors and rotors in solid materials will be given.

1.4. Going organic: Covalent Organic Frameworks

Chapters 4 and 5 of this work deal with the design, synthesis and characterization of a total of five new fully organic porous frameworks. In this paragraph, a brief overview of Porous Organic Frameworks (POFs) will be given.

As mentioned in paragraph 1.1, the family of POFs is rather large and contains many sub-categories of materials, some of which are considerably different one from the other. The common tract among all these relatives, beside their fully organic nature, is the covalent bond network that held them together. A variety of chemical bonds have been successfully exploited to build POFs, ranging from boronic esters, to amides, to carbon-carbon bonds. Giving a full description of all the existing categories of POFs is beyond the scope of this thesis and the reader can refer to the cited literature for further information[18-22]. Here we will deal only with Covalent Organic Frameworks (COFs), Conjugated Microporous Polymers (CMPs), and Porous Aromatic Frameworks (PAFs).

COFs offers an easy link to the world of MOFs as they are crystalline porous materials constructed upon rigid building blocks with defined geometries[21]. This last characteristic makes possible to adopt the principle of MOFs reticular synthesis and foresee the crystal structure of the COF that would be obtained from building blocks with a certain geometry (**Figure 1.12**).

Of course, COFs networks are built upon covalent bonds and this make them generally more robust against high temperatures, chemical aggression and aging compared to MOFs. This last characteristic is precisely why we started investigating covalent frameworks in our research. The first work on COFs was reported by Yaghi and co-workers in 2005 when they synthesized COF-1 and COF-5[46]. They are both based on condensation of boronic acid derivatives to give boroxine rings. COF-1 is obtained from condensation of 1,4-benzenediboronic acid (BDBA), while COF-5 is prepared reacting BDBA with 2,3,6,7,10,11-hexahydroxytriphenylene (HHTP) (**Figure 1.11**). After that pioneering paper, tenths of new structure have been published on the topic. Much alike MOFs, the flourishing of this research topic is mostly due to the infinite possibilities offered by the organic synthesis of the building blocks that can be used in COFs preparation. Moreover, COFs offer a further degree of freedom during the design step as many different covalent bonds are eligible in their preparation (boroxines, boronic esters, amides, imines, azines, alkenes and more)

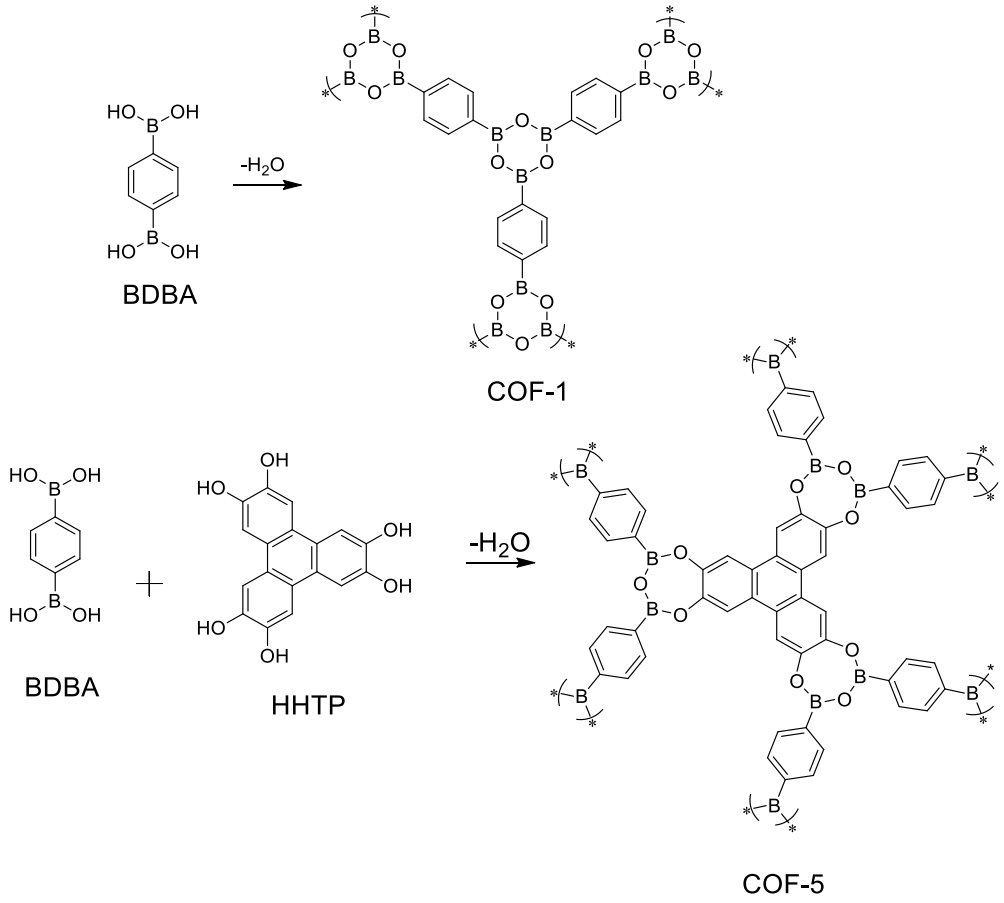

***Figure 1.11**. Schematic synthesis and structure of COF-1 and COF-5.*

Consequently, a great variety of applications has been proposed for COFs, ranging from gas storage[47], purification[48] and separation[49] to energy storage[50], from catalysis[51] to proton conduction[52], from optoelectronics[53] to biomedical applications[54].

An interesting example of an advanced application for COFs material was reported by Jianquan Lv and coworkers in 2018[50]. They reacted 1,4,5,8-naphthalene-tetracarboxylic dianhydride (MTDA) with tris(4-aminophenyl)amine (TAPA) to build NT-COF, so it consists of the extended aromatic 1,4,5,8-naphthalenediimide (NDI) as electron-poor building units and triphenylamine (TPA) electron-rich building units. They demonstrated that NT-COF is able to directly transform solar energy in electrochemical energy thanks to the ultrahigh efficient intramolecular charge transfer from the TPA to the NDI and the highly reversible electrochemical reaction in NT-COF. To do so, they built a prototype electrochemical device with NT-COF as cathode and Li as anode for direct solar-to-electrochemical energy conversion and storage and showed that, when operated under direct sunlight, the device efficiency increased by 38.7%.

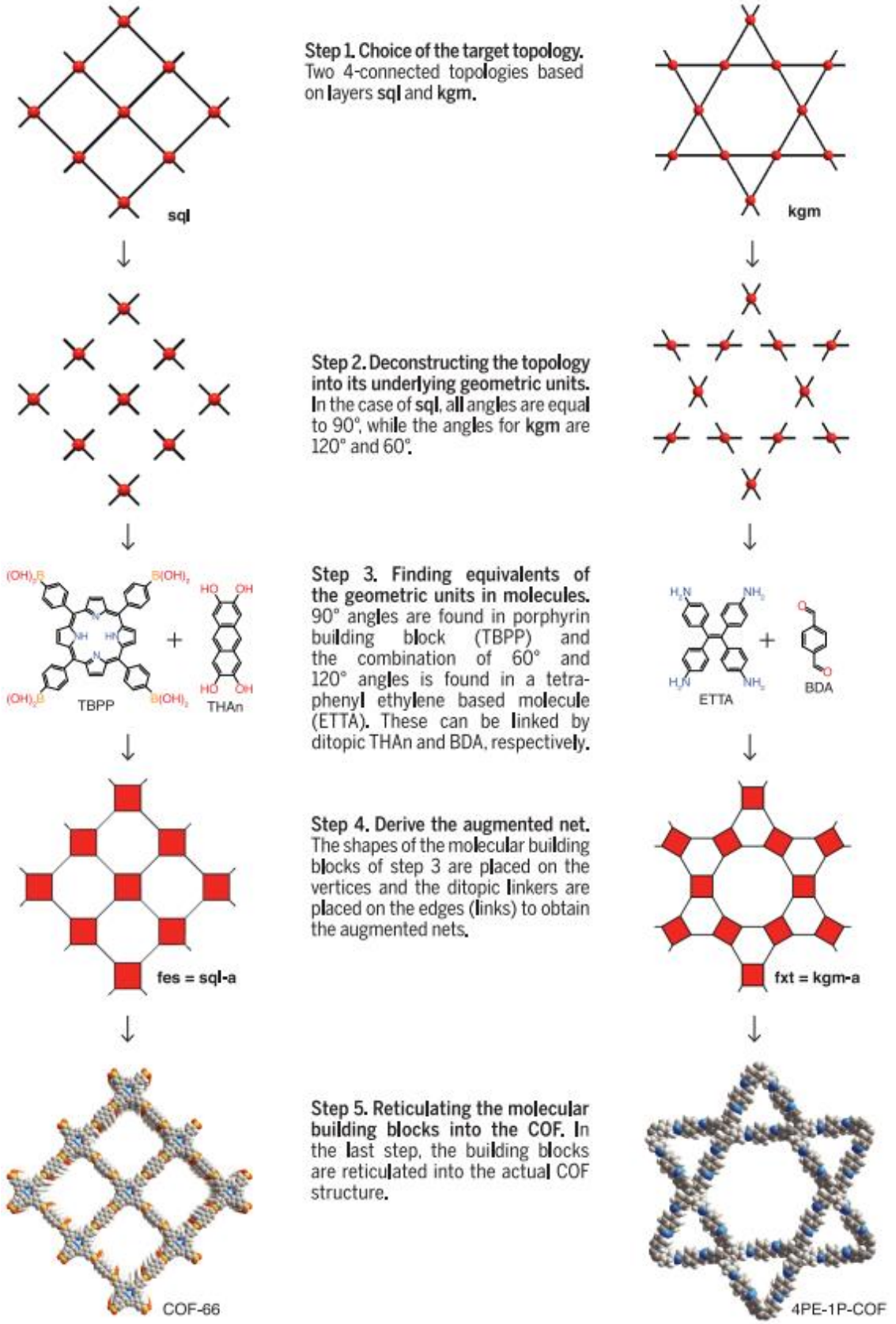

Figure 1.12. The principles of reticular synthesis applied to COFs synthesis. Image reproduced from Diercks et al., Science, 2017, 355, aal1585.

Closely related to COFs, but amorphous in nature, are CMPs. The name CMP refers to a macromolecule that possesses a microporous network that has building blocks within the system that give rise to π-conjugation[55]. This conjugation is a result of alternating single and multiple bonds which arise from the overlap of two *p* orbitals (or *d* orbitals) crosswise with an intermediary σ-bond. CMPs possess this conjugation to a certain degree. The alternation of π and σ bonds throughout the network readily allows their structure to be utilized electronically. In tandem with inefficient molecular packing, CMPs offer properties for not only electronic but also porous applications. These materials are amorphous due to the freedom of rotation about the s bonds formed between building blocks. CMPs made their first appearance in a 2007 paper by Cooper and co-workers: in that work, a series of poly(aryleneethynylene) networks, namely, CMP-1, CMP-2, CMP3 and CMP4, was synthesized employing the Sonogashira-Hagira cross-coupling of alkyne and halogen monomers[56]. Again, thanks to the possibility of both pre and post-synthesis functionalization of building blocks, many CMPs frameworks have been synthesized since the first report. In this thesis, we adopted the methodology introduced for the synthesis of CMPs (i.e. the Sonogashira coupling and the use of aryl halogenide and terminal alkynes building blocks) to prepare two new fluorinated frameworks (**1FCOP** and **2FCOP**, see Chapter 5).

Lastly, at least for the purposes of this work, PAFs will be briefly overviewed. PAFs are open framework porous polymers bearing high surface area and stability[22]. They owe their outstanding surface area (more than 5000 m^2/g) to monomer's structure and reaction conditions. The superb stability of PAFs can be ascribed to its covalent bonds and rigid phenyl framework. PAFs came into the scientific limelight in 2009 when PAF-1 was synthesized by Yamamoto homocoupling of tetrakis(4-bromophenyl)methane[57]. The differing factor between PAFs and CMPs is that PAFs lose their framework conjugation since the conjugation is broken by the central atom of the tetrahedral monomers, whereas CMPs maintain the conjugation that originates from the monomers. The crystalline structure of diamond acted as the cue for the design of PAF-1 wherein it was reasonably speculated that substituting phenyl groups for C-C covalent bonds of diamond would sustain the stability (comparable to diamond) in the structure of PAF-1 besides indulging in ample exposure of the phenyl groups, which might help expand the internal surface area of PAF-1. Once again, chemical synthesis of building blocks and post-synthetic functionalization protocols paved the way to a still increasing number of new PAF structures. In Chapter 5 of this thesis, we extended the original work of Teng Ben to prepare two new fluorinated PAF materials.

It is worth pointing out that in all the new fluorinated materials reported in this work, the fluorine substituents were introduced on the *p*-phenylene rings to study their effects on gas adsorption properties respect to non-fluorinated analogues. Furthermore, we wanted to induce a net dipole moment and prepare a series of porous organic frameworks bearing dipolar molecular rotors possibly being able to move in the solid state.

In chapter 4, it is presented a completely new field of research where we focused on bringing the outstanding properties of Feringa's molecular machines from the solution to the solid state. A new PAF-like material containing bistable molecular switches able to operate in the solid state was prepared and characterized.

1.5. And yet it moves: design and characterization of advanced materials showing solid-state dynamics

In the title of this thesis and in the previous paragraphs of the introduction, it was anticipated that one the central topic of this work is the study of the dynamics of mobile elements in solid porous structures. In this paragraph, a brief overview about molecular rotors in solid-state and photo-switchable systems in solid-state will be given.

Sci-Fi literature is rich of futuristic materials and devices able to operate at the microscale much alike macroscopic machines does in our XXI century world. The most known (and most terrifying) example in this regard are the self-replicating nano-machines that constitute the *grey goo*[58]*:* in this futuristic apocalyptic scenario, mankind loses control over these nano-bot that start de-assembly every organic substance they find to produce more and more copies of themselves, transforming the entire Earth in a dead, grey wasteland.

Figure 1.13*. Well, that orange thingy is most probably a virus, dear killer nano-bot, but we get the message.*

Of course, building such advanced machines poses so many - at the moment - unsolvable problems, that the scientific community doesn't even bother to think about the possibility of such a scenario. However, this example is useful to demonstrate the central point of my thesis: advanced nanotechnology applications require precise control over positions and movements of microscopic objects. In truth, it is not necessary to invoke fantasy to find examples of what one could achieve with accurate control over microscale motion. Nature, as usual, had already done it, way in advance and better than us: the enzyme ATP synthase[59] (molecular rotor), the bacterial flagellar motor[60] (molecular motor), the animal muscle tissue[61] (molecular shuttle) are three examples that are typically cited when talking about the endless possibilities offered by the ability to control microscale dynamics.

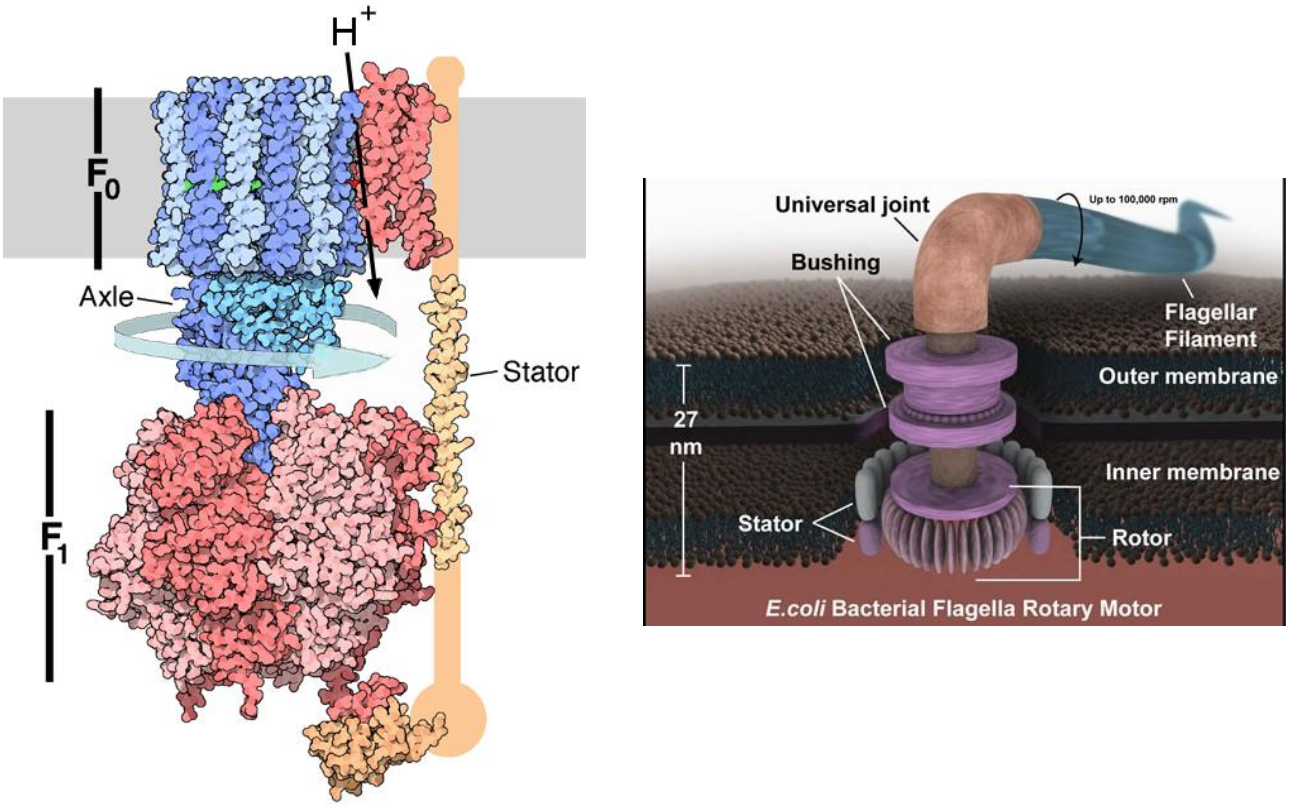

Figure 1.14. Left: graphic representation of the structure of enzyme ATP synthase. Right: schematic representation of bacterial flagellar motor.

Adenosine triphosphate (ATP) is the molecule that provides energy to many processes occurring in living organisms, such as muscles contraction or nerve impulses. ATP is produced by an enzyme called ATP synthase (**Figure 1.14 Left**) whose functioning is based on the rotation of the F_0 portion, which is immersed in the cellular membrane. The rotation is fuelled by a gradient in proton concentration. The F_0 fragment is connected to the F_1 segment through an axle that conveys the rotation to F_1. The rotation, in turn, generates a series of conformational changes that results in the opening and closing of the subunits that form F_1 and this is the beginning of a complex series of events that lead to the consumption of Adenosine diphosphate (ADP) to produce ATP. Bacterial flagellar motor (**Figure 1.14 Right**) is a true masterpiece of supramolecular assembly. It is an extremely complex structure composed of many different fragments all interconnected together, whose common task is to propel bacteria in liquid environments. It is powered by either a proton or Na^+ concentration gradient, depending on the bacterium, and it is capable of both clockwise and counter clockwise motion. It has also been shown that the motor assemble is sensitive to chemotactic signals and can modify its behaviour as the external environment changes.

With these premises it not surprising that an increasing number of scientist dedicated their efforts to the study of molecular dynamics in the last century. As it is often the case, the first fundamental studies regarded simple dynamics of small molecules or molecular fragments (methyl groups, crowded biphenyls, phenyls) in solution and in gas phase. However, the interest soon shifted to more complex systems showing interlocked motion

that resembled that of macroscopic objects such as gears, propellers and turnstiles. The review from Kottas et al. retrace in great details the early days of artificial molecular rotors research[62].

As a representative example of the studies performed on geared systems in solution, the works from Iwamura and Mislow are the ideal candidates. They independently demonstrated for the first time truly geared motion in ditriptycyl ethers and ditriptycyl methanes (**Figure 1.15**). They consist of two three-toothed gears, and the intermeshing between the phenyl groups on the two triptycenes leads to little or no slippage of the gears, even at high temperatures. In these systems, there is no doubt that rotation of one triptycene unit causes the disrotation of the other in a frame of reference that keeps the central linker atom static.

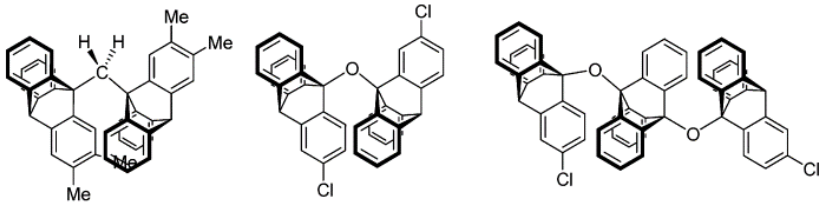

Tp_2C Tp_2 Tp'OTpO

Figure 1.15. Triptycene-based molecular gears

Already in these first works, the idea of controlling the motion of these rotors and eventually exploiting it to build complex devices able to operate at the micro- or even at the macro-scale was the driving force behind them. From those fundamental studies, more complex systems were designed and synthesized, such as molecular shuttles[63], rotaxanes[64], molecular switches[65] and motors[66]. However, many of these systems were designed to work in solution and a liquid is definitely not suitable to build a device, not only because of engineering difficulties but mostly because of a fundamental problem: solutions are isotropic. This means that, even employing the exceptional unidirectional molecular motors of Feringa[67–69], one cannot achieve unidirectional collective motion as long as molecules are dissolved in solution, and, thus, one cannot bring microscopic movements to the macroscale. Because of this, scientists started studying motional phenomena in solid-state. Solid matter is not so immobile as it looks: in addition to examples of soft materials, such as cross-linked polymers above their glass transition[70], even shape-persistent structures, such as crystals, can show remarkable dynamics in their various components. We were particularly interested in the latter, which are also known as amphidynamic crystals[71]. Motion in these materials should occur in a highly anisotropic manner and within a well-defined frame of reference, which should be ideal for the development of artificial molecular machines.

Some of the most promising structures to form amphidynamic crystals are based upon *molecular rotors*. These molecules should be designed with rigid frames, which can generate local free volume within an otherwise densely-packed environment, linked through pivots and axles to support rotary parts. While this entire

molecular "assembly" can be referred to as a *molecular rotor*, the portion of the molecule that provides a static frame of reference is known as the *stator*, and the part undergoing motion is known as the *rotator*. The most common -and most successful- design of molecular rotor employs a 1,4-diethynylbenzene rotor[72–76]: the central *para*-phenylene ring is the actual rotating fragment, while the triple bonds work as an *axle* that facilitates the rotor motion. It is known, in fact, that rotation around a *sp*-*sp*^{2} bond is essentially barrierless in the gas phase[77,78]. The fundamental requirement to achieve fast dynamics in the solid-state is enough free space around the rotor so it could undergo unhindered rotation. In early examples of solid-state rotors, this was achieved by linking the central *p*-phenylene ring to bulky side groups that would function as both stator and spacers[75]. The voluminous stators prevent efficient packing of molecules 1-5, thus generating low density crystals. The results of this strategy are summarized in **Figure 1.16**.

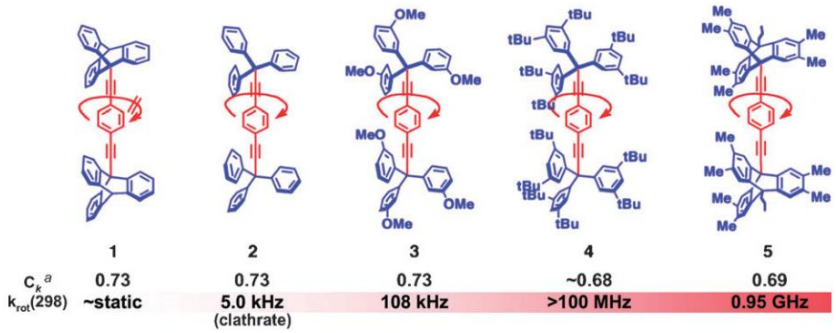

***Figure 1.16**. A series of molecular gyroscopes with* para*-phenylene rotators exemplifies that alterations in stator structure translate to packing differences in the crystalline state, which are ultimately reflected in rotator dynamics (where $k_{rot} = (1/\tau_0)exp[Ea/RT]$ as determined by SS NMR)*

Molecules 1-5 were crystallized in appropriate conditions and the speed of the rotors was then measured in solid-state. Bulkier stators provide more free space in the rotor vicinity; this results in lower activation barrier for the rotation and, consequently, faster reorientation. However, frustrated packing is not the most efficient strategy to generate free volume in a solid bulk material. Moreover, rotors are totally inaccessible from the external environment as they are closed inside the molecular cage that provides them the necessary free space. In previous paragraphs, we described various strategies to prepare highly porous materials, that is, materials with plenty of free volume. Inserting molecular rotors in porous framework would be an interesting method to prepare a new class of functional materials, since the dynamics of the rotors collection would be tunable by an external chemical stimulus such as guest adsorption. This is the idea that was pursued by Sozzani group and that led to the preparation of several rotor-containing porous materials. For example, in 2010 they demonstrated the ultra-fast dynamics of the *p*-phenyl ring rotors in a Periodic Mesoporous Organisilica (PMO)[79]: rotors were able to rotate at frequencies as high as 56 MHz at room temperature and their dynamics could be regulated by guest adsorption. Even higher rotational speed was measured for the phenyl rings in a PAF-3 sample (>10^8 Hz at room temperature)[80]. Again, rotors dynamics was finely tuned by guest adsorption. Both these materials constitute a new type of chemical sensor.

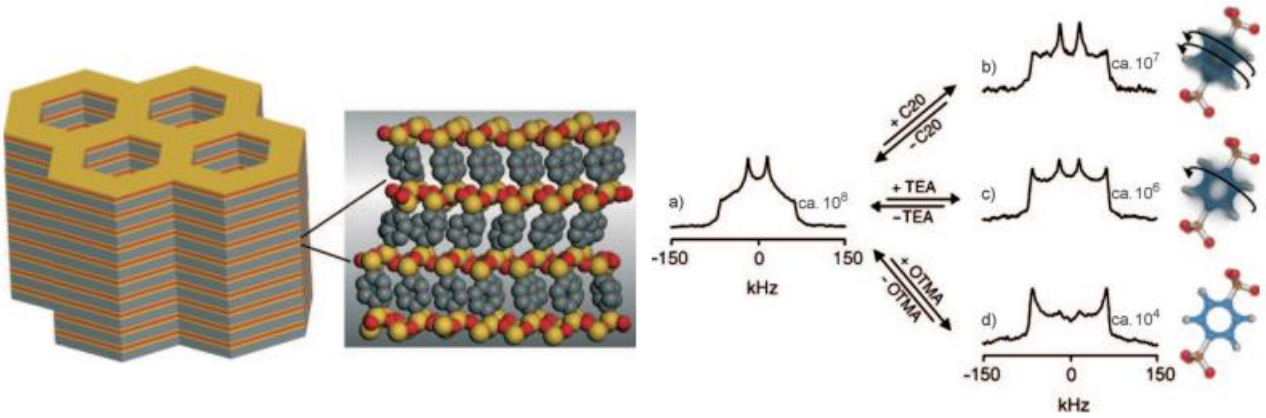

*Figure 1.17. **Left**: Schematic representation of the mesoporous* p*-phenylenesilica (PPS). Each p-phenylene rotor pivots on two silicon atoms through C-Si bonds that are inserted in inorganic siloxane layers. Rotors are aligned along the channel axes and exposed to the internal free volume of the empty channels. **Right**: Deuterium NMR spectra of mesoporous [D_4]PSS with b) eicosane (C_{20}), c) triethylamine (TEA), and d) Octadecyltrimethylammonium bromide (OTMA) guests compared to the empty matrix (a). The samples containing C_{20} (b) and TEA (c) show mobility intermediate between the two extreme cases (a, d). The exchange rates (k in Hz) for each spectrum are given*

Figure 1.17 (right) allows to introduce one of the most powerful techniques used in the study of molecular dynamics in solid state, that is deuterium solid-state NMR[81]. Deuterium has an integer nuclear magnetic spin moment, I(^{2}H) = 1 and thus has a quadrupolar nuclear magnetic moment. Since I(^{2}H) = 1, the nuclear magnetic spin number of a deuterium nucleus in an external magnetic field can assume three values: m_I = 1 (parallel to the external field), m_I = -1 (antiparallel to the external field) and m_I = 0 (perpendicular to the external field). As a result, in case of a C-D bond, the interactions between deuterium nucleus and the external magnetic field strongly depends on the orientation of the C-D vector respect to the external magnetic field. In a solid sample, C-D vectors will generally be fixed in their position. If a polycrystalline sample is analysed, one would observe a collection of all the possible orientations. This, in turn, gives rise to a particular signal pattern known as *Pake pattern* (**Figure 1.18**). The distance between the two peaks in **Figure 1.18** is equal to the energy difference between the state with m_I = 1 and with m_I = -1. If the C-D vectors are not fixed in space, but can move, the shape of the corresponding ^{2}H-NMR will vary accordingly to the mechanism and the speed of motion. Thus, by collecting ^{2}H-NMR spectra of a sample ad different temperature, one can deduce important parameters such as the mechanism of motion and its frequency, as already mentioned, the energy barrier and the pre-exponential factor ω_0.

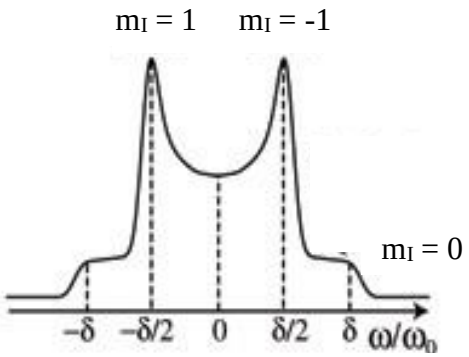

Figure 1.18. Simulated ^{2}H-NMR of a polycristalline sample.

These last two parameters are derived from an Arrehnius plot of the frequency versus the temperature as the frequency depends from the temperature according the following equation

$$\omega = \omega_0 e^{E_A/RT} \qquad [1.2]$$

Where E_A is the energy activation barrier for the motion and the pre-exponential factor ω_0 is called *attempt frequency*.

Driven by the outstanding results already obtained in the field of solid-state dynamics in porous material by the research group of Sozzani, we started working on the design of a ligand able to sustain ultra-fast rotation of molecular rotors in the solid structure of a MOF (see **Figure 1.10**). Fast rotation of molecular rotors in MOF structures has never been demonstrated before, although some attempt have been made[82]. This led to the results discussed in Chapter 2 of this thesis where fast dynamics of *p*-phenylene rotors in a MOF structure is demonstrated for the first time.

One of the most thrilling application proposed for molecular rotors concern dipolar rotors having a net dipole on the rotating ring. In principle, the position of the rotating dipole could be regulated by external stimuli such as electric fields or light. If the external electric field is strong enough, it would align dipoles in the same direction, thus generating a reorientable macroscopic net dipole that would allow to envisage new materials based on dipolar molecular rotors such as switchable ferroelectrics, optoelectronic materials and radiofrequency filters[83–85]. In this scenario, low energy barriers for rotation are desirable so weak electric field will be sufficiently strong to control rotors position and fast dynamics is attractive to design devices with short response speed. The most efficient strategy to generate dipoles on *p*-phenylene rotors is to introduce one or two fluorine substituents: the high electronegativity of the fluorine atom would create an asymmetry in the electric charge distribution of the ring, thus producing the desired electric dipole moment (**Figure 1.19**). Furthermore, the small dimensions of fluorine atoms ensure that the dipole is generated without increasing

significantly the steric hindrance between the rotor and its surrounding, thus ensuring that the necessary free space for fast dynamics is retained.

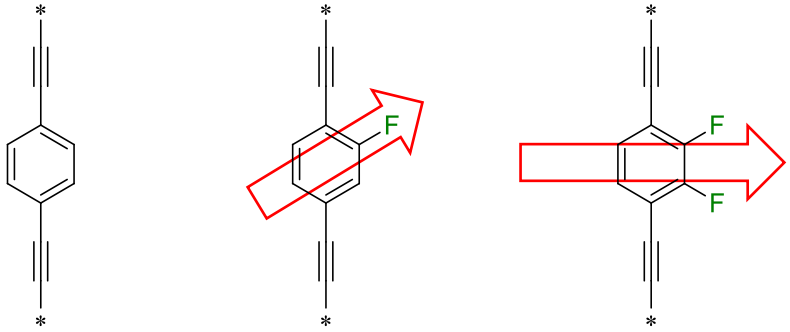

Figure 1.19. Schematic representation of the most common and efficient dipolar molecular rotors. The red arrows represent the net electric dipole moment across the rotor.

A few examples of fast dipolar rotors can be found in literature, both regarding non-porous and porous materials. For instance, Garibay synthesized a series of so called molecular compasses bearing dipolar rotors (compounds 11a-e in **Figure 1.20**)[86–88].

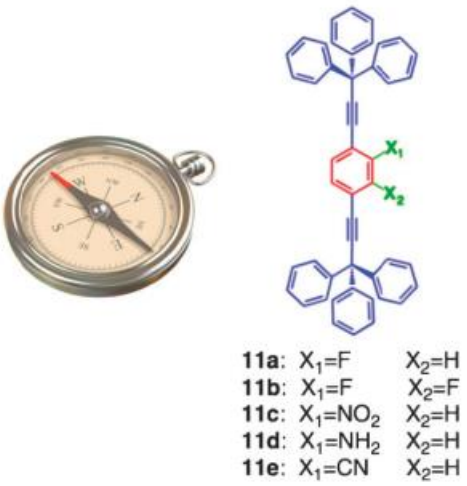

Figure 1.20. Chemical structures of a series of dipolar molecular rotors synthesized by Garcia-Garibay and co-workers.

Similarly to molecules reported in **Figure 1.16**, compounds **11a-e** crystallize in close packed structures and the free space around the rotors is generated by inefficient packing due to the bulky stator groups. The mobility of compound **11**, for example, was demonstrated by Dielectric Loss Spectroscopy (DLS) measurements[89]. This technique is based on the interaction between an electric dipole of the sample and an external oscillating electric field. The dielectric properties of the material are measured as a function of temperature at a fixed

frequency of the external electric field applied. A maximum dielectric dissipation signal occurs when the frequency of the internal rotation matched that of the applied AC field. In this way, an energy barrier of 14-15 kcal/mol and a rotational frequency of 100 kHz at 340 K were measured. The challenge to conjugate dipolar rotors and porous solid materials was once again picked up by Sozzani and co-workers who realized a PMO bearing a dipolar *p*-phenylene ring supported by a di-vinylene axis[90]. In their paper they showed that the fast dynamics of the dipolar rotors collection could be stopped by adsorption of iodine vapors that reacted with ligand double-bonds.

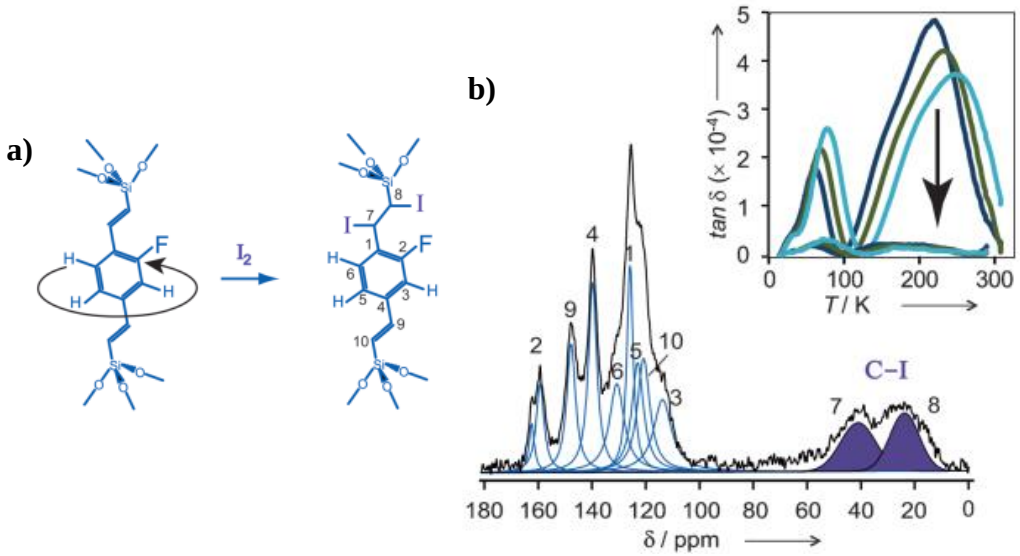

***Figure 1.21**. a) Schematic representation of I_2 addition on unsaturated double bonds of FOS-1. b) ^{13}C CP MAS NMR spectrum of FOS-1 after reaction with I_2. In the inset, the reduction of dielectric loss of iodine reacted FOS-1, as compared to pristine FOS-1, is shown at the three distinct observation frequencies. Black: 140 Hz, green: 1400 Hz, and light blue: 14 kHz*

However, the field of dipolar rotors in porous materials is still mostly unexplored. In particular, fast dynamics of dipolar rotors in MOFs have never been demonstrated. Motivated by the results obtained from our rotor-containing MOF (Chapter 2), we designed a new ligand, H_2BPEFB, bearing a dipolar rotor obtained through the addition of a fluorine atom on the central *p*-phenylene rotor and we used it to prepare a Zn(II) and a Ni(II) MOF. The synthesis and characterization of the ligand and its MOFs are presented in Chapter 3 of this thesis. Investigations about dipolar rotors dynamics are currently ongoing, but preliminary data seem to suggest fast dynamic for the dipolar rotors array.

Similar arguments led to the development of Chapter 5, where the synthesis of four new fully organic covalent frameworks is presented along with their characterization. All the new frameworks bear asymmetrically fluorinated phenyl rings that could possibly behave as molecular rotors. Differently from the MOFs of Chapter 3, in Chapter 5 we decided to exploit the robustness of covalent carbon-carbon bonds to build more robust porous frameworks.

Molecular rotors in solid materials are undoubtedly the more mature topic in the field of dynamics in artificial solid systems. This is because the relatively simple dynamics of the rotors allowed scientists to focus their attention on rotors surroundings, so we learned how to control the space around rotors to reach faster and faster dynamics and an entire new research field developed. However, molecular rotors suffer from one major drawback: although their dynamics can be regulated by external stimuli (as Sozzani repeatedly proved), they cannot be really turned on and off. If we think at every macroscopic machine humanity has built, their activity, and so their motion, can always be switched on and off at need. It is then reasonable that, to design devices based on microscopic motion, their components should show a similar behaviour. To address this topic, in recent years scientists started to look at different systems that might behave as molecular switches in solid-state. Molecular switches are compounds that can reversibly transforms into two or more (meta)stable states in response to environmental stimuli (pH, redox, light, temperature, etc.)[91]. The most studied and the most used in stimuli responsive materials is the azobenzene group[92,93]. It is known that azobenzenes undergo a trans-to-cis isomerization upon irradiation with UV light and the process can be reverted by irradiation with visible light or heat. Of course, the isomerization implies a radical change in molecule's shape that is accompanied by an electric dipole moment and occupied volume change (*trans* is planar, while *cis* is not).

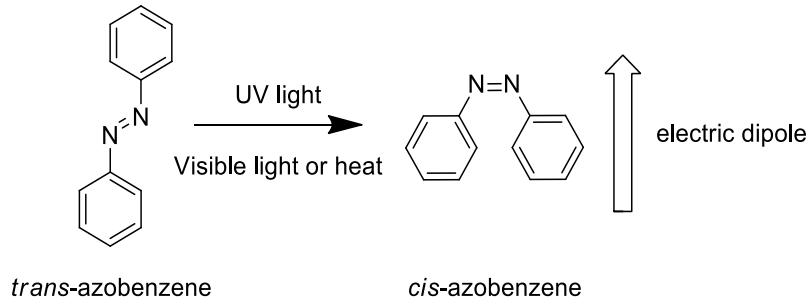

Figure 1.22. Schematic azobenzene trans-cis *isomerization*

These peculiar characteristics of azobenzene have been exploited in a variety of materials. One beautiful example was reported by Katsonis et al[94]: they prepared a liquid-crystal polymer containing azobenzenes units along its backbone. The polymer was then doped with chiral molecules to induce a left- or right-handed helix. They showed that a string cut from a polymer film reacted macroscopically to UV light (**Figure 1.23**) according to the direction of the cut respect to the direction of the helices and that was possible to extract work from an opportunely prepared polymer string.

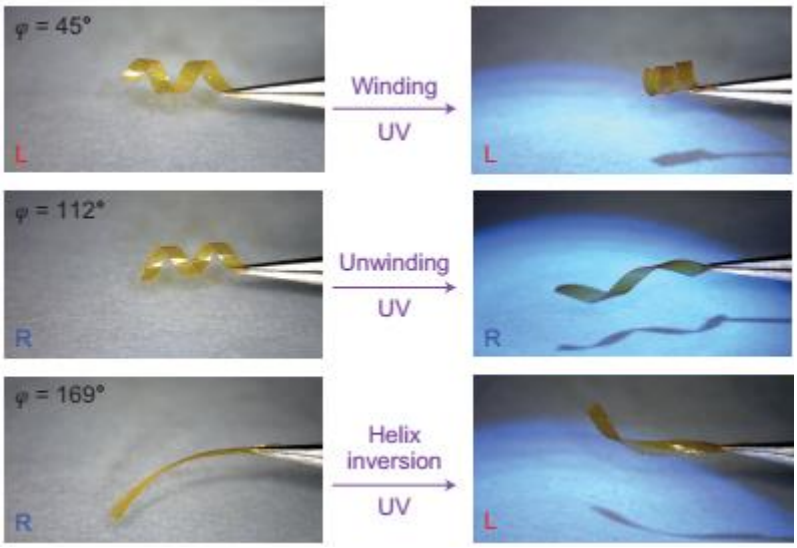

***Figure 1.23**. Spiral ribbons irradiated for two minutes with ultraviolet light (λ=365 nm) display isochoric winding, unwinding and helix inversion as dictated by their initial shape and geometry*

Regarding porous materials, which remain the main interest of this work, a number of MOFs containing azobenzene as side group have been reported.

For example, H. C. Zhou et al. used 2-(phenyldiazenyl)terephthalic acid to prepare a MOF-5 derivative with azobenzene side groups, referred to as PCN-123. They demonstrated that CO_2 uptake capacity of PCN-123 depends on the conformational state of the azo-benzene side groups (*trans*-form adsorbed more CO_2 than *cis*-form)[95].

A few examples of azo-benzene containing COFs are found as well. Zhang and coworkers[96] synthesized Azo-COF by condensation reaction between azobenzene-4,4′-diboronic acid (ABDA) and HHTP (**Figure 1.24**) and demonstrated that about 17% of diazo units changed from *trans*-form to *cis*-form upon irradiation with 365 nm light for 100 minutes. However, the switching occurred without changing significantly the structure of the framework, neither from a crystallographic, nor from porosity point of view.

Azo-benzene is the investigated molecular switch used in the preparation of stimuli-responsive materials because it can be easily functionalized and its switching mechanism both in solution and solid state has been extensively studied in the past. However, azo-benzenes are not ideal bistable switches as their metastable form (usually the *cis*-form) easily relax to the stable form (the *trans* state) even at room temperature in the dark.

To prepare porous materials containing efficient bistable molecular switches, we joined forces with Prof. Feringa research group from Groningen University. Feringa is most known for the design and synthesis of various unidirectional molecular motor that shows continuous dynamics upon irradiation with the appropriate wavelength[67,97,98]. However, with the right design, a molecular motor can be used as a very efficient bistable molecular switch. We focused our attention on second generation molecular motors, as Feringa calls them.

They are chiral asymmetric overcrowded alkenes composed by a lower half, that act as stator, an axle, the C-C double bond, and an upper part, that can be viewed as the rotor[68,99].

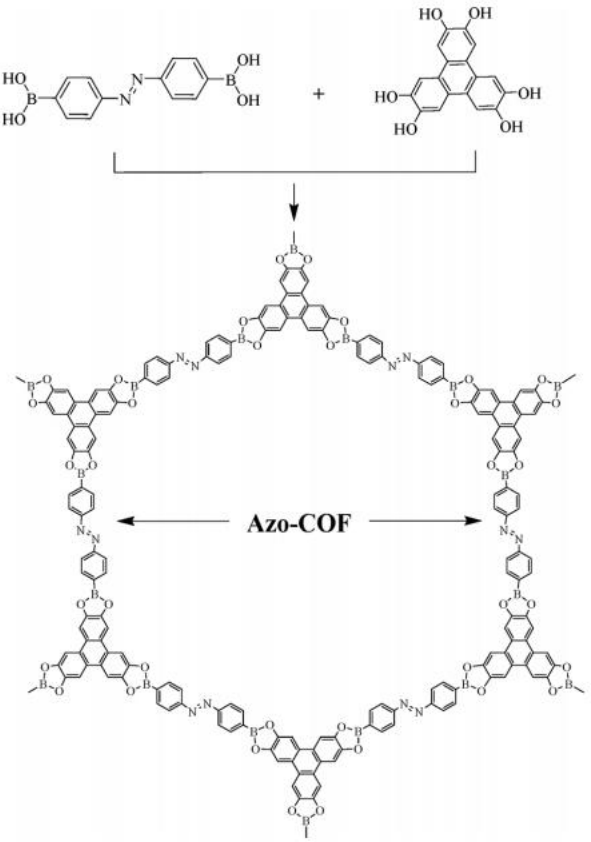

Figure 1.24. Schematic representation of the synthesis of Azo-COF

Previous research on second generation molecular motors showed that the metastable-to-stable ratio at photostationary state (PSS) and the room temperature half-life time of the metastable state (i.e. the time required for the concentration of metastable state in solution to be reduced by half by thermal relaxation at certain temperature) can be controlled by the molecular design. In particular, they demonstrated that connecting a fluorene lower half with a naphtalene upper half through a six-membered aliphatic ring having a methyl substituent in α to the double bond guarantees high metastable/stable ratios at PSS and long half-life times (structure **i** in **Figure 1.25**).

Molecular switch **i** possesses the characteristics of an ideal bistable switch: its conversion to the metastable state and the back-conversion to the stable state are almost quantitative. The switching process is activated by 365 nm light, while the backswitching requires 470 nm light. It has extremely high half-life times, meaning that it will not return from the metastable to the stable state unless irradiated with 470 nm or heated at high temperatures (100 °C in solution). For these reasons, we based the design of the molecular switch to be inserted in porous matrices on **i**

However, molecule **i** as it is shown in **Figure 1.25** is not suitable to prepare any material as it lacks reactive groups that can be exploited to link the switch to a porous matrix. We designed a new molecular switch similar to **i** but with bromine atoms on position 2 and 7 of the fluorene lower half.

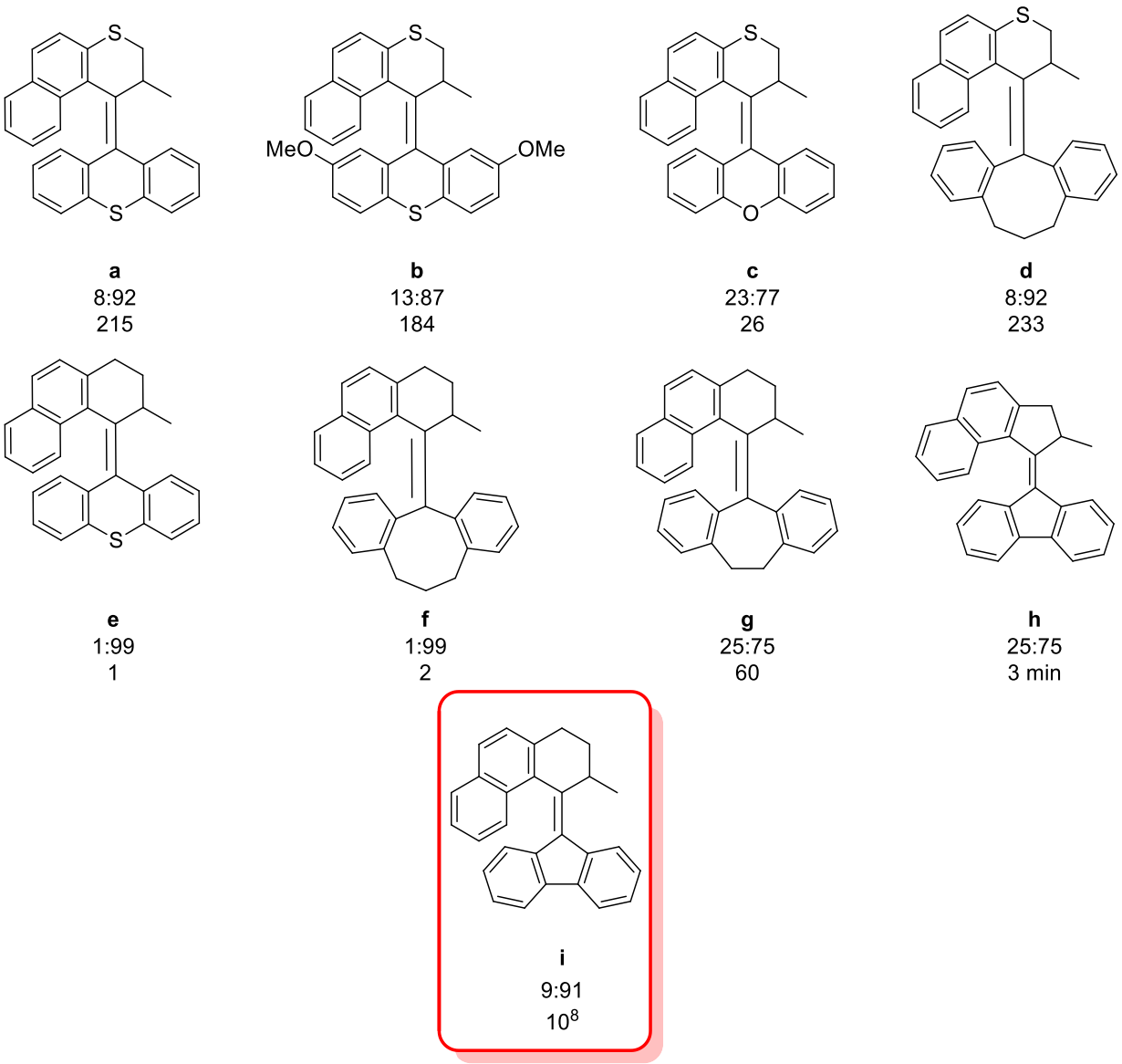

***Figure 1.25**. Molecular structure of various second generation molecular rotors synthesized by Feringa groups. Fractions express stable-to-metastable ratios at PSS, while the second number is the half-life time in hours at 0 °C.*

We then exploited bromine groups to copolymerize the switch with tetrakis(4-bromophenyl)methane in a Yamamoto-type cross coupling reaction to prepare new organic porous material containing bistable molecular switches. The synthesis and the characterization of these materials are presented in Chapter 4.

Bibliography for Chapter 1

1. OxfordUniversityPress. Definition of Science - Oxford Dictionary. (2018). Available at: https://www.oxforddictionaries.com/.

2. Corey Brendan Richard. Lumbar vertebra bone structure. Available at: https://slideplayer.com/slide/8813563/.

3. Radboud University Nijmegen. Electron micrography of Pinus Wood. Available at: http://www.vcbio.science.ru.nl/en/image-gallery/show/PL0223/.

4. Dartmouth Electron Microscope Facility/Dartmouth College. Scanning electron image of a Walnut leaf. Available at: http://archive.boston.com/bigpicture/2008/11/peering_into_the_micro_world.html.

5. Neogene Bryozoa of Britain. Scanning electron micrography of coral Hornera Striata. Available at: http://neogenebryozoans.myspecies.info/nontaxonomy/term/50?page=17.

6. Rouquerol, J., Rodriguez-Reinoso, F., Sing, K.S.W., Unger, K. K. *Robens E. in Characterization of Porous Solids III*. (Elsevier, 1994).

7. Auerbach, S. M., Carrado, K. A. & Dutta, P. K. *Handbook of Zeolite Science and Technology*. *Science* (2003). doi:10.1016/S1351-4180(04)00164-3

8. Intarnational Zeolite Association. Clinoptilolite - IZA Database. Available at: http://www.iza-online.org/natural/Datasheets/Clinoptilolite/clinoptilolite.htm.

9. International Zeolite Association. Mordenite - IZA Database. Available at: http://www.iza-online.org/natural/Datasheets/Mordenite/mordenite.htm.

10. IZA. Database of the International Zeolite Association. Available at: http://www.iza-online.org/natural/default.htm.

11. Grand View Research. Zeolite Market Size, Share & Trends Analysis Report By Product, By Application (Catalysts, Detergent Builders), By Region (North America, Europe, Asia Pacific, CSA, MEA), And Segment Forecasts, 2012 - 2022. (2018). Available at: https://www.grandviewresearch.com/industry-analysis/zeolites-market.

12. Shafeeyan, M. S., Daud, W. M. A. W., Houshmand, A. & Shamiri, A. A review on surface modification of activated carbon for carbon dioxide adsorption. *Journal of Analytical and Applied Pyrolysis* **89,** 143–151 (2010).

13. Yin, C. Y., Aroua, M. K. & Daud, W. M. A. W. Review of modifications of activated carbon for enhancing contaminant uptakes from aqueous solutions. *Separation and Purification Technology* **52,** 403–415 (2007).

14. Grand View Research. Activated Carbon Market Size, Share & Trends Analysis Report By Product (Powdered Activated Carbon, Granular Activated Carbon), By Application, By End-use, And Segment Forecasts, 2018 - 2024. (2018). Available at: https://www.grandviewresearch.com/industry-analysis/activated-carbon-market.

15. Liu, P. S. & Chen, G. F. *Porous Materials - Process and Application*. (Elsevier, 2014). doi:10.1016/B978-0-12-407788-1.09993-7

16. Van Der Voort, P. *et al.* Periodic mesoporous organosilicas: From simple to complex bridges; A comprehensive overview of functions, morphologies and applications. *Chem. Soc. Rev.* **42,** 3913–3955 (2013).

17. Gangu, K. K., Maddila, S., Mukkamala, S. B. & Jonnalagadda, S. B. A review on contemporary Metal-Organic Framework materials. *Inorganica Chimica Acta* **446,** 61–74 (2016).

18. Das, S., Heasman, P., Ben, T. & Qiu, S. Porous Organic Materials: Strategic Design and Structure-Function Correlation. *Chemical Reviews* **117,** 1515–1563 (2017).

19. Tsyurupa, M. P. & Davankov, V. A. Hypercrosslinked polymers: Basic principle of preparing the new class of polymeric materials. *React. Funct. Polym.* **53,** 193–203 (2002).

20. Ramimoghadam, D., Gray, E. M. A. & Webb, C. J. Review of polymers of intrinsic microporosity for hydrogen storage applications. *International Journal of Hydrogen Energy* **41,** 16944–16965 (2016).

21. Ding, S. Y. & Wang, W. Covalent organic frameworks (COFs): From design to applications. *Chemical Society Reviews* **42,** 548–568 (2013).

22. Pei, C., Ben, T. & Qiu, S. Great Prospects for PAF-1 and its derivatives. *Materials Horizons* **2,** 11–21 (2015).

23. Rouquerolt, J. *et al.* Recommendations for the characterization of porous solids. *Pure Appl. Chem.* **66,** 1739–1758 (1994).

24. Sing, K. S. W. Reporting physisorption data for gas/solid systems with special reference to the determination of surface area and porosity (Recommendations 1984). *Pure Appl. Chem.* **57,** 603–619 (1985).

25. Giesche, H. Mercury porosimetry: A general (practical) overview. in *Particle and Particle Systems Characterization* **23,** 9–19 (2006).

26. Bailar, J. C. *Preparative Inorganic Reactions - Volume 1*. (1964).

27. Kitagawa, S., Kitaura, R. & Noro, S. I. Functional porous coordination polymers. *Angew. Chemie - Int. Ed.* **43,** 2334–2375 (2004).

28. Li, H., Eddaoudi, M., Groy, T. L. & Yaghi, O. M. Establishing microporosity in open metal-organic frameworks: Gas sorption isotherms for Zn(BDC) (BDC = 1,4-benzenedicarboxylate) [28]. *Journal of the American Chemical Society* **120,** 8571–8572 (1998).

29. Cambridge Crystallographic Data Centre. Number of MOFs Structure. Available at: https://www.ccdc.cam.ac.uk/support-and-resources/support/case/?caseid=9833bd2c-27f9-4ff7-8186-71a9b415f012.

30. Yaghi, O. M. *et al.* Reticular synthesis and the design of new materials. *Nature* **423,** 705–714 (2003).

31. Eddaoudi, M. *et al.* Systematic Design of Pore Size and Functionality in Isoreticular MOFs and Their Application in Methane Storage Published by : American Association for the Advancement of Science Linked references are available on JSTOR for this article : Systematic Design. **295,** 469–472 (2016).

32. Farha, O. K. *et al.* Metal-organic framework materials with ultrahigh surface areas: Is the sky the limit? *J. Am. Chem. Soc.* **134,** 15016–15021 (2012).

33. Li, H. *et al.* Recent advances in gas storage and separation using metal–organic frameworks. *Materials Today* **21,** 108–121 (2018).

34. Doonan, C. J. & Sumby, C. J. Metal-organic framework catalysis. *CrystEngComm* **19,** 4045–4049 (2017).

35. Wu, M. X. & Yang, Y. W. Metal–Organic Framework (MOF)-Based Drug/Cargo Delivery and Cancer Therapy. *Advanced Materials* **29,** 1606134 (2017).

36. Sava Gallis, D. F. *et al.* Multifunctional, Tunable Metal-Organic Framework Materials Platform for Bioimaging Applications. *ACS Appl. Mater. Interfaces* **9,** 22268–22277 (2017).

37. Xu, G. *et al.* Exploring metal organic frameworks for energy storage in batteries and supercapacitors. *Materials Today* **20,**

191–209 (2017).

38. Stavila, V., Talin, A. A. & Allendorf, M. D. MOF-based electronic and opto-electronic devices. *Chemical Society Reviews* **43,** 5994–6010 (2014).

39. Zhang, J. P., Zhang, Y. B., Lin, J. Bin & Chen, X. M. Metal azolate frameworks: From crystal engineering to functional materials. *Chemical Reviews* **112,** 1001–1033 (2012).

40. Halcrow, M. A. Pyrazoles and pyrazolides—flexible synthons in self-assembly. *J. Chem. Soc. Dalt. Trans.* **0,** 2059–2073 (2009).

41. He, J., Yin, Y.-G., Wu, T., Li, D. & Huang, X.-C. Design and solvothermal synthesis of luminescent copper(i)-pyrazolate coordination oligomer and polymer frameworks. *Chem. Commun.* **0,** 2845 (2006).

42. Zhang, J. P., Horike, S. & Kitagawa, S. A flexible porous coordination polymer functionalized by unsaturated metal clusters. *Angew. Chemie - Int. Ed.* **46,** 889–892 (2007).

43. Choi, H. J., Dincă, M., Dailly, A. & Long, J. R. Hydrogen storage in water-stable metal-organic frameworks incorporating 1,3- and 1,4-benzenedipyrazolate. *Energy Environ. Sci.* **3,** 117–123 (2010).

44. Galli, S. *et al.* Adsorption of harmful organic vapors by flexible hydrophobic bis-pyrazolate based MOFs. *Chem. Mater.* **22,** 1664–1672 (2010).

45. Galli, S. *et al.* When long bis(pyrazolates) meet late transition metals: Structure, stability and adsorption of metal-organic frameworks featuring large parallel channels. *J. Mater. Chem. A* **2,** 12208–12221 (2014).

46. Cote, A. P. Porous, Crystalline, Covalent Organic Frameworks. *Science (80-.).* **310,** 1166–1170 (2005).

47. Lee, G.-Y. *et al.* Amine-Functionalized Covalent Organic Framework for Efficient SO2 Capture with High Reversibility. *Sci. Rep.* **7,** 557 (2017).

48. Gopalsamy, K., Desgranges, C. & Delhommelle, J. Selectivity and desorption free energies for methane-ethane mixtures in covalent organic frameworks. *J. Phys. Chem. C* **121,** 24692–24700 (2017).

49. Shan, M. *et al.* Azine-Linked Covalent Organic Framework (COF)-Based Mixed-Matrix Membranes for CO2/CH4Separation. *Chem. - A Eur. J.* **22,** 14467–14470 (2016).

50. Lv, J. *et al.* Direct Solar-to-Electrochemical Energy Storage in Functionalized Covalent Organic Framework. *Angew. Chemie Int. Ed.* (2018). doi:10.1002/anie.201806596

51. Sun, Q., Aguila, B. & Ma, S. A bifunctional covalent organic framework as an efficient platform for cascade catalysis. *Mater. Chem. Front.* **1,** 1310–1316 (2017).

52. Xu, H., Tao, S. & Jiang, D. Proton conduction in crystalline and porous covalent organic frameworks. *Nat. Mater.* **15,** 722–726 (2016).

53. Medina, D. D., Sick, T. & Bein, T. Photoactive and Conducting Covalent Organic Frameworks. *Adv. Energy Mater.* **7,** 1700387 (2017).

54. Zhao, F., Liu, H., Mathe, S., Dong, A. & Zhang, J. Covalent Organic Frameworks: From Materials Design to Biomedical Application. *Nanomaterials* **8,** 15 (2017).

55. Cooper, A. I. Conjugated microporous polymers. *Adv. Mater.* **21,** 1291–1295 (2009).

56. Jiang, J. X. *et al.* Conjugated microporous poly(aryleneethynylene) networks. *Angew. Chemie - Int. Ed.* **46,** 8574–8578

(2007).

57. Ben, T. *et al.* Targeted synthesis of a porous aromatic framework with high stability and exceptionally high surface area. *Angew. Chemie - Int. Ed.* **48,** 9457–9460 (2009).

58. Science Fiction Encyclopedia. Grey Goo definition. Available at: http://www.sf-encyclopedia.com/entry/grey_goo.

59. Itoh, H. *et al.* Mechanically driven ATP synthesis by F1-ATPase. *Nature* **427,** 465–468 (2004).

60. Sowa, Y. & Berry, R. M. Bacterial flagellar motor. *Quarterly Reviews of Biophysics* **41,** 103–132 (2008).

61. Holmes, K. C. & Geeves, M. A. The structural basis of muscle contraction. *Philos. Trans. R. Soc. B Biol. Sci.* **355,** 419–431 (2000).

62. Kottas, G. S., Clarke, L. I., Horinek, D. & Michl, J. Artificial Molecular Rotors. *Physics (College. Park. Md).* **105,** 1281–1376 (2005).

63. Silvi, S., Venturi, M. & Credi, A. Artificial molecular shuttles: From concepts to devices. *J. Mater. Chem.* **19,** 2279–2294 (2009).

64. Xue, M., Yang, Y., Chi, X., Yan, X. & Huang, F. Development of Pseudorotaxanes and Rotaxanes: From Synthesis to Stimuli-Responsive Motions to Applications. *Chemical Reviews* **115,** 7398–7501 (2015).

65. Natali, M. & Giordani, S. Molecular switches as photocontrollable 'smart' receptors. *Chemical Society Reviews* **41,** 4010–4029 (2012).

66. Kassem, S. *et al.* Artificial molecular motors. *Chem. Soc. Rev.* **46,** 2592–2621 (2017).

67. Koumura, N., Zijistra, R. W. J., Van Delden, R. A., Harada, N. & Feringa, B. L. Light-driven monodirectional molecular rotor. *Nature* **401,** 152–155 (1999).

68. Koumura, N., Geertsema, E. M., Van Gelder, M. B., Meetsma, A. & Feringa, B. L. Second Generation Light-Driven Molecular Motors. Unidirectional Rotation Controlled by a Single Stereogenic Center with Near-Perfect Photoequilibria and Acceleration of the Speed of Rotation by Structural Modification. (2002). doi:10.1021/ja012499i

69. Kudernac, T. *et al.* Electrically driven directional motion of a four-wheeled molecule on a metal surface. *Nature* **479,** 208–211 (2011).

70. Cohen-Addad, J. P. NMR of polymers. *J. Phys.* **43,** 1509 (1982).

71. Karlen, S. D. & Garcia-Garibay, M. A. Amphidynamic crystals: Structural blueprints for molecular machines. *Topics in Current Chemistry* **262,** 179–227 (2005).

72. Dominguez, Z., Dang, H., Strouse, M. J. & Garcia-Garibay, M. A. Molecular 'compasses' and 'gyroscopes'. I. Expedient synthesis and solid state dynamics of an open rotor with a bis(triarylmethyl) frame. *J. Am. Chem. Soc.* **124,** 2398–2399 (2002).

73. Godinez, C. E., Zepeda, G. & Garcia-Garibay, M. A. Molecular compasses and gyroscopes. II. Synthesis and characterization of molecular rotors with axially substituted bis[2-(9-triptycyl)ethynyl]arenes. *J. Am. Chem. Soc.* **124,** 4701–4707 (2002).

74. Dominguez, Z., Dang, H., Strouse, M. J. & Garcia-Garibay, M. A. Molecular 'compasses' and 'gyroscopes.' III. Dynamics of a phenylene rotor and clathrated benzene in a slipping-gear crystal lattice. *J. Am. Chem. Soc.* **124,** 7719–7727 (2002).

75. Godinez, C. E., Zepeda, G., Mortko, C. J., Dang, H. & Garcia-Garibay, M. A. Molecular Crystals with Moving Parts:

Synthesis, Characterization, and Crystal Packing of Molecular Gyroscopes with Methyl-Substituted Triptycyl Frames. *J. Org. Chem.* **69,** 1652–1662 (2004).

76. Comotti, A., Bracco, S. & Sozzani, P. Molecular Rotors Built in Porous Materials. *Acc. Chem. Res.* **49,** 1701–1710 (2016).

77. Saebø, S., Almlöf, J., Boggs, J. E. & Stark, J. G. Two approaches to the computational determination of molecular structure: the torsional angle in tolane and the effect of fluorination on the structure of oxirane. *J. Mol. Struct. THEOCHEM* **200,** 361–373 (1989).

78. Sipachev, V. A., Khaikin, L. S., Grikina, O. E., Nikitin, V. S. & Trætteberg, M. Structure, spectra and internal rotation of bis(trimethylsilyl) acetylene: Spectral analysis by scaling quantum-chemical force fields and two methods for calculating vibrational effects. *J. Mol. Struct.* **523,** 1–22 (2000).

79. Comotti, A., Bracco, S., Valsesia, P., Beretta, M. & Sozzani, P. Fast molecular rotor dynamics modulated by guest inclusion in a highly organized nanoporous organosilica. *Angew. Chemie - Int. Ed.* **49,** 1760–1764 (2010).

80. Comotti, A., Bracco, S., Ben, T., Qiu, S. & Sozzani, P. Molecular rotors in porous organic frameworks. *Angew. Chemie - Int. Ed.* **53,** 1043–1047 (2014).

81. Hoatson, G. L. & Vold, R. L. 2H-NMR spectroscopy in solids and liquid crystals. in *Solid state NMR III Organic Matter* 1–67 (Springer Berlin Heidelberg, 1994). doi:10.1007/978-3-642-61223-7_1

82. Morris, W., Taylor, R. E., Dybowski, C., Yaghi, O. M. & Garcia-Garibay, M. A. *Framework mobility in the metal-organic framework crystal IRMOF-3: Evidence for aromatic ring and amine rotation*. *Journal of Molecular Structure* **1004,** (Elsevier, 2011).

83. Zhang, Y. *et al.* Ferroelectricity induced by ordering of twisting motion in a molecular rotor. *J. Am. Chem. Soc.* **134,** 11044–11049 (2012).

84. Akutagawa, T. *et al.* Ferroelectricity and polarity control in solid-state flip-flop supramolecular rotators. *Nat. Mater.* **8,** 342–347 (2009).

85. Setaka, W. & Yamaguchi, K. Thermal modulation of birefringence observed in a crystalline molecular gyrotop. *Proc. Natl. Acad. Sci.* **109,** 9271–9275 (2012).

86. Dominguez, Z. *et al.* Molecular compasses and gyroscopes with polar rotors: Synthesis and characterization of crystalline forms. *J. Am. Chem. Soc.* **125,** 8827–8837 (2003).

87. Horansky, R. D. *et al.* Dielectric response of a dipolar molecular rotor crystal. *Phys. Rev. B - Condens. Matter Mater. Phys.* **72,** 014302 (2005).

88. Horansky, R. D. *et al.* Dipolar rotor-rotor interactions in a difluorobenzene molecular rotor crystal. *Phys. Rev. B - Condens. Matter Mater. Phys.* **74,** (2006).

89. Barsoukov, E. & Macdonald, J. R. *Impedance Spectroscopy: Theory, Experiment, and Applications*. *Impedance Spectroscopy: Theory, Experiment, and Applications* (2005). doi:10.1002/0471716243

90. Bracco, S. *et al.* Dipolar rotors orderly aligned in mesoporous fluorinated organosilica architectures. *Angew. Chemie - Int. Ed.* **54,** 4773–4777 (2015).

91. Feringa, B. L. & Browne, W. R. *Molecular Switches*. *Molecular Switches* **1,** (Wiley-VCH, 2011).

92. Oscurato, S. L., Salvatore, M., Maddalena, P. & Ambrosio, A. From nanoscopic to macroscopic photo-driven motion in azobenzene-containing materials. *Nanophotonics* **7,** 1387–1422 (2018).

93. Weis, P. & Wu, S. Light-Switchable Azobenzene-Containing Macromolecules: From UV to Near Infrared. *Macromol.*

Rapid Commun. **39,** (2018).

94. Iamsaard, S. *et al.* Conversion of light into macroscopic helical motion. *Nat. Chem.* **6,** 229–235 (2014).

95. Park, J. *et al.* Reversible alteration of CO 2 adsorption upon photochemical or thermal treatment in a metal-organic framework. *J. Am. Chem. Soc.* **134,** 99–102 (2012).

96. Zhang, J. *et al.* A novel azobenzene covalent organic framework. *CrystEngComm* **16,** 6547–6551 (2014).

97. Eelkema, R. *et al.* Nanomotor rotates microscale objects. *Nature* **440,** 163 (2006).

98. Van Delden, R. A. *et al.* Unidirectional molecular motor on a gold surface. *Nature* **437,** 1337–1340 (2005).

99. Van Leeuwen, T., Danowski, W., Otten, E., Wezenberg, S. J. & Feringa, B. L. Asymmetric Synthesis of Second-Generation Light-Driven Molecular Motors. *J. Org. Chem.* **82,** 5027–5033 (2017).

2. Chapter 2

Ultrafast molecular rotors and their CO_2 tuning in MOFs with rod-like ligands

This chapter has been published as full paper in *Chem. Eur. J*., 2017, 23, 11210 –11215

2.1. Introduction

Molecular rotors and motors have become an important issue today, being a prominent challenge to present-day research where the target is to reorganize molecular motion from a chaotic to a coherent state[1–4]. When opportunely governed, molecular motion can be exploited for its response to electric-field stimuli in optical devices, switches and sensors[5]. To date, light energy has aided the promotion of unidirectional propulsion for the fabrication of nanorobots and nanomachines[6–8]. Artificial molecular pumps have been fabricated, mimicking rotary machines that, in nature, perform fundamental functions such as proton pumps[9,10]. Thus, solid state structures, periodically organized in 2D and 3D, have the potential to offer a reliable venue for the controlled motion of molecular rotors, though they often suffer from a tendency towards close-packing inducing reciprocal interference among rotors[11–13]. However, crystalline porous materials with their low density and structural order can overcome this limitation and are excellent candidates for the fabrication of molecular rotors in the solid state[14–17]. Furthermore, porosity allows rotor exposure to diffusing species through adsorption, this occurrence enlarging the application perspectives[18–22]. Indeed, the easy rotor accessibility results in an active manipulation of rotary motion through interaction with guests, revealing the feasibility of molecular rotors as responsive elements sensitive to chemical perturbation[14-17]. The architecture of porous materials can be realized by a variety of chemical bonds and supramolecular interactions[23–25]. Specifically, in metal-organic frameworks (MOFs) metal organic nodes and proper organic struts ensure both crystallinity and robustness[26–29]. The large variety of MOFs offers a valid platform. to build solid state molecular rotors in a porous environment, providing, in principle, the free volume needed for motion to occur. However, in the MOFs presented in literature, the typically-adopted chemical bonds on which molecular rotors are pivoted are rather inadequate to ensure a low barrier for rotation[14-17, 30–34]. Attempts to lower this energy barrier have been carried out by destabilizing the ground state through the introduction of lateral substituents on *p*-phenylene units in the struts, although this causes the molecular mass of the rotor and its inertia momentum to increase, leading to relatively slow rotational frequencies[35,36]. To increase the rotational spinning speed, an alternative strategy adopted in porous molecular crystals is to insert into the struts triple bonds as pivots for the molecular rotor, thus for lowering the energy barrier for rotation[11-13, 18-22]. In the present chapter we show extremely fast rotor dynamics, already 10^{11} Hz at 150 K, comparable to liquid matter, in a bis(pyrazolate)-based MOF architecture. Moreover, the CO_2 entering the porous material could actively tune the spinning speed and govern the mechanics of motion (Figure 1). This opens up the perspective of actively manipulating rotor response in a robust framework, simply by the adsorption of a gas.

2.2. Design and synthesis of the ligand and of the MOF structure

The porous and absorptive architecture was realized through the robustness of metal-organic bonds and the use of rigid molecular rods bearing the rotors. We selected a suitable rod-like strut that contains a central *p*-phenylene unit (the rotor) connected through ethynyl groups to two pyrazole moieties 1,4-bis(1H-pyrazol-4-ylethynyl)benzene (BPEB)which interacts with Zn(II) ions to fabricate the microporous MOF α-[Zn(BPEB)][37].

The isostructural MOF α-[Zn(BPEB-d_4)] selectively deuterated on the central p-phenylene moiety was prepared to investigate the rotor dynamics. ^{2}H solid-state NMR is a powerful technique that can be used to investigate dynamics in the solid state, as the line shape of ^{2}H signal is strongly dependant on both the mechanism and the speed of motion[38] The synthesis of the ligand followed the Sonogashira protocol[39] for the carbon-carbon cross coupling between a terminal alkyne and an aromatic halide and it is schematically reported in **Scheme 2.1**. Precursor **2** was synthesised following a published procedure, while details of the synthesis of **3** are reported in the experimental section.

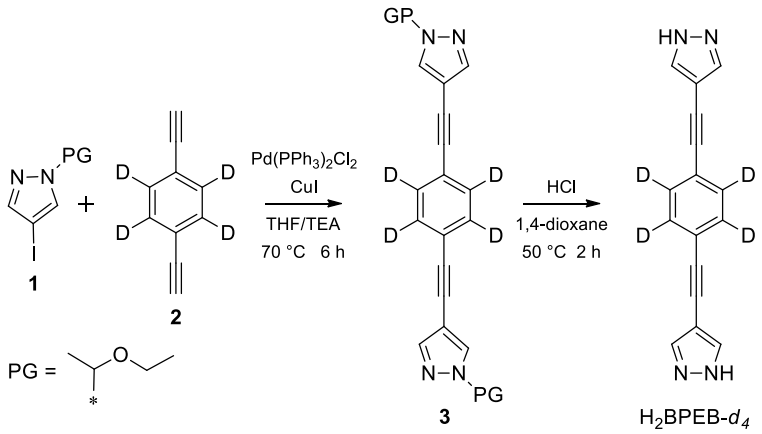

Scheme 2.1. *Scheme of ligand H_2BPEB-*d*$_4$ synthesis*

The synthesis of ligand H_2BPEB-d_4 followed a similar protocol to the one published for the synthesis of non-deuterated H_2BPEB[37]. To our surprise, however, ligand-d_4 precursors were less reactive and their reactions required higher temperatures and longer reaction times to reach completion.

After that preparation of H_2BPEB-d_4 was completed, we started investigating various synthetic strategies changing parameters such as metal ion salt, solvent, base and temperature, in order to identify the most straightforward reaction path toward the target MOF. Unexpectedly, the same conditions used for the synthesis of non-deuterated α-[Zn(BPEB)] were not suitable for the preparation of highly crystalline α-[Zn(BPEB-d_4)]. MOF α-[Zn(BPEB-d_4)] was eventually obtained following a microwave assisted route in pyridine, using Zn(ClO_4) hexahydrate in presence of triethylamine as base (**Figure 2.2**)

α-[Zn(BPEB-d_4)] precipitates in satisfactory yields in the form of air- and light-stable powder insoluble in water and in the most common solvents, thereby suggesting the polymeric nature of its crystal structure.

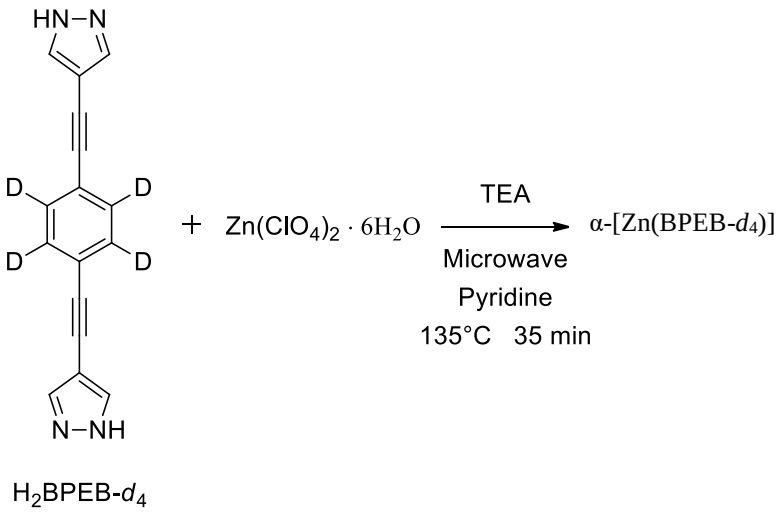

Scheme 2.2 *Reaction conditions for the synthesis of MOF α-[Zn(H₂BPEB-d₄)]*

2.3. Characterization of α-[Zn(BPEB-*d*₄)]

2.3.1. Structural analysis

α-[Zn(BPEB-*d*₄)] is isomorphous and isostructural to α-[Zn(BPEB)], as revealed from the comparison between their powder diffraction patterns[37].

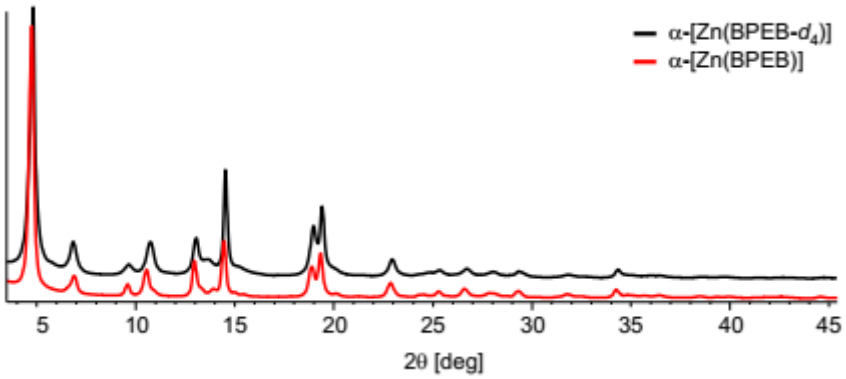

Figure 2.1. *Comparison of the low-to-medium angle portion of the PXRD patterns of α-[Zn(BPEB-d₄)] (black trace) and Zn(BPEB) (red trace), suggesting that the two compounds are isostructural, as proved by the refinement of the crystal structure of α-[Zn(BPEB-d₄)].*

Based on this evidence, the refinement of the crystal structure of α-[Zn(BPEB-*d*₄)] was carried out starting from the crystal structure of Zn(BPEB) by applying the Rietveld method[40], as implemented in TOPAS-R[41]. Details of the refinement procedure are given in Appendix 2. α-[Zn(BPEB-*d*₄)] crystallizes in the orthorhombic space group *Cccm*. The metal centers are coordinated by four nitrogen atoms of four (BPEB-*d*₄)^{2} ligands and shows a distorted tetrahedral stereochemistry. The linkers are *exo*-tetradentate: with the nitrogen atoms of one pyrazolate moiety they bridge nearest-neighbours metal ions building up 1-D chains running along the crystallographic *c*-axis. Each chain is connected to four adjacent ones by the spacers along the [110] direction,

generating two mutually interpenetrated 3-D networks, reciprocally displaced by ~7.66 Å along the **b**-axis. As in Zn(BPEB), the insurgence of interpenetration in α-[Zn(BPEB-d_4)] can be ascribed to the limited steric hindrance of the C≡C triple bonds: the two interpenetrated networks actually cross about them.

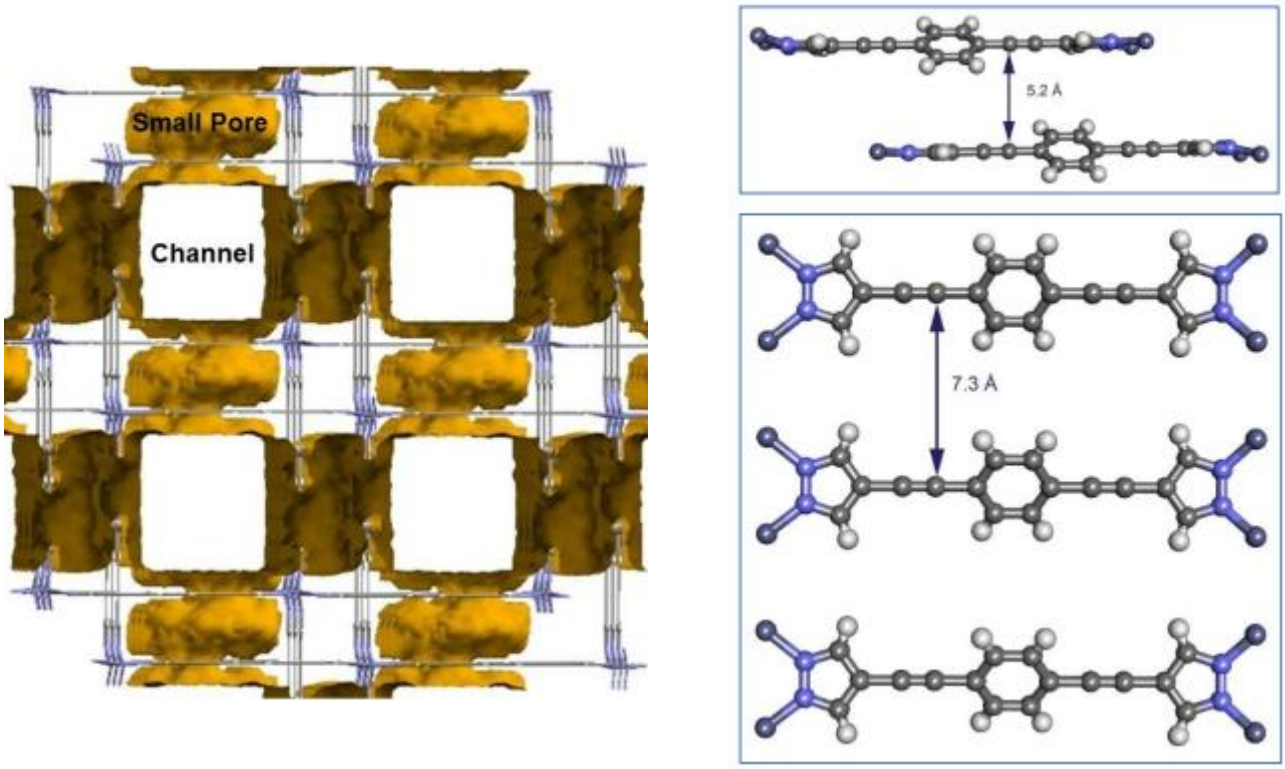

Figure 2. 2. Representation of the crystal structure of α-[Zn(BPEB-d_4)] *showing the wide channels and small pores running along the [001] direction (above). Portions of the crystal structure featuring distances between two adjacent linkers as viewed in the ab plane (5.2 Å) and perpendicular to the c-axis (7.3 Å) (below)*

The phenyl ring of the ligand is affected by orientational disorder: the two rings modelling the disorder are reciprocally oriented at an angle of ~29° with respect to the main axis of the ligand. Despite interpenetration, the crystal structure of α-[Zn(BPEB-d_4)] features 1-D rectangular channels running along the *c*-axis and small pores: the vertices of the channels are defined by the Zn(II) ions, while the walls are decorated by the ligands. The large square channels, centered in [½,0,*z*], account for an empty volume of 1356 Å^3 *per* unit cell, while the small pores, centered in [1/4,1/4, *z*], account for an empty volume of 696 Å^3 *per* unit cell. On the whole, at ambient conditions the crystal structure possesses 48% of potentially accessible empty volume [8], which corresponds to an estimated bulk density of 0.89 g/cm^3

2.3.2. Solid state NMR analysis

^{13}C solid-state NMR was performed on MOF α-[Zn(BPEB-d_4)] and the resulting spectra are reported in **Figure 2.3**.

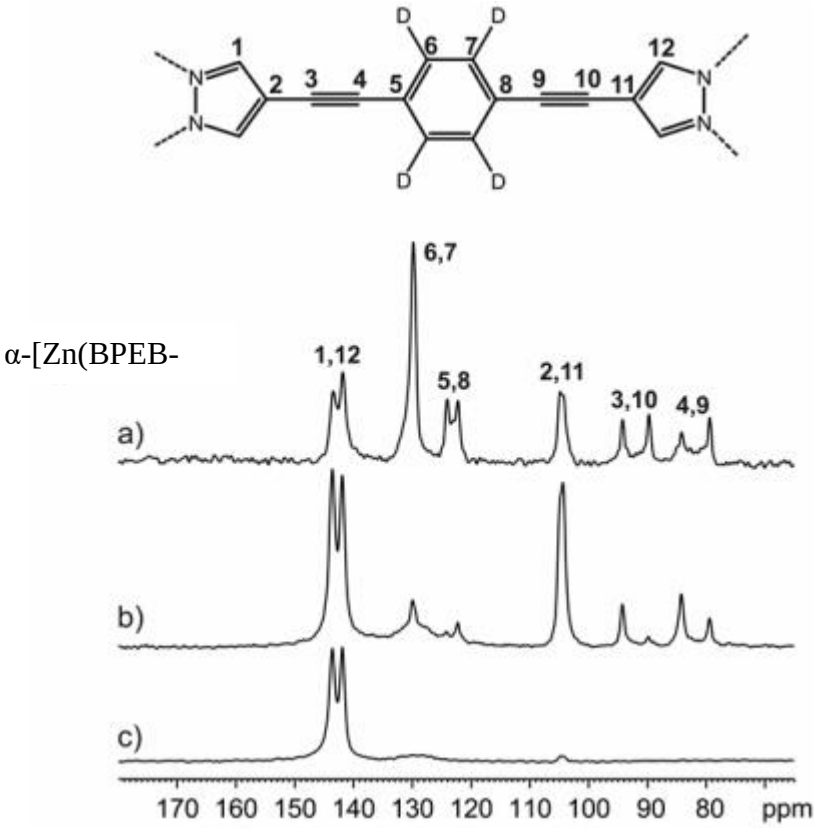

***Figure 2.3**. **a)** ^{13}C MAS spectrum of α-[Zn(BPEB-d$_4$)] recorded with a recycle delay of 20 s; **b)** ^{13}C CP MAS spectra of d4-Zn(BPEB) collected with contact times of 2 ms and **c)** 50 μs*

According to the molecular structure of ligand (BPEB-d_4)$^{2-}$, we expected only 6 carbon signals, because of the two mirror planes present, one along the main molecular axis and the another one that cuts the molecule in half perpendicularly to the phenyl ring. This is exactly what we saw in solution (see Experimental Section). However, **Figure 2.3a** shows 10 different peaks. This is due to the interpenetrated nature of the framework: the unit cell contains two crystallographically independent halves of ligand (BPEB-d_4)$^{2-}$ that generate the doubling of NMR signals. The narrow spectral linewidth and the low signal-to-noise ration of NMR spectra confirms the high crystallinity of α-[Zn(BPEB-d_4)] prepared with the conditions described above.

2.3.3. Gas adsorption analysis

To evaluate α-[Zn(BPEB-d_4)] permanent porosity, N_2 adsorption/desorption isotherm was collected at 77 K. Results of the analysis are reported in **Figure 2.4**, while **Table 2.1** sums up the main textural parameters of the material.

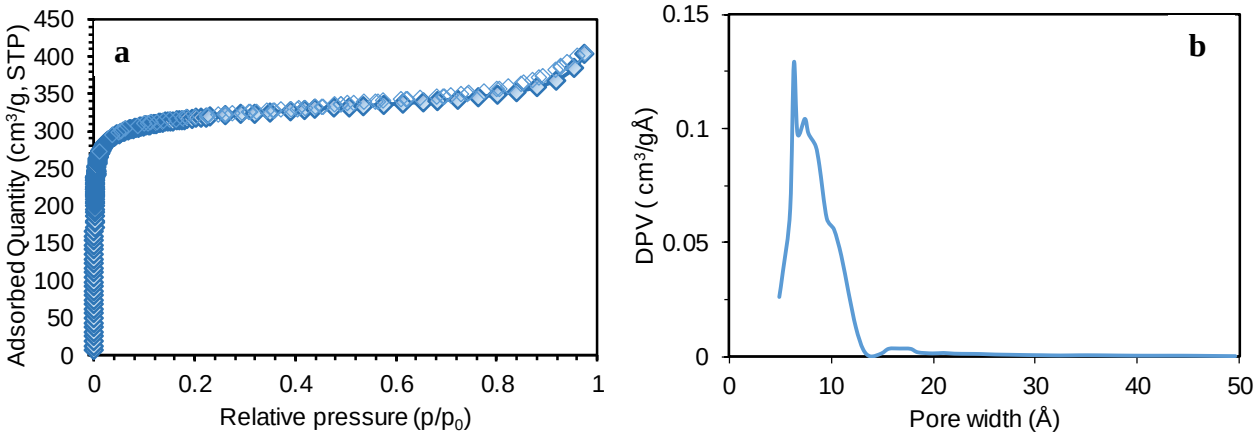

***Figure 2.4**. **a)** N_2 adsorption/desorption isotherm of α-[Zn(BPEB-d_4)] collected at 77 K. Empty symbols represent the desorption branch. **b)** Pore size distribution calculated for α-[Zn(BPEB-d_4)] applying Non-Local DFT using the Tarazona model for cylindrical pores. DPV = differential pore volume*

The adsorption isotherm shows a Type I profile, as typical of microporous materials. Moreover, the isotherm line shape is very close to an ideal Langmuir isotherm, indicating the absence of mesoporosity. This is ascribable to the very high crystallinity of the sample analysed. This result is further supported by the pore size distribution calculated by Non-Local Density Functional Theory applying the Tarazona model for cylindrical pores: as shown in **Figure 2.4** only pores whose dimensions are compatible with the crystal structure are present.

***Table 2 1**. Textural parameters of α-[Zn(BPEB-d_4)] as derived from N_2 adsorption isotherms at 77 K.*

	S_{BET} (m^2/g)	$S_{Langmuir}$ (m^2/g)	V_{total}[a] (cm^3/g)	Dominant pore diameter[a,b] (Å)
α-[Zn(BPEB-d_4)]	1214	1366	0.63	7.4

[a] calculated using Non-Local Density Functional Theory and the Tarazona model on cylindrical pores
[b] highest peak in pore size distribution graphs is reported

Deuterated Zn(II) MOF shows a significantly higher surface area compared to its protonated analogue. This might be due to the smaller dimensions of the deuterium isotope compared to the proton and to a higher quality of the material produced by the different synthetic conditions used for the preparation of α-[Zn(BPEB-d_4)].
As our main objective was to control rotors dynamics in solid-state trough CO_2 adsorption in the porous MOF α-[Zn(BPEB-d_4)], CO_2 adsorption/desorption isotherms were collected at 195 K up to 1 bar and at 273, 283 and 298 K up to 10 bar, in order to evaluate α-[Zn(BPEB-d_4)] carbon dioxide uptake capacity. Results are reported in **Figure 2.5**.

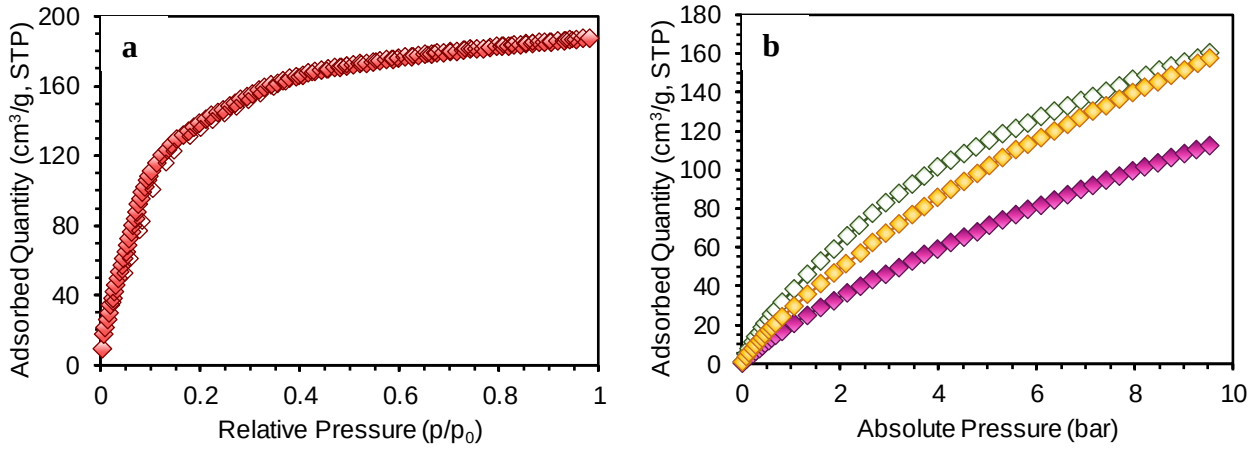

***Figure 2.5**. **a)** CO2 adsorption isotherm of α-[Zn(BPEB-d4)] collected at 195 K up to 1 bar. Empty symbols define the desorption branch. **b)** CO2 adsorption isotherms of α-[Zn(BPEB-d4)] collected at 273 K (green diamonds), 283 K (orange diamonds) and 298 K (purple diamonds) up to 10 bar.*

CO_2 uptake at 195 K reaches 187 cm^3/g which is equal to 48% of host weight. The Langmuir profile of the CO_2 isotherm at 195 K suggests strong interactions between α-[Zn(BPEB-d_4)] and CO_2 molecules. Indeed, heat of adsorption calculated applying the isosteric method and the van't Hoff equation to the three high temperature isotherms results to be 25.1 kJ/mol. In our opinion, this high value is ascribable to the well known *molecular sieve* effect according to which CO_2 adsorption is enhanced by micropores.

2.3.4. Evaluation of rotors reorientation frequencies by ^{2}H-NMR and ^{1}H T_1 relaxation times measurements.

Structure analysis reveals that the minimum distance between adjacent axes of central p-phenylene rings is 7.3 Å along the **c**-axis. On the other hand, being an interpenetrated network, in the **ab** plane each *p*-phenylene ring faces both the ethynyl and the pyrazolate groups of the adjacent linker. The pyrazolate plane is at a distance of 5.2 Å and does not interfere with the rotor. Such a relatively large distance allows for the rotation of the *p*-phenylene ring and, considering the low rotation barrier about Csp^2-Csp bonds (as the *p*-phenylene-ethynylbond), the *p*-phenylene moieties are expected to be efficient as fast molecular rotors. This was demonstrated by wide-line ^{2}H-NMR spectroscopy of selectively deuterated α-[Zn(BPEB-d_4)], on the central *p*-phenylene ring of MOF. At room temperature the spectrum exhibits a restricted spectral profile (with singularities separated by 27.7 kHz), which does not change appreciably down to 150 K, except for a minor increase of the spectral shoulders. The simulated line-shapes show that the mechanism of motion consists of a rapid two-site 180° flip reorientation of the *p*-phenylene moieties about their main axis, passing through the pivotal ethynyl groups, and extremely fast reorientation ($k>10^8$ Hz) of the aromatic C-D bonds (**Figure 2.6**).

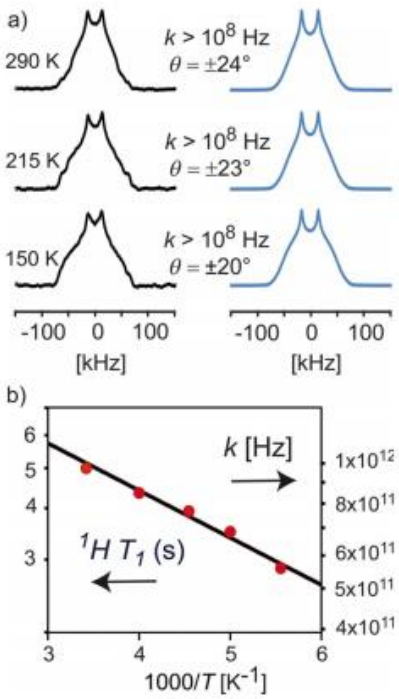

***Figure 2.6**. **a)** Experimental (left) and simulated (right) ^{2}H NMR spectra of α-[Zn(BPEB-d$_4$)]. k corresponds to reorientational rates and Θ to libration amplitude. **b)** ^{1}H T_1 relaxation times and k versus the reciprocal of temperature for α-[Zn(BPEB)]*

Rapid librations of the *p*-phenylene ring about the energy minimum, witnessed by the weakening of the spectral shoulder, must also be taken into account, together with the 180° flip mechanism that is preserved in the strut. Surprisingly, rates in the fast exchange limit (>10^8 Hz) and libration amplitudes q of more than ±20° occur even down to 150 K. In order to explore higher frequency regimes, ^{1}H T_1 spin-lattice relaxation times were measured in α-[Zn(BPEB)], because they provide information on the rotary frequencies at variable temperature, following, the master curve generated by Kubo-Tomita relation. When spin-lattice relaxation times increase with temperature, the system is exploring the extreme narrowing limit and the dynamics are faster than the observation frequencies (typically from 10^8 to 10^{12} Hz), complementing ^{2}H NMR data. This was the case in α-[Zn(BPEB)] in the ^{1}H domain, in which Ln(T_1) proved to be inversely proportional to 1/T (**Figure 2.6b** and Appendix 4). At 150 K the reorientational frequencies k are as fast as 10^{11} Hz. The activation energy was calculated to be 0.5 kcal/mol.

The *p*-phenylene dynamics discovered in this MOF is orders of magnitude faster than those observed in other MOFs, which are still in slow exchange regimes at room temperature (**Table A2.1**)[30-34, 42,43]. The extremely fast dynamics and the low energy barrier we observed are a benchmark in the class of MOFs, and overcome the best molecular rotation value recently published for non-porous crystalline compounds[44].

2.3.5. Fine tuning of rotors speed by CO_2 adsorption

The permanent porosity of the crystals enables CO_2 control of the molecular rotor dynamics while exploring the MOF nanochannels. As a matter of fact, CO_2 adsorption isotherms, run at various temperatures from 298 K down to 195 K (**Figure 2.5**), enabled us to assess the loading of the material at each temperature, and the adsorption energy at low coverage. As discussed above, the interaction energy, as evaluated by the van't Hoff equation, is 25 kJ/mol, indicating a good interaction of CO_2 with the channel walls. ^1H T_1 and ^2H NMR made it possible to investigate the rotor dynamics in the presence of the gas into the channels. At variance with the empty MOF, ^1H relaxation times of α-[Zn(BPEB)] loaded with CO_2 are close to the minimum values and, below 260 K, increased with temperature, with motional frequencies in the regime of motion of solids ($\nu < 3\ 10^8$ MHz at 7.04 T), with a frequency drop of a few orders of magnitude as compared to the empty sample. The deuterated sample α-[Zn(BPEB-d_4)] was sealed under pressurized CO_2 at 9 bar and room temperature (denoted as α-[Zn(BPEB-d_4)]/ CO_2) and ^2H NMR spectra were collected at variable temperature (**Figure 2.7**).

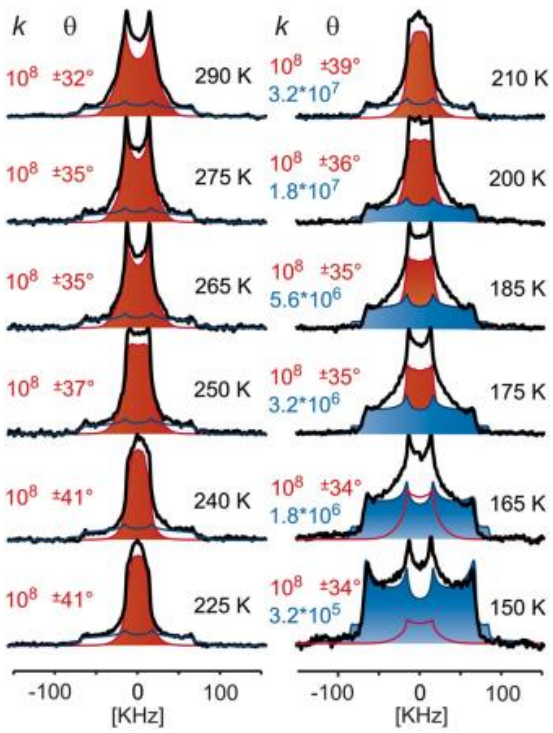

Figure 2.7. Experimental ^2H NMR spectra (black lines) of α-[Zn(BPEB-d$_4$)]/CO2 at variable temperature. Blue and red profiles represent the fast and slow components (configuration I and II, respectively). Rotational frequencies k *and libration amplitudes Θ for the two components are expressed in Hz and degrees, respectively.*

The dramatic change of the spectral series with respect to that of the empty matrix in the same range of temperatures from 150 K to 290 K, is apparent. The spectra were simulated by considering two distinct components, represented in **Figure 2.7** as blue and red profiles. At 150 K the spin-echo ^2H NMR spectrum exhibits a dominant profile associated with a rotation rate k of 10^5 Hz and a two-site 180°-flip reorientation mechanism (**Figure 2.7**, blue profile). Thus, the rotation rate is slowed by more than 6 orders of magnitude compared to the empty MOF (in the order of 10^{11} Hz at 150 K), owing to the hampering effect of CO_2

molecules filling the channels. At this temperature virtually complete loading of the channels occurs and CO molecules surround the rotor with the maximum efficiency. On increasing the temperature, the CO_2 loading of the sample decreases (Appendix 2, **Table A2.2**) and consequently the fraction of rotors fully surrounded by CO_2 is reduced, as observed by the decrease of blue area. At higher temperatures (>200 K) a narrower profile, representing a motional dynamic faster than 10^8 Hz, clearly emerges and dominates progressively evolving with temperature (**Figure 2.7**, red profile). This line shape was simulated with the occurrence of large librations from $\Theta = \pm 32°$to $\pm 41°$ in addition to the two-site 180° flip reorientation. Characteristic tower-shaped profiles are produced by this mechanism when large librations take place and, to date, they have only been observed at much higher temperatures in rotor-containing porous materials[19]. Such large librations suggest a higher rotor degree of freedom because a lower number of CO_2 molecules surround each rotor and CO_2 molecules undergo rapid diffusion along the channels. Grand Canonical Monte Carlo simulations established the number and partition of CO_2 molecules around a rotor, particularly the distribution between the small and large pores as a function of loading (**Figure 2.8** and **Figures A2.11-13**).

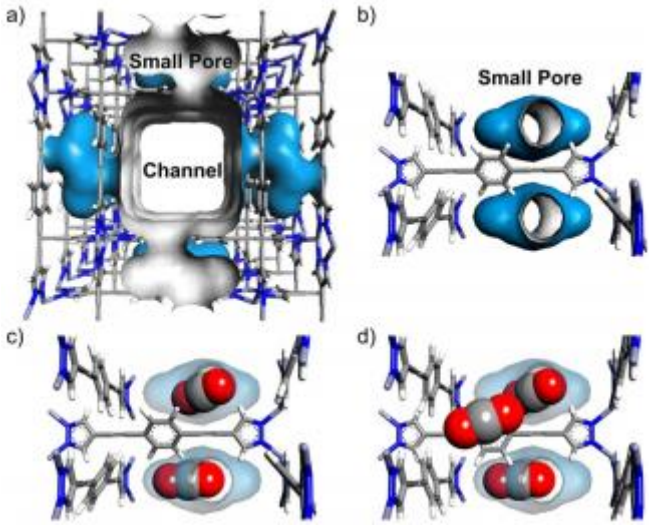

*Figure 2.8. **a)** The small pores and the large channel in α-[Zn(BPEB)] described by a sphere of 1.6 Å radius. **b)** The molecular rotor surrounded by the small pores in the channel walls. Exploration of the cavities by CO_2: **c)** low and **d)** high loadings (configuration I and II, respectively)*

At high temperature and low loading, CO_2 occupies only the small cavities and 2 gas molecules (or less) surround a single rotor (**Figure 2.8c**, configuration I), while on decreasing the temperature the system reaches its full loading and CO_2 molecules also fill the main channels (**Figure 2.8d**, configuration II). In the latter configuration, each rotor is surrounded by 3 CO2 molecules simultaneously: two in the small pores (one on either side of the rotor) and one in the large channels (facing the rotor at the short distance of 3.4 a). Thus, the CO_2 molecules wrap the rotor and slow down its motion, as observed in the blue profile of **Figure 2.7**. In the temperature range from 150 K to 200 K, in the configuration II with the 3 CO_2 molecules about a single rotor progressively its rotational rates increases on increasing the temperature (blue profile). The measured energy barrier, by the Arrhenius plot, is 4.5 kcal/mol (calculated for the most crowded configuration), that is, 4

kcal/mol higher than that recorded in the empty sample (**Figure A2.5**). These results clearly show that CO_2 controls the rotor dynamics, yet without changing the main two-fold flip mechanism. On increasing temperature and decreasing the CO_2 loading, the probability of 3 CO_2 molecules surrounding simultaneously a single rotor decreases, and CO_2 molecules flow away from the larger channels, reducing the constriction on the rotors, that gain mobility. Consequently, in the ^2H NMR spectra the red component with large librations (coupled with fast 180° flip reorientation) prevails. Anyway, the two configurations coexist in different proportions in the overall range of temperature depending on the probability of 3 or 2 CO_2 molecules to be about a single rotor. The profiles of both components evolve progressively with temperature according to the recovery of dynamics due to increased thermal energy.

2.4. Conclusions

In our search for fast molecular rotors in porous solids we designed the fastest dynamics of molecular rotors in MOFs and achieved a benchmark in the field of fast molecular rotors in general. This was made possible by rod-like ligands endowed with virtually barrierless pivotal bonds (owing to the presence of Csp^2 – Csp bonds), which keep the rotors in register. The large empty space, isolating the individual rotors, ensures that there is no interference from one rotor to another. These features render the material an ideal candidate to detect the effects on the rotation frequencies of a gas flowing into the pores. Indeed, CO_2 adsorbed by the material could play an active role in modulating the dynamics of the rotors. Indeed, a few solid-state NMR parameters were sensitive to the presence of CO_2 inside the channels. Moreover, molecular modeling reproduced adsorption-isotherms and portrayed the progressive loading of pores of distinct size and shape, entailing distinct CO_2 clustering around individual rotors. This challenging project of having realized dynamics in crystals as fast as in liquids opens new perspectives such as the control of molecular dynamics by the influence of mild chemical stimuli, that is, gas loading. The rapid reorientation of mobile elements in crystals enables the activation of switchable ferroelectric properties that can be used in opto-electronic devices. This unique response of the materials to CO^2 is of great importance for the environment, enlarging perspectives in the field of sensors and gas detection.

2.5. Experimental Section

2.5.1. Materials and Methods

^1H and ^{13}C(APT) solution NMR spectra were recorded at 400 and 100 MHz, respectively, on a Bruker Avance 400 spectrometer. In the following, ^1H data are reported as follows: chemical shifts (in ppm and referenced to internal TMS), integration, multiplicity (s = singlet, d = doublet, t = triplet, q = quartet, m = multiplet), and coupling constants (in Hz). ^{13}C data are reported as follows: chemical shifts (in ppm and referenced to internal TMS), coupling constant (in Hz) and assignation.

IR spectra were acquired in attenuated total reflectance (ATR) by means of a Nicolet iS10 instrument over the range 4000-600 cm-1. In the following, signal intensities are denoted as br = broad, vs = very strong, s = strong, m = medium, and w = weak.

Elemental analyses were obtained with a Perkin Elmer CHN Analyzer 2400 Series II.

Gas chromatography-mass spectrometry (GC-MS) analyses were performed on a ThermoquestTraceGC equipped with a 30 m DB5 silica column coupled with a quadrupolar mass analyzer FinniganTraceMS. The protocol used begun with heating the sample at 70 °C for 4 min. Then, the temperature was raised up to 180 °C at 10 °C/min, and the system was kept at this temperature for 5 min. Finally, the temperature was raised up to 270 °C at 10 °C/min, and the system was kept at this temperature for 15 min. The inlet temperature was set at 200 °C, while the split flow at 15 mL/min.

Microwave heating was performed by means of a CEM Discover SP instrument with a single-mode microwave cavity producing continuous irradiation at 2.45 GHz and power up to 0.3 kW. All the reactions carried out with microwave heating were performed in 10-mL vessels equipped with a Teflon septum and a magnetic stir bar. The temperature, pressure and irradiation power were continuously monitored during the reaction

Differential Scanning Calorimetry (DSC) measurements were performed on a Mettler-Toledo StarE instrument from 25 to 425 °C, at a heating rate of 10 °C/min and under a 80 mL/min flow of N2.

Details of X-Ray Powder Diffraction, Variable Temperature X-Ray Powder Diffraction, solid-state ^{13}C and ^{2}H NMR, ^{1}H T_1 spin-lattice relaxation time and gas adsorption experiments are reported in Appendix 2, along with details of energy activation barrier for rotation nad isosteric heat of adsorption calculations and CO_2 adsorption simulations.

All chemicals and solvents were purchased from Sigma Aldrich, Alfa Aesar or TCI and used without further purification, unless otherwise specified.

2.5.2. Synthesis of 1,4-diethynil-benzene-d4

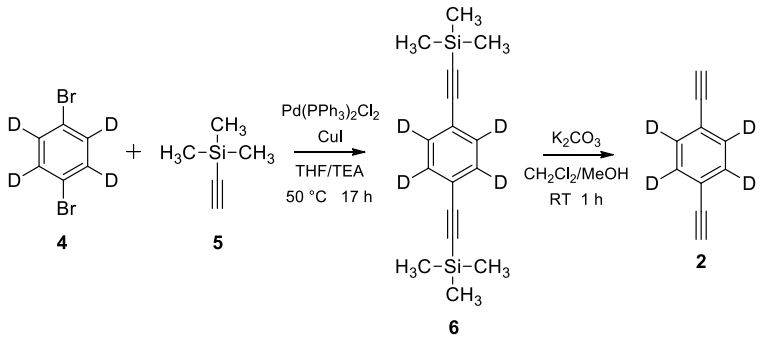

An oven-dried Schlenk flask was purged with N_2 and charged with 1,4-dibromo-benzene-d_4 (**4**) (400 mg, 1.67 mmol), $PdCl_2(PPh_3)_2$ (75 mg, 0.11 mmol), and CuI (30 mg, 0.16 mmol). The flask was then sealed with a rubber septum and N2-purged triethylamine (TEA, 5 mL) was added by means of a syringe. N_2-purged tetrahydrofurane (THF, 5 mL), previously filtered over Al_2O_3, was then added following the same procedure. The obtained solution, purged by bubbling N_2, was stirred for 20 min at room temperature; afterwards, trimethylsilylacetylene (**5**) (TMSA, 950 µL, 6.68 mmol) was added. The resulting yellow mixture was sealed under N_2 atmosphere, heated up to 50°C and kept at this temperature under stirring for 17 h. The extent of the reaction was controlled by GC-MS. Small additional aliquots of TMSA (100 µL each) were periodically added. After 17 h, GC-MS analysis showed complete consumption of 1,4-dibromo-benzene-d_4 and an 8:2 ratio of the final product over the mono-substituted intermediate. At this point, the reaction medium was cooled down to room temperature and filtered over Celite, eluting with EtOAc. The organic fractions thus obtained were combined and dried by rotary evaporation to obtain a black solid. The latter was dissolved in EtOAc (100 mL) and washed with aqueous ammonium hydroxide (28 wt/wt % NH_3, 2×50 mL) and distilled water (50 mL). The organic layer was dried over Na_2SO_4 and concentrated under vacuum. The black residue was purified by silica-gel gravimetric chromatography (pure exane;) to afford 1,4- trimethylsylil-diethynyl-benzene-d_4 (**6**) as a white solid (300 mg, 65.4% yield). IR (ATR, cm^{-1}): 2956(m), 2899(w), 2153(s), 1407(s), 1322(w), 1243(s), 1129(s), 11088(w), 875(s), 831(vs), 754(s), 744(s), 726(s), 697(m), 626(m). ^{1}H-NMR (DMSO-*d*6, ppm): 0.25 (s, $SiMe_3$). ^{13}C-NMR (DMSO-*d*6, ppm): 131.5 (^{1}JC-D = 24.5 Hz, C6D4), 122.3 (*i*-C6D4), 105.2 (C≡C), 96.5 (C≡C), 0.2 (SiMe3). Intermediate **6** (165 mg, 0.61 mmol) was dissolved in a 1:1 mixture of THF (6 mL) and methanol (MeOH, 6 mL) and heated up to 50 °C under stirring. KF (86 mg, 1.5 mmol) was then added to the solution. After 2 h, a GC-MS analysis showed complete consumption of **6**. The organic phase was then extracted with CH_2Cl_2. All the organic layers were combined, dried over Na_2SO_4 and concentrated under vacuum to give 1,4-diethynyl-tetradeutero-benzene (**2**) as a white solid (75 mg, 94% yield). ^{1}H-NMR (DMSO-*d*6, ppm): 3.22 (s, 2H). ^{13}C-NMR (DMSO-d_6, ppm): 132.1 (^{1}JC-D = 24.5 Hz, C_6D_4), 122.5 (*i*-C_6D_4), 83.2.2 (C≡C), 81.2 (C≡C).

2.5.3 Synthesis of 1,4-bis(1H-pyrazol-4-ylethynyl)-benzene-d4, H2BPEB-d4

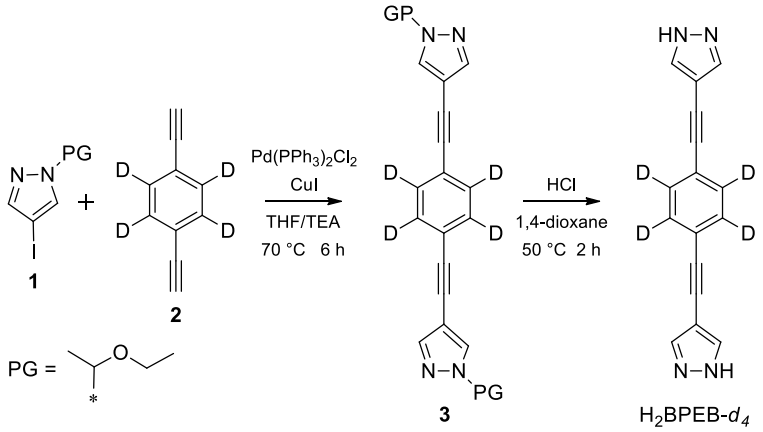

4-Iodo-1-(1-ethoxyethyl)-1*H*-pyrazole (**1**) was synthesized according to the procedure described in Q. Lin, *Org. Lett.*, 2009, 11, 9, 1999.

An oven-dried Schlenk flask was purged with N_2 and charged with 4-iodo-1-(1-ethoxyethyl)-1*H*-pyrazole (850 mg, 3.19 mmol), $Pd(PPh_3)_2Cl_2$ (60 mg, 0.084 mmol), and CuI (20 mg, 0.11 mmol). The flask was sealed with a rubber septum and N_2-purged TEA (5 mL) was added by means of a syringe. N_2-purged THF (5 mL), previously filtered over Al_2O_3, was then added with the same procedure. The obtained yellowish solution was purged by bubbling N_2 at room temperature for 20 min; afterwards, intermediate **2** (180 mg, 1.39 mmol) was added and the resulting mixture was heated up to 70 °C and kept at this temperature under stirring. After 4 h, a thin-layer chromatography (TLC) analysis (silica gel; hexane:EtOAc 4:1) showed complete consumption of **2** and the presence of two spots with different luminescence that we ascribed to the desired product **3** and the mono-substituted intermediate. In order to achieve the highest yield, 4-iodo-1-(1-ethoxyethyl)-1*H*-pyrazole (300 mg) was further added to the suspension. After 2 h at 70 °C, the reaction was stopped. The mixture was cooled down to room temperature and then filtered on a Hirsch funnel; the filtrate was dried by rotary evaporation giving an orange/brown paste. The latter was dissolved in EtOAc and washed with an aqueous solution of ammonia (28 wt/wt % NH_3, 2×25 mL) and distilled water (25 mL). The organic phase was dried over Na_2SO_4 and concentrated under vacuum to afford an orange paste. This solid was washed with little amounts of pentane and filtered on a Hirsch funnel to remove the excess of 4- iodo-(1-ethoxyethyl)-1*H*-pyrazole. Pure Bis(ethoxylethyl)-1,4-bis(*1H*-pyrazol-4-ylethynyl)benzene-d_4 (**3**) was obtained as a yellow powder (300 mg, 53.1% yield). Elem. Anal. Calc. for C24H22D4N4O2 (FW = 406.22 g/mol): C = 70.90%, H = 5.42%, N = 13.79%; found C = 70.05%, H = 6.25%, N = 13.29%. IR (ATR, cm-1): 3106(w), 3076(w), 2978(w), 2907(w), 2212(m), 1669(w), 1553(w), 1438(s), 1388(s), 1344(m), 1328(s), 1295(w), 1252(m), 1174(m), 1120(vs), 1101(vs), 1064(s), 1002(m), 980(s), 943(m), 927(w), 865(vs), 745(s), 725(vs), 663(vs). 1H-NMR (DMSO-*d*6, ppm): 8.36 (1H, s), 7.78 (1H, s), 5.56 (1H, q, 3J = 6.0 Hz), 3.48 (1H, m), 3.21(1H, m), 1.61 (3H, d, 3J = 6.0 Hz), 1.04 (3H, t, 3J = 8.2 Hz). 13C-NMR (DMSO-*d*6, ppm): 141.5 (CH), 130.8 (1JC-D = 24.7 Hz, C6D4), 128.9 (CH), 122.8 (*i*-C6D4), 103.9 (C), 89.9 (C≡C), 87.9 (CH), 82.5 (C≡C), 64.3 (CH2), 22.2 (CH3), 14.8 (CH3).

Intermediate **3** (170 mg, 0.418 mmol) was dissolved in 1,4-dioxane (3 mL) and an aqueous solution of HCl (6 N, 2 mL) was added. The solution was heated up to 50 °C and kept at this temperature under stirring for 2 h. Pure 1,4-bis(1*H*-pyrazol-4-ylethynyl)-benzene-*d*4 (H2BPEB-*d*4) precipitated from the reaction mixture as a pale-yellow solid which was recovered by filtration on a Hirsch funnel and washed with 1,4-dioxane (0.5 mL) and MeOH (10 mL) (70 mg, 72% yield). Elem. Anal. Calc. for $C_{16}H_6D_4N_4$ (FW = 262.30 g/mol): C = 73.20%, H = 3.80%, N = 21.35%; found C = 73.95%, H = 4.02%, N = 21.50%. IR (ATR, cm-1): 3119(s, br), 3048(w), 2960(s, br), 2213(m), 1659(w, br), 1557(w), 1506(w), 1425(s), 1369(s), 1335(m), 1142(m), 1034(m), 993(s), 949(s), 860(vs), 788(s, br), 722(vs), 660(vs), 617(vs). 1H-NMR (DMSO-*d*6, ppm): 7.94 (s). 13C-NMR (DMSO-*d*6, ppm): 138.4 (CH), 131.2 (1JC-D = 24.1 Hz, C6D4), 122.8 (*i*-C6D4), 101.3(C), 89.6 (C≡C), 84.5 (C≡C).

2.5.4. Synthesis of α-[Zn(BPEB-d4)]

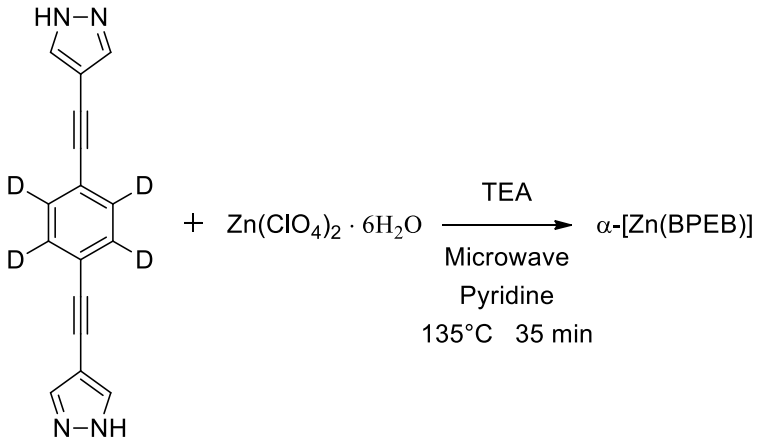

H_2BPEB-d_4

H_2BPEB-d_4 (50 mg, 0.19 mmol) was added to a 10-mL microwave vessel containing pyridine (5 mL). The mixture was stirred until complete dissolution of the ligand: an orange solution was obtained. Then, $Zn(ClO_4)_2 \cdot 6\ H_2O$ (67 mg, 0.18 mmol) was added in a single portion. Eventually, TEA (0.5 mL) was carefully layered over the solution. The mixture was irradiated at 0.3 kW till the temperature reached 100 °C and was kept in this condition for 35 min. Then, the reaction vessel was cooled down to 50 °C and the mixture was filtered on a Hirsch funnel to recover a yellow solid, which was washed with pyridine (2 mL) and MeOH (15 mL). After that, the product was dried under vacuum at 130 °C for 12 h, yielding α-[Zn(BPEB-d_4)] as a yellowish powder (50 mg, 80% yield). Elem. Anal. Calc. for $C_{16}H_4D_4N_4Zn$ (FW = 321.65 g/mol): C = 58.96%, H = 1.24%, N = 17.19%; found C = 58.62%, H = 1.63%, N = 16.81%. IR (ATR, cm-1): 2217(m, br), 1560(m), 1433(s), 1382(s), 1338(m), 1233(m), 1161(w), 1057(vs), 1011(s), 855(s), 738(m), 723(s), 637(vs).

2.5.5. Synthesis of 1,4-bis(1H-pyrazol-4-ylethynyl)benzene (H_2BPEB) and α-[Zn(BPEB)]

1,4-bis(1*H*-pyrazol-4-ylethynyl)benzene (H_2BPEB) and α-[Zn(BPEB)] were synthesized according to the procedure described in S. Galli et al., *J. Mater. Chem. A* **2014**, 2, 12208-12221.

Bibliography for Chapter 2

1. Ali Coskun, T. *et al.* Chemical Society Reviews Great expectations: can artificial molecular machines deliver on their promise? *Chem. Soc. Rev* **41,** 19–30 (2012).

2. Kassem, S. *et al.* Artificial molecular motors. *Chem. Soc. Rev.* **46,** 2592–2621 (2017).

3. Kottas, G. S., Clarke, L. I., Horinek, D. & Michl, J. Artificial molecular rotors. *Chem. Rev.* **105,** 1281–1376 (2005).

4. Erbas-Cakmak, S., Leigh, D. A., McTernan, C. T. & Nussbaumer, A. L. Artificial Molecular Machines. *Chem. Rev.* **115,** 10081–10206 (2015).

5. Kudernac, T. *et al.* Electrically driven directional motion of a four-wheeled molecule on a metal surface. *Nature* **479,** 208–211 (2011).

6. Greb, L. & Lehn, J. M. Light-driven molecular motors: Imines as four-step or two-step unidirectional rotors. *J. Am. Chem. Soc.* **136,** 13114–13117 (2014).

7. Koumura, N., Zijistra, R. W. J., Van Delden, R. A., Harada, N. & Feringa, B. L. Light-driven monodirectional molecular rotor. *Nature* **401,** 152–155 (1999).

8. Ragazzon, G., Baroncini, M., Silvi, S., Venturi, M. & Credi, A. Light-powered, artificial molecular pumps: A minimalistic approach. *Beilstein J. Nanotechnol.* **6,** 2096–2104 (2015).

9. Pezzato, C. *et al.* An efficient artificial molecular pump. *Tetrahedron* **73,** 4849–4857 (2017).

10. Pederson, B. P., Buch-Pedersen, M. J., Morth, J. P., Palmgren, M. G. & Nissen, P. Crystal structure of the plasma membrane proton pump. *Nature* **450,** 1111–1114 (2009).

11. Vogelsberg, C. S. & Garcia-Garibay, M. A. Crystalline molecular machines: Function, phase order, dimensionality, and composition. *Chemical Society Reviews* **41,** 1892–1910 (2012).

12. Setaka, W. & Yamaguchi, K. Thermal modulation of birefringence observed in a crystalline molecular gyrotop. *Proc. Natl. Acad. Sci.* **109,** 9271–9275 (2012).

13. Zhang, Q. C. *et al.* Modulating the rotation of a molecular rotor through hydrogen-bonding interactions between the rotator and stator. *Angew. Chemie - Int. Ed.* **52,** 12602–12605 (2013).

14. Comotti, A., Bracco, S. & Sozzani, P. Molecular Rotors Built in Porous Materials. *Acc. Chem. Res.* **49,** 1701–1710 (2016).

15. Bracco, S. *et al.* CO 2 regulates molecular rotor dynamics in porous materials. *Chem. Commun. Chem. Commun* **7776,** 7776–7779 (2017).

16. Vogelsberg, C. S. *et al.* Dynamics of molecular rotors confined in two dimensions: Transition from a 2D rotational glass to a 2D rotational fluid in a periodic mesoporous organosilica. *J. Phys. Chem. B* **116,** 1623–1632 (2012).

17. Brustolon, M. *et al.* Dynamics of alkoxy-oligothiophene ground and excited states in nanochannels. *J. Am. Chem. Soc.* **126,** 15512–15519 (2004).

18. Comotti, A. *et al.* Engineering switchable rotors in molecular crystals with open porosity. *J. Am. Chem. Soc.* **136,** 618–621 (2014).

19. Comotti, A., Bracco, S., Ben, T., Qiu, S. & Sozzani, P. Molecular rotors in porous organic frameworks. *Angew. Chemie - Int. Ed.* **53,** 1043–1047 (2014).

20. Comotti, A., Bracco, S., Valsesia, P., Beretta, M. & Sozzani, P. Fast molecular rotor dynamics modulated by guest inclusion in a highly organized nanoporous organosilica. *Angew. Chemie - Int. Ed.* **49,** 1760–1764 (2010).

21. Bracco, S. *et al.* Dipolar rotors orderly aligned in mesoporous fluorinated organosilica architectures. *Angew. Chemie - Int. Ed.* **54,** 4773–4777 (2015).

22. Aguilar-Granda, A. *et al.* Transient Porosity in Densely Packed Crystalline Carbazole-(p-Diethynylphenylene)-Carbazole Rotors: CO2and Acetone Sorption Properties. *J. Am. Chem. Soc.* **139,** 7549–7557 (2017).

23. Desiraju, G. R. & Steiner, T. *The Weak Hydrogen Bond*. *Structural Chemistry* (1999). doi:10.1093/acprof:oso/9780198509707.001.0001

24. Das, S., Heasman, P., Ben, T. & Qiu, S. Porous Organic Materials: Strategic Design and Structure-Function Correlation. *Chemical Reviews* **117,** 1515–1563 (2017).

25. Rodríguez-Velamazán, J. A. *et al.* A switchable molecular rotator: Neutron spectroscopy study on a polymeric spin-crossover compound. *J. Am. Chem. Soc.* **134,** 5083–5089 (2012).

26. Furukawa, H. *et al.* Ultrahigh porosity in metal-organic frameworks. *Science (80-.).* **329,** 424–428 (2010).

27. Zhou, H. C. J. & Kitagawa, S. Metal-Organic Frameworks (MOFs). *Chemical Society Reviews* **43,** 5415–5418 (2014).

28. Elsaidi, S. K. *et al.* Effect of ring rotation upon gas adsorption in SIFSIX-3-M (M = Fe, Ni) pillared square grid networks. *Chem. Sci.* **8,** 2373–2380 (2017).

29. Yang, W. *et al.* Selective CO2 uptake and inverse CO2/C2H2 selectivity in a dynamic bifunctional metal–organic framework. *Chem. Sci.* **3,** 2993 (2012).

30. Gould, S. L., Tranchemontagne, D., Yaghi, O. M. & Garcia-Garibay, M. A. Amphidynamic character of crystalline MOF-5: Rotational dynamics of terephthalate phenylenes in a free-volume, sterically unhindered environment. *J. Am. Chem. Soc.* **130,** 3246–3247 (2008).

31. Shustova, N. B. *et al.* Phenyl ring dynamics in a tetraphenylethylene-bridged metal-organic framework: Implications for the mechanism of aggregation-induced emission. *J. Am. Chem. Soc.* **134,** 15061–15070 (2012).

32. Rodríguez-Velamazán, J. A. *et al.* A switchable molecular rotator: Neutron spectroscopy study on a polymeric spin-crossover compound. *J. Am. Chem. Soc.* **134,** 5083–5089 (2012).

33. Kolokolov, D. I. *et al.* Dynamics of benzene rings in MIL-53(Cr) and MIL-47(V) frameworks studied by2H NMR spectroscopy. *Angew. Chemie - Int. Ed.* **49,** 4791–4794 (2010).

34. Kolokolov, D. I. *et al.* Dynamics of Benzene Rings in MIL-53 (Cr) and MIL-47 (V) Frameworks Studied by 2 H NMR Spectroscopy **. *Angew. Chemie* **53,** 4791–4794 (2010).

35. Winston, E. B. *et al.* Dipolar molecular rotors in the metal-organic framework crystal IRMOF-2. *Phys. Chem. Chem. Phys.* **10,** 5188–5191 (2008).

36. Morris, W., Taylor, R. E., Dybowski, C., Yaghi, O. M. & Garcia-Garibay, M. A. *Framework mobility in the metal-organic framework crystal IRMOF-3: Evidence for aromatic ring and amine rotation*. *Journal of Molecular Structure* **1004,** (Elsevier, 2011).

37. Galli, S. *et al.* When long bis(pyrazolates) meet late transition metals: Structure, stability and adsorption of metal-organic frameworks featuring large parallel channels. *J. Mater. Chem. A* **2,** 12208–12221 (2014).

38. Duer, M. J. *Solid-State NMR Spectroscopy*. (2002). doi:10.1002/9780470999394

39. Negishi, E. & Meijere, A. de. *Handbook of Organopalladium Chemistry for Organic Synthesis*. (Wiley-Interscience, 2002). doi:10.1002/0471473804

40. Young, R. The Rietveld Method. *by RA Young, Oxford University Press, Oxford* 312 (1993). doi:10.1017/CBO9781107415324.004

41. Bruker. TOPAS R. Version 3.0 (2005).

42. Inukai, M. *et al.* Control of Molecular Rotor Rotational Frequencies in Porous Coordination Polymers Using a Solid-Solution Approach. *J. Am. Chem. Soc.* **137,** 12183–12186 (2015).

43. Kolokolov, D. I. *et al.* Probing the dynamics of the porous Zr terephthalate UiO-66 framework using 2H NMR and neutron scattering. *J. Phys. Chem. C* **116,** 12131–12136 (2012).

44. Catalano, L. *et al.* Rotational dynamics of diazabicyclo[2.2.2]octane in isomorphous halogen-bonded co-crystals: Entropic and enthalpic effects. *J. Am. Chem. Soc.* **139,** 843–848 (2017).

3. Chapter 3

Synthesis and characterization of Metal-Organic Frameworks with bis(pyrazolates) rod-like linkers containing a dipolar molecular rotor

3.1. Introduction

In Chapter 2 we discussed the relevant role of solid-state molecular rotors research and how low-density porous crystalline materials can be exploited to precisely design the space around the rotors array, so they can experience unhindered fast dynamics. In particular, we demonstrated ultra-fast rotation of *p*-phenylene rings inserted into the rigid porous structure of a Zn-based MOF and we showed how, thanks to the open structure of the material, their dynamics could be influenced by an external chemical stimulus, such as CO_2 adsorption. This last property reveals the possibility to exploit molecular rotors in porous solids as responsive elements sensitive to chemical perturbation. Other advanced applications have been proposed for solid materials possessing dynamic elements, such as switchable ferroelectrics or material with tunable optical properties[1–3]. However, these last goals cannot be achieved unless electric dipole moments are integrated onto the rotors to create oscillating dipoles whose orientation could be controlled by an external stimulus, such as an electric field or light. Materials containing dipolar molecular rotors are still uncommon and, so far, most of them have been realized exploiting the gain in freedom provided by surfaces[4–6] and by molecular crystals with frustrated packing[7,8], as well as by mobile guests included in suitable hosts[9]. In 2010, Sozzani and co-workers reported for the first time dipolar rotating moieties in a crystalline Periodic Mesoporous Organosilica (PMO) and they also demonstrated guest-modulated rotor dynamics[11], but that remained the sole example of fast dipolar rotors in porous materials. In the present work, we further exploited the open volume guaranteed by MOF structures and the rigidity of bis-pyrazolate rod-like ligands to design a new material with rotating dipoles. The ligand of choice possesses a 1,4-diethynylbenzene core that will constitute the molecular rotor, while fluorine substituents have been introduced on the *p*-phenyl ring to induce an asymmetry on the electronic charge distribution on the ring and thus generate the dipole. Pyrazoles have been chosen as metal-binding sites for the preparation of the metal-organic network. The dynamic properties of dipolar rotors in MOFs structures in vacuo and in presence of CO_2 guest molecules will be studied by solid-state NMR measuring T_1 relaxation times and Dieletric Loss Spectroscopy (DLS).

Furthermore, fluorinated porous materials are promising candidates for the selective adsorption of CO_2. It is believed that highly electronegative fluorine moieties would interact with CO_2 molecules via a dipole-quadrupole interaction, thus improving the carbon dioxide adsorption performances of the material[12,13]. However, it is still unclear to what extent this really occurs, as contradicting papers have been published[14]. The lack of understanding is mainly due to the scarceness of fluorinated and non-fluorinated isostructural matrices that could be used to study the phenomenon. The fluorinated [Zn(**BPEFB**)] and [Ni(**BPEFB**)] MOFs presented in this chapter are isostructural to the previously reported non-fluorinated [Zn(BPEB)] and [Ni(BPEB)][15]. Hence, we also evaluated the CO_2 adsorption properties of the new materials and we compared the results with the non-fluorinated analogues to help shed light on the topic.

3.2. Design and synthesis of the linker and of the MOFs

In the last two decades the solidity of pyrazolate groups as metal-coordinating sites for the preparation of metal-organic frameworks has been fully demonstrated[16]. In 2008 Long et al. synthesized for the first time 1,4-benzenedipyrazole (H_2BDP), which was used as ligand to prepare a Co(II) MOF[17] with unprecedent multi-step adsorption. In following years, new structures were prepared using H_2BDP as ligand and Zn(II)[18], Ni(II)[19] and Fe(III)[20] as metal nodes. All these materials showed a very high stability towards water, which is typically very detrimental for carboxylate-based MOFs.

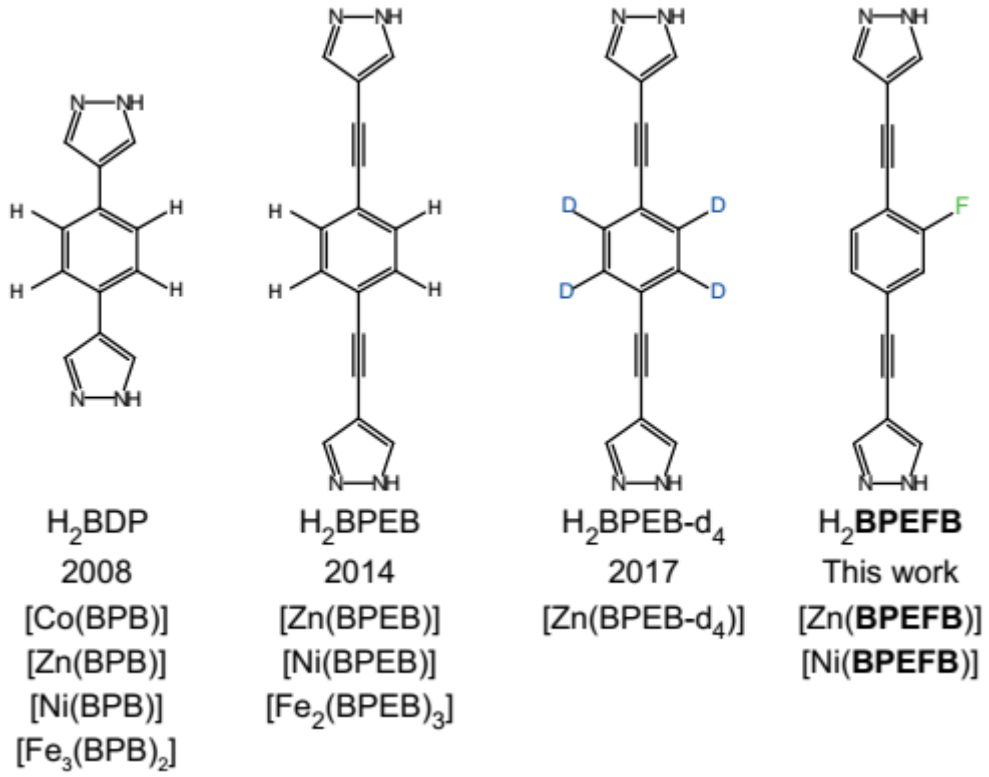

Figure 3.1. *Series of bis-pyrazolate rod-like linker for MOFs preparation*

In 2014 three new MOFs were synthesized and characterized from our group using an extended rod-like bis(pyrazolate) linker, 1,4-bis(1H-pyrazol-4-ylethynyl)benzene (H_2BPEB)[15], with the aim of increasing the free volume of the resulting materials, and, thus, their gas storage capacity. The increase in ligand length was achieved through addition of triple bonds in 1,4 positions of the central phenylene ring. Moreover, these triple bonds were added with the supplementary objective of enhancing the mobility of the central *para*-phenylene ring around its 1,4-axis, so it could experience fast rotational dynamics (molecular rotor)[21–24]. It is known that rotation of *p*-phenylene moieties around a sp^2-*sp* carbon-carbon bond occurs with a low energy barrier[25,26]. The empty space provided by the porous nature of the frameworks was expected to guarantee enough free space around the rotors, so they could undergo unhindered rotation. Furthermore, the porosity would allow the rotors to communicate with the external environment, giving the possibility to tune their motion by guest adsorption. To fully characterize the dynamics of the rotors in the crystalline structure of MOFs, a ligand with a

perdeuterated rotor, H_2BPEB-d_4 was synthesized and used to prepare α-[Zn(BPEB-d_4)]. Deuterium solid-state NMR is one of the most powerful techniques for the study of dynamics in solid-state, thanks to the peculiar line shape of ^{2}H signals, which is strictly dependant from the mechanism and speed of motion. The results of the solid-state ^{2}H-NMR experiments on the high mobility of the *p*-phenyl rings in α-[Zn(BPEB-d_4)] were published in 2017 and constitutes the Chapter 2 of this thesis. An extremely low barrier (0.5 kcal/mol) for rotation of deuterated rotors in α-[Zn(BPEB-d_4)] was measured, so low that it actually falls in the liquid state motion regime, demonstrating the goodness of the design of both the ligand and the MOF crystal structure. In addition, we demonstrated that rotors dynamics could be finely tuned by interactions with CO_2 adsorbed in the porous structure.

To further explore the possibilities offered by the ultra-fast rotational dynamics of the rotors arrays in porous bis-pyrazolated MOF structures, ligand H_2**BPEFB** was designed to exhibit a net electric dipole moment on the rotating *p*-phenyl ring. The dipole moment is generated by the introduction of a fluorine substituent on the central aromatic ring; the high electronegativity of the fluorine atom induces an asymmetry in the electron density distribution on the phenyl ring that result in the desired electric dipole moment. Dipolar molecular rotors[27,28] are particularly interesting because rotors position and dynamics could be regulated by external stimuli like electric fields[9,11,29–31], giving the opportunity to envisage new and exciting applications such as switchable ferroelectrics, tunable opto-electronic materials and information processing devices.

Furthermore, there is an open debate whether MOFs with fluorinated ligands are more efficient materials for CO_2 adsorption and separation compared with non-fluorinated materials[14]. It is generally accepted that the presence of electric dipoles on the framework, such as those generated by fluorine moieties, establishes favourable interactions with the electric quadrupole moment of CO_2 molecules[32]. However, it not clear to what extent this is beneficial towards CO_2 adsorption. This uncertainty is due to the scarceness in literature of fluorinated and non-fluorinated MOFs having the same crystal structure. The fluorinated MOFs reported here are isostructural with their non-fluorinated analogue published in 2014, thus the analysis of their CO_2 adsorption properties will be carried out to better understand the fluorine effect.

The synthesis of ligand H_2**BPEFB** is illustrated in **Scheme 3.1**. Starting materials **2** and **3** were synthesized according to previously published procedures and were subsequently coupled utilizing the Sonogashira protocol[33] for the cross-coupling reaction between terminal alkynes and aromatic halides. Protection of pyrazole nitrogen with an ether group was necessary to avoid coordination of metal catalysts to pyrazole reactants during the coupling reaction. Detailed reaction conditions for the preparation of H_2**BPEFB** and its precursors are reported in the Experimental Section. Purification of intermediate **4** was complicated by the formation of a series of by-products, yellow-orange in colour, with solubility similar to the desired product in most solvents and with almost identical retention factors on Thin Layer Chromatography (TLC) with all the eluents tested. The mixture of the desired molecule and of these unknown impurities was isolated from the crude by column chromatography (eluent hexane/ethyl acetate 8:2); observation of ^{1}H-NMR spectra of the mixture revealed the presence of a series of minor signals that could not be ascribed to the desired product (see Appendix 3, **Figure A3.1** and **A3.2**). The presence of these minor proton signals led us to hypothesize that

these impurities might be the result of an alkyne-alkyne coupling reaction (**Figure 3.2**). Terminal alkyne-alkyne coupling reactions are known in organic chemistry as Eglinton reaction[34] and they are catalysed by Cu(II). In our reaction media, Cu(II) should not be present, but minor amounts might be introduced either because present as impurity in the CuI catalyst or generated in situ from oxidation of Cu(I) by traces of O_2.

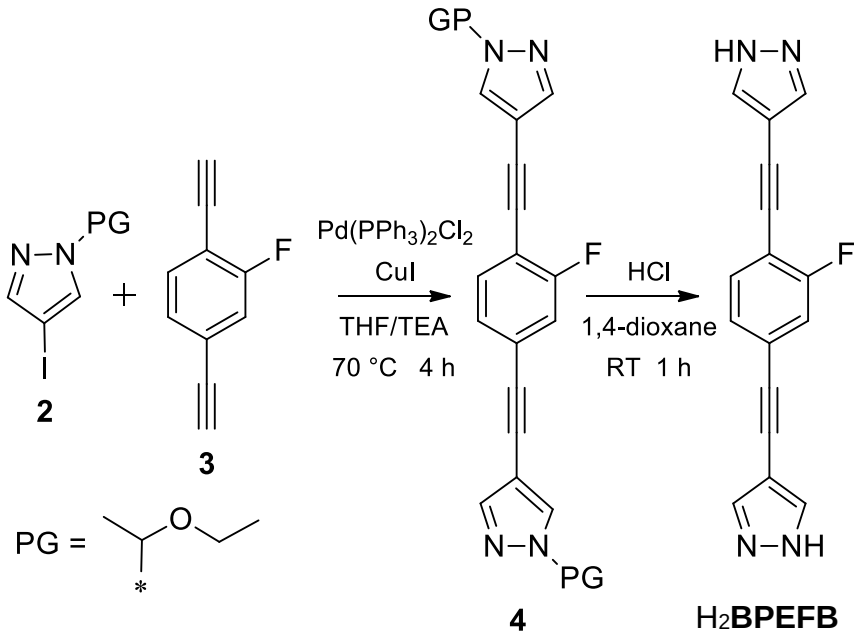

*Scheme 3.1. Schematic synthesis of MOF ligand H_2**BPEFB***

A more recent paper from Trunk et al.[35] suggested the possibility that unprotected terminal diynes like **3** might undergo homo-coupling even in solid state at room temperature. Again, this is most probably caused by residual traces of Cu(II) coming from the previous synthetic step, as terminal alkynes are often prepared by Pd(0)/Cu(I) catalysed Sonogashira coupling between aromatic halides and trimethylsilylacetylene. If, after removal of protecting trimethylsilyl groups, traces of Cu(I) co-catalyst remain mixed with the product, they would be quickly oxidized to Cu(II) by oxygen in air, thus generating the catalyst for Eglinton coupling. In our opinion, formation of ligand precursor **4** and impurities **4a-c** proceeds as follows (**Scheme 3.2**): first, the Pd(0)/Cu(I) catalytic system promotes the coupling between a molecule of **2** and one alkyne group of a molecule of **3**. Now, the second coupling of **2** with **10** to form **4** is slower because intermediate **10** has a stronger electron-donating character compared with **3** and a second electron-rich pyrazole must be coupled. It is known that electron-rich species decrease the rate of the Sonogashira catalytic cycle as the oxidative addition of electron-rich species to Pd(0) is disadvantaged[36]. Because of this, Eglinton coupling becomes competitive with Sonogashira coupling, despite Cu(II) being present only in traces, and both **4** and **4a-c** are formed. Purification of product **4** from these by-products via column chromatography was not viable in any of the eluent tested.

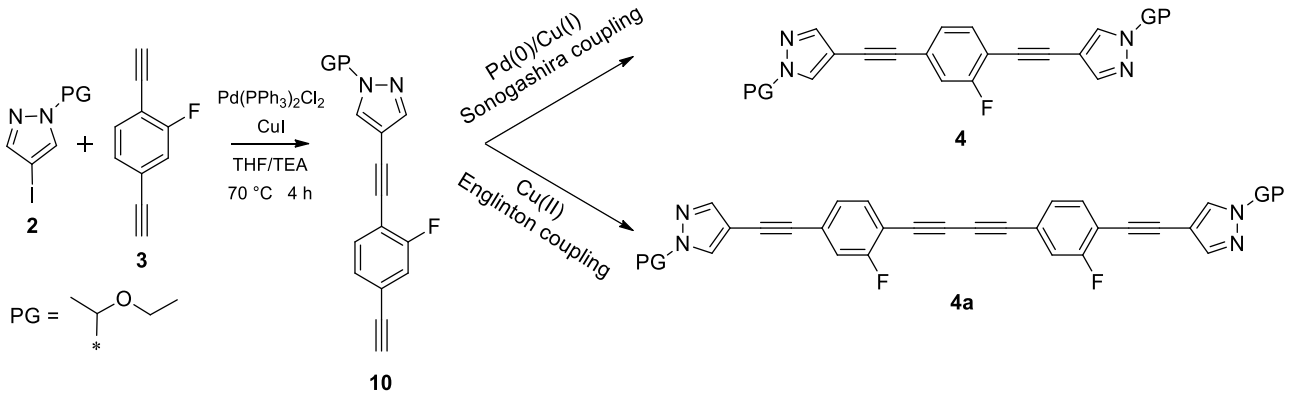

*Scheme 3.2. Proposed reaction path for the formation of by-products **4a-c**. In the scheme, only **4a** is reported for simplicity.*

Eventually, we found out that **4** could be purified exploiting its superior solubility in pentane respect to molecules **4a-c**; this method (described in detail in the Experimental Section) gave **4** with a high degree of purity, although in low yields. Nevertheless, in MOFs synthesis, high purity of the organic ligand is often a crucial factor for the preparation of high quality materials, so sacrificing yield in favour of purity is always a good compromise.

One might inquire why didn't we avoided formation of species **4a-c** simply by reacting 4-ethynylpyrazole with 1,4-dibromo-2-fluorobenzene. In such a reaction, alkyne-alkyne coupling product would produce 1,4-di(1H-pyrazol-4-yl)buta-1,3-diyne and this would have been for sure easier to separate from **4**. Actually, this alternative route was tested, but the conditions we used gave an even more complex mixture of products. Since we already obtained pure **4** with the previously described methodology and the optimization of the reaction conditions for the synthesis of the ligands was not out primary objective, we decided to not explore further this second route for the time being.

After that preparation of H_2**BPEFB** was completed, we started investigating various synthetic strategies changing parameters such as metal ion salt, solvent, base and temperature, in order to identify the most straightforward reaction path toward each target MOF. In this work we aimed specifically at the preparation of the fluorinated versions of Ni(II)- and Zn(II)-compounds; Fe(III)-containing material was excluded from our synthetic efforts. This choice was dictated by our intention of studying the dynamics of the rotors arrays by solid-state NMR. Fe(III) is not compatible with NMR techniques as it is a paramagnetic ion. Zn(II), on the other end, is always diamagnetic, while Ni(II) is diamagnetic in the square planar configuration that it is expected to adopt in this MOF structure.

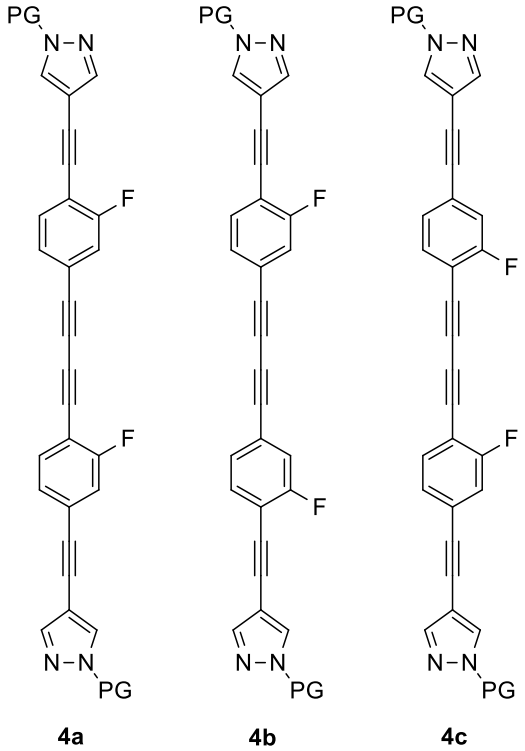

*Figure 3.2. Molecular structure of the most probable by-products formed during the synthesis of ligand **1***

Surprisingly, the conditions described in our previous work for the preparation of the non-fluorinated Ni(II) and Zn(II) MOFs analogue did not produce high quality materials when ligand H_2**BPEFB** was used. In general, the preparation of MOFs materials with high degrees of crystallinity employing H_2**BPEFB** was found to be more challenging. Interestingly, we found out that [Zn(**BPEFB**)] can crystallize in two different phases, named α and β, just as like its non-fluorinated predecessors [Zn(BPEB)] and deuterated [Zn(BPEB-d_4)] (see Appendix 3, **Figure A3.5**). Different reaction conditions favour one phase over the other. Both α and β phase of [Zn(BPEB)] were isolated, but only α phase was structurally resolved. Because of this, all our efforts were focused on the isolation of α-[Zn(**BPEFB**)]. As a result of this preparative screening, α-[Zn(**BPEFB**)] could be successfully isolated by following a solution-phase one-pot reaction, reacting $Zn(NO_3)_2$ and H_2**BPEFB** in benzonitrile in presence of DBU at 150 °C for 6 hours, while [Ni(H_2**BPEFB**)] required a microwave-assisted route in pyridine at 100 °C for 25 min with triethylamine as base.

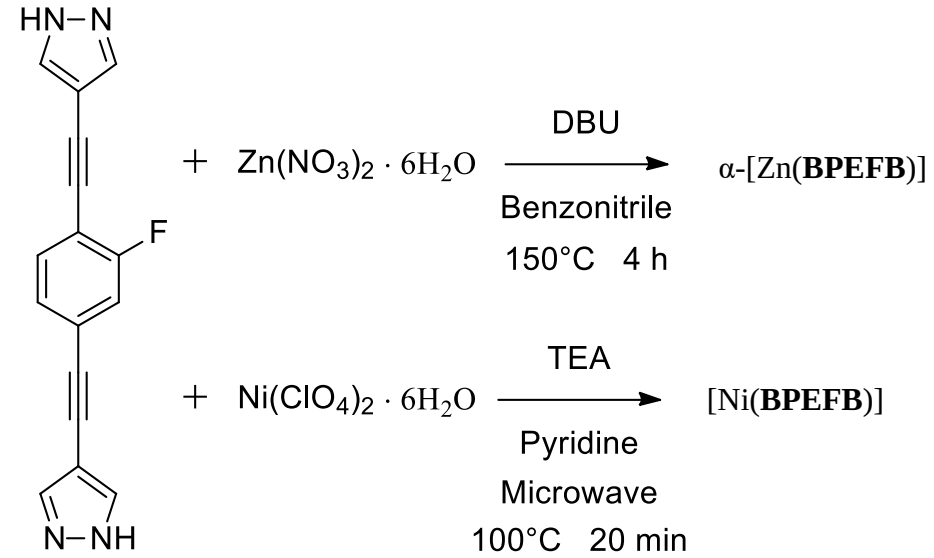

*Scheme 3.3. Reaction conditions for the synthesis of MOFs α-[Zn(**BPEFB**)] and [Ni(**BPEFB**)]*

Both species precipitate in satisfactory yields in the form of air- and light-stable powders insoluble in water and in the most common solvents, thereby suggesting the polymeric nature of their crystal structures.

3.3. Characterization of α-[Zn(**BPEFB**)] and [Ni(**BPEFB**)]

3.3.1. Structural analysis

α-[Zn(**BPEFB**)] is isomorphous and isostructural to α-[Zn(BPEB)] and to α-[Zn(BPEB-d_4)]. Similarly to the latter two materials, α-[Zn(**BPEFB**)] can crystallize either into an α- or β-phase, depending on the synthetic conditions; usually, both phases are formed during the synthesis, but the right preparative conditions can favour one or the other phase. Since the structure of the β-phase of this Zn-MOFs series was never resolved, all our efforts were focused on the isolation of the α-phase, which was eventually obtained with the conditions shown in **Scheme 3.2.** α-[Zn(**BPEFB**)] crystallizes in the orthorhombic group *Cccm*; the asymmetric unit of α-[Zn(**BPEFB**)] contains one independent Zn(II) ion and one independent $(\mathbf{BPEFB})^{2-}$ ligand, both lying on special positions. Each metal centre is coordinated by four nitrogen atoms of four ligands and possesses a distorted tetrahedral stereochemistry (**Figure 3.3a**). As expected, the linkers adopt the *exo*-tetradentate coordination mode: the nitrogen atoms of the same pyrazolate moiety bridge nearby metal ions 3.65 Å apart, building up 1-D chains of collinear metal centres running along the crystallographic axis **c**. Adjacent chains are further connected by the spacers in the [1,1,0] direction (and the crystallographically related ones) in such a way as to generate two mutually interpenetrated 3-D networks reciprocally displaced by about 7.75 Å along **b (Figure 3.3b)**. Despite the presence of interpenetration, the crystal structure of α-[Zn(**1**)] features two sets of square-shaped 1-D channels running along **c**, the vertices of which are defined by the Zn(II) nodes, while the walls are decorated by the spacers. The smaller channels have a cross section of 4.9 × 4.9 $Å^2$, while the

wider ones, have a larger side of 13.3 Å. Taking into account van der Waals radii of atoms, smaller channels in α-[Zn(**BPEFB**)] can host a cylindrical pore with a diameter of 3 Å, while the bigger channels can host a cylinder with base diameter of 9.9 Å.

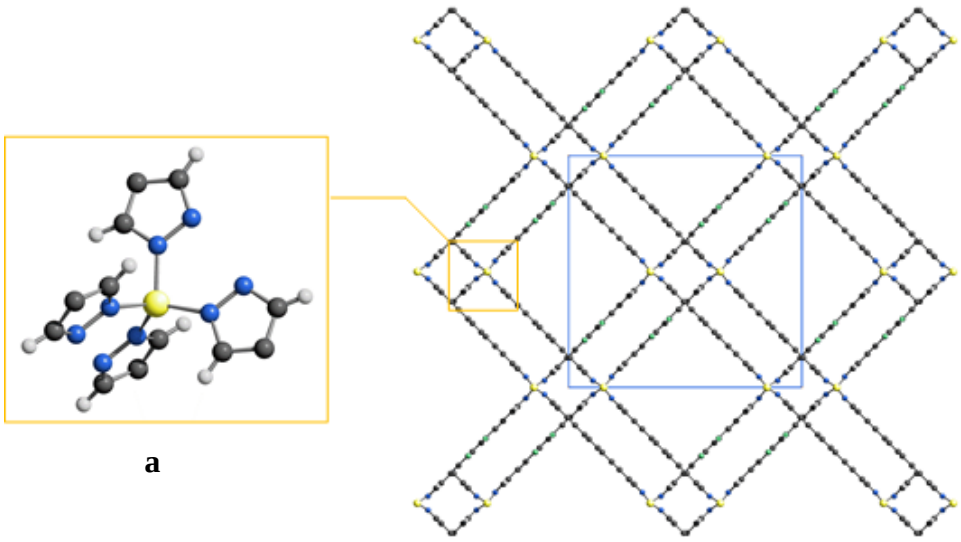

a

b)

Figure 3.3*. Representation of the crystalline structure of α-[Zn(**BPEFB**)]: **a)** the tetrahedral coordination of the metallic center; **b)** the crystal packaging seen along **c** axis (horizontal axis **a**; vertical axis **b**) the two interpenetrated networks and the two different types of channels can be clearly distinguished. Grey = carbon, Light grey = hydrogen, Blue = nitrogen, Green = fluorine, Zinc = yellow*

[Ni(**BPEFB**)] is isomorphous and isostructural to [Ni(BPEB)]: it crystallizes in the orthorhombic space group *Imma*, the asymmetric unit featuring one Ni(II) ion and one $(\mathbf{BPEFB})^{2-}$ ligand, both lying in special positions. Each metal centre is coordinated in square-planar stereochemistry by four nitrogen atoms of four $(\mathbf{1})^{2-}$ moieties (**Figure 3.4a**), acting overall in the *exo*-tetradentate coordination mode. With one of their pyrazolate rings, the ligands bridge Ni···Ni vectors 3.4 Å long (**a**/2) and generate parallel 1-D chains of metal ions. Along the [0,1,1] direction, each chain is further linked to four nearby ones by the spacers, with the consequent formation of a 3-D network possessing large rhombic channels running along **a** (**Figure 3.4b**). According to crystallographic data of [Ni(**BPEFB**)], the rhombic channels have a major diagonal 31.5 Å long and a minor diagonal of 18.2 Å and can host an ellipse 9.7 × 5.7 $Å^2$ wide.

It must be pointed out that [Ni(**BPEFB**)] contains a small portion of amorphous material, as evidenced by its PXRD pattern (see Appendix 3, **Figure A3.4**). Despite all our synthetic efforts, this small fraction of amorphous material was invariably found in all our batches.

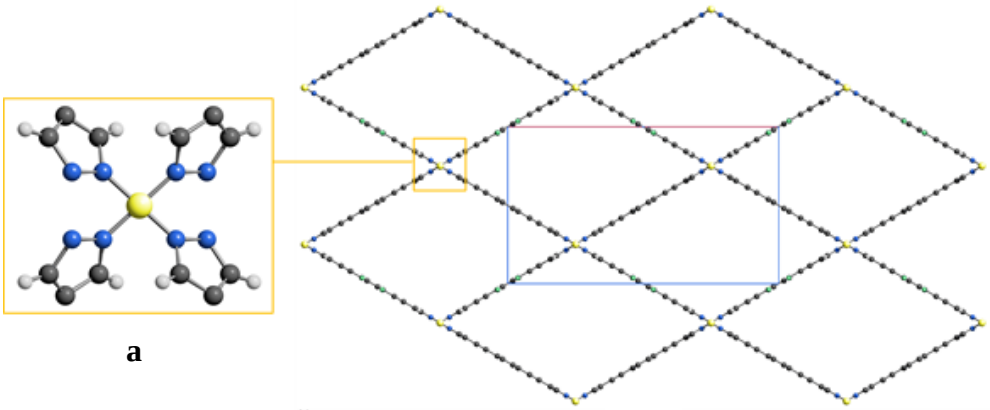

*Figure 3.4. Schematic representation of the crystal structure of [Ni(**BPEFB**)]: **a)** the square planar coordination sphere of the metal center; **b)** the crystal packing, visualized along **a** (horizontal axis **b**; vertical axis **c**) The 1-D rhombic channels can be clearly seen running along **a**. Grey = carbon; Light grey = hydrogen; Blue = nitrogen; Green = fluorine; Yellow = nickel*

3.3.2 Solid-State NMR analysis

The two materials were further examined by ^{13}C CP/MAS solid-state. Spectra are shown in **Figure 3.5** along with signal assignation.

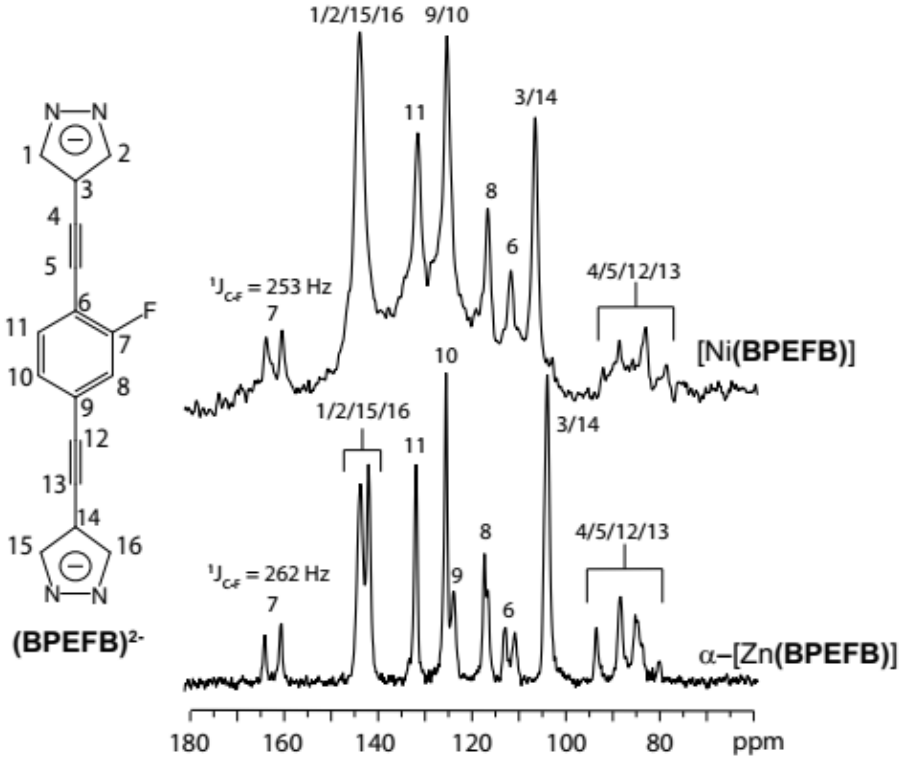

*Figure 3.5. ^{13}C solid state CP/MAS NMR spectra of MOFs [Ni(**BPEFB**)] and α-[Zn(**BPEFB**)] collected at room temperature with a contact time of 2 ms and a rotor speed of 12.5 kHz.*

The number of signals and their positions are consistent with the solution spectrum of ligand H_2**BPEFB** (see Experimental Section). However, regarding signal multiplicity in α-[Zn(**BPEFB**)] spectrum, it must be remembered that the two halves of the ligand are not identical neither from a crystallographic perspective because of interpenetration (see Chapter 2 of this thesis), nor chemically because of the presence of the fluorine atom. Because of this crystallographic inequality, solid state ^{19}F-NMR of α-[Zn(**BPEFB**)] shows two signals, with a 1:1 internal ratio (see Appendix 3, **Figure A3.11**).

In both ^{13}C spectra of **Figure 3.5**, the signal arising from the C-F group can be appreciated at about 165 ppm, with a typical $^1J_{C\text{-}F}$ around 250 Hz. We also collected a series of ^{13}C CP/MAS experiments on α-[Zn(**BPEFB**)] cross polarizing carbon atoms with ^{19}F nuclei (**Figure A3.12**): it can be seen that on increasing contact times ^{13}C nuclei further away from the fluorine atom can receive fluorine magnetization and give rise to new signals. Resolution of ^{13}C CP/MAS spectrum of α-[Zn(**BPEFB**)] spectrum is much higher compared to Ni-complex and the $^2J_{C\text{-}F}$ couplings of carbon 6 and 8 (159 Hz and 56 Hz, respectively) can be appreciated. The higher resolution (sharper peaks) of α-[Zn(**BPEFB**)] spectrum is due to a higher degree of crystallinity of the Zn(II) sample compared to the Ni(II) framework, which is partially amorphous, as already noticed by PXRD analyses. Moreover, the signal-to-noise ratio in [Ni(**BPEFB**)] spectrum is lower. This is most probably due to the presence, in the amorphous phase, of Ni(II) ions in octahedral coordination, which are paramagnetic and perturb NMR experiments. As a consequence, [Ni(**BPEFB**)] is not eligible for rotors dynamics studies trough T_1 relaxation times measurements as the presence of this small amount of paramagnetic octahedral Ni(II) will offer a fast relaxation mechanism to ^{13}C atoms, thus making difficult the study of dynamics through T_1 measurements.

3.3.3. Thermal analysis

The thermal behaviour of α-[Zn(**BPEFB**)] and [Ni(**BPEFB**)] was investigated by Differential Scanning Calorimetry (DSC) under inert atmosphere and Variable-Temperature X-Ray Powder Diffraction (VT-XRPD) measurements in air. The DSC traces are shown in **Figure A3.6**, while VT-XRPD experiments are shown in **Figure 3.6**. Compounds α-[Zn(**BPEFB**)] and [Ni(**BPEFB**)] possess high thermal stability: as demonstrated by their DSC profiles, thermal decomposition occurs at 425 °C and 442 °C, respectively. A more careful observation of DSC analysis of [Ni(**BPEFB**)] shows that a minor exothermic phenomenon takes place around 250 °C. This might indicate that thermal decomposition of the Ni-compound starts at lower temperatures and is concluded at 442 °C. This hypothesis is confirmed by VT-XRPD measurements: [Ni(**BTEFB**)], despite not collapsing, starts losing crystallinity already at 250°C (**Figure 3.6**). After that, no other phenomena occur until decomposition. VT-XRPD analysis on α-[Zn(**BPEFB**)] demonstrates the high thermal stability of this material, which does not collapse nor undergoes phase transitions up to decomposition, starting, in air, at about 400 °C. A Le Bail parametric treatment of the VT-XRPD data acquired in the temperature range 30-350 °C highlighted that progressively raising the temperature brings about a small unit cell volume decrease (i.e. a negative thermal expansion) of about -1.0%.

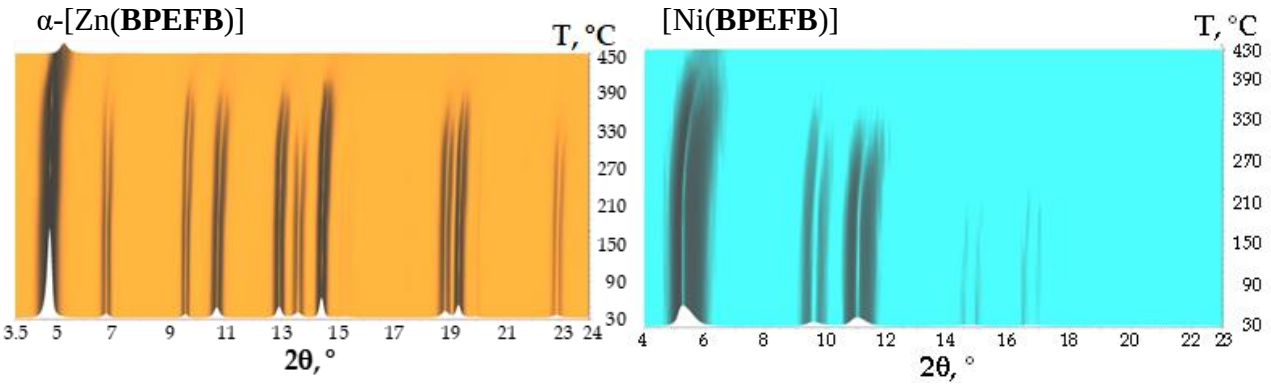

***Figure 3.6**. Thermal behavior of α-[Zn(**BPEFB**)] (left) and of [Ni(**BPEFB**)] (right): plot of the X-ray powder diffraction patterns as a function of temperature, measured by heating in air, with steps of 20 °C, from 30 °C up to decomposition.*

VT-XRPD measurements on the two materials confirmed their high thermal stability and demonstrated their permanent porosity: increasing the temperature does not influence their structural features, and their network does not collapse.

3.3.4. Gas adsorption measurements

The permanent porosity of the title MOFs was demonstrated by N_2 adsorption–desorption measurements performed at 77 K, as reported in **Figure 3.7**. The main textural parameters of the two materials, as derived from the N_2 isotherms, are collected in **Table 3.1**.

***Table 3.1**. Textural parameters of α-[Zn(**BPEFB**)] and [Ni(**BPEFB**)] as derived from N_2 adsorption isotherms at 77 K.*

	S_{BET} (m^2/g)	$S_{Langmuir}$ (m^2/g)	V_{total}[a] (cm^3/g)	V_{micro}[b] (cm^3/g)
α-[Zn(**BPEFB**)]	1000	1178	0.41	0.41
[Ni(**BPEFB**)]	1219	1363	0.72	0.50

[a] calculated using Non-Local Density Functional Theory and the Tarazona model on cylindrical pores

[b] calculated considering the total volume of pore less than 20 Å wide

The adsorption isotherms display Type I profiles, which are characteristic of microporous solids: the Ni(II)-compound exhibits a higher surface area compared to the Zn(II)-MOFs (1363 and 1178 m^2/g with Langmuir model, 1219 and 1000 m^2/g with BET method, respectively), as a consequence of the interpenetrated nature of the latter. Compared to its non-fluorinated analogue, [Ni(**BPEFB**)] show a reduced specific surface area (1219 versus 1900 m^2/g); this effect might be ascribable to the presence of partially amorphous MOF, as was observed by solid-state NMR and PXRD measurements. Furthermore, [Ni(**BPEFB**)] isotherm exhibits a continuous increase in N_2 adsorbed quantity as $p/p^O \rightarrow 1$ that might be ascribable to a partial mesoporosity introduced by the amorphous phase. On the other hand, surface area of α-[Zn(**BPEFB**)] is higher than that α-[Zn(BPEB)] (1000 versus 985 m^2/g with BET method, respectively), despite the presence of heavier and bulkier fluorine atoms in the former. This might be explained by the exceptionally high crystallinity of the α-[Zn(**BPEFB**)] sample analysed, which present an isotherm very close to an ideal Langmuir isotherm.

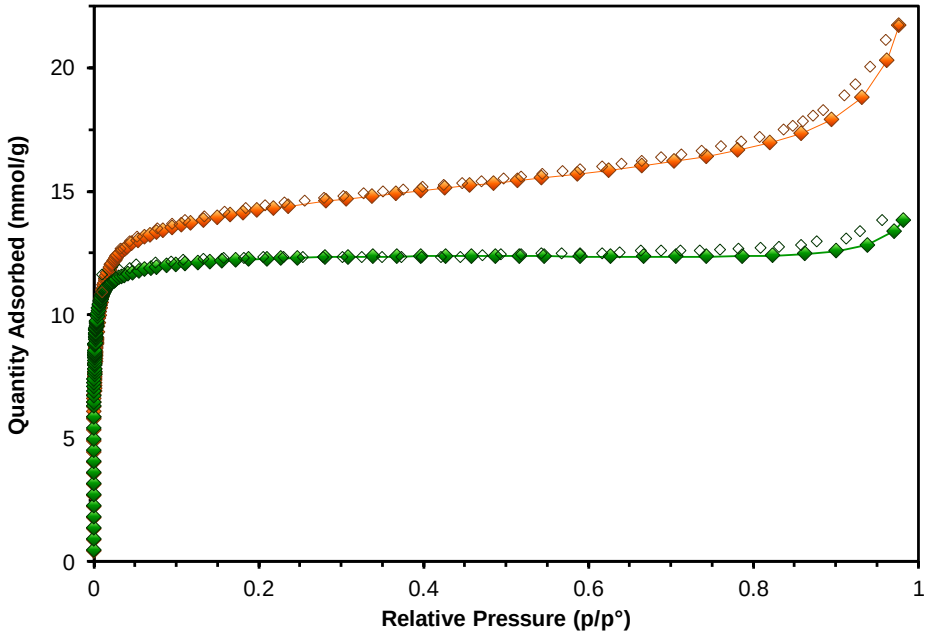

*Figure 3.7. N_2 adsorption isotherms at 77 K for α-[Zn(**BPEFB**)] (green diamonds) and [Ni(**BPEFB**)] (orange diamonds). Desorption branches are depicted as empty diamonds.*

The porosity of the two MOFs was further explored for the capture of environmentally and industrially important gas carbon dioxide (**Figure 3.8**). The CO_2 adsorption isotherms for α-[Zn(**BPEFB**)] and [Ni(**BPEFB**)] collected at 195 K exhibit Langmuir profiles that reach 9.86 and 12.61 mmol/g, respectively. The measured CO_2 capacities correspond to 0.72 cm^3/g for [Ni(**BPEFB**)] and 0.57 cm^3/g for α-[Zn(**BPEFB**)] ($d$$CO_2$(l) = 0.77 g/cm^3 was used) and they are to be compared to the total pore volume calculated by the Tarazona method from the N_2 isotherms at 77 K (0.72 cm^3/g for Ni-compound and 0.41 for the Zn-MOF). [Ni(**BPEFB**)] adsorbed CO_2 volume match its maximum capacity calculated by nitrogen adsorption, while, surprisingly, α-[Zn(**BPEFB**)] CO_2 adsorption reach 138% of its maximum theoretical value measured by nitrogen isotherm. This curious behaviour might be justified considering the bigger kinetic diameter of the N_2

molecule compared with CO_2 (3.64 and 3.30 Å, respectively). This hypothesis was formulated observing the shape of α-[Zn(**BPEFB**)] CO_2 isotherm at 195 K As shown in **Figure 3.8a** (green trace), the concavity of the curve reverts around 7 mmol/g. This adsorbed quantity corresponds to the maximum theoretical CO_2 adsorbed quantity calculated from the pore volume derived from the N_2 isotherm. We might think that the extra CO_2 adsorbed is accommodated in the smaller side channels present α-[Zn(**BPEFB**)]. As discussed in Section 3.3.2, these channels can host a cylinder with a diameter of only 3 Å, which is comparable with CO_2 kinetic diameter and significantly smaller than N_2 kinetic diameter. We might then suppose that CO_2 can enter these channels, while N_2 cannot. Another interesting interpretation of this phenomenon is given by the theoretical model set up by Simon and co-workers[37]. They observed that MOFs with mobile elements often give isotherms with peculiar line shapes (presenting inflections, steps or hysteresis). To reproduce this behaviour, they modelled an ideal porous material with rotating elements. In the empty framework, the mobile elements adopt a certain configuration, but in presence of guest molecules, thanks to host-guest interactions, the energy minimum is reached in another configuration. Thus, the state of the rotating moieties is determined by a balance between competing effects. With their model, they show that inflection points are generated from cooperative adsorption: when a gas molecule occupies an empty pore, it induces a neighbouring ligand to rotate into the energetically favourable configuration. This, in turn, generates a new more favourable binding site in the neighbouring cage, facilitating the adsorption of another guest molecule. The adsorption curve then switches to be concave as the cages saturate with guest molecules

Comparing the two CO_2 isotherms at 195K, it can be observed that α-[Zn(**BPEFB**)] isotherm is much steeper than that of [Ni(**BPEFB**)]. This might indicate that α-[Zn(**BPEFB**)] has stronger interactions with CO_2 molecules. This hypothesis is confirmed by the calculated value of the isosteric heat of adsorption derived from CO_2 isotherms collected at 273, 283 and 298 K up to 10 bar of pressure (see **Figure 3.8b,c**): $Q_{st}(CO_2)$ of α-[Zn(**BPEFB**)] is higher than that of [Ni(**BPEFB**)] (28 and 24 kJ/mol, respectively, calculated at Q_{ads} = 0.01 mmol). Details about $Q_{st}(CO_2)$ calculations are reported in Appendix 3 This behaviour might be explained considering the crystallographic structure of the two frameworks: α-[Zn(**BPEFB**)] has an interpenetrated structure with narrower channels compared to those of [Ni(**BPEFB**)]. Hence, CO_2 is forced to stay closer to F-moieties in the Zn-compound and this results in a stronger interaction and a higher $Q_{st}(CO_2)$.

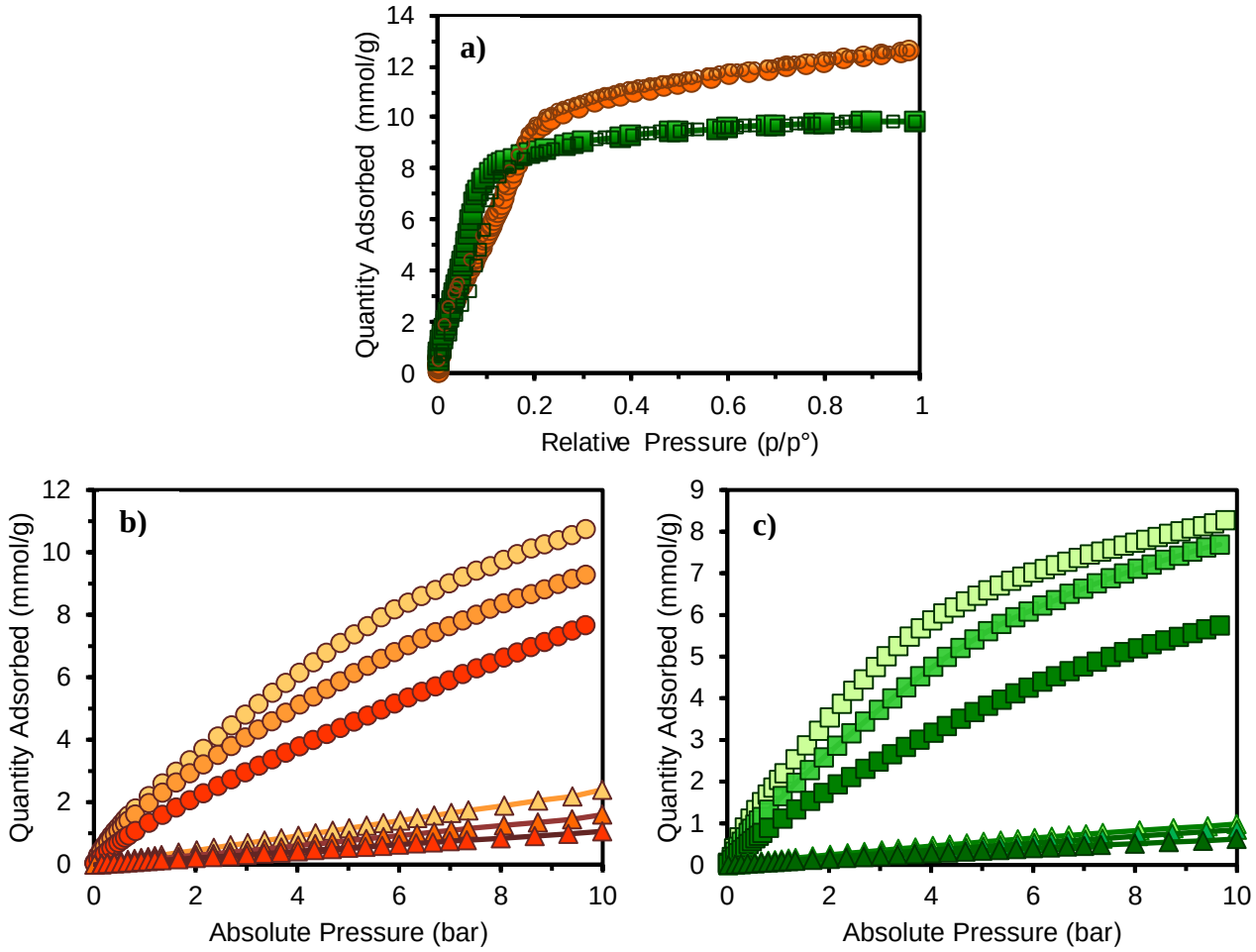

***Figure 3.8**. **a)** CO_2 adsorption isotherms of α-[Zn(**1**)] (green trace) and [Ni(**1**)] (orange trace) collected at 195 K up to 1 bar; **b)**, CO_2 (circles) and N_2 (triangles) adsorption isotherms of [Ni(**1**)] collected at 273 K (light orange), 283 K (orange) and 298 K (dark orange) up to 10 bar; **c)** CO_2 (squares) and N_2 (triangles) adsorption isotherms of [Ni(**1**)] collected at 273 K (light green), 283 K (green) and 298 K (dark green) up to 10 bar.*

273 and 298 K CO_2 and N_2 isotherms of both MOFs (**Figure 3.8**) indicate a preferential adsorption of carbon dioxide over nitrogen. To quantify the CO_2/N_2 selectivity of the two materials, we applied the Ideal Adsorbed Solution Theory (IAST): as reported in **Table 3.2**, the low-pressure selectivity of the Zn(II)-MOF for CO_2 adsorption at 273 K calculated applying the IAST to a 15:85 CO_2/N_2 mixture is higher than that of Ni(II)-compound. At 298 K, on the other hand, the selectivity of the two materials is comparable. Ultimately, fluorinated MOFs performs better towards CO_2 capture than their non-fluorinated counterpart at room temperature. For example, despite the lower surface area, [Ni(**BPEFB**)] CO_2 uptake at 273 K and 10 bar reaches 47.1% of host weight, against the 37.4% reported for [Ni(BPEB)]. Similarly, α-[Zn(**BPEFB**)] uptake at 298 K and 10 bar is 25.1% wt compared to 22.9% of α-[Zn(BPEB)] (Appendix 3, **Table A3.2**).

*Table 3.2. CO_2 adsorption parameters derived from experimental CO_2 of α-[Zn(**BPEFB**)] and [Ni(**BPEFB**)]*

	T (K)	P (bar)	$Q_{max}(CO_2)$ (mmol/g)	$Wt(Q_{max})$ %	$Q_{1\ bar}(CO_2)$ (mmol/g)	$Wt(Q_{1bar})$ %	Q_{st}[b] (kJ/mol)	Selectivity[c]
[Zn(**BPEFB**)]	195	1[a]	9.9	43.6	/	/	28	/
	273	10	8.3	36.5	2.04	9.0		40
	283	10	7.7	33.9	1.55	6.8		/
	298	10	5.7	25.1	1.05	4.6		25
[Ni(**BPEFB**)]	195	1[a]	12.6	55.4	/	/	24	/
	273	10	10.7	47.1	2.09	9.2		31
	283	10	9.3	40.9	1.85	8.1		/
	298	10	7.7	33.9	1.26	5.5		26

[a] p/p^o is reported
[b] Calculated at 0.01 mmol/g applying the van't Hoff equation
[c] low pressure value (0.1 bar) calculated applying the IAST theory to a 15:85 CO_2/N_2 mixture

According to these data, fluorinated MOFs do perform better towards CO_2 capture, although the improvement is small. It must be said, however, that the extent of fluorination on our ligand is modest with just one fluorine per organic linker. This could be the reason way improvements are moderate and increasing the number of fluorine atoms in the structure might bring further enhancements.

3.3.4. T_1 relaxation times measurements of α-[Zn(**BPEFB**)] with solid state NMR

Spin−lattice NMR relaxation times (T_1) are sensitive to motional phenomena over a wide frequency range 10^3–10^8 Hz and they depend from the temperature. The maximum relaxation rate occurs when thermal agitation frequencies match the observation frequency, according to the formula $\tau \times \omega \cong 1$. The data can be fitted by the Kubo−Tomita equation, which describes the modulation of relaxation by carbon−hydrogen vector reorientation.

Thus, we aimed at measuring T_1 relaxations times of ^{13}C nuclei of α-[Zn(**BPEFB**)] at different temperatures to derive the parameters of the rotational dynamics of the dipolar rotors. Unfortunately, by the time of the deadline for this thesis, we did not succeed in completing rotors characterization.

Preliminary data, however, suggest that the energy barrier for rotation of *p*-phenyl rings in α-[Zn(**BPEFB**)] is around 0.4 kcal/mol and k_0 is around 10^{11} Hz. These data are comparable with the one measured for α-

[Zn(BPEB-d_4)] and suggest that dipolar rotors in α-[Zn(**BPEFB**)] are able to undergo fast dynamic at room temperature. Further measurements are currently ongoing to corroborate this preliminary result.

3.3.5. Conclusions

A new fluorinated rod-like bis pyrazolate ligand, H_2**BPEFB**; has been synthesized. It was designed so the central *p*-phenylene ring could possibly show fast dynamics around its 1,4-axis. This was achieved by the introduction of triple bonds in 1,4 positions, as it is known that rotation around Csp^2 C*sp* bonds occurs with a low energy barrier. Furthermore, a single fluorine substituent has been introduced on the phenylene ring to generate an asymmetry in the electric charge density distribution, thus inducing a net electric moment dipole. H_2**BPEFB** was then used to prepare two new MOFs: α-[Zn(**BPEFB**)] and [Ni(**BPEFB**)]. The fluorinated MOFs resulted to be isostructural to their previously reported non-fluorinated analogues α-[Zn(BPEB)] and [Ni(BPEFB)]. This result is uncommon in literature. Because of the structural isomorphism, we studied the behavior of α-[Zn(**BPEFB**)] and [Ni(**BPEFB**)] towards CO_2 capture and compared it with the one of α-[Zn(BPEB)] and [Ni(BPEFB)] to better understand the role of fluorine in carbon dioxide capture. Our investigations suggest that fluorination enhance MOFs CO_2 capture. As a representative example of the improved properties, the isosteric heats of adsorption of α-[Zn(**BPEFB**)] and [Ni(**BPEFB**)] are 28 and 24 kJ/mol respectively, which are to be compared with 23 kJ/mol measured for [Zn(BPEB)] and [Ni(BPEFB)]. Furthermore, we started investigating the dynamic properties of dipolar rotors in α-[Zn(**BPEFB**)]. Preliminary data suggest fast room temperature dynamics of the dipolar rotor array. Nonetheless a more extensive set of experiments is going to be run to confirm this data and further analyse rotors behaviour in α-[Zn(**BPEFB**)].

3.4. Experimental Section

3.4.1. Materials and methods

^{1}H, ^{13}C(APT) and ^{19}F solution NMR spectra were recorded at 400, 100 and 377 MHz, respectively, on a Bruker Avance 400 spectrometer. In the following, ^{1}H data are reported as follow: chemical shifts (in ppm and referenced to internal TMS), integration, multiplicity (s = singlet, d = doublet, t = triplet, q = quartet, m = multiplet), coupling constants (in Hz) and assignation. ^{13}C data are reported as follow: chemical shifts (in ppm and referenced to internal TMS), multiplicity (s = singlet, d = doublet), coupling constants (in Hz) and assignation. ^{19}F data are reported as follows: chemical shifts (in ppm and referenced to internal $CFCl_3$), and multiplicity (s = singlet).

IR spectra were acquired in attenuated total reflectance (ATR) by means of a Nicolet iS10 instrument over the range 4000-600 cm-1. In the following, signal intensities are denoted as br = broad, vs = very strong, s = strong, m = medium, and w = weak.

Elemental analyses were obtained with a Perkin Elmer CHN Analyzer 2400 Series II.

Gas chromatography-mass spectrometry (GC-MS) analyses were performed on a ThermoquestTraceGC equipped with a 30 m DB5 silica column coupled with a quadrupolar mass analyzer FinniganTraceMS. The protocol used began with heating the sample at 70 °C for 4 min. Then, the temperature was raised up to 180 °C at 10 °C/min, and the system was kept at this temperature for 5 min. Finally, the temperature was raised up to 270 °C at 10 °C/min, and the system was kept at this temperature for 15 min. The inlet temperature was set at 200 °C, while the split flow at 15mL/min.

Microwave heating was performed by means of a CEM Discover SP instrument with a single-mode microwave cavity producing continuous irradiation at 2.45 GHz and power up to 0.3 kW. All the reactions carried out with microwave heating were performed in 10-mL vessels equipped with a Teflon septum and a magnetic stir bar. The temperature, pressure and irradiation power were continuously monitored during the reaction.

Powdered, polycrystalline batches of compounds [Ni(**BPEFB**)] and α-[Zn(**BPEFB**)] were ground in an agate mortar; then, they were deposited in the hollow of an aluminium-framed, zero-background silicon sample holder. Diffraction data were collected at room temperature on a Bruker AXS D8 Advance θ:θ diffractometer, equipped with Ni-filtered Cu-Ka radiation (λ = 1.5418 Å), a Lynxeye linear position-sensitive detector, and the following optics: primary beam Soller slits (2.3°), fixed divergence slit (0.5°), receiving slit (8 mm). The generator was set at 40 kV and 40 mA. To carry out the structure determinations, overnight scans were performed in the 2θ range of 3–105°, with steps of 0.02°. A standard peak search in the region between 3 and 30° (2θ) was followed by indexing through the singular value decomposition method implemented in TOPAS-R, allowing the determination of the unit cell parameters. Systematic absences permitted individuation of the most probable space groups. Prior to the structure solution, Le Bail refinements were carried out to confirm unit cells and space groups. Preliminary structural models were determined *ab initio* for [Ni(**BPEFB**)] and α-[Zn(**BPEFB**)] by the simulated annealing approach implemented in TOPAS-R. An idealized rigid model was used to describe the crystallographically independent portion of the ligand. Structure refinements were carried out by means of the Rietveld method with TOPAS-R, maintaining the rigid bodies adopted during the structure solution stage. Beneficial for the values of the figures of merit, rotational disorder with respect to the main axis of the ligand was introduced for the central aromatic ring in all the three species, allowing for two equiprobable orientations. The peak shapes were described with the fundamental parameters approach. In all the cases the anisotropic broadening of the peaks was modeled by means of spherical harmonics. The background was modeled by a Chebyshev polynomial function. The thermal effect was simulated by using a single isotropic parameter for the metal ions, augmented by 2.0 $Å^2$ for lighter atoms.

Variable-temperature X-ray powder diffraction (VT-XRPD) experiments were performed on [Ni(**BPEFB**)] and α-[Zn(**BPEFB**)] to highlight their structural response to temperature variation. To the aim, progressive heating from room temperature up to decomposition was performed in air, in a sensible low-angle 2θ range, using a custom-made sample heater assembled by Officina Elettrotecnica di Tenno (Ponte Arche, IT). Polycrystalline batches [Ni(**BPEFB**)] and α-[Zn(**BPEFB**)] were ground in an agate mortar and deposited in

the hollow of an aluminum sample holder. The thermal behavior was followed up to decomposition heating the samples *in situ* with steps of 20 °C. The parametric treatment of the VT-XRPD data with the Le Bail method allowed to depict the variation of the unit cell parameters as a function of the temperature.

Differential Scanning Calorimetry (DSC) measurements were performed on a Mettler-Toledo StarE instrument from 0 to 450 °C, at a heating rate of 10 °C/min and under an 80 mL/min flow of N_2

Nitrogen adsorption−desorption isotherms were measured at liquid nitrogen temperature using a Micromeritics ASAP 2020 HD analyzer. The samples were outgassed overnight at 120 °C under vacuum right before the analysis. Specific surface areas were calculated using the Brunauer, Emmett, and Teller (BET) model and the Langmuir model. The pore-size distributions and the total pore volume were evaluated following non-local density functional theory (NLDFT) analysis for cylindrical pores and the Tarazona method. CO_2 adsorption-desorption isotherms were measured at 195 K up to 1 bar, and at 273, 283 and 298 K up to 10 bar using a Micromeritics ASAP 2050 analyzer. N_2 adsorption/desorption isotherms were collected at 273 and 298 K up to 10 bar using a Micromeritics ASAP 2050 analyzer. Samples were degassed at 120 °C for 3 hours before each analysis.

Solid-state NMR spectra were run at 75.5 MHz for ^{13}C and at 282.4 MHz for ^{19}F MHz on a Bruker Avance 300 instrument operating at a static field of 7.04 T equipped with high-power amplifiers (1 kW) and a 4 mm double resonance MAS probe. $^{13}C\{^1H\}$ ramped-amplitude cross polarization (CP) experiments were performed at a spinning speed of 12.5 kHz, using a contact time of 2 ms. The 90° pulse used for proton was 2.9 μs. $^{13}C\{^{19}F\}$ ramped-amplitude cross polarization (CP) experiments were performed at a spinning speed of 10 kHz, using a 90° pulse of 3.2 μs and a contact time of 0.5, 1, 5 and 8 ms. Crystalline polyethylene was taken as an external reference at 32.8 ppm from TMS. ^{19}F SPE MAS NMR spectra were collected at a spinning speed of 12.5 kHz using a 90° pulse of 3.2 μs and a recycle delay of 20 s. The ^{19}F chemical shift was referenced to NaF. The spectra were collected at 300 K. Preliminary 1H spin lattice relaxation experiments $T_1(^1H)$ of α-[Zn(BPEFB)] were recorded using the inversion recovery pulse sequence at a spinning speed of 8 kHz in the range of 200 K - 298 K, with 32 scans for each recovery time. The 90° pulse for proton was 3.65 μs. The stability and accuracy of the temperature controller (Bruker B-VT2000) were approximately 0.1 K. The empty sample was sealed under vacuum before collecting ^1H T_1 relaxation times.

All chemical and solvents were purchased from Sigma Aldrich, Alfa Aesar or Fluorochem and used without further purification, unless otherwise specified.

3.4.2. Synthesis of 4-iodopyrazole (**2**)

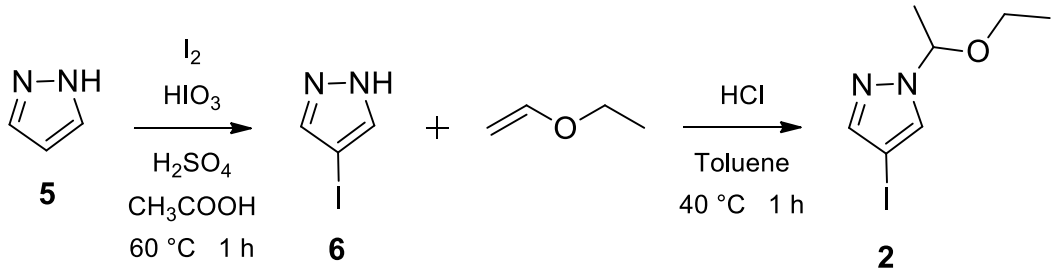

Synthesis of **6** was done following the procedure described in G. Zoppellaro, *Org. Lett.*, 2004, 6, 26, 4929.

Synthesis of **2** was done following the procedure described in Q. Lin, *Org. Lett.*, 2009, 11, 9, 1999.

3.4.3 Synthesis of 1,4-diethynil-2-fluoro-benzene (**3**)

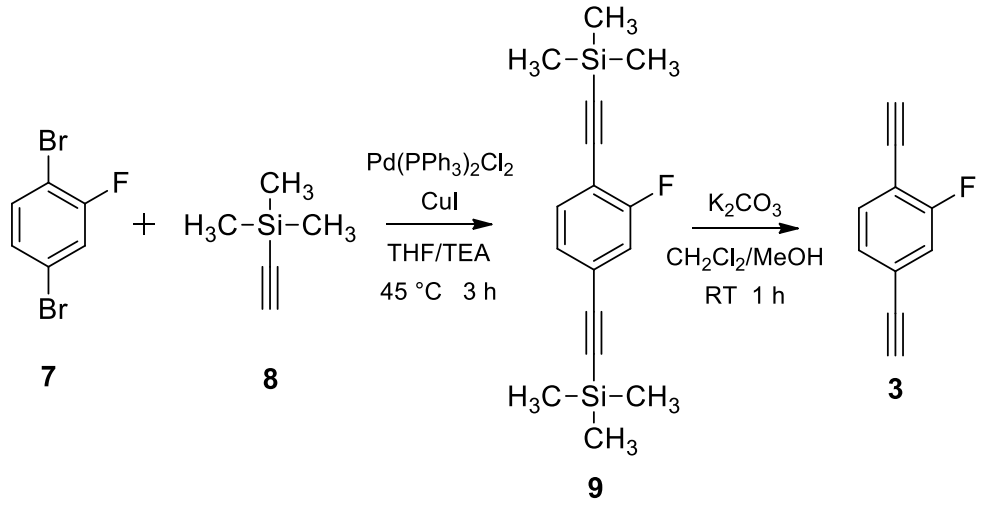

Synthesis of **3** was done following the procedure described in Tri H. V. Huynh, *Org. Lett.*, 2009, 11, 4, 999

3.4.4. Synthesis of 1,4-bis(1*H*-pyrazol-4-ylethynyl)-2-fluorobenzene (H_2**BPEFB**)

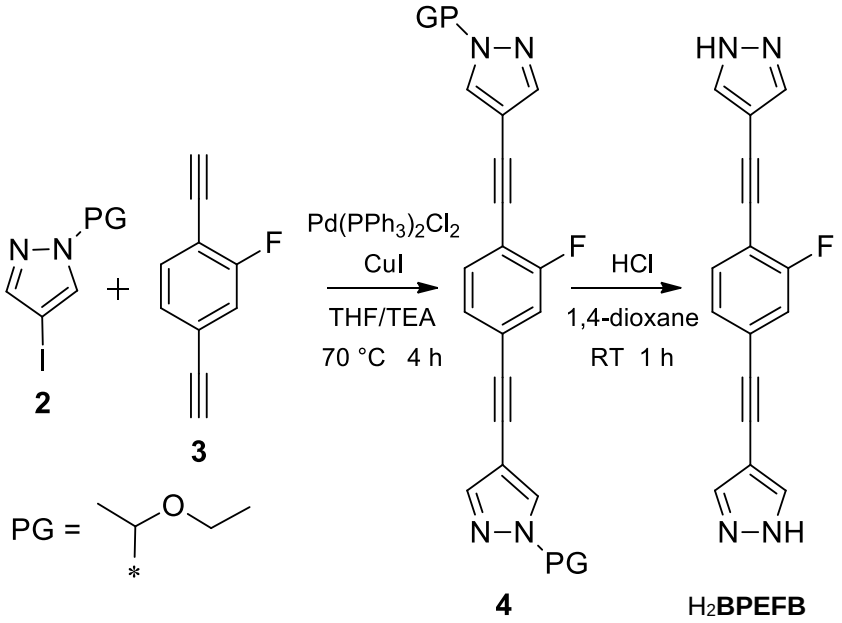

In a Schlenk tube, **3** was dissolved in a 1:1 mixture of triethylamine (TEA) and tetrahydrofurane (THF). The solution was degassed (3 x freeze/pump/thaw) and $Pd(PPh_3)_2Cl_2$ (0.05 eq.) and CuI (0.05 eq.) were added, followed by **2** (2.2 eq.). The mixture was heated at 70 °C for 4 h.

After cooling at room temperature, the reaction mixture was filtered over a Celite pad, washed with EtOAc. The solvent was evaporated under reduced pressure affording a brown residue, which was solubilized in EtOAc and washed with 30 % aq. NH4OH and water. The organic layer was dried over Na_2SO_4 and evaporated under reduced pressure v. Crude **4** was obtained as a sticky brown solid which was redissolved in AcOEt and suspended over K_2CO_3. The obtained free flowing solid was extracted with pentane using a Sohxlet extractor. The pentane was evaporated under reduced pressure and the obtained solid was purified by flash column chromatography (silica gel, Hexane/EtOAc 7:3) to afford pure **4** as pale-yellow solid in 27% yield. ^{1}H NMR (400 MHz, DMSO-d_6, 298 K): δ (ppm) 8.39 (s, 1H, Ar**H**), 8.35 (s, 1H, Ar**H**), 7.81 (s, 1H, Ar**H**), 7.79 (s, 1H, Ar**H**), 7.57 (t, 1H, J = 7.8 Hz, Ar$\mathbf{H_6}$), 7.46 (dd, 1H, J = 10.2 Hz, J = 1.6 Hz, Ar$\mathbf{H_5}$), 7.35 (dd, 1H, J = 8.0 Hz, J = 1.6 Hz, Ar$\mathbf{H_3}$), 5.58 (q, 2H, J = 6.0 Hz, NC**H**), 3.44 (m, 2H, OC$\mathbf{H_2}$), 3.22 (m, 2H, OC$\mathbf{H_2}$), 1.61 (d, 6H, J = 6.0 Hz, NCHC$\mathbf{H_3}$), 1.05 (t, 6H, J = 7.1 MHz, $OCH_2C\mathbf{H_3}$); ^{13}C NMR (100 MHz, DMSO-d_6, 298 K): δ (ppm) 161.7 (d, $^1J_{CF}$ = 248.3 Hz), 141.8, 133.8, 132.3, 128.0, 124.9, 118.3 (d, $^2J_{CF}$ = 22.3 Hz), 111.7, 102.1, 88.8, 87.1, 85.0, 83.3, 63.7, 21.6, 15.2; ^{19}F NMR (376 MHz, DMSO-d_6, 298 K) δ (ppm) - 110.49 (s, 1F); IR (ATR, cm^{-1}): 3108 (w), 3083 (w), 2977(w), 2906(w) 2222(s), 1613(w), 1563(w), 1538(w), 1488(s), 1436(m), 1417(m), 1361(m), 1237(w), 1118(vs), 1064(vs), 1009(s), 980(s), 943(s), 864(vs), 826(vs), 787(m), 751(s), 704(s), 663(m), 640(vs).

Intermediate **4** (300 mg) was dissolved in 10 mL of 1,4-dioxane, then 1.5 mL of 6 M HCl_{aq} solution were added dropwise. After vigorous stirring at room temperature for 3 hours, the precipitate was filtered, washed with water and dried *in vacuo* to afford H_2**BPEFB** as an off-white solid in 76% yield. ^{1}H NMR (400 MHz,

DMSO-d_6, 298 K): δ (ppm) 13.17 (bs, 2H, N**H**), 7.91 (bs, 4H, Ar**H**), 7.48 (t, 1H, J = 7.9 Hz, Ar$\mathbf{H_6}$), 7.36 (dd, 1H, J = 10.3 Hz, J = 1.6 Hz, Ar$\mathbf{H_5}$), 7.25 (dd, 1H, J = 8.0 Hz, J = 1.6 Hz, Ar$\mathbf{H_3}$); ^{13}C NMR (100 MHz, DMSO-d_6, 298 K): δ (ppm) 161.7 (d, $^1J_{CF}$ = 249.2 Hz), 133.7, 127.9, 125.0, 118.2 (d, $^2J_{CF}$ = 22.6 Hz), 111.7 (d, $^2J_{CF}$ = 16.0 Hz), 100.9, 89.4, 88.7, 85.6, 83.1; ^{19}F NMR (376 MHz, DMSO-d_6, 298 K) δ (ppm) - 110.64 (s, 1F); IR (ATR, cm^{-1}):): 3095(w), 2934(w), 2430(m, br), 2225(m, sharp), 1615(w), 1539(m), 1482(m), 1470(m), 1372(m), 1272(w), 1180(w), 1111(m), 1071(w), 994(m), 943(m), 810(s), 742(m).

3.4.5. Synthesis of MOF α-[Zn(**BPEFB**)]

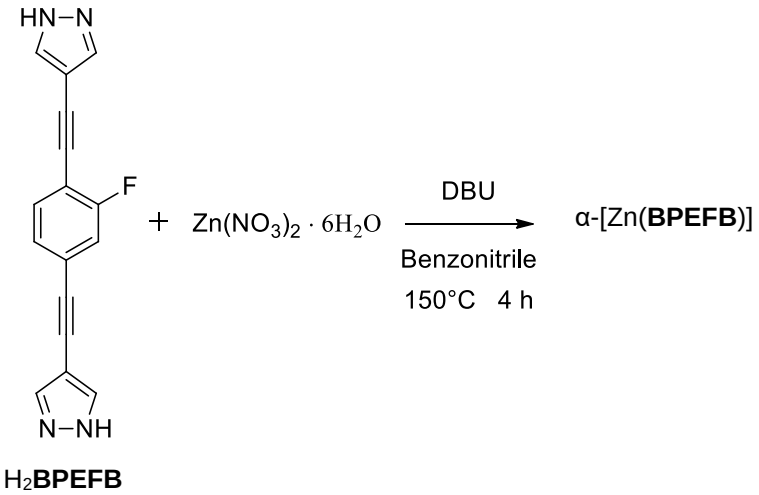

H_2**BPEFB**

H_2**BPEFB** (50 mg, 0.188 mmol) and benzonitrile (5 ml) were added to a Schlenk tube and the mixture was heated up to 100°C until complete dissolution of the ligand. Then $Zn(NO_3)_2 \cdot 6H_2O$ (53 mg, 0.179 mmol) was added in a single portion. The resulting mixture was stirred at 100°C for 5 minutes. Finally, 1,8-Diazabicyclo[5.4.0]undec-7-ene (DBU) (0.1 ml) was added; The mixture was heated to 150°C and kept at this temperature under stirring for 4 hours. After this time, the heating plate was turned off and the reaction mixture was slowly cooled down to room temperature. Then, the pale-yellow solid was recovered by filtration on a Hirsch funnel and transferred to a glass vial. MeOH (3 ml) was added and the resulting slurry was stirred for 1 hour at room temperature. Eventually, the mixture was filtered on a Hirsch funnel to recover α-[Zn(**BPEFB**)] as a pale yellow solid which was dried at 150°C in vacuo for 4 hours (47 mg, 73% yield).
Elem. Anal. Calc. for $C_{16}H_9FN_4Zn$ (FW = 339.65 g/mol): C = 56.58%, H = 2.08%, N = 16.50%; found C = 55.95%, H = 3.01%, N = 16.09%. IR (ATR, cm^{-1}): 2227(m), 1615 (w), 1543 (m), 1488(s), 1416(m), 1384(m), 1359(s), 1266(w), 1237(w), 1219(w), 1111 (m), 1063(s), 1015(s), 944(w), 855(s), 847(s), 823(m), 785(w), 746(s), 636(vs).

3.4.6. Synthesis of [Ni(**BPEFB**)]

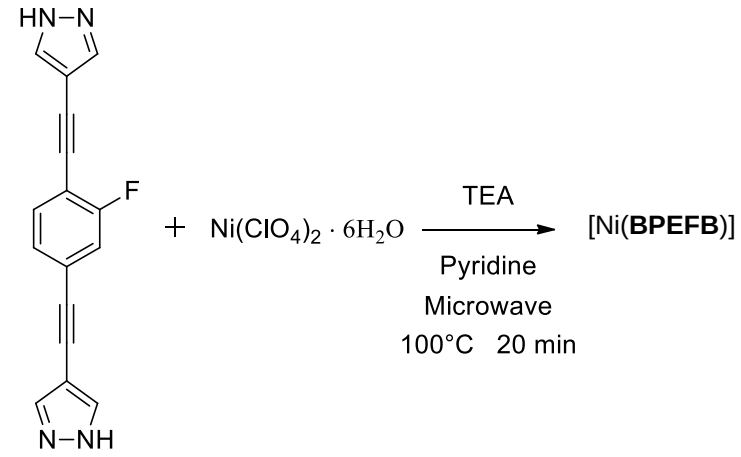

H_2**BPEFB**

H_2**BPEFB** (70 mg, 0.253 mmol) and pyridine (4 ml) were added to a 10 ml microwave vessel and the mixture was stirred until complete dissolution of the ligand. Then $Ni(ClO_4)_2 \cdot 6H_2O$ (88 mg, 0.241 mmol) was added in a single portion.and the mixture was stirred at RT for 5 min. After that, the stirring was stopped and TEA (1 ml) was carefully layered over the solution. The mixture was irradiated at 0.3 kW till the temperature reached 100°C and kept in these conditions for 25 min under stirring Then the reaction vessel was cooled down to 50°C and the mixture was filtered on a Hirsch funnel. The obtained solid was washed with pyridine (2 ml) and MeOH (20 ml). Then, [Ni(**BPEFB**)] was dried *in vacuo* at 100°C for 12 h (61 mg, 74% yield).

Elemen. Anal. Calc for $C_{16}H_7N_4FNi$ (FW = 333.69 g/mol): C = 57,32 %, H = 2,68%, 16,72%; found: C = 57,68%, H = 3,03%, N = 15,42%. IR (ATR, cm^{-1}): 2208 (s), 1613(m), 1538(m), 1484(s), 1414(m), 1360(m), 1269(w), 1229(w), 1164(w), 1106(w), 1054(w), 1012(m), 944(w), 844(s), 822(s), 789(w), 745(m), 675(m), 639(vs).

Bibliography for Chapter 3

1. Zhang, Y. *et al.* Ferroelectricity induced by ordering of twisting motion in a molecular rotor. *J. Am. Chem. Soc.* **134,** 11044–11049 (2012).
2. Akutagawa, T. *et al.* Ferroelectricity and polarity control in solid-state flip-flop supramolecular rotators. *Nat. Mater.* **8,** 342–347 (2009).
3. Setaka, W. & Yamaguchi, K. Thermal modulation of birefringence observed in a crystalline molecular gyrotop. *Proc. Natl. Acad. Sci.* **109,** 9271–9275 (2012).
4. Zheng, X. *et al.* Dipolar and Nonpolar Altitudinal Molecular Rotors Mounted on an Au(111) Surface. *J. Am. Chem. Soc.* **126,** 4540–4542 (2004).
5. Horinek, D. & Michl, J. Surface-mounted altitudinal molecular rotors in alternating electric field: single-molecule parametric oscillator molecular dynamics. *Proc. Natl. Acad. Sci. U. S. A.* **102,** 14175–14180 (2005).
6. Kaleta, J. *et al.* Arrays of Molecular Rotors with Triptycene Stoppers: Surface Inclusion in Hexagonal Tris(o -phenylenedioxy)cyclotriphosphazene. *J. Org. Chem.* **80,** 6173–6192 (2015).
7. Horansky, R. D. *et al.* Dipolar rotor-rotor interactions in a difluorobenzene molecular rotor crystal. *Phys. Rev. B - Condens. Matter Mater. Phys.* **74,** (2006).
8. Horansky, R. D. *et al.* Dielectric response of a dipolar molecular rotor crystal. *Phys. Rev. B - Condens. Matter Mater. Phys.* **72,** (2005).
9. Kobr, L. *et al.* Tris-o-phenylenedioxycyclotriphosphazene (TPP) inclusion compounds containing a dipolar molecular rotor. *Cryst. Growth Des.* **14,** 559–568 (2014).
10. Kobr, L. *et al.* Inclusion compound based approach to arrays of artificial dipolar molecular rotors: Bulk inclusions. *J. Org. Chem.* **78,** 1768–1777 (2013).
11. Bracco, S. *et al.* Dipolar rotors orderly aligned in mesoporous fluorinated organosilica architectures. *Angew. Chemie - Int. Ed.* **54,** 4773–4777 (2015).
12. Yang, Z.-Z. *et al.* Fluorinated microporous organic polymers: design and applications in CO 2 adsorption and conversion. *Chem. Commun.* **50,** 13910–13913 (2014).
13. Noro, S. & Nakamura, T. Fluorine-functionalized metal–organic frameworks and porous coordination polymers. *NPG Asia Mater.* **9,** e433 (2017).
14. Pachfule, P., Chen, Y., Jiang, J. & Banerjee, R. Fluorinated metal-organic frameworks: Advantageous for higher H2and CO2adsorption or not? *Chem. - A Eur. J.* **18,** 688–694 (2012).
15. Galli, S. *et al.* When long bis(pyrazolates) meet late transition metals: Structure, stability and adsorption of metal-organic frameworks featuring large parallel channels. *J. Mater. Chem. A* **2,** 12208–12221 (2014).
16. Zhang, J. P., Zhang, Y. B., Lin, J. Bin & Chen, X. M. Metal azolate frameworks: From crystal engineering to functional materials. *Chemical Reviews* **112,** 1001–1033 (2012).
17. Hye, J. C., Dincă, M. & Long, J. R. Broadly hysteretic H2 adsorption in the microporous metal-organic framework Co(1,4-benzenedipyrazolate). *J. Am. Chem. Soc.* **130,** 7848–7850 (2008).
18. Choi, H. J., Dincă, M., Dailly, A. & Long, J. R. Hydrogen storage in water-stable metal-organic frameworks incorporating 1,3- and 1,4-benzenedipyrazolate. *Energy Environ. Sci.* **3,** 117–123 (2010).
19. Galli, S. *et al.* Adsorption of harmful organic vapors by flexible hydrophobic bis-pyrazolate based MOFs. *Chem. Mater.* **22,** 1664–1672 (2010).

20. Nie, J. F., Zhu, Y. M., Liu, J. Z. & Fang, X. Y. Periodic segregation of solute atoms in fully coherent twin boundaries. *Science (80-.).* **340,** 957–960 (2013).

21. Bracco, S. *et al.* Ultrafast MolecularR otors and Their CO 2 Tuning in MOFs with Rod-Like Ligands. *Chem. Eur.J* **231,** 1210–11215 (2017).

22. Comotti, A., Bracco, S., Ben, T., Qiu, S. & Sozzani, P. Molecular rotors in porous organic frameworks. *Angew. Chemie - Int. Ed.* **53,** 1043–1047 (2014).

23. Comotti, A., Bracco, S., Valsesia, P., Beretta, M. & Sozzani, P. Fast molecular rotor dynamics modulated by guest inclusion in a highly organized nanoporous organosilica. *Angew. Chemie - Int. Ed.* **49,** 1760–1764 (2010).

24. Comotti, A. *et al.* Engineering switchable rotors in molecular crystals with open porosity. *J. Am. Chem. Soc.* **136,** 618–621 (2014).

25. Saebø, S., Almlöf, J., Boggs, J. E. & Stark, J. G. Two approaches to the computational determination of molecular structure: the torsional angle in tolane and the effect of fluorination on the structure of oxirane. *J. Mol. Struct. THEOCHEM* **200,** 361–373 (1989).

26. Sipachev, V. A., Khaikin, L. S., Grikina, O. E., Nikitin, V. S. & Trætteberg, M. Structure, spectra and internal rotation of bis(trimethylsilyl) acetylene: Spectral analysis by scaling quantum-chemical force fields and two methods for calculating vibrational effects. *J. Mol. Struct.* **523,** 1–22 (2000).

27. Brankov, J. G. & Danchev, D. M. Ground state of an infinite two-dimensional system of dipoles on a lattice with arbitrary rhombicity angle. *Phys. A Stat. Mech. its Appl.* **144,** 128–139 (1987).

28. Abolins, B. P., Zillich, R. E. & Whaley, K. B. Quantum phases of dipolar rotors on two-dimensional lattices. *J. Chem. Phys.* **148,** 102338 (2018).

29. Zhang, Y. *et al.* Simultaneous and coordinated rotational switching of all molecular rotors in a network. *Nat. Nanotechnol.* **11,** 706–712 (2016).

30. Horansky, R. D. *et al.* Dielectric response of a dipolar molecular rotor crystal. *Phys. Rev. B - Condens. Matter Mater. Phys.* **72,** 014302 (2005).

31. Masuda, T. *et al.* Molecular Gyrotops with a Five-Membered Heteroaromatic Ring: Synthesis, Temperature-Dependent Orientation of Dipolar Rotors inside the Crystal, and its Birefringence Change. *Cryst. Growth Des.* **16,** 4392–4401 (2016).

32. Yang, Q., Zhong, C. & Chen, J.-F. Computational Study of CO 2 Storage in Metal−Organic Frameworks. *J. Phys. Chem. C* **112,** 1562–1569 (2008).

33. Negishi, E. & Meijere, A. de. *Handbook of Organopalladium Chemistry for Organic Synthesis*. (Wiley-Interscience, 2002). doi:10.1002/0471473804

34. Edenborough, M. *Organic Reaction Mechanisms: A Step by Step Approach, Second Edition*. **27,** (Taylor & Francis, 1998).

35. Trunk, M. *et al.* Copper-Free Sonogashira Coupling for High-Surface-Area Conjugated Microporous Poly(aryleneethynylene) Networks. *Chem. - A Eur. J.* **22,** 7179–7183 (2016).

36. Schilz, M. & Plenio, H. A guide to sonogashira cross-coupling reactions: The influence of substituents in aryl bromides, acetylenes, and phosphines. *J. Org. Chem.* **77,** 2798–2807 (2012).

37. Simon, C. M., Braun, E., Carraro, C. & Smit, B. Statistical mechanical model of gas adsorption in porous crystals with dynamic moieties. (2017). doi:10.5281/zenodo.208230

4. Chapter 4

Light-controlled bistable molecular switches in a porous organic framework: design and synthesis of Porous Switching Frameworks

4.1. Introduction

In the last twenty years the quest to achieve control of dynamics at molecular level had drawn the interest of an increasing number of scientists[1]. This trend reached its maximum with the 2016 Nobel Prize in Chemistry to Savauge, Stoddart and Feringa "for the design and synthesis of molecular machines"[2–4]. The ultimate goal of this challenging and interdisciplinary field of research is to mimic nature and learn how to build artificial molecular machines able to perform complex tasks, like transportation at microscopic scale[5], synthesis of other molecules or storing and processing of information[6]. Many of these futuristic applications requires a fine control over the positions and movements of devices' constituting parts, and because of this, great efforts have been spent to deeply understand molecular motion at a microscopic level[7]. The most promising candidates to build such complex systems are organic molecule that can be reversibly transformed in two or more (meta)stable states in response to temperature variations, chemical stimuli (pH, redox), light or electromagnetic fields. These compounds are often referred as organic-based molecular switches (OMS)[8,9]. In our opinion, light is one of the most interesting stimuli to be used to promote the switching process, as it can be precisely controlled in all its aspects (irradiation time, irradiation spot, wavelength, photon flux) without introducing additional chemical species in the system. Up to this days, methods derived from centuries of knowledge in organic chemistry have been used to synthesize hundreds of different OMS. However, the overwhelming majority of these systems work as single molecule in solution. For further applications, in particular device fabrication, it is inevitable to incorporate these molecules into solid-state materials and make them operate cooperatively[10]. Going from a random collection of molecules working independently in solution to an ordered array of machines able to cooperatively respond to an external stimulus calls for the solution of numerous problematics. More often than not, molecules in solid systems behave differently than in solution, especially when dynamics is concerned, presumably because of spatial confinement or inefficient conversion in densely packed solid phases[11]. Despite the many challenges to face, researcher have already successfully assembled a few examples of solid-state molecular machines. A recent and interesting strategy to fabricate stimuli-responsive materials is to immobilize OMS into metal-organic frameworks (MOFs)[12]. MOFs are a well-known class of organic-inorganic hybrid porous crystalline materials. They are considered an ideal platform for the introduction of molecular switches because their intrinsic and permanent porosity grants to OMS the required free space to undergo the stimuli-induced configurational change in solid-state. Moreover, the organic linker can be predesigned to incorporate OMS directly into the framework backbone[13]. Alternatively, functional groups can be inserted on the linker and OMS can be subsequently introduced by postsynthetic modification techniques[14,15]. Postsynthetic methods include also the so-called Solvent Assisted Ligand Exchange (SALE)[16] and the Solvent Assisted Ligand Incorporation (SALI)[17] techniques. All these approaches led to the successful synthesis of MOFs containing molecular fragments able to show a stimuli-responsive behaviour in the solid-state that resembled the one observed in solution. This same thesis contains examples of stimuli-controlled dynamics in MOFs (see chapters 2 and 3). However, MOFs stability is often a serious issue as they are sensitive to aging, temperature and chemical agents. The very stimulus needed to operate the OMS might led to

structural collapsing. Porous organic covalent frameworks are a class of material that can be considered a valid alternative to MOFs to prepare solid materials containing molecular switches[18–20]. They generally show an extremely high stability towards temperature and chemicals thanks to the robustness of the covalent bonds that form their backbone. Similarly to MOFs, pore size in COFs can be tuned by the choice of the building blocks for the synthesis of the material. An adequate free volume to accommodate the switch configurational changes upon stimulus application is a fundamental requirement the final material must satisfy; otherwise, the switching of the OMS will be sterically hindered, and it will not occur. To the best of our knowledge, very few examples of dynamics in solid covalent organic frameworks are known in literature[21,22]. In this chapter is reported for the first time a covalent organic porous material containing bistable molecular switches able to undergo a reversible photo-activated isomerization in solid-state.

4.2. Design and synthesis of a porous organic framework containing light-controlled bistable molecular switches

The aim of this work was to synthesize a robust porous organic framework containing bistable molecular switches that could be photoisomerized in solid-state by irradiation with the appropriate wavelength. The ideal target material should not only show the desired photo-activated switching process, but exhibits open pores and optimal thermal stability. Porosity is a fundamental requirement because switches will need adequate free space around them to properly operate. Furthermore, open porosity will allow communication between the switch and the external environment, thus permitting to imagine advanced applications for this material, as, for example, selective and switchable adsorption of guest species. High stability is desirable in any application that might be proposed for these materials. Covalent carbon-carbon bonds are the ideal linkage to build the network thanks to their high thermal and chemical stability and their synthetic versatility[23]. Among the many existing carbon-carbon coupling reactions, Ullmann-type Yamamoto coupling reaction repeatedly proved to be extremely efficient in the preparation of extended hypercrosslinked porous frameworks with very high specific surface area and elevated stability, both thermal and chemical[24,25]. Yamamoto coupling is a Ni(0) catalyzed C-C coupling reaction between aromatic halides. In the field of covalent porous materials, its most known and successful application is in the preparation of the so-called Porous Aromatic Framework (PAF) family. **PAF1** is the forefather of the PAFs series[26], obtained by homopolymerization of tetrakis(4-bromophenyl)methane (**2, Scheme 4.1**). This material shows surface area values up to 5600 m^2/g and it is stable up to 500 °C. Moreover, its 14 Å wide pores provide a large free volume that could be exploited to allow unhindered photo-activated isomerization of bistable switches inserted in the matrix. Yamamoto protocol was also employed to successfully prepare porous random co-polymers through cross-coupling reaction between **2** and other aromatic halides species[27,28]

For these reasons, Yamamoto coupling reaction was chosen to prepare the material presented in this work. It was decided to adopt the random copolymerization method between the photo-active species and

tridimensional tetrahedral building blocks **2**, since the latter repeatedly demonstrated to form high surface area networks even when mixed with non-tridimensional co-monomers.

The ideal bistable molecular switch for this project must offer the possibility to insert the molecule into the rigid porous framework in such a way that the binding does not interfere with the photo-activated isomerization. To allow network formation during the polymerization reaction, the molecular switch design must consider the insertion of two reactive sites in suitable positions, so that the photo-switch could be placed as bridging unit between tetraphenylmethane units. Furthermore, the switching process of the OMS of choice must be efficient (i.e., with a very high metastable-to-stable ratio at photostationary state and good quantum yield) and its metastable state should have long half-life times.

Second-generation molecular switches synthesized by Feringa's group are the ideal candidate for this purpose[29–31]. They are chiral asymmetric overcrowded alkenes composed by a lower-half, that can be regarded as the stator, and an upper-half that can be viewed as the rotor, and which contains a stereogenic center. The photo-isomerization process involves rotation around the double-bond of the upper-part respect to the lower-half and it occurs without significantly affecting the conformation of the lower-half (**Figure 4.1**). It has been shown that, when the upper-half is connected to the lower-half through a six-membered ring, the molecule will have high metastable-to-stable ratio at photostationary state (PSS) and long half-life times (up to thousands of years). In other words, these molecules can be designed so they will behave as efficient bistable switches. Furthermore, the lower-half of second generation molecular switches can be functionalized to introduce halogen moieties that can be exploited in the following Yamamoto reaction to copolymerize the photo-active molecule **1** with **2** (**Scheme 4.1**). Since the lower-half is not directly involved in the switching process, it can be used as binding site without preventing the rotation of the upper-half. In **1** molecular structure, bromine atoms are in suitable positions for the following polymerization reactions: tetraphenylmethane units will be far enough from the rotating upper-half so they will not generate steric hindrance and they will be in opposite positions respect to the molecule main axes, so that the framework can keep on growing from both sides of the switch.

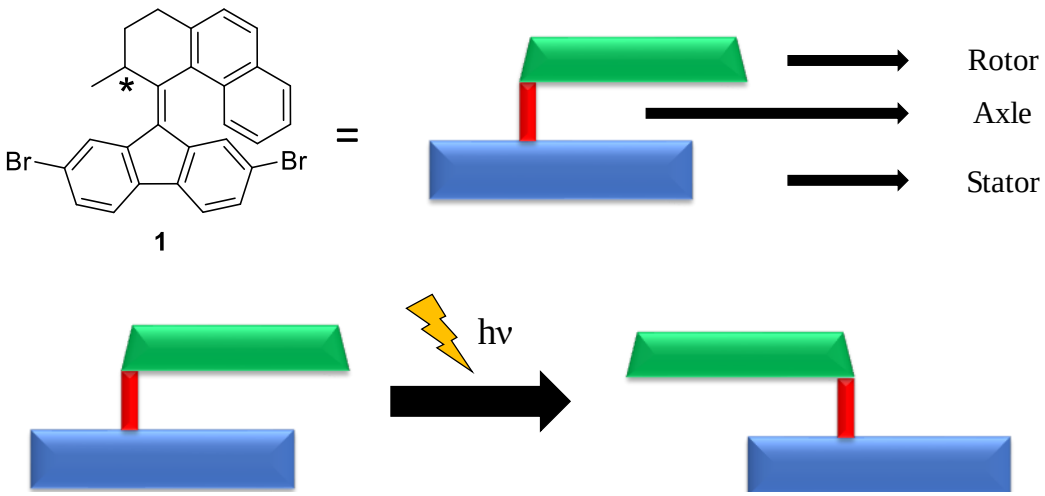

***Figure 4.1**. Chemical structure of the bistable molecular photo-switch used in this work. The asterisk indicates the stereogenic center. The drawings schematically reproduce the photo-isomerization of **1**.*

The photo-switching behavior of racemic **1** was studied by solution ^{1}H-NMR (see Appendix 4, **Figure A4.5**): it was observed that, upon irradiation with 365 nm light for 30 min, **1** reaches its PSS with a stable/metastable ratio of 6/94. The metastable form **1** can be reverted to the stable state by irradiation with 470 nm light; irradiating with 470 nm light for 1 hour generates a stable/metastable ratio of 97/3 at PSS. The half-life time, t_0, of **1,** defined as the time required for the concentration in solution of metastable **1** to be reduced by half due to thermal relaxation at 20 °C after PSS is reached, was too long to be directly measured; we can safely assume that the metastable state will not spontaneously return to the stable state at room temperature. These analyses confirm that **1** is a very efficient bistable switch.

As previously mentioned, second generation switches are chiral molecules. Molecule **1** possesses a stereogenic center (indicated by a star in **Figure 4.1**), which can be either R or S, and that gives the molecule point chirality. Moreover, due to steric hindrance, the lower- and the upper-half of the molecule are not planar, but are shaped into a helix. This means that the molecule also possesses axial chirality (P or M). It has been shown by Feringa and coworkers that, due to steric hindrance of the methyl group with the lower-half of the motor, out of the four possible diasteroisomers (RP, RM, SP, SM) of **1**, only two are formed (for example RM and SP). In other words, the configuration at the stereogenic center determines the handedness of the helix. The photo-activated photoisomerization of second-generation motors always occurs with a change in the handedness of the helix, i.e. the metastable state has opposite axial chirality respect to the stable state. This means, in simple words, that chirality of second generation switches can be controlled by light. In principle, the two diasteroisomers of **1** could be separated through chiral chromatography. By preparing the covalent framework with only one pure diasteroisomer of **1**, one would obtain a chiral framework which chirality would depend on the molecular switch state and that could be controlled by light. Chiral resolution of **1**, however, proved to be extremely difficult and time consuming. In this proof-of-concept work, all the efforts were focused on demonstrating that complex photo-activated dynamics is achievable in the solid-state and that a second-generation bistable switch is still able to undergo photo-isomerization once inserted in the covalent porous framework. For these reasons, racemous **1** (50:50 mixture of R and S) was used.

Molecule **1** was synthesized according to the procedure presented in **Scheme 4.1** and subsequently copolymerized with **2** to prepare Porous Switching Frameworks (**PSF**s). The detailed conditions for the synthesis of **1**, **2** and **PSFs** are given in the Experimental Section. Synthesis of **1** follows a 9-step route; the most difficult and important step is the Barton-Kellog cross-coupling reaction between thioketone **12** and diazo-derivative **10** (step *h* in **Scheme 4.1)**, followed by a desulfurization reaction to afford the final dibromo switch **1**. It is important to note that the diazo-compound **10** is highly unstable and it was prepared immediately before its use in the following coupling reaction.

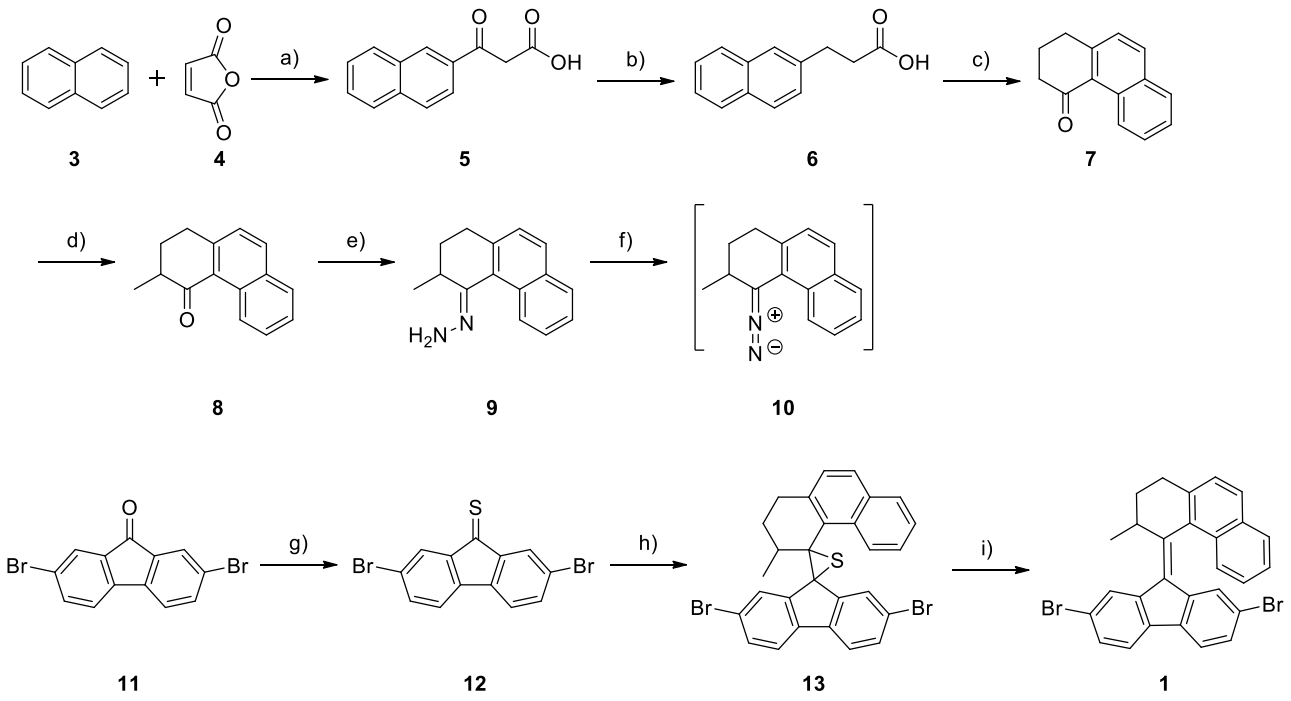

*Scheme 4.1. Schematic synthesis of bistable switch **1**. a) $AlCl_3$, DCM, 0 °C → RT, 5h, 30%; b) N_2H_4, KOH, ethylenglycol, 200 °C, overnight, 72%; c) CF_3SO_3H, 90 °C, 1 h, 80%; d) LDA, MeI, THF, -78 °C → RT, 3 h, 68%; e) N_2H_4, EtOH, reflux, 3 d, 44 %; f) PIFA, DMF, -50 °C, 5 min; g) Lawesson's reagent, toluene, 85 °c, 3 h, 51%; h) **10**, DCM, DMF, -50 °C → RT, 24 h; i) HMPT, DCM, DMF, RT, 24 h, 35%.*

The reaction scheme for the synthesis of **PSF**s is presented in **Scheme 4.2**. Since **1** is a linear monomer, it is not able to form a tridimensional porous framework by itself. Because of this, the molar ratio of **1** respect to **2** in the co-polymerization reaction should not be too high, otherwise a non-porous linear polymer would be formed. Two different reactions were carried out: **PSF1** was obtained from a reaction mixture containing 1/10 molar ratio of **1** respect to **2**, while **PSF2** was prepared from a solution containing 1/4 molar ratio of **1** respect to **2**. The concentration of **2** must be high enough to ensure good surface area and pore values, but, at the same time, the concentration of **1** must be high enough to produce a measurable effect when the photoactive moieties are switched from the stable to the metastable state.

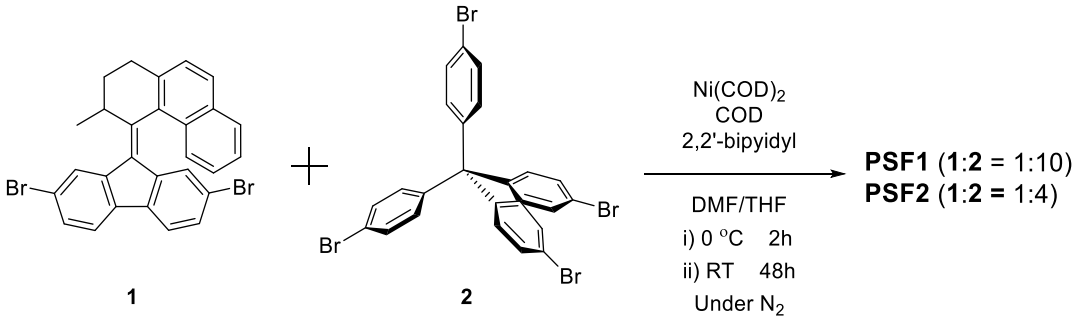

*Scheme 4.2. Schematic synthesis of **PSF** materials*

4.2. Characterization of PSF materials

In the following, $\mathbf{1}_{fr}$ and $\mathbf{2}_{fr}$ will be used to indicate molecules **1** and **2**, respectively, when they are part of the porous framework, after the polymerization reaction. **PSF1** and **PSF2** were obtained as yellowish light powders insoluble in all common organic solvents.

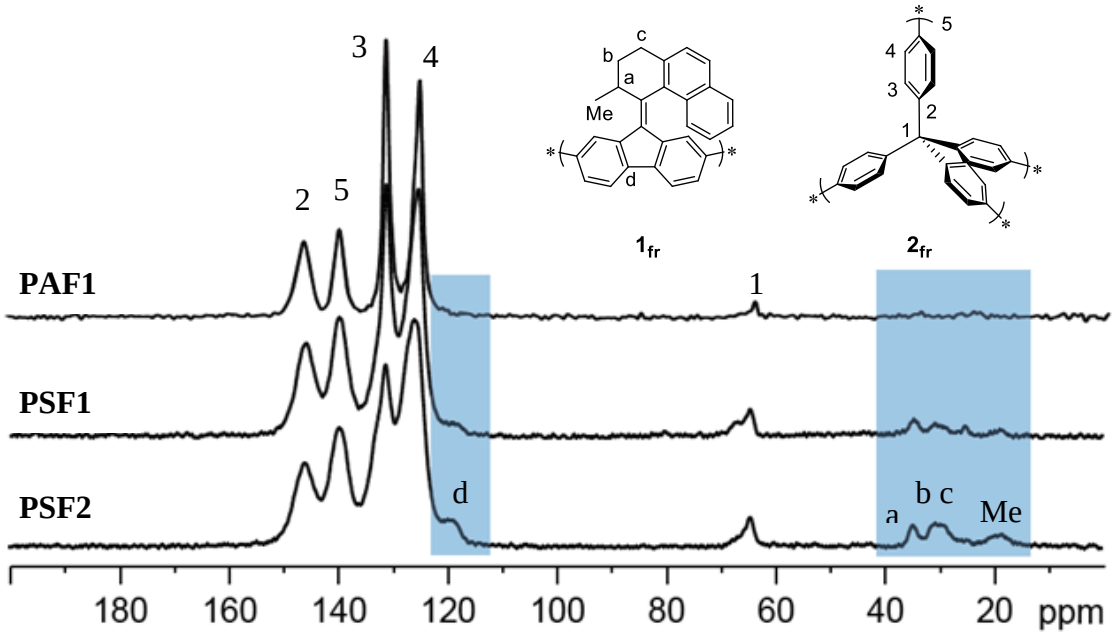

*Figure 4.2. ^{13}C CP/MAS NMR spectrum of **PAF1** (top trace), **PSF1** (middle trace) and **PSF2** (bottom trace) recorded with ct = 2 ms and spinning speed of 12.5 kHz.*

PXRD experiments (see Appendix 4, **Figure A4.8**) revealed that both materials are amorphous, as expected from this type of frameworks. To prove that bistable switches have been incorporated in the solid matrix, ^{13}C solid-state NMR experiments were performed. In **Figure 4.2** ^{13}C CP/MAS NMR spectra of **PSF1** and **PSF2** collected with a contact time of 2 ms are reported, together with the spectrum of **PAF1**, added for comparison. It can be clearly seen that additional signals are present in the aliphatic region (40-15 ppm, signals a, b, c and Me) of **PSF1** and **PSF2**; in the same region no signals are observed for the pristine **PAF1** spectrum. Another difference is the shoulder at 118 ppm (signal d). Both the aliphatic signals and the signal at 118 ppm increase in intensity going from **PSF1** to **PSF2**. According to solution ^{13}C-NMR collected in CD_2Cl_2 of **1** (see **Figure 4.6** and **Figure A4.7**), these peaks can be undoubtedly ascribed to bistable switch moieties. Molecule **1** shows other peaks in the aromatic region that are not visible due to the superposition with signals coming from the phenyl rings of **2.** All the signals that have been assigned to $\mathbf{1}_{fr}$ moieties were still present after the two frameworks have been extensively washed with different solvents (THF, DMF, $CHCl_3$, Acetone), proving that the bistable switches are covalently connected to tetraphenylmethane units to form the hypercrosslinked matrix. Another peculiarity of the series of ^{13}C-NMR spectra comes from signals of tetraphenylmethane moieties (125-145 ppm): they become increasingly broader going from **PAF1** to **PSF2.** This effect might be

explained considering the number of possible chemical environments that could exist about $\mathbf{2_{fr}}$ units as the amount of switch moieties is increased. In **PAF1** the framework is composed entirely by tetrahedral tetraphenylmethane unit: each one of them is surrounded by the same chemical environment and bond angles and distances cannot vary much due to the nature of covalent bonding (i.e. short-range order). Consequently, line broadening only arises from the lack of crystallinity (i.e. long-range disorder) and the resulting peaks are sharper than **PSF1** and **PSF2**. Adding switch moieties to the framework implies that additional signals are introduced in the 110-155 ppm region and each tetrahedral tetraphenylmethane unit can be linked from zero to four molecules of $\mathbf{1_{fr}}$. This leads to line broadening due to superposition of signals in the aromatic region and to larger variety of chemical environments around $\mathbf{2_{fr}}$ units. These effects are linearly dependent from switch concentration, thus peaks in **PSF2** spectrum are broader than in **PSF1** spectrum.

To determine the actual quantities of $\mathbf{1_{fr}}$ in **PSF1** and **PSF2**, ^{13}C MAS experiments were performed with a recycle delay of 100 s. Unfortunately, switch signals in **PSF1** were too weak to perform an adequate integration process. Thus, only switch concentrations in **PSF2** was determined with this method. Integrating the area of the peaks of the aliphatic region (15-40 ppm) respect to the area of the all the aromatic signals (115-155 ppm) and knowing the total number of aromatic carbon atoms allowed to calculate the ratio between $\mathbf{1_{fr}}$ and $\mathbf{2_{fr}}$ in **PSF2** to be 25.6% (see Appendix 4, **Figure A4.17**). This value is in good agreement with the amount of switch used in the preparation step of the material, indicating that monomers co-polymerized to give a homogenous network.

The permanent porosity of the two materials was demonstrated by N_2 adsorption/desorption isotherms collected at 77 K; the results are shown in **Figure 4.3**, while in **Table 4.1** are reported the main textural parameters derived from the isotherm analysis. Data from a **PAF1** sample (BET surface area = 5206 m^2/g) are included for comparison.

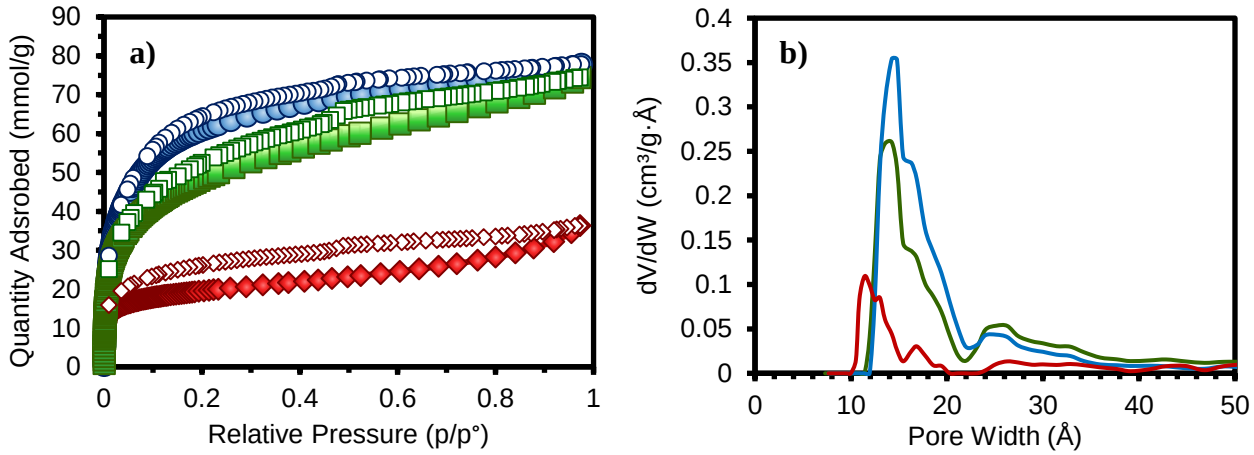

*Figure 4.3. a) N_2 adsorption/desorption curves collected at 77 K for **PAF1** (blue circles), **PSF1** (green squares) and **PSF2** (red diamonds). Empty symbols represent desorption branches. b) Pore size distribution curves of **PAF1** (blue trace), **PSF1** (green trace) and **PSF2** (red trace). N_2@carbon slit pores by NLDFT model was used.*

All the materials show type I adsorption isotherms (**Figure 4.3a**), indicating a microporous nature the frameworks. **PSF1** has a very high BET surface area, reaching almost 4000 m^2/g, while **PSF2** reaches 1615

m^2/g, a value that is remarkable, considering the high percentage of switch present. These results confirm the validity of the design which uses tetraphenylmethane as the network-forming building block and of Yamamoto coupling as the polymerization reaction. From **PAF1** to **PSF2** the hysteresis of the desorption branch increases, nonetheless remaining small in absolute value, another indication that both **PSF1** and **PSF2** are highly microporous materials. The hysteresis indicates flexibility of the framework. The deviation from the Langmuir profile is ascribable to a contribution of mesopores to the overall porosity of the framework. Mesoporosity might be generated from interparticle interstices that are formed when polymer particles aggregate during the polymerization reaction. The observed increase in mesoporosity from **PAF1** to **PSF2** could be explained considering that the increasing concentration of co-monomer **1** results in the formation of polymer particles that do not pack efficiently, leaving interstices that behave as mesopores. Pore Size Distributions (PSDs) (**Figure 4.3b**) calculated by Non-Local Differential Functional Theory (NLDFT) applying the N_2@carbon slit pores model further support the conclusion drawn by the analysis of the isotherm shape: both **PSF1** and **PSF2** are microporous materials and **PSF1** has a higher microporous character.

Table 4.1. Textural parameters of PSF1, PSF2 and PAF1 as derived from N2 adsorption isotherms at 77 K.

	S_{BET} (m^2/g)	$S_{Langmuir}$ (m^2/g)	V_{total}[a] (cm^3/g)	V_{micro}[b] (cm^3/g)	V_{micro}/V_{total} (%)
PSF1	3947	4545	2.39	1.24	52
PSF2	1615	1830	1.19	0.53	45
PAF1	5206	6020	2.47	1.71	69

[a] Calculated applying NLDFT adopting N_2@77K Carbon slit pore model

[b] Calculated considering pored up to 20 Å wide

PSD of **PSF1** closely resembles that of **PAF1** as they are both centered on pores of 14.2 Å, while **PSF2** shows slightly smaller pore size, peaking at 11.4 Å. Even the smaller pores of **PSF2** should offer enough free space to the bistable switches to undergo unhindered photo-isomerization in the solid materials.

The thermal stability of the new compounds was tested by Differential Scanning Calorimetry (DSC) and Thermogravimetric Analysis (TGA). DSC experiments (see Appendix 4, **Figure A4.9**) shows that no thermal phenomena occur up to 300 °C, while TG analysis (Appendix 4, **Figure 4.10**) indicates that no weight loss is observed up to 420 °C, temperature at which the frameworks start decomposing. These results confirm high thermal stability, as expected from a fully covalent organic framework.

To prove that bistable switches undergo photoisomerization in solid-state in the covalent porous framework, we made use of the different properties of stable and metastable states. It is known that stable and metastable states of **1** have different IR, Raman, Uv/Vis and fluorescence spectra (see Appendix 4). Furthermore, **1**-stable and **1**-metastable have different ^1H and ^{13}C chemical shifts in solution NMR. The observed differences are a consequence of the different configurations of the stable and metastable states. In Appendix 4 are reported solution spectra of **1** before and after irradiation with 365 nm light of all the aforementioned techniques. It was expected that similar differences would be observed in solid-state if $\mathbf{1}_{fr}$-metastable was formed upon irradiation

with 365 nm light. In the following **PSF1-PSS-365** and **PSF2-PSS-365** indicate **PSF1** and **PSF2**, respectively, irradiated with 365 nm light up to photostationary state. Similarly, **PSF1-PSS-470** and **PSF2-PSS-470** represent 470 nm irradiated samples.

The main differences in IR and Raman spectroscopy of stable and metastable state of second generation molecular motors concerns the olefinic bond stretching mode. In both techniques, C=C stretching appears typically in the 1400-1700 cm^{-1} region.

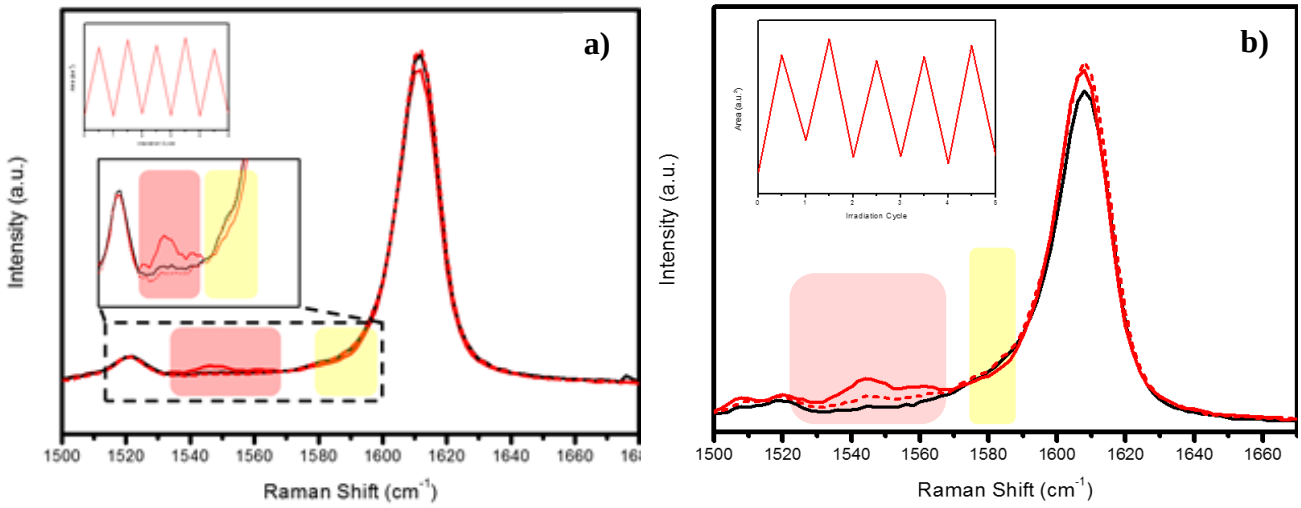

*Figure 4.4. **a)** Changes in Raman spectrum (785 nm, 50 mW) of **PSF1** (black line) upon sequential irradiation with 365 nm (red solid line) and 470 nm (red dotted line). Inset shows changes in area of the peak at 1550 cm^{-1} over 5 cycles. **b)** Changes in Raman spectrum (785 nm, 50 mW) of **PSF2** (black line) upon sequential irradiation with 365 nm (red solid line) and 470 nm (red dotted line). Inset shows changes in area of the peak at 1550 cm^{-1} over 5 cycles.*

Generally speaking, double bond stretching signal of metastable state appears at smaller wavenumbers with respect to the stable state. This effect can be clearly seen in both IR (ATR method) and Raman spectra of a drop-casted thin film of molecule **1** (see Appendix 4, **Figures A4.1** and **A4.2**). Similar experiments were performed on powders of **PSF1** and **PSF2**. In **Figure 4.4** are reported Raman spectra of pristine and irradiated **PSF1** (**Figure 4.4a**) and **PSF2** (**Figure 4.4b**). First of all, the two spectra of the stable form of **PSF1** and **PSF2** (black solid trace) show the same pattern, with an intense peak at 1608 cm^{-1} and a weaker one at 1519 cm^{-1}. This, of course, was expected since the only difference between the two samples is the switch concentration. Secondly, in both spectra can be clearly seen that, upon irradiation for 30 minutes with 365 nm light, there is a reduction in intensity around 1585 cm^{-1} in favor of a new signal appearing at 1555 cm^{-1}. The effect is much more intense and clear in **PSF2** thanks to the higher concentration of switch. This behavior in solid **PSF1** and **PSF2** resembles what was observed for pure **1** (**Figure A4.2**) and it is associable with the formation of $\mathbf{1_{fr}}$-metastable at the expanse of $\mathbf{1_{fr}}$-stable. This first analysis already demonstrates that the solid-state photoswitching of $\mathbf{1_{fr}}$ is possible and occurs fastly. Upon irradiation with 470 nm light, experiments run on pure **1** show a complete restoration of the initial conditions; after irradiating **PSF1** for 45 minutes with 470 nm light, the initial spectrum was recovered, thus proving that photo-switching of $\mathbf{1_{fr}}$ is reversible inside the porous matrix, as well. When the same experiment was run on **PSF2**, the back-switch occurred, but it was not

complete, probably because the higher concentration of switches required a longer exposure to 470 nm light to fully restore the initial condition (**Figure 4.4b**). The irradiation experiments were repeated for 5 cycles and both **PSF1** and **PSF2** showed very good cycling properties (see insets in **Figure 4.4**), further indicating that molecular switches are able to smoothly operate in the solid porous materials.

We then tried to observe the same effect with IR spectroscopy (ATR method) on **PSFs**, but unfortunately, due to the generally weak signal of carbon double bonds in IR and the low concentration of switches in the materials, it was not possible to detect any significant difference between the spectra of the pristine and irradiated **PSFs** (**Figure A4.11** and **A4.12**).

Typically, the stable-to-metastable photo-isomerization of second generation motor can be easily followed using solution UV/Vis spectroscopy. Metastable forms usually show red-shifted spectra with clear isosbestic points, indicative of the isomerization of the stable form to the metastable. The isomerization of **1** in solution was studied with UV/Vis spectroscopy and the results are reported in Appendix 4 (see **Figure A4.3**): upon irradiation with 365 nm light, the peak at 365 nm loses intensity in favor of a new peak centered at 415 nm. The process is reversible upon irradiation with 470 nm light. We then collected the solid-state UV/Vis absorption spectra of **PSF1** and **PSF2** (**Figure 4.5**)

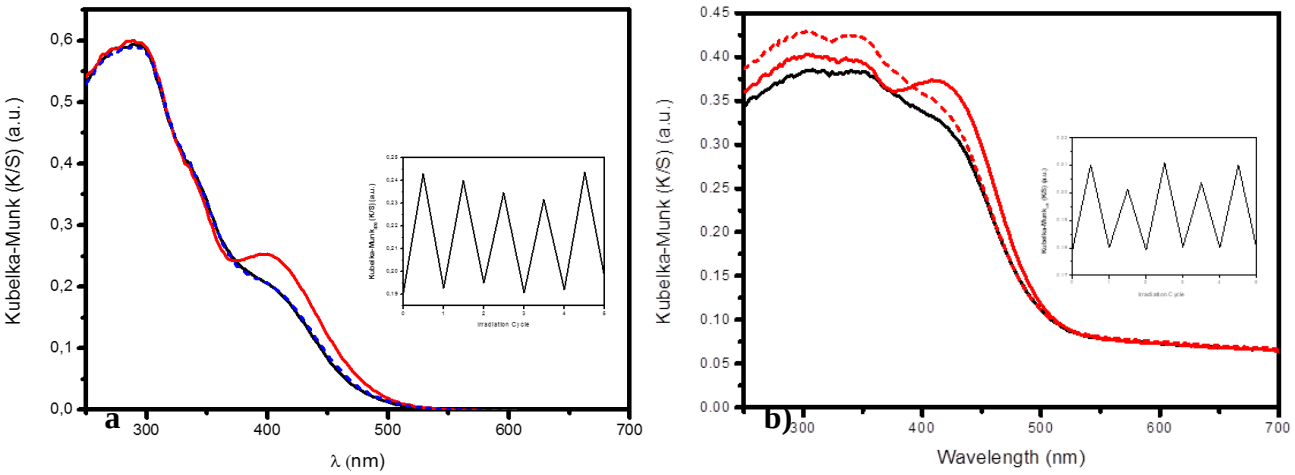

*Figure 4.5. **a)** UV/Vis adsorption spectra of pristine **PSF1** (solid black trace), **PSF1-PSS-365** (solid red trace) and **PSF1-PSS-470** (dotted blue trace) Inset shows relative intensities at 420 nm over 5 cycles. **b)** UV/vis adsorption spectra of pristine **PSF2** (solid black line), **PSF2-PSS-365** (solid red trace) and **PSF2-PSS-470**. Inset shows relative intensities at 440 nm over 5 cycles. In both cases irradiation with 365 nm irradiation was performed for 30 minutes, while 470 nm irradiation lasted 45 minutes.*

Solid-state UV/Vis spectra of **PSF1** and **PSF2** preserve the main characteristic of solution UV/Vis absorption of **1**, although the main peak of stable-**PSF1** is blue-shifted at about 310 nm, while stable-**PSF2** exhibits a broader signal centered around 350 nm. Exposing **PSF1** to 365 nm light for 30 minutes causes the apparition of a new peak at 420 nm. This peak completely disappears after irradiation with 470 nm light for 45 minutes. As showed in the inset of **Figure 4.5a**, the phenomenon has a very good reproducibility over 5 cycles. In a similar way, a new signal around 440 nm is generated after exposure of **PSF2** to 365 nm light, but, as already observed with Raman spectroscopy, the light-induced backswitch is not complete. Nonetheless, the photo-isomerization of **1** inside **PSF2** is very reproducible, as is shown in the inset of **Figure 4.5b**.

The results of both Raman and UV/Vis spectroscopy prove that bistable switch $\mathbf{1_{fr}}$ is able to reversibly undergo photo-induced isomerization around the double bound while covalently linked in the network of a porous material. This is already a very important finding that demonstrate the validity of the design of both the switch itself and the final material. However, with Raman and UV/Vis spectroscopy we probed only the switches contained in the first few micrometers of material, depending on the penetration depth of the wavelength used as probe. In other words, we are looking at a surface effect and we cannot say whether the switches in the bulk of the framework are switching or not. For this reason, we decided to exploit both solid-state NMR and gas adsorption measurements to check the effect on the bulk of the porous frameworks upon irradiation.

First of all, the solution ^{13}C-NMR of **1**-stable and **1**-metastable have been collected. The full spectra are shown in Appendix 4 (**Figure A4.7**), while in **Figure 4.6** is reported a selected region of the spectra, specifically the aliphatic region. We focused our attention on this region for two reasons: aliphatic signals show the highest chemical shift differences between stable and metastable state and they are the only signals of the switches that are clearly visible in the solid-state spectra of **PSF1** and **PSF2**, since the aromatic signals are covered by the tetraphenylmethane peaks (see **Figure 4.2**). As it can be observed in **Figure 4.6**, each aliphatic signal of the metastable form (red trace) is shifted respect to its corresponding signal in the stable form (black trace); the shift may be upfield (*a* and *c*) or downfield (*b* and *Me*) and the absolute value of the shift vary from nucleus to nucleus, with peaks *a* and *c* shifting more than *b* and *Me* (see **Table 4.2)**. In solution, conversion of the stable state to the metastable state is almost quantitative (94/6 metastable/stable). Exploiting this behavior, we tried to quantify the amount of $\mathbf{1_{fr}}$-metastable formed upon irradiation with 365 nm light of **PSF2** with ^{13}C CP MAS NMR experiments. It must be said that these experiments were performed only on **PSF2** because switch signals on **PSF1** material are very weak and quantifying the formation of the metastable state would have been very difficult. Similarly, CP technique was used because switch signals in quantitative MAS experiments are very feeble and badly resolved (see Appendix 4, **Figure A4.18**) and it would have been impossible to detect the small chemical shift changes the we expected. Usually, one cannot determine relative concentrations of carbon atoms from their peak area with a CP experiment since, using cross-polarization technique, the intensity of a C atom signal depends on the number of proton nuclei to which it is bonded. For example, at equal concentrations, a primary aliphatic carbon atom would give a signal more intense than a tertiary carbon atom or an aromatic C atom. However, going from stable to metastable state, only the surroundings of the atoms are changing, not their connectivity (i.e., they are bonded to the same atoms). CP signals intensities are strongly dependent only on the number of protons bonded to the carbon nuclei. This means that it is safe to assume that, in a CP MAS experiment, analogue carbon atoms will have the same signal intensities in the stable and metastable forms. Furthermore, before working on **PSF2-PSS-365** spectrum, we simulated the aliphatic region of **PSF2** ^{13}C CP MAS spectrum and noticed that the area of carbons labelled *a*, *b*, *c* and *Me* in **Figure 4.8** is equal for all four signals. This means that a CP MAS with a 2 ms contact time is quantitative for these aliphatic carbons atoms.

Table 4 2. *Chemical shift of aliphatic carbon atoms of **1** before and after irradiation with 365 nm light obtained from solution NMR studies. Values are expressed in ppm.*

	a	b	c	Me
1-stable	37.64	33.13	32.07	22.99
1-metastable	36.68	33.20	30.59	23.15

Thus, we then can use the relative integrated areas of the aliphatic signals to determine the stable-to-metastable ratio after irradiation. Irradiation on **PSF2** was performed distributing 40 mg of pristine sample over the surface of a petri dish with a diameter of about 4 cm utilizing a 6 W UV lamp. The powder was mixed with a spatula every 60 minutes to expose new surface to the light and the total irradiation time was prolonged to 54 hours. Such a long irradiation time was necessary to ensure that PSS was reached throughout the bulk of the particles. After the irradiation, the color of the powder visibly changed to a deeper hue of yellow (**Figure 4.7**).

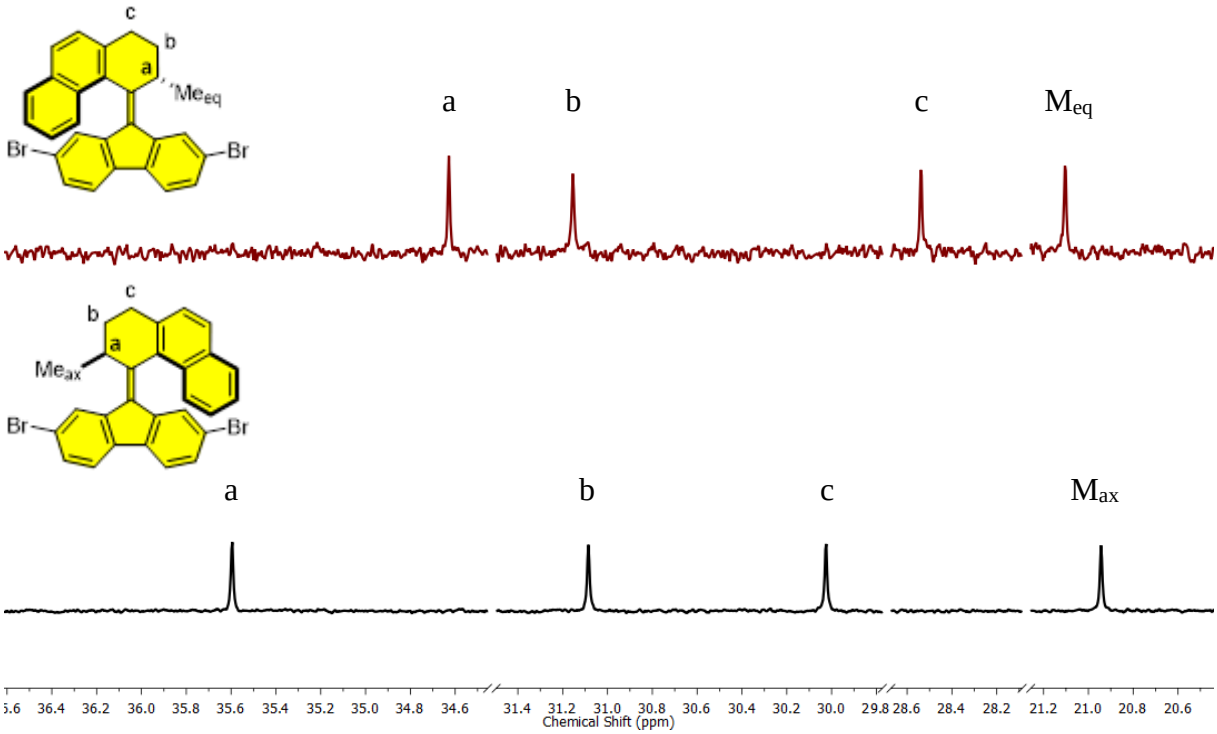

*Figure 4.6. Selected part of ^{13}C NMR (CD_2Cl_2, 100 MHz, RT) spectra showing changes upon irradiation with 365 nm for 30 minutes. **1**-stable (black), photostationary state mixture (PSS_{365}) containing 94% of **1**-mestable (red).*

Results of ^{13}C CP MAS NMR experiments collected on pristine **PSF2** and **PSF2-PSS-365** are shown in **Figure 4.8**. It can be immediately seen that there is a net difference between the two spectra, especially regarding the tertiary aliphatic carbon (labeled *a* in **Figure 4.8**). The solid-state signal shifting before and after irradiation reflects what was observed in solution, with peaks *a* and *c* downfield shifted and with much smaller shifts for

b and *Me*. Because of this resemblance between solution and solid-state NMR, we can undoubtedly say that the observed changes in solid-state NMR are associated with the formation of the metastable form of switch $\mathbf{1}_{fr}$ inside the porous framework. To quantify the extent of the isomerization process, we deconvoluted the pristine and irradiated spectra. The results are shown in **Figure 4.9**.

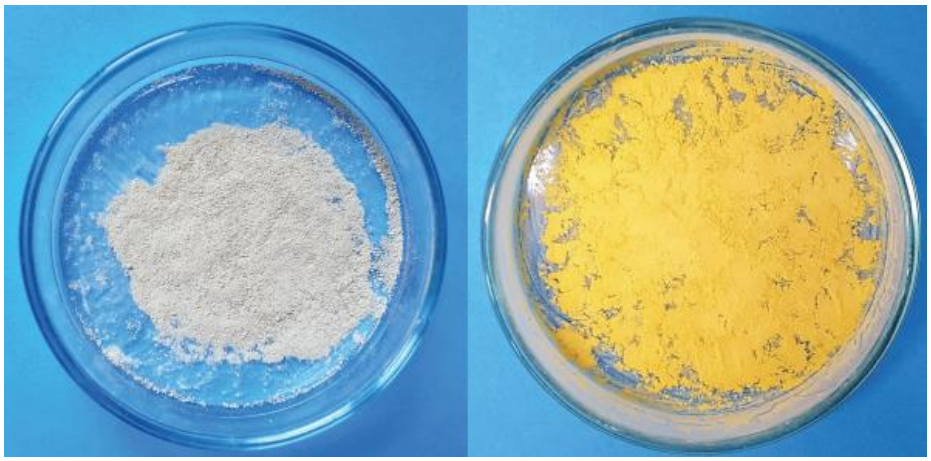

Figure 4.7. PSF2 before (left) and after (right) exposure to 365 nm light for 24 hours.

The peak coming from the methyl group (*Me*) has been excluded from the simulation process, as it is so broad that no difference can be observed between the methyl in axial position (stable state) and in equatorial position (metastable state). As a first condition to be satisfied to correctly simulate the spectra, the area of peaks coming from $\mathbf{1}_{fr}$-stable (blue peaks) must be equal; a similar condition applies to peaks coming from $\mathbf{1}_{fr}$-metastable (red peaks).

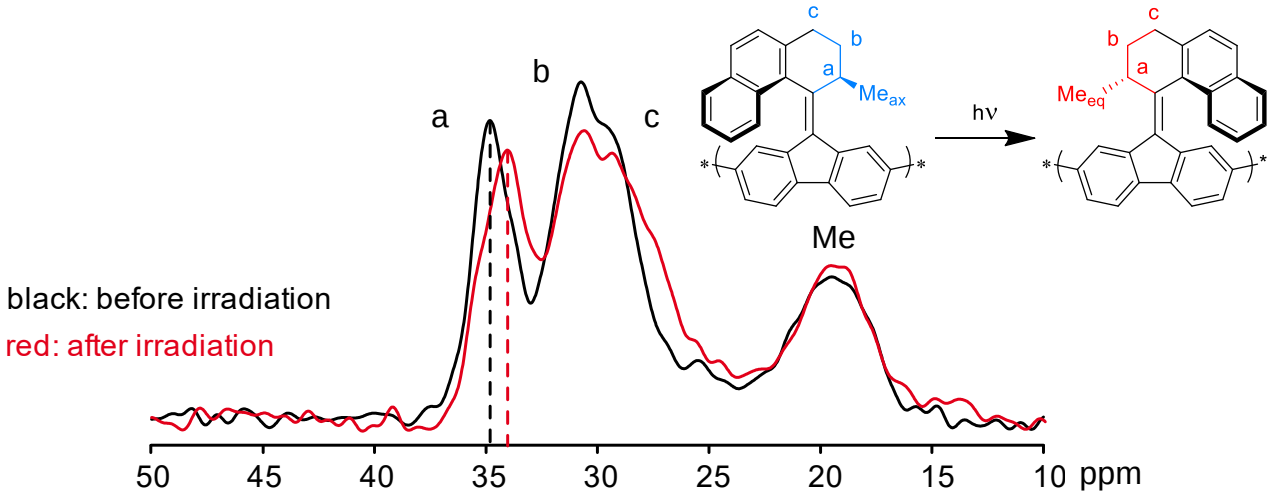

*Figure 4.8. ^{13}C CP/MAS NMR of **PSF2** (black trace) and of **PSF2-PSS-365** (red trace) collected with a contact time of 2 ms. The shift of the tertiary carbon atom is highlighted by dotted lines.*

Furthermore, the sum of the area of peaks of the same C atom in the stable and metastable state must be equal to the area of the methyl peak (for example area[a+a*] = area[*Me*]). This last condition is derived from the fact that Me_{ax} and Me_{eq} are not distinguishable. Once these conditions were satisfied, the resulting simulation allowed us to determine that, after 54 h of irradiation, 93% of switches were in the metastable state. (**Figure 4.9**). This result demonstrates that the photo-switching process of molecular switch $\mathbf{1_{fr}}$ in the solid porous frameworks is in all respects a bulk phenomenon and that is very efficient, promoting the isomerization of more than 90% of switches to the metastable state. As far as we know, this is the first time that a photo-switch process in solid state is precisely quantified and proven to reach such high conversion.

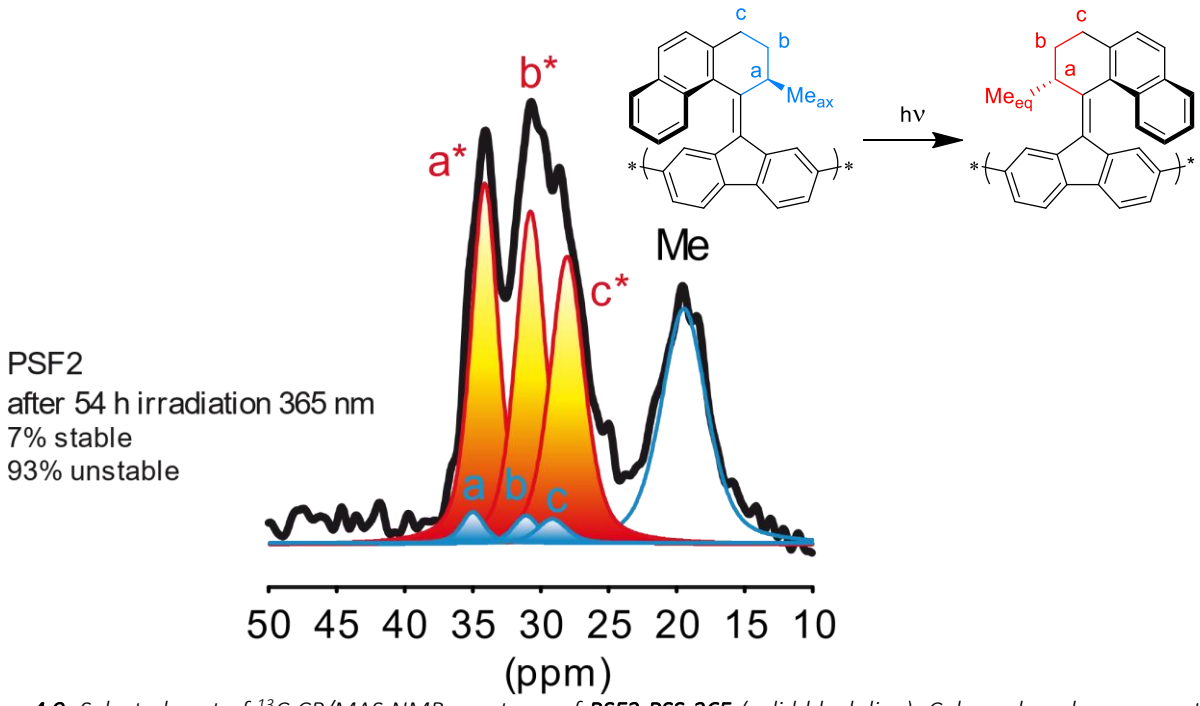

*Figure 4.9. Selected part of ^{13}C CP/MAS NMR spectrum of **PSF2-PSS-365** (solid black line). Coloured peaks represent the deconvoluted spectrum. Red peaks indicate signals coming from **1_{fr}**-metastable, blue peaks denote signals coming from **1_{fr}**-stable. The ratio between the total area of the blue and red peaks was used to determine the stable-to-metastable ratio.*

The very high metastable-to-stable ratio reached prompted us to further investigate the properties of **PSF2-PSS-365**. Calculations run over molecular switch **1** shows that the metastable state is bulkier than the stable state of about 20% (**Figure 4.10**). Knowing this, we wondered if this effect would influence the gas adsorption properties of the material. **Figure 4.11** shows the results of N_2 adsorption isotherms collected at 77 K on **PSF2** and on **PSF-PSS-365**.

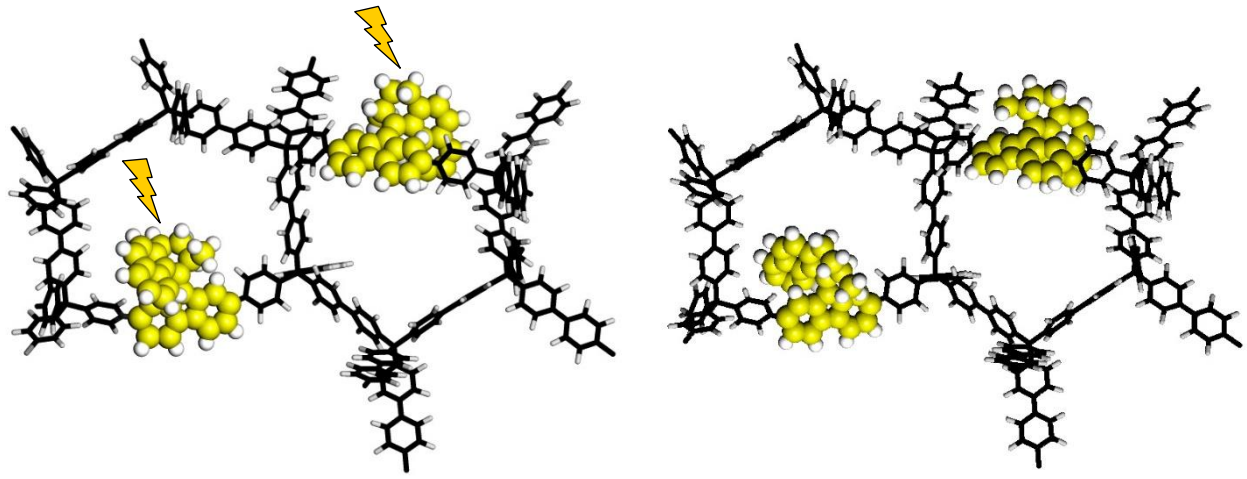

Figure 4.10. Schematic representation of photoswitching process of $\mathbf{1}_{fr}$ *in PSF2. Left) in stable configuration. Right) After adsorption of a 365 nm photon,* $\mathbf{1}_{fr}$*-metastable is formed.*

After irradiation with 365 nm light, the resulting isotherm collected on **PSF2-PSS-365** retains the same shape as the pristine isotherm (type I isotherm, similar hysteresis), but the maximum adsorbed quantity of nitrogen is reduced of about 20%. This reduction in adsorbed quantity is translated into a minor Langmuir and BET specific surface areas that are diminished from 1830 and 1615 m^2/g of pristine **PSF2** to 1374 and 1213 m^2/g, respectively, of irradiated **PSF2-PSS-365**.

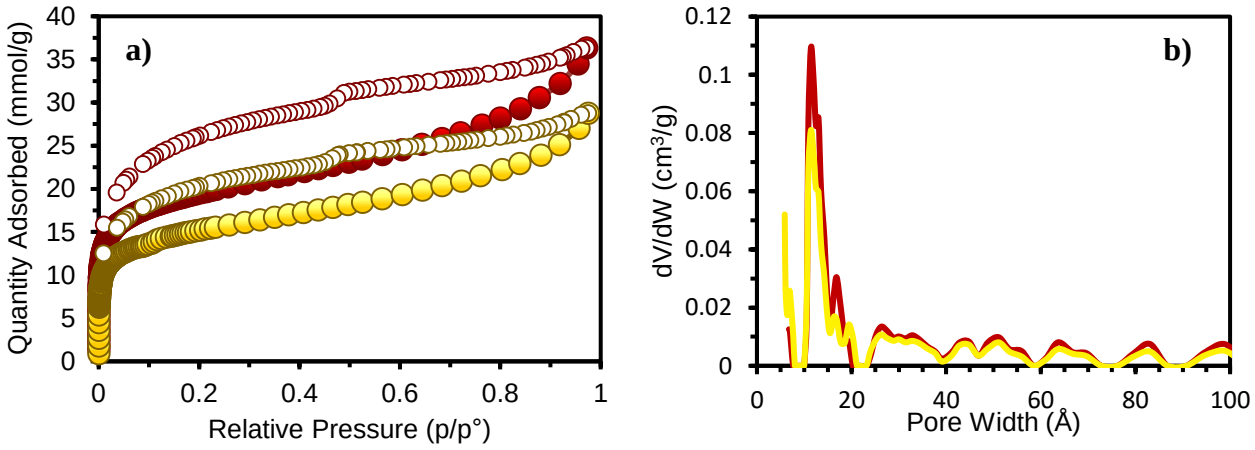

Figure 4.11. a) N_2 *adsorption isotherms collected at 77 K of PSF2 (red trace) and of PSF2-PSS-365 (yellow trace); b) Pore size distributions calculated by NLDFT with the* N_2*@ carbon slit pore mode of PSF2 (red trace) and of PSF2-PSS-365*

Table 4.3. Textural parameters of PSF2 and PSF2-PSS-365 as derived from N_2 adsorption isotherms

	S_{BET} (m^2/g)	$S_{Langmuir}$ (m^2/g)	V_{total}[a] (cm^3/g)	V_{micro}[b] (cm^3/g)	V_{micro}/V_{total} (%)
PSF2	1615	1830	1.19	0.53	45
PSF2-PSS-365	1213	1374	0.94	0.41	44

Interestingly, pore size distribution of **PSF2** is not changed upon irradiation (**Figure 4.10b**), although the total pore volume is reduced of about 20% (see **Table 4.2**). All these results further demonstrate that the photo-isomerization of molecular switches is a process that takes place homogenously throughout the bulk of the material. As expected from the calculation on the monomer, the bulkier metastable state reduces the accessible free volume of the material, causing a reduction in the specific surface area.

Adsorption experiments on **PSF2** and **PSF2-PSS-365** were performed also with CO_2 at 195, 273, 283 and 298 K up to 1 bar of pressure. Results are shown in **Figure 4.11**. In all the experiments there are not significant differences regarding isotherms shapes, meaning that interactions between CO_2 molecules and the host matrix are unchanged upon irradiation. At 195 K we observed a reduction of the maximum adsorbed CO_2 quantity of about 20% (from 22.33 to 17.93 mmol/g), which is the same reduction observed for N_2 at 77 K. Nitrogen isotherms at 77 K and CO_2 isotherms at 195 K are collected to measure the maximum adsorption capacity of a porous materials for the two gases. The fact that both experiments show a reduction of 20% of the maximum adsorption capacity after irradiation is a further proof that isomerization of $\mathbf{1_{fr}}$ to the metastable state causes a reduction in the free volume of the material. Raising the temperature decrease the difference in adsorbed quantity between **PSF2** and **PSF2-PSS-365**: at 298 K we cannot observe any substantial difference up to 1 bar. This effect is consistent with the available volume occupation: at higher temperatures, the amount of adsorbed gas is smaller and it fills a very small fraction of the available free volume of the two materials, thus the difference observed at high loading is negligible in these conditions.

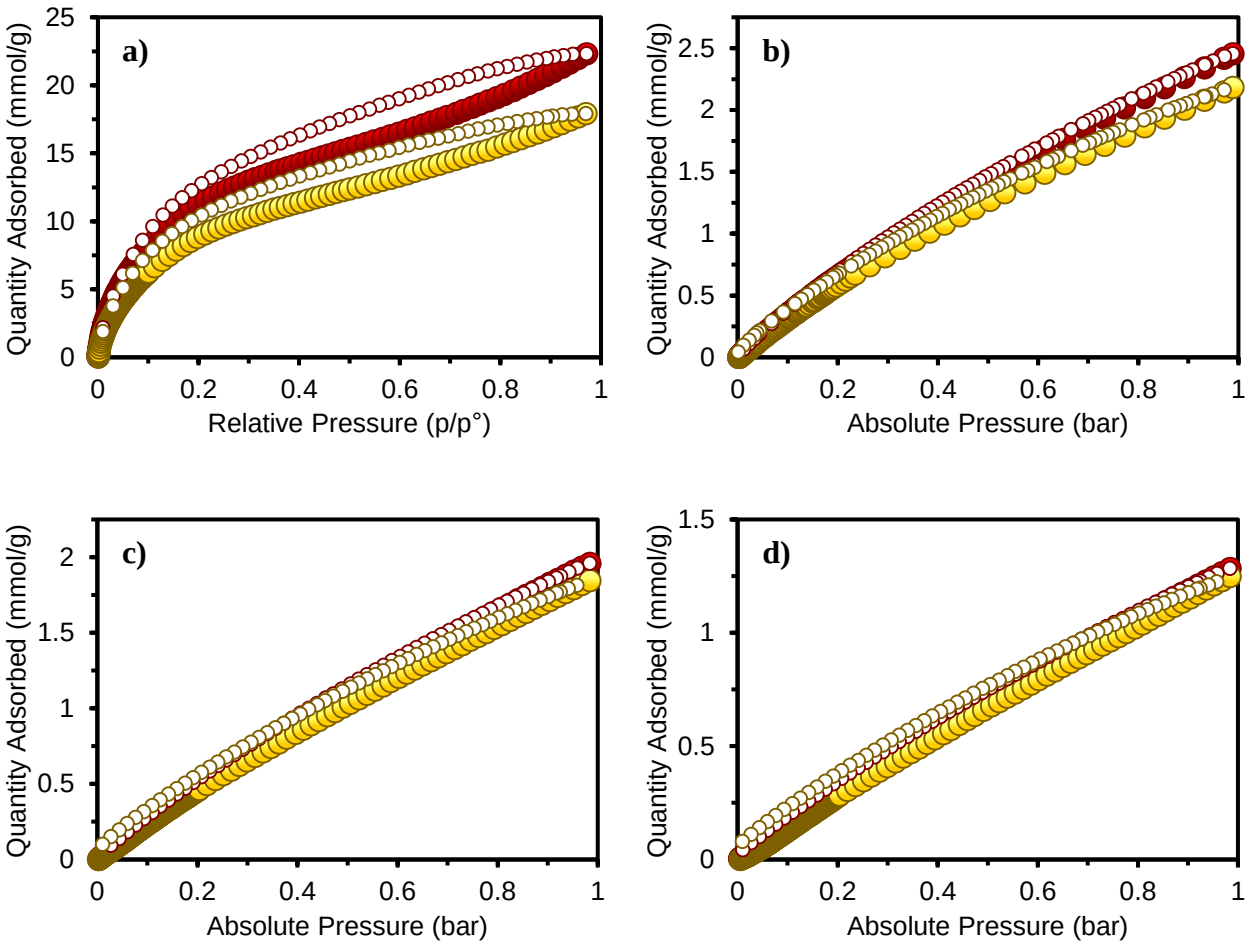

*Figure 4.12. CO_2 adsorption isotherms of **PSF2** (red trace) and **PSF2-PSS-365** (yellow trace) collected at **a)** 195 K, **b)** 273 K, **c)** 283 K and **d)** 298 K up to 1 bar of pressure.*

The CO_2 isotherms collected at 273, 283 and 298 K were fitted with the dual-site Langmuir equation and the resulting fitted isotherms were used to calculate the isosteric heat of adsorption (Q_{st}) applying the van't Hoff equation. Results of the fitting procedure are reported in Appendix 4 (**Figure A4.15**). Q_{st} of **PSF2** and **PSF2-PSS-365** were calculated to be 24.3 and 24.1 kJ/mol, respectively, indicating that interactions between the host matrix and the guest CO_2 molecules do not change upon irradiation.

*Table 4.4. CO_2 adsorption capacities of **PSF2** and **PSF2-PSS-365**.*

	Q_{max}(195K) (mmol/g)	Q_{max}(273K) (mmol/g)	Q_{max}(283K) (mmol/g)	Q_{max}(298K) (mmol/g)	$Q_{st}(CO_2)$ (kJ/mol)
PSF2	22.33	2.46	1.96	1.28	24.3
PSF2-PSS-365	17.93	2.18	1.84	1.24	24.1

PSF2-PSS-365 was then irradiated with 470 nm light (**PSF2-PSS-470**) to study the back-switch behavior of $\mathbf{1}_{fr}$. Unfortunately, even prolonged exposure to 470 nm light did not completely restore the initial conditions (see Appendix 4, **Figure A4.19**). After 100 h of irradiation, deconvolution of the ^{13}C-NMR spectrum shows that 37% of the switches is in the stable state and 63% is in the metastable state. We believed that the difficulties encountered in the back-switch experiments were to be ascribed to a lack of penetration of the 470 nm radiation in the bulk of the particles, rather than to an actual impossibility of the system to return to the stable state. To prove this, we heated the sample at 200 °C for 15 hours under vacuum (**PSF2-heated**). Heating is another efficient way to promote the back-switching process even for bistable switches with very high half-life times. **PSF2-heated** was analyzed by SS-NMR and the result is shown in **Figure 4.12**. It can be immediately noticed that the initial spectrum was recovered. This prove that molecular switches $\mathbf{1}_{fr}$ are able to undergo reversible switch in solid state in a porous organic framework.

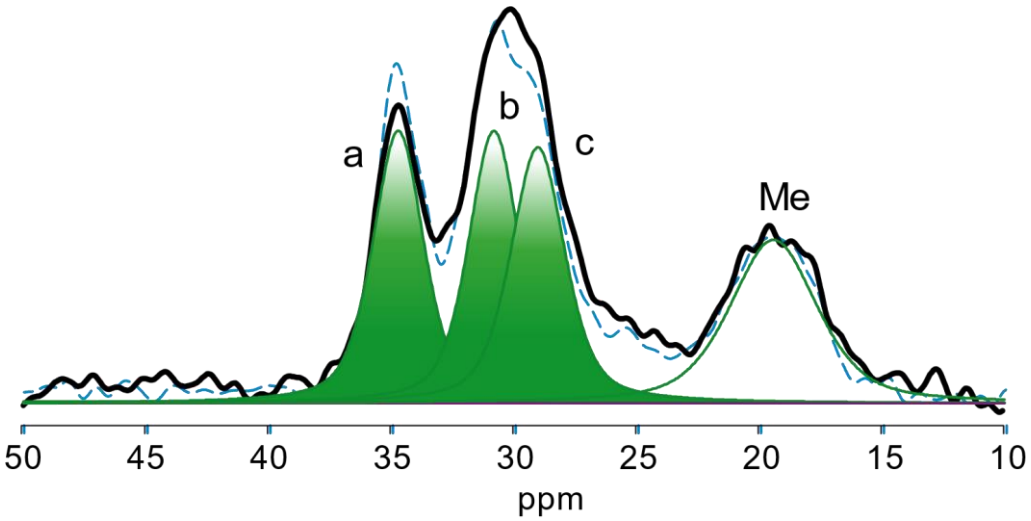

*Figure 4.13. Selected part of ^{13}C CP/MAS NMR spectra of **PSF2-heated** (solid black line) and **PSF2** (dashed blue line). Green coloured peaks represent the deconvolution of **PSF2-heated** spectrum.*

After that, we measured again the surface area of **PSF2-heated** by N_2 adsorption (**Figure 4.13a**). Ideally, we expected the surface area to return to a value close to the initial one, but, to our surprise, the surface area of the heated sample was almost the same as **PSF2-PSS-365** (see Appendix 4, **Table A4.2**). However, isotherms shape changed drastically after the thermal treatment: the isotherm of **PSF2-heated** is closer to an ideal Langmuir and the hysteresis is smaller compared to pristine **PSF2**. Both these effects might be ascribable to a increased microporosity of the framework, most probably caused by a curing effect promoted by the prolonged exposure to the high temperature. The higher microporosity of the material after heating is clearly demonstrated by the normalized cumulative pore volume graph (**Figure 4.12b**): more than 60% of **PSF-heated** pore volume is due to pores narrower than 20 Å, while this value reaches only 45% for **PSF2.** This is an interesting effect on its own since it is the first time in our experience with PAF materials that we observe it and we are wondering whether it is caused by the presence of the switches or it is more general. Investigations are currently ongoing.

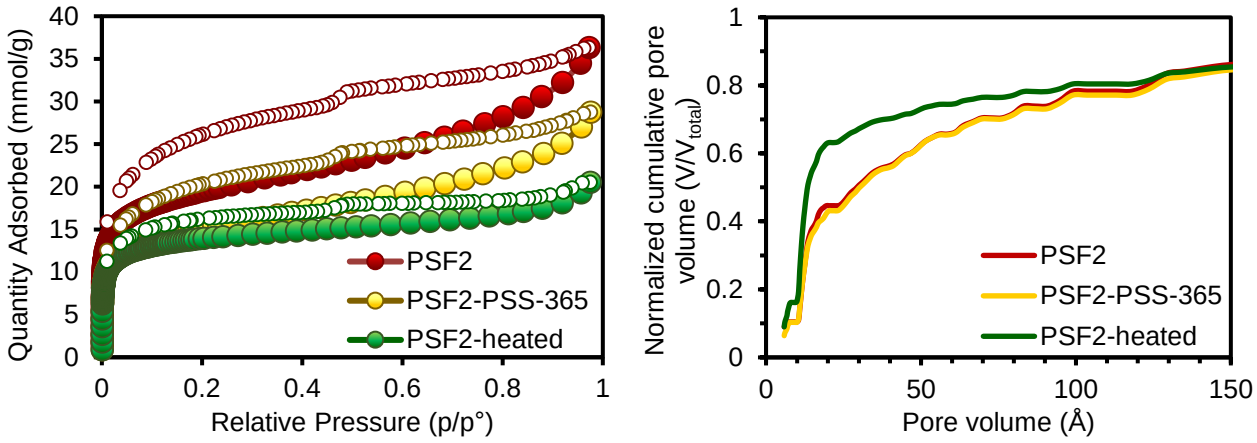

Figure 4.14. a) *N_2 adsorption/desorption isotherms and* ***b)*** *cumulative pore volume normalized over the total pore volume of* ***PSF2*** *(red traces),* ***PSF2-PSS-365*** *(yellow traces) and* ***PSF-heated*** *(green traces). Empty symbols represent the isotherms desorption branches.*

To undoubtedly demonstrate that temperature only is responsible for the evolution of the material and not the back-switching process, we treated a new aliquot of **PSF2** at 200 °C for 10 h and measured its surface area. As shown in Appendix 4 (**Figure A4.12**), the total pore volume of the heated material decreased from 1.19 to 0.82 cm^3/g, while microporosity increased to 61% from 45%. Since in this sample, switches were all in their stable state, then we can confirm that temperature only is responsible for the observed increased mesoporosity of **PSF2**

We then wondered if the reversible switch-induced modification of **PSF2** adsorption properties were observable now that the material was already been exposed to the high temperature curing. We then performed a second irradiation-heating cycle on **PSF2-heated** and measured the N_2 adsorption isotherm at 77 K after each treatment. Results of the second cycle are shown in **Figure 4.15.**

After irradiation with 365 nm light, total pore volume of **PSF2-PSS-365-2** decreased from 0.66 cm^3/g to 0.59 cm^3/g, a reduction of 12%. This result corroborates what we already observed after the first irradiation and strengthen the hypothesis that is the photoswitching process that is responsible for the variation in surface area. In fact, since we know for sure that heating changes the porosity of the framework, one might suppose that the first effect the we observed after the first irradiation was caused by the heat generated by irradiation itself. However, to produce the heat-induced framework modification we had to heat the sample at 200°C for a prolonged time, while, even after 12 hours of continuous irradiation, the sample was barely warm.

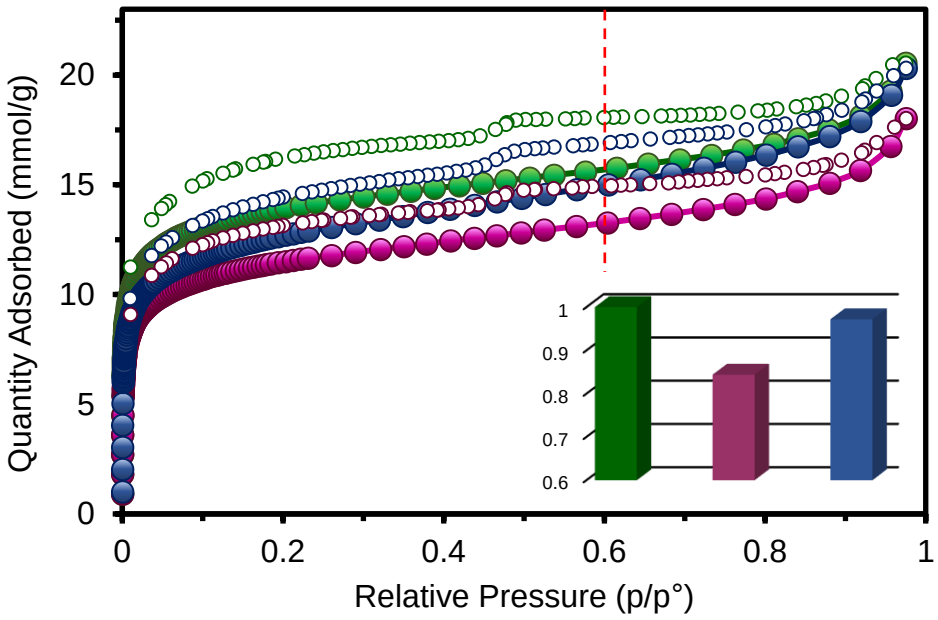

***Figure 4.15**. N_2 adsorption/desorption isotherms collected at 77 K for **PSF2-heated** (green trace), **PSF2-PSS-365-2** (purple trace), **PSF2-heated-2** (blue trace). Empty symbols represent desorption branches. The dashed red line intersects isotherms at $p/p^o = 0.6$. Inset: N_2 adsorbed quantities measured at $p/p^o = 0.6$ and normalized over the quantity adsorbed at this relative pressure by **PSF2-heated**.*

Furthermore, if heating and the consequent curing of the porous matrix is the only responsible for the variations in porosity, then, after the thermal treatment, the new irradiation at 365 nm should have caused no effect at all. Moreover, it can be observed that irradiation does not change isotherms shapes (**Figures 4.11 and 4.14**), while heating always cause observable changes (**Figures 4.13 and A4.13**).

PSF2-PSS-365-2 was then thermally treated to restore the stable state of photo-switches. This time, to avoid further modification of the structure, we heated at 160 °C for 15 h to obtain **PSF2-heated-2**. The N_2 adsorption isotherm of this sample (blue trace in **Figure 4.15**) shows almost no changes in shape and a considerable recover in adsorbed quantity, demonstrating that the available free volume of **PSF2** is fully dependent on the photo-switches state and that it can be reversibly decreased and increased.

*Table 5.5. N_2 adsorption parameters derived from adsorption/desorption isotherms collected at 77 K for **PSF2-heated**, **PSF2-PSS-365-2** and **PSF2-heated-2**.*

	S_{BET} (m^2/g)	V_{total}[a] (cm^3/g)	$Q_{ads}(p/p^o = 0.6)$ (mmol/g)	$\frac{Q_{PSF2\text{-}heated}(p/p^o = 0.6)}{Q_{ads}(p/p^o = 0.6)}$
PSF2-heated	1177	0.663	15.7	1
PSF2-PSS-365-2	963	0.585	13.3	0.844
PSF2-heated-2	1056	0.659	15.0	0.972

4.4.3 Conclusions

A new class of stimuli-responsive porous materials, Porous Switching Frameworks (PSFs) was designed and realized from co-polymerization reaction of tetraphenyl methane building blocks **2** and linear bistable molecular switches **1** utilizing Yamamoto cross-coupling reaction. Two materials were realized, **PSF1** and **PSF2**, employing different concentration of switch moieties. Both compounds revealed high specific surface areas (4000 and 1600 m^2/g, respectively) and thermal stability up to 300°C. The switching properties of **PSF2**, the sample with the highest switch concentration, were analyzed by Raman, UV/Vis and NMR spectroscopy. All the techniques showed reversible solid-state photoisomerization of active species upon irradiation with 365 and 470 nm light or heat. Furthermore, NMR spectroscopy allowed the precise quantification of the stable-to-metastable isomerization, which was determined to be 7/93 after 50 h of irradiation, indicating a very efficient process also in solid state. It is the first time that the photoisomerization of a molecular switch in a porous material is precisely quantified. Furthermore, it was demonstrated that the state of the switches influence adsorption properties. In particular, we showed that the formation of bulkier metastable state of molecular switches decrease the available free volume of the porous matrix with a consequent reduction in N_2 and CO_2 adsorbed quantities.
In future works, new strategies for the synthesis of porous materials containing bistable photoactive molecules will be developed employing different reactions schemes to expand the range of properties that could be controlled by switch states, thus increasing the possible applications of such materials.

4.3 Experimental Section

4.3.1. General Methods

N_2 adsorption/desorption isotherms were collected at liquid nitrogen temperature (77 K) and up to 1 bar of pressure by means of a Micromeritics ASAP 2020 HD analyzer. All samples were degassed by heating at 130°C for 5 hours under vacuum (approx. 10^{-3} mmHg) right before the analysis. Specific surface area values were calculated using the Brunauer, Emmett, and Teller (BET) model and the Langmuir model. Pore size distributions were calculated considering a slit pore geometry and the Non-Local Density Functional Theory (NLDFT). CO_2 adsorption/desorption isotherms were measured at 195, 273, 283 and 298 K up to 1 bar of pressure utilizing a Micromeritics ASAP 2020 HD analyzer. Samples were degassed at 130°C for 5 hours before each analysis. Isosteric heats of adsorption were calculated first by fitting CO_2 adsorption isotherms utilizing a dual-site Langmuir model, then by applying the van't Hoff equation to the calculated curves. Detailed description about the mathematical fitting process are given in Appendix 1.

Powder X-Ray Diffraction measurements were performed on Rigaku Miniflex 600 2θ-θ diffractometer equipped with a Cu-Kα tube (1.54059 Å). Acquisitions were performed in the 3-40 2θ angle range, with steps of 0.02° and speed of 1.5 s/step.

Differential Scanning Calorimetry (DSC) analyses were performed on a Mettler-Toledo StarE instrument from 25 to 300 °C with a heating rate of 10 °C/min under an 80 ml/min flux of nitrogen. ^{1}H and ^{13}C solution NMR were recorded at 400 MHz and 100 MHz, respectively, on a Varian Mercury Plus instrument in $CDCl_3$ or CD_2Cl_2. In the following, ^{1}H data are reported as follow: chemical shifts (in ppm and referenced to internal TMS), integration, multiplicity (s = singlet, d = doublet, dd = doublet of doublets, t = triplet, p = quintet, m = multiplet) and coupling constants (in Hz). ^{13}C data are reported as follow: chemical shifts (in ppm and referenced to internal TMS).

Thermogravimetric Analyses (TGA) were performed on a Mettler-Toledo DSC/TGA 1 StarE System from 0 to 800 °C at a 10°C/min heating rate under a 50 ml/min flux of air.

Irradiation experiments on compound **1** (IR, UV/Vis, Raman and NMR spectroscopy) and irradiation experiments on materials **PSF1** and **PSF2** for Uv/Vis, IR, and Raman solid-state spectroscopy were performed using Thorlabs LEDs (M365F1 for 365 nm light and M470F3 for 470 nm light).

Irradiation experiments for solid-state NMR and gas adsorption analyses were performed using a Spectroline ENF-20C/FE lamp (6W) for 365 nm irradiation and a home-made LED lamp built with 9 LEDs (3W each) for 470 nm irradiation. About 40 mg of sample were distributed over a petri dish (Ø = 4 cm) and mixed every 60 minutes with a spatula. The lamps were set at approximately 3 cm from the powder. Heat-promoted back-switching experiments were performed heating the sample at 200 °C or 160°C for 15 hours under vacuum by means of a Buchi B-585 glass oven.

IR spectroscopy (ATR method) was performed on a PerkinElmer FT-IR Nexus spectrometer over the range 400-4000 cm^{-1}. Compound **1**-stable was drop-casted from a 10^{-3} M solution in DCM directly over the ATR crystal. Compound **1**-metastable was obtained irradiating a 10^{-3} M solution with 365 nm light for 20 minutes, then the sample was drop-casted over the ATR crystal and analysed. **PSF1** and **PSF2** were irradiated while deposited over the ATR crystal, then spectra of **PSF1-PSS-365** and **PSF2-PSS-365** were collected.

Raman spectra were recorded using a Perkin Elmer Raman Station connected to a Olympus BX51M microscope equipped with a 785 nm 50 mW laser.

Diffuse Reflectance UV/Vis spectra were measured Jasco V-570 UV/Vis NIR spectrophotometer equipped with Jasco ISN-470 integrating sphere.

^{13}C solid-state NMR experiments were carried out with a Bruker Avance 300 instrument operating at a static field of 7.04 T equipped with high-power amplifiers (1kW) and a 4 mm double resonance MAS probe. The ramped-amplitude cross polarization experiments (^{13}C CP MAS) were performed at a spinning speed of 12.5

kHz using a contact time of 2 ms, a 90° pulse for proton of 2.9 μs and a recycle delay of 5 s. Spectral profiles, recorded with 30840 scans, were simulated by mixed Gaussian/Lorentzian line shapes in the ratio of 0.5:0.5. Quantitative ^{13}C single pulse (^{13}C SPE) MAS NMR experiments were performed at a spinning speed of 12.5 kHz with a recycle delay of 100 s and a 90° pulse of 3.6 μs length. Crystalline polyethylene was taken as an external reference at 32.8 ppm from TMS.

Chemicals and solvents were purchased by Sigma Aldrich or TCI and used without further purification, unless otherwise specified.

4.3.2. Synthesis of 3-(naphthalen-2-yl)-3-oxopropanoic acid (**5**)

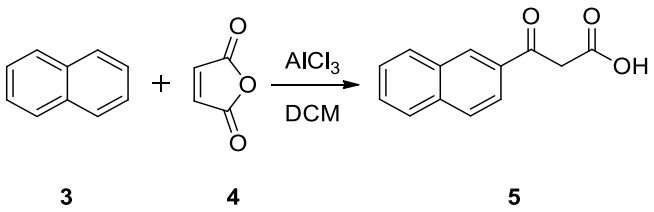

3 **4** **5**

In a 500 ml three-neck round-bottom flask equipped with a nitrogen inlet, naphthalene (**3**, 30 g, 0.23 mol) and succinic anhydride (**4**, 16 g. 0.16 mol) were transferred and three vacuum-nitrogen cycles were performed. Then, DCM (200 ml) was added; one of the neck was connected to a Drexel bottle filled with an aqueous NaOH solution. The mixture was stirred until complete dissolution of the solids. After that, the solution was cooled to 0 °C and $AlCl_3$ was added in portions every 30 minutes (5 g per portion, 0.037 mol) under vigorous stirring. A total of 41.7 g (0.31 mol) of $AlCl_3$ were used. At the end of the addition, the mixture was allowed to war to RT and it was stirred overnight under fluxing nitrogen. The next day, the mixture was poured into crushed ice and 150 ml of HCl (10% wt) were added. The white precipitated was filtered, washed with water and dried under vacuum. Then it was redissolved in hot ethanol and left to recrystallize to afford **5** as a crystalline white solid (10.8 g, 30% yield). ^1H-NMR ($CDCl_3$, ppm): 8.51 (1H, s), 8.03 (1H, d, J = 8.8 Hz), 7.96 (1H, d, J = 8.8 Hz), 7.89 (2H, m), 7.59 (2H, m), 3.47 (2H, t, J = 6.4 Hz), 2.88 (2H, t, J = 6.4 Hz).

4.3.3. Synthesis of 3-(naphthalen-2-yl)propanoic acid (**6**)

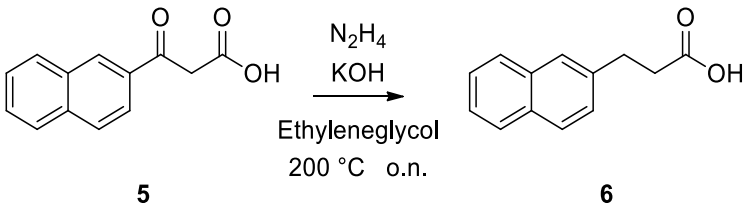

5 **6**

In a 250 ml round-bottom flask, **5** (10.4 g, 46 mmol), KOH (4.4 g, 78 mmol) and hydrazine monohydrate (4.3 ml, 57 mmol) were suspended in ethyleneglycol (60 ml). The temperature was raised to 200 °C and a clear yellow solution was obtained. After 2 hours, the reaction was cooled to RT and the water formed as a byproduct was removed by rotary evaporation. After that, the solution was heated again to 200 °C and left to react overnight. The color of the solution gradually changed from yellow to orange to red. The next day, the reaction was cooled to RT, quenched with HCl (1 M) and extracted with diethyl ether. The organic fractions were collected, dried over $MgSO_4$ and the solvent was removed by rotary evaporation.

The obtained yellow solid was recrystallized from benzene/hexane (1:2 v/v) to afford **6** as a yellowish crystalline solid (7 g, 72% yield). ^{1}H-NMR ($CDCl_3$, ppm): 7.79 (3H, m), 7.62 (1H, s), 7.44 (2H, m), 7.32 (1H, dd, J = 8.4 Hz; 1.2 Hz), 2.85 (2H, t, J = 7.4 Hz), 2.41 (2H, t, J = 7.4 Hz), 2.07 (2H, p, J = 7.6 Hz; 7.6 Hz).

4.3.4. Synthesis of 2,3-dihydrophenanthren-4(1H)-one (**7**)

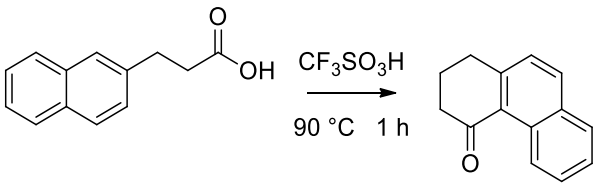

6 **7**

Trifluoromethanesulfonic acid (12 ml, 47 mmol) was transferred to a 50 ml round bottom flask and heated to 90 °C. Then **6** (2.85 g, 13.3 mmol) was added in one portion under vigorous stirring. After 1 h at 90 °C, the mixture was poured in crushed ice and the organics were extracted with diethyl ether. The organic layer was washed with a saturated $NaHCO_3$ solution, dried over $MgSO_4$ and dried by rotary evaporation. **7** was recovered as a brown oil that crystallized upon standing (2.02 g, 77 % yield). ^{1}H-NMR ($CDCl_3$, ppm): 9.40 (1H, d, J = 8.8 Hz), 7.91 (1H, d, J = 8.4 Hz), 7.80 (1H, d, J = 8 Hz), 7.63 (1H, t, J = 7.8 Hz), 7.49 (1H, t, J = 7.4 Hz), 7.31 (1H, d, J = 8.4 Hz), 3.13 (2H, t, J = 6.1 Hz), 2.79 (2H, t, J = 6.6 Hz), 2.20 (2H, p, J = 6.4 Hz).

4.3.5. Synthesis of 3-methyl-2,3-dihydrophenanthren-4(1H)-one (**8**)

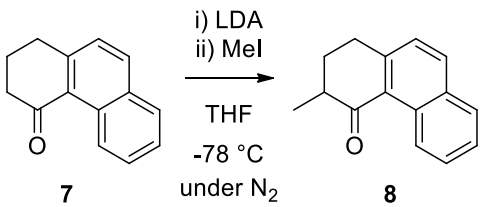

7 **8**

In a 100 ml round-bottom Schlenk flask, di-isopropylamine (2.8 ml, 20 mmol), was dissolved in dry THF (15 ml) under inert atmosphere. The solution was cooled to -78 °C and Buthyllithium (1.6M in hexane, 9.6 ml, 15.4 mmol) was added dropwise. The solution was left to react at -78 °C for 30 min. After that, a solution of

7 (2.01 g, 10.2 mmol) in dry THF (50 ml) was slowly added at -78 °C and the obtained solution was left to react for 60 min. Finally, methyl iodide (1.12 ml, 18 mmol) was added and the reaction was allowed to warm to RT. After 60 min at RT, the reaction was quenched with a saturated NH_4Cl solution and the organics were extracted with diethyl ether. The organic layers were combined, dried over $MgSO_4$ and evaporated to dryness. The crude product was purified by column chromatography (pentane/ethyl acetate 20:1) to afford **8** as a viscous liquid that crystallized overnight in the freezer (1.46 g, 68% yield). ^{1}H- NMR ($CDCl_3$, ppm): 9.35 (1H, d, J = 8.7 Hz), 7.90 (1H, d, J = 8.4), 7.80 (1H, d, J = 8.0 Hz), 7.61 (1H, m), 7.29 (1H, d, J = 8.4 Hz), 3.18 (2H, m), 2.77 (1H, m), 2.27 (1H, m), 1.99 (1H, m), 1.31 (3H, d, J = 8.6 Hz).

4.3.6. Synthesis of 2,3-dihydro-3-methyl-4(1*H*)-phenanthrenone hydrazine (**9**)

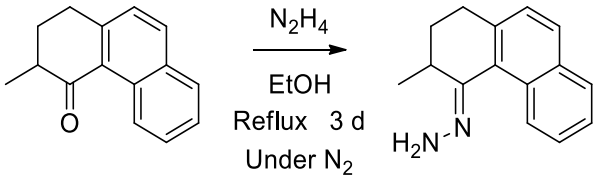

8 **9**

Under nitrogen atmosphere, starting material **8** (1.46 g, 6.9 mmol), was suspended in EtOH (30 ml). Then, hydrazine monohydrate (35 ml, 720 mmol) was added and the resulting mixture was heated to reflux for 3 days. After that, the solution was cooled to RT, the ethanol was removed by rotary evaporation and the organics were extracted with DCM. All the organic layers were collected, dried over $MgSO_4$ and evaporated to dryness.

The crude product was redissolved in hot hexane and pure **9** recrystallized as white crystals after cooling in the freezer overnight (680 mg, 44 % yield). ^{1}H-NMR ($CDCl_3$, ppm): 8.77 (1H, d J = 8.6 Hz), 7.78 (1H, d, J = 8.1), 7.70 (1H, d, J = 8.3 Hz), 7.49 (1H, t, J = 7.2 Hz), 7.41 (1H, t, J = 7.4 Hz), 7.24 (1H, d, J = 8.8 Hz), 4.11 (2H, s, very broad), 3.18 (1H, m), 2.82 (1H, m), 2.67 (1H, m), 2.31 (1H, m), 1.45 (1H, m), 1.27 (3H, d, J = 6.8 Hz).

4.3.7. Synthesis of diazo-compound **10**

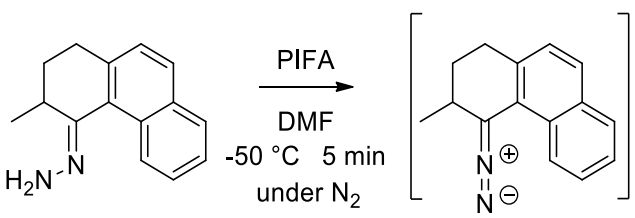

9 **10**

Compound **10** is highly unstable and it decompose rapidly at room temperature. Hence, it was prepared moments before being used in the Barton-Kellog coupling reaction with thioketone **12**. Under inert atmosphere, compound **9** (1 equivalent respect to thioketone **12**), was dissolved in dry DMF (10 ml). The solution was then cooled to -50 °C. Meanwhile, [Bis(trifluorocetoxy)iodo]benzene (PIFA, 1 eq.) was dissolved in dry DMF (5 ml) and slowly added to the cold solution of **9**. The solution quickly turned pink, indicating the formation of the diazo-compound **10.** At this point, the pink solution was added dropwise to thioketone **12** solution to complete the Barton-Kellog coupling (*vide infra*).

4.3.8. Synthesis of molecular switch **1**

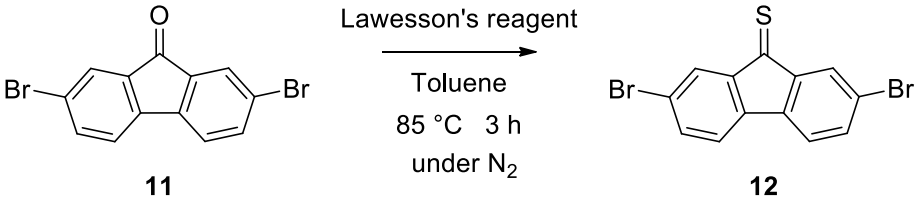

11 **12**

In a two-neck 250 ml round bottom flask equipped with a nitrogen inlet, compound **11** (400 mg, 1.18 mmol) was dissolved in dry toluene (35 ml) and Lawesson's reagent (950 mg, 2.36 mmol) was added in a single portion. The temperature was raised to 85 °C and the progress of the reaction was monitored by TLC (pentane/DCM 1:1). After about 3 hours, almost all starting material **11** was consumed. The mixture was then warmed to RT, filtered over a cotton plug, concentrated in vacuo and loaded on a silica column and flash chromatographed with pentane/DCM 5:1. The thioketone was recovered, dried by rotary evaporation and immediately used in the following step (204 mg, yield 51%)

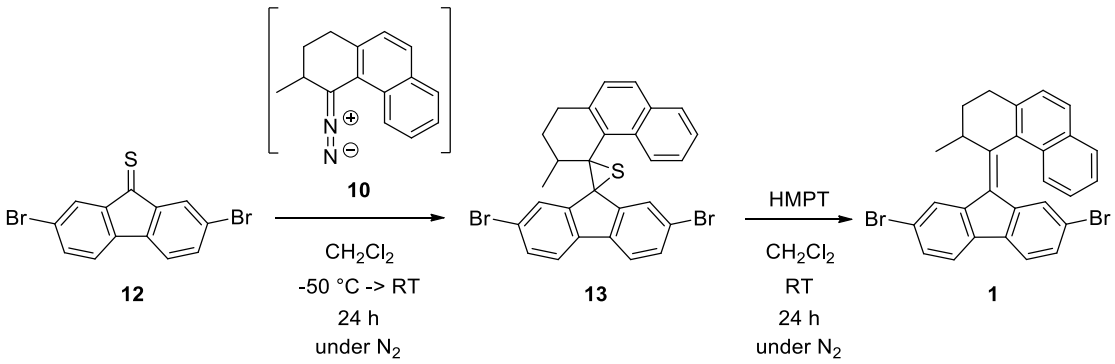

Compound **10** was prepared as previously described. The pink solution of **10** was added dropwise to a solution of **12** in CH_2Cl_2 at -50 °C. After the addition was completed, the solution was allowed to slowly warm to RT and kept at RT under nitrogen for 24 h. After that, HMPT (3 eq.) was added and the solution was kept at RT

under nitrogen for other 24 hours. Then, the obtained yellow solution was repeatedly washed with brine to remove the DMF. The organic fractions were collected, dried over $MgSO_4$ and evaporated to dryness. The obtained crude product was purified by column chromatography (eluent). The chromatographed product was further purified by recrystallization from DCM/heptane. **1** was recovered ad bright yellow crystals (244 mg, 40% yield). ^{1}H-NMR (CD_2Cl_2, ppm): 8.24 (1H, d, *J* = 1.3 Hz), 7.98 (1H, d, *J* = 8.3 Hz), 7.94 (1H, d, *J* = 8.2 Hz), 7.81 (1H, d, *J* = 8.6 Hz), 7.69 (1H , d, *J* = 8.1 Hz), 7.57 (1H, dd, *J* = 8.1, 1.7 Hz), 7.52 (2H, t, *J* = 7.9 Hz), 7.43 (1H, t, *J* = 7.1 Hz), 7.29 – 7.22 (1H, m), 7.20 (1H, dd, *J* = 8.1, 1.8 Hz,), 5.98 (1H, d, *J* = 1.8 Hz), 4.24 (1H, m), 2.84 (1H, m), 2.53 (2H, m), 1.29 (3H, d, *J* = 6.8 Hz), 1.23 (1H, m). ^{13}C-NMR (CD_2Cl_2, ppm): 150.84, 143.15, 142.18, 142.00, 141.08, 139.89, 134.94, 134.39, 133.95, 132.84, 132.22, 131.83, 131.00, 130.83, 130.43, 129.56, 128.54, 127.76, 126.95, 123.69, 123.55, 122.96, 122.74, 37.64, 33.13, 32.07, 22.99.

4.3.10. Synthesis of **2**

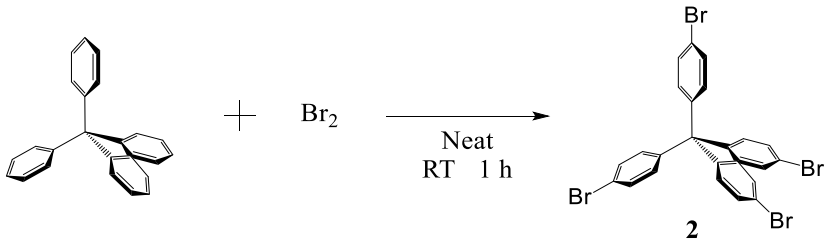

Tetrakis(4-bromophenyl)methane was synthesized according to the procedure published in J. Org. Chem., 69(5), 1524-1530, 2004.

Commercial tetraphenylmethane was further purified by sublimation at 180°C under vacuum before being used in this reaction. Br_2 (12.8 ml, 250 mmol) was transferred to a round-bottom 100 ml flask. Sublimed tetraphenylmethane (2g, 6.25 mmol was added in small portions under vigorous stirring. A white smoke (HBr) evolved from the reaction. The mixture was left at room temperature under stirring until no more white smoke was produced (approx. 60 minutes). Then, the mixture was cooled with an ice bath and EtOH (50 ml) was slowly added. A white precipitate formed. The mixture was then stirred at RT for 2 hours; after that, the excess of bromine was quenched with a saturated aqueous sodium bisulfite solution. The white solid was recovered by filtration, washed with abundant water and EtOH. The crude product was crystallized from $CHCl_3$/EtOH to afford pure **1** as white crystalline needles (3.2 g, 80% yield). ^{1}H-NMR ($CDCl_3$, ppm): 7.40 (8H, J = 6.0 Hz), 7.02 (8H, J = 6.0 Hz). ^{13}C-NMR ($CDCl_3$, ppm): 144.0, 132.1, 130.8, 120.6, 65.9.

4.3.11. Synthesis of **PSF1**

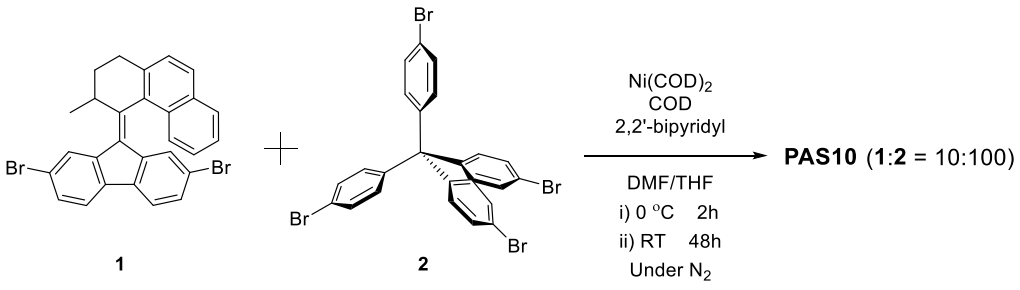

1 (32.4 mg, 0.063 mmol) and **2** (400 mg, 0.63 mmol) were transferred in an oven-dried 50 ml two-neck round-bottom flask. The flask was closed with a silicon septum and three vacuum-nitrogen cycles were performed. Then, dry THF (30 ml) was transferred by means of a syringe and the mixture was stirred at RT under N2 until complete dissolution of the solids. Meanwhile, inside a glovebox, $Ni(COD)_2$ (1 g, 3.64 mmol) and 2,2'-bipyridyl (570 mg, 3.65 mmol) were transferred to an oven-dried 250 ml three neck flask equipped with a nitrogen inlet. One of the necks was sealed with a silicon septum. The closed flask was brought outside the glovebox, covered with aluminium foil and quickly put under fluxing N_2. Then, dry DMF (90 ml), dry THF (20 ml) and cyclooctadiene (COD) (0.5 ml, 4.08 mmol) were added. The violet mixture was stirred at RT for a few seconds, before cooling it to 0 °C with an ice bath. As the mixture was cooling down, an oven-dried 50 ml pressure-equilibrating dropping funnel was mounted on the last neck of the flask, flushed with N_2 and finally sealed with a rubber septum. The solution of **1** and **2** was transferred to the dropping funnel by means of a syringe and added to the violet mixture over 15-20 minutes. At the end of the addition, the resulting mixture was stirred at 0 °C for additional 15 minutes, then it was allowed to cool at RT and left to react under N_2 for 48 h. After that, the flask was opened to air and diluted HCl was added (10 ml, 2.5% wt); the mixture was stirred at RT until it turned to a bright blue color. At this point, the suspended white solid was recovered by filtration and washed with THF (2 X 30 ml), water (3 X 30 ml), chloroform (2 X 30 ml) and acetone (2 X 30 ml). PSF1 was recovered as yellow powder (156 mg, 70 % yield).

4.3.12. Synthesis of **PSF2**

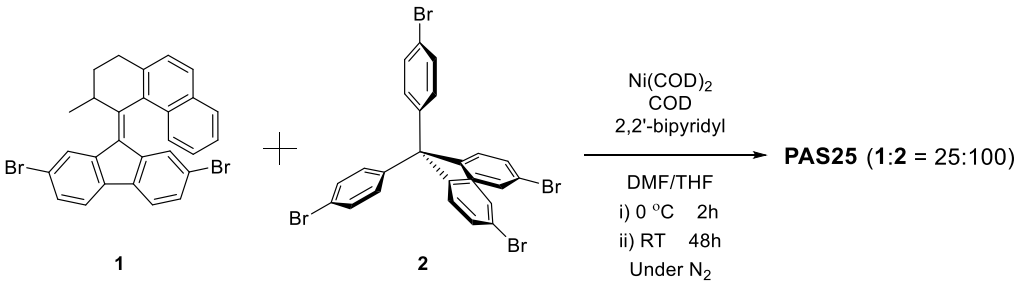

PSF2 was synthesized following the same procedure described for **PSF1**. The following quantities were used: **1** (75 mg, 0.145 mmol), **2** (370 mg, 0.581 mmol), $Ni(COD)_2$ (1g, 3.64 mmol), COD (0.5 ml, 4.08 mmol), 2,2'-bipyridyl (570 mg, 3.65 mmol), DMF (90 ml), THF (20+30 ml).

PSF2 was recovered as deep yellow powder (183.6 mg, 78%).

Bibliography for Chapter 4

1. Erbas-Cakmak, S., Leigh, D. A., McTernan, C. T. & Nussbaumer, A. L. Artificial Molecular Machines. *Chem. Rev.* **115,** 10081–10206 (2015).
2. Feringa, B. L. The Art of Building Small: From Molecular Switches to Motors (Nobel Lecture). *Angewandte Chemie - International Edition* **56,** 11060–11078 (2017).
3. Lecture, N. & Stoddart, J. F. *Sir J. Fraser Stoddart - Nobel Lecture: Mechanically Interlocked Molecules (MIMs) - Molecular Shuttles, Switches, and Machines*. (2016).
4. Sauvage, J.-P. Jean-Pierre Sauvage - Nobel Lecture: From Chemical Topology to Molecular Machines. *Nobel Lect.* 111–137 (2016).
5. Lund, K. *et al.* Molecular robots guided by prescriptive landscapes. *Nature* **465,** 206–209 (2010).
6. Su, T. A., Neupane, M., Steigerwald, M. L., Venkataraman, L. & Nuckolls, C. Chemical principles of single-molecule electronics. *Nature Reviews Materials* **1,** 16002 (2016).
7. Ariga, K., Li, J., Fei, J., Ji, Q. & Hill, J. P. Nanoarchitectonics for Dynamic Functional Materials from Atomic-/Molecular-Level Manipulation to Macroscopic Action. *Advanced Materials* **28,** 1251–1286 (2016).
8. Feringa, B. L. & Browne, W. R. *Molecular Switches*. *Molecular Switches* **1,** (Wiley-VCH, 2011).
9. Sauvage, J.-P. *et al. Molecular Machines and Motors*. (Springer, 2001).
10. Browne, W. R. & Feringa, B. L. Making molecular machines work. *Nat. Nanotechnol.* **1,** 25–35 (2006).
11. Klajn, R., Bishop, K. J. M. & Grzybowski, B. A. Light-controlled self-assembly of reversible and irreversible nanoparticle suprastructures. *Proc. Natl. Acad. Sci.* **104,** 10305–10309 (2007).
12. Gui, B. *et al.* Immobilizing Organic-Based Molecular Switches into Metal–Organic Frameworks: A Promising Strategy for Switching in Solid State. *Macromol. Rapid Commun.* **39,** 1–11 (2018).
13. Li, H. *et al.* A Robust Metal-Organic Framework for Dynamic Light-Induced Swing Adsorption of Carbon Dioxide. *Chem. - A Eur. J.* **22,** 11176–11179 (2016).
14. Tan, L. L. *et al.* Stimuli-responsive metal-organic frameworks gated by pillar[5]arene supramolecular switches. *Chem. Sci.* **6,** 1640–1644 (2015).
15. Islamoglu, T. *et al.* Postsynthetic Tuning of Metal-Organic Frameworks for Targeted Applications. *Acc. Chem. Res.* **50,** 805–813 (2017).
16. Karagiaridi, O., Bury, W., Mondloch, J. E., Hupp, J. T. & Farha, O. K. Solvent-assisted linker exchange: An alternative to the de novo synthesis of unattainable metal-organic frameworks. *Angewandte Chemie - International Edition* **53,** 4530–4540 (2014).
17. Deria, P. *et al.* MOF Functionalization via Solvent-Assisted Ligand Incorporation: Phosphonates vs Carboxylates. *Inorg. Chem* **54,** 7 (2015).
18. Ding, S. Y. & Wang, W. Covalent organic frameworks (COFs): From design to applications. *Chemical Society Reviews* **42,** 548–568 (2013).
19. Diercks, C. S. & Yaghi, O. M. The atom, the molecule, and the covalent organic framework. *Science* **355,** eaal1585 (2017).

20. Huang, N., Wang, P. & Jiang, D. Covalent organic frameworks: A materials platform for structural and functional designs. *Nature Reviews Materials* **1,** 16068 (2016).
21. Liu, C., Zhang, W., Zeng, Q. & Lei, S. A Photoresponsive Surface Covalent Organic Framework: Surface-Confined Synthesis, Isomerization, and Controlled Guest Capture and Release. *Chem. - A Eur. J.* **22,** 6768–6773 (2016).
22. Zhang, J. *et al.* A novel azobenzene covalent organic framework. *CrystEngComm* **16,** 6547–6551 (2014).
23. Das, S., Heasman, P., Ben, T. & Qiu, S. Porous Organic Materials: Strategic Design and Structure-Function Correlation. *Chemical Reviews* **117,** 1515–1563 (2017).
24. Schmidt, J., Werner, M. & Thomas, A. Conjugated microporous polymer networks via yamamoto polymerization. *Macromolecules* **42,** 4426–4429 (2009).
25. Pei, C., Ben, T. & Qiu, S. Great Prospects for PAF-1 and its derivatives. *Materials Horizons* **2,** 11–21 (2015).
26. Ben, T. *et al.* Targeted synthesis of a porous aromatic framework with high stability and exceptionally high surface area. *Angew. Chemie - Int. Ed.* **48,** 9457–9460 (2009).
27. Xiang, Z. *et al.* Systematic Tuning and Multifunctionalization of Covalent Organic Polymers for Enhanced Carbon Capture. *J. Am. Chem. Soc.* **137,** 13301–13307 (2015).
28. Fischer, S. *et al.* Cationic microporous polymer networks by polymerisation of weakly coordinating cations with CO2-storage ability. *J. Mater. Chem. A* **2,** 11825–11829 (2014).
29. Koumura, N., Geertsema, E. M., Van Gelder, M. B., Meetsma, A. & Feringa, B. L. Second Generation Light-Driven Molecular Motors. Unidirectional Rotation Controlled by a Single Stereogenic Center with Near-Perfect Photoequilibria and Acceleration of the Speed of Rotation by Structural Modification. (2002). doi:10.1021/ja012499i
30. Van Leeuwen, T., Danowski, W., Otten, E., Wezenberg, S. J. & Feringa, B. L. Asymmetric Synthesis of Second-Generation Light-Driven Molecular Motors. *J. Org. Chem.* **82,** 5027–5033 (2017).
31. Vicario, J., Meetsma, A. & Feringa, B. L. Controlling the speed of rotation in molecular motors. Dramatic acceleration of the rotary motion by structural modification. *Chem. Commun.* 5910–5912 (2005). doi:10.1039/b507264f

5. Chapter 5

Asymmetrically fluorinated organic porous matrices for CO_2 and CH_4 adsorption and separation and dipolar rotors dynamic studies.

5.1 Introduction

Scientific literature is rich of examples of functionalized porous materials for advanced applications, ranging from catalysis, to electronics, to bio-medical[1–4]. Chapter 2, 3 and 4 we discussed special utilization of porous materials. Nonetheless, the most common application for porous matrices is still gas adsorption and separation. This area of research is mainly fuelled by the concerns regarding atmospheric pollution and climate change[5]. We know that carbon dioxide is the main responsible for the temperature increase registered in the last few decades[6] and it is also involved in other serious environmental problematics, such as the augmented acidity of oceans[7]. One of the most promising strategies to reduce CO_2 concentration in the atmosphere, apart from switching to more environmentally friendly technologies, is, indeed, its capture and storage utilizing porous materials specifically engineered for the task[8]. Furthermore, a golden candidate for the replacement of petroleum as fuel source is methane, another gas. Thus, there is a strong interest around the synthesis of porous materials able to efficiently adsorb, separate and store these guests. Metal-Organic Frameworks (MOFs)[9,10] and Covalent Organic Frameworks (COFs)[11–13] have emerged as versatile platforms for gas storage. They are microporous material with high surface area accessible volume values. The main difference between them regard their chemical nature, as MOFs are hybrid organic-inorganic materials based on the ligand-to-metal coordinative bond, while COFs are fully organic materials built on strong covalent bonds. The success of both these classes of material in CO_2 and CH_4 storage is due to the high tunability of pore size. Since the targeted guest are small molecules, micropores are more apt to capture them thanks to a *molecular sieve* effect[14]. Additionally, host-guest interactions may be enhanced by insertion of functional groups[15]. Fluorination[16–18] is one of the most promising strategies to increase the host matrix affinity towards the two target gases thanks to a double effect: the slightly bigger dimension of fluorine compared to hydrogen should decrease pore size and thus enhance the sieve effect of the fluorinated matrix compared to the non-fluorinated analogue. Furthermore, fluorine is the element with the highest electronegativity of the periodic table and thus it generates an electric dipole moment when bonded to carbon atoms. This dipole is expected to favourably interact with target guest because of dipole- induced dipole (methane)[19] or dipole-quadrupole (carbon dioxide)[20] interactions. Although these promising perspectives, the synthesis of fluorinated MOFs and COFs for gas storage is still a highly unexplored field and, thus, the real effect of fluorination towards gas adsorption is still unclear[21]. The main reason behind this uncertainty is the lack of data on materials with similar structure, but different fluorine content.

In chapter 3 of this thesis, we dealt with the synthesis and characterization of two new fluorinated MOFs and we compared their adsorption properties with those of their isostructural non-fluorinated analogues. In this Chapter, we decided to deal with the design and synthesis of four new fluorinated fully organic COFs. The CO_2 and CH_4 adsorption properties of these new materials were tested and results compared to similar non-fluorinated and fluorinated COFs reported in literature to help to shed light on the role of fluorine in carbon dioxide and methane capture.

Furthermore, all the new four fluorinated materials were designed in such a way that fluorination would produce an asymmetry in the electric charge distribution across *p*-phenylene rings. As discussed in the introduction of this thesis, this method is often exploited to introduce fast dipolar rotors in solid porous matrices. Because of this, a side project regarding the characterization of the dynamics of the fluorinated materials is currently ongoing.

5.2 Design and synthesis of the fluorinated porous frameworks

To prepare robust, fully organic, covalent porous frameworks bearing fluorinated *p*-phenyl rings four different strategies were identified (**Scheme 5.1**). The first one employed the Sonogashira[22] protocol to create an extended ABAB type copolymer network between the tetrahedral tetrakis(4-bromophenyl)methane (**1**) and a bifunctional linear monomer bearing a phenylene ring with two terminal alkyne functionalities and one or two fluorine substituents (1,4-diethynil-2-fluoro-benzene (**2**) or 1,4-diethynil-2,3-difluoro-benzene (**3**)). Molecules **1** and **2** were synthesized following published procedures. Due to their chemical similarity, compound **3** was obtained through the same protocol employed for **2**, despite a different procedure is reported in literature. The detailed synthesis conditions are described in the Experimental Section. In this approach towards fluorinated porous materials, the tetrahedral building block (**1**) was chosen to form the tridimensional network and to enhance the porosity of the final material; since it repeatedly proved to be an efficient synthon in porous materials preparation[23]. The linear bifunctional monomers (**2** or **3**) bear fluorine substituents. Alkyne functionalities were chosen as bridging groups between tetrahedral and linear building block since we are eventually interested in the study of solid state dynamics of these *p*-phenyl rings and it is known that activation barriers for the rotation of the *p*-phenyl ring around a C(sp^2)-C(sp) bond are generally low[24,25]. Thus, pivoting *para*-phenylene rotors between triple bonds could possibly allow dipolar rotor **2** and **3** to explore fast rotating dynamics. Adopting the aforementioned methodology, materials named **1FCOP** (building blocks **1**+**2**) and **2FCOP** (building blocks **1**+**3**) have been synthesized. The presence of two adjacent fluorine atoms on the rotors of **2FCOP** provides a stronger net electric dipole moment across the phenyl ring, which, in turn, could translate into stronger dipole-dipole and dipole-external electric field interactions in the final material. Furthermore, comparing adsorption properties of **1FCOP** and **2FCOP** with the already published **MOP-1** (non-fluorinated analogue) and **F-MOP1**[16] (which is analogous to **1FCOP**, but with 1,4-diethylnyl-2,3,5,6-tetrafluorobenzene as linear monomer) it will possible to shed light on the role of fluorine on CO_2 and CH_4 adsorption.

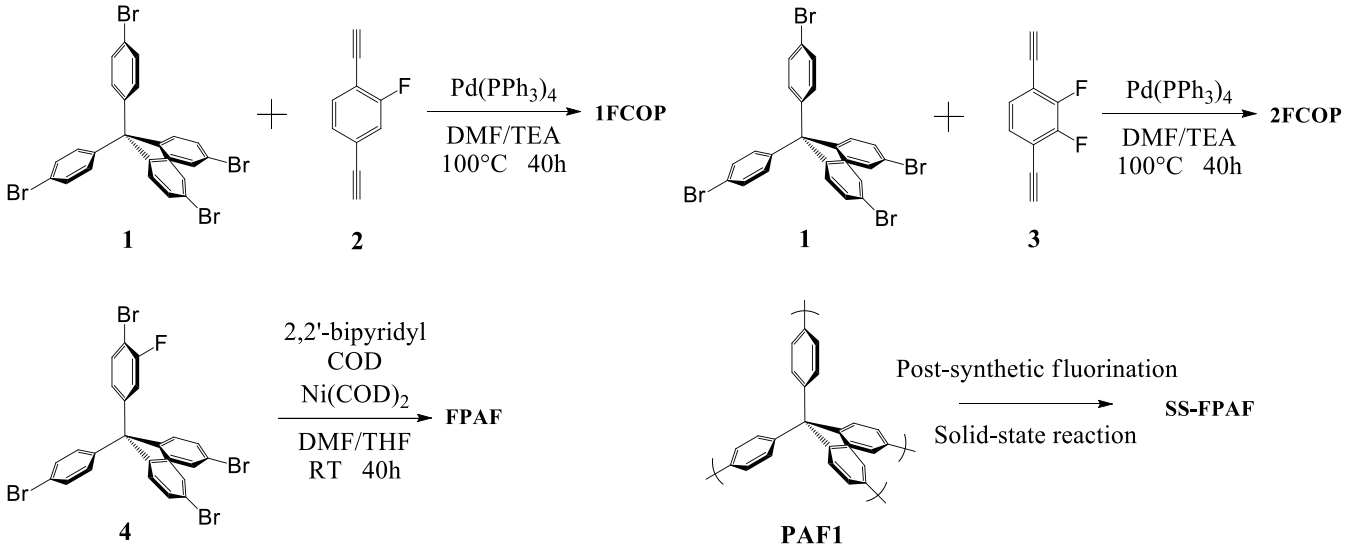

*Scheme 5.1. Synthetic strategies adopted for the preparation of **1FCOP, 2FCOP, FPAF** and **SS-FPAF**. The detailed procedures are reported in the experimental section.*

The second strategy employed for the preparation of fluorinated organic porous materials was based on homopolymerization through Ullmann-type Yamamoto carbon-carbon coupling reaction[26] of 4,4',4''-((4-bromo-3-fluorophenyl)methantryl)tris(bromobenzene) (**4**) to prepare **FPAF**. This approach was derived from the work of Teng Ben[27] and Hong-Cai Zhou[28] on the synthesis of Porous Aromatic Frameworks (PAFs). The so called **PAF1** is a fully organic porous material obtained through homopolymerization of tetrakis(4-bromophenyl)methane utilizing Yamamoto coupling; **PAF1** shows extremely high surface area values (up to 5600 m^2/g), and high thermal and chemical stability. After their pioneering work, many other polyaromatic monomers were successfully polymerized to obtain high surface area materials, some of them bearing perfluorinated *p*-phenyl rings as bridging groups (see Appendix 5, **Table A5.3**). However, to the best of our knowledge, fluorine substituents have never been introduced directly on the aromatic rings of a tetraphenylmethane building block. Furthermore, Comotti and coworkers previously demonstrated that *p*-phenyl rings in **PAF3** structure can undergo ultra-fast rotation around their 1,4-axis and behave as molecular rotors[29]. To prepare a novel fluorinated PAF material possessing reorientable dipoles possibly able to undergo fast dynamics in solid state, compound **4** was designed: the tetrahedral geometry of the tetraphenylmethane building unit was exploited to guaranteed high free volume to the final material, while the fluorine substituent on one of the four phenyl rings in a *meta* position respect to the central quaternary carbon atom generates the aforementioned electric dipoles. The synthetic route to prepare **4** is showed in **Scheme 5.2**; the detailed reaction conditions are given in the Experimental Section.

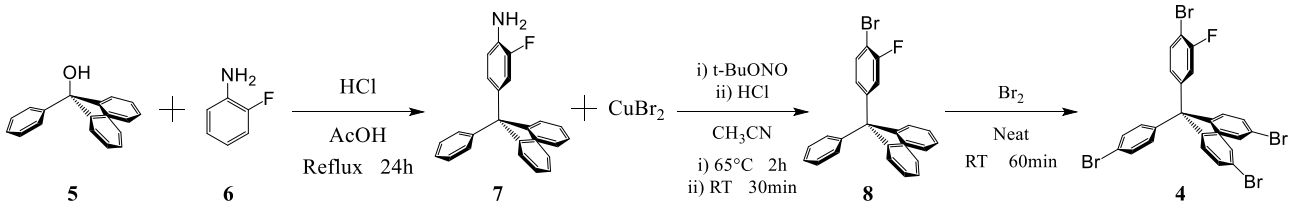

*Scheme 5.2. Synthetic route followed to prepare compound **4**. The detailed procedures are reported in the experimental section.*

Synthesis of **4** starts with the electrophilic attack of **5** on the 4-position (*para* to the amine group) of **6**. The carbocation is generated on the aliphatic carbon atom of **5** by the acidic conditions and the position of the attack on **6** is determined by the amine group. After that, the amino group is converted in a diazo group by oxidation with t-BuONO and then exchanged with a bromine group in a Sandmeyer reaction with $CuBr_2$. Finally, the *para*-position of the three unfunctionalized aromatic rings are brominated with elemental bromine adopting the same strategy used in bromination of tetraphenylmethane.

In the first part of the results discussion, **1FCOP**, **2FCOP** and **FPAF** characterization will be presented.

Finally, the third approach is closely related to the second as the reference material is again **PAF1**. In this case, however, a post-synthetic functionalization protocol of pristine **PAF1** was designed to introduce fluorine atoms on the solid network through Sandmeyer reaction to obtain **SS-FPAF**. The first two steps of this methodology followed the work of Zhang and co-workers[30], who nitrated pristine **PAF1** with HNO_3 in acetic anhydride followed by reduction of nitro groups to amino groups with $SnCl_2$. Then, amino groups were reacted with $NaNO_2$ to form a diazonium salt with $(BF_4)^-$ as counter anion, which was eventually thermally decomposed to get for the first time a post-synthesis fluorinated matrix. The main advantages of this strategy are its simplicity from a synthetic point of view (no complex reactions are involved, and filtration is the only workup required), the reduced time necessary to obtain the final product and the need of commercial and low-cost reagents. The main drawbacks, however, are the lack of control over both the extent of reaction and the position of the fluorine atoms on the phenyl rings of the final fluorinated material. In the second part of results discussion, the synthesis of **SS-FPAF** will be discussed in detail and the adsorption properties of **FPAF** and **SS-FPAF** will be compared to determine how the two different preparation protocols influence the gas adsorption properties of the final materials.

All the four materials were obtained in good to high yields as amorphous powders insoluble in all common solvents. Powder X-Ray diffraction patterns proving the lack of long-range order are showed in Appendix 5.

5.3 Characterization of the fluorinated porous frameworks

To evaluate the chemical structure of the fluorinated frameworks, solid-state NMR experiments were collected on the **1FCOP, 2FCOP** and **FPAF**. In **Figure 5.1** solid-state CP/MAS ^{13}C-NMR experiments collected at room temperature with a 2 ms delay time are reported.

All three spectra present considerable line broadening, as expected from the absence of both short- and long-range order in the frameworks. Signals assignament was deduced starting from solution ^{13}C-NMR spectra of the starting materials and of other similar compounds known in literature. In **1FCOP** and **FPAF** spectra is clearly visible around 160 ppm the characteristic signal of the C-F group, thus confirming the presence of fluorine moieties in the final materials. On the other hand, in **2FCOP** spectrum the C-F signal falls around 153 ppm and is covered by the aromatic region. This agrees with the solution ^{13}C spectrum, where the C-F signal is observed at 150 ppm. The parallel between solution and solid-state confirms the identity of **2FCOP.**

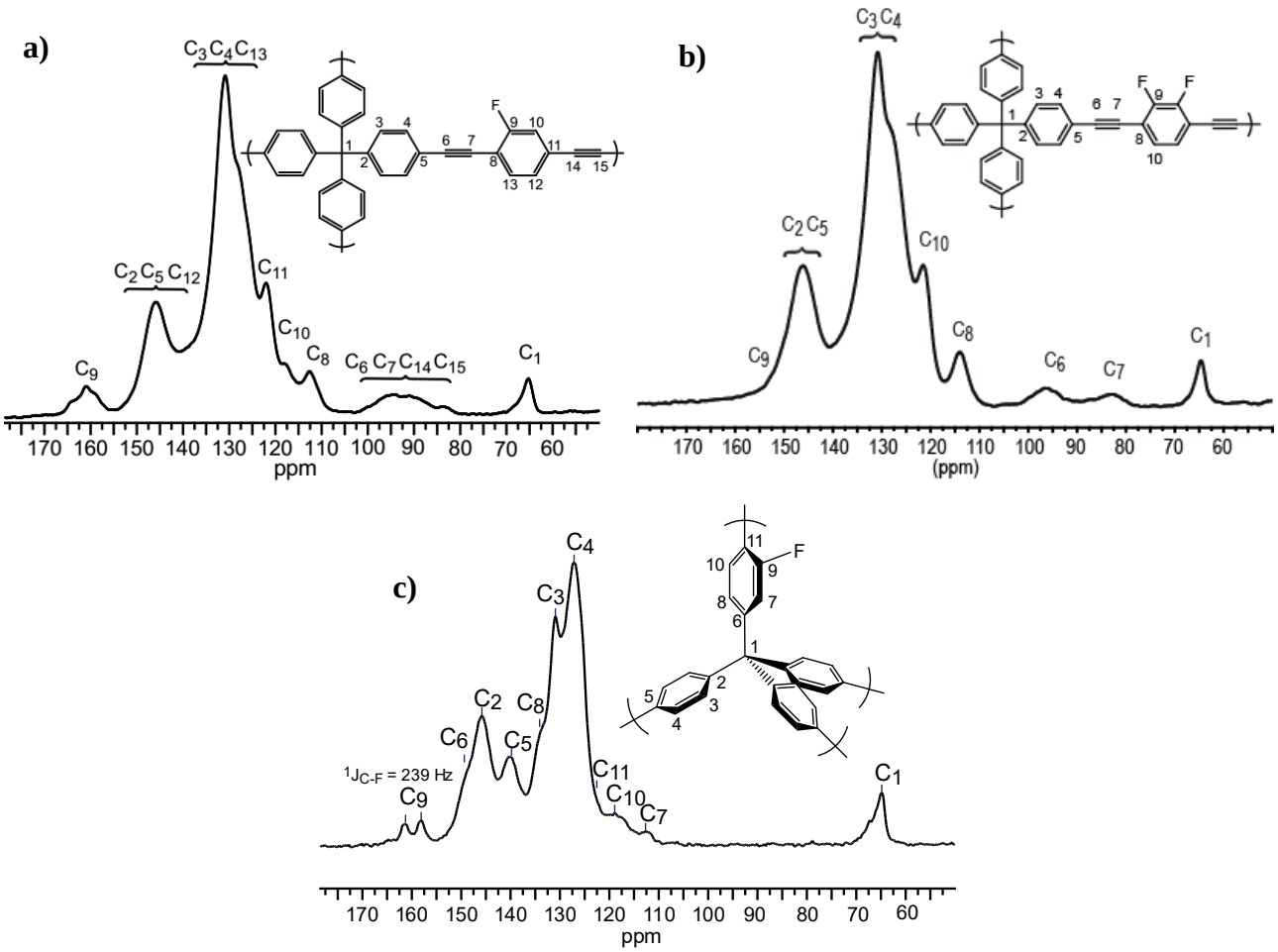

*Figure 5.1. Solid state ^{13}C CP/MAS NMR spectra of **a) 1FCOP**; **b) 2FCOP**; **c) FPAF** collected at room temperature with a delay time of 2 ms.*

Another common feature of the spectra are the signals arising from the tetraphenylmethane building blocks, especially regarding the quaternary aliphatic carbon which always falls around 65 ppm, with only small variations between different materials

To demonstrate the high thermal stability of the fluorinated covalent frameworks, DSC and TG analyses were performed. The results are shown in Appendix 5, **Figure A5.1** and **A5.2**. DSC traces indicate that any relevant thermal phenomenon occurs up to 400 °C, while TGA curves show that **1FCOP** and **2FCOP** have similar stability and that a minor weight loss starts around 340 °C. At 400 °C both materials have lost about 5% of their weight and after that thermal decomposition occurs. **FPAF** and **SS-FPAF** thermograms are similar and show a small weight loss in the range 200-400 °C, reaching about 90% at 400°C. After 400°C, complete thermal decomposition occurs. All TGA traces end at 0 residual weight, as expected from fully organic materials. The high thermal stability of the frameworks is ascribable to the fully covalent bond network that constitutes them.

Next, to evaluate the porosity of the four materials, nitrogen adsorption/desorption isotherms were collected at 77 K. The results are shown in **Figure 5.2**. The main parameters derived from isotherms analysis are reported in **Table 5.1**.

1FCOP and **2FCOP** have type I isotherms characteristic of microporous frameworks and they show almost no hysteresis in the desorption branch, indicating a narrow pore size distribution. **FPAF** exhibits a type IV isotherm meaning that the material possesses considerable mesoporosity, in addition to microporosity. It also shows important hysteresis in the desorption curve, as expected from a type IV isotherm. A similar behavior in a PAF-like material was observed by J. Hupp and coworkers[31] who synthesized **PAF-CH$_3$** through homopolymerization of a building block having a substituent in the same position of the fluorine atom in **4**. In their case the substituent was a -CH_3 group and they observed a type IV nitrogen isotherm with considerable hysteresis. Considering these observations, it may be hypothesized that the presence of a substituent next to the reactive bromine generates a difference in the reactivity of this bromine atom respect to the other three. This, in turn, would lead to an anisotropic growth of the polymer particle during the polymerization which would eventually result in mesoporosity formation when particles start to coalescence.

The conclusions drawn from the isotherm are confirmed by the total pore volume, V_{total}, and the micropore volume, V_{micro}, calculated using Non-Local Density Functional Theory (NLDFT) adopting the N_2@carbon slit pore model. Pore size distribution graphs are show in Appendix 5, **Figure A5.9**.

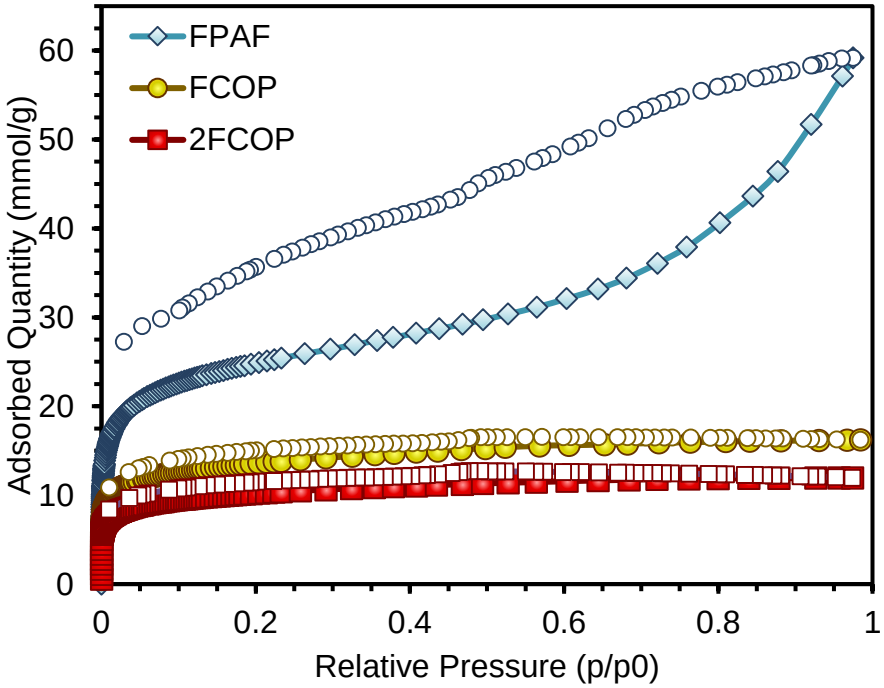

*Figure 5. 2. Adsorption/desorption N_2 isotherms collected at 77 K for **FPAF** (blue trace), **1FCOP** (yellow trace) and **2FCOP** (red trace). Empty symbols represent the desorption curve.*

Table 5.1 summarize porosity parameters of the three material as derived from N_2 isotherms. **FPAF** has the lowest V_{micro}/V_{total} value of the series, equal to 32%, meaning that mesoporosity contributes heavily on the material's adsorption properties, while micropores are dominant in both **1FCOP** (78%) and **2FCOP** (79%).

*Table 5.1. Textural parameters of **1FCop**, **2FCop**, and **FPAF** as derived from N2 adsorption isotherms at 77 K.*

	S_{BET} (m^2/g)	$S_{Langmuir}$ (m^2/g)	V_{total}[a] (cm^3/g)	V_{micro}[b] (cm^3/g)	V_{micro}/V_{total} (%)	Dominant pore [a,c] (Å)
1FCop	1132	1285	0.51[a]	0.40	78	6 (12)
2FCop	853	970	0.38[a]	0.30	79	<6 (12)
1FPAF	2054	2338	1.96[a]	0.63	32	12

[a] calculated using Original Density Functional Theory and the N_2@carbon slit pore model

[b] calculated considering the cumulative pore volume up to pore 20 Å wide

[c] highest peak in pore size distribution graphs is reported; second highest peak (if relevant) is reported in brackets

It is interesting to note that all the materials show very similar dominant pore diameters, the difference being only in their relative occurrence in the pore size distribution calculations (See Appendix 5, **Figure A5.9**). This observation can be justified considering that all four networks are built using tetrahedral tetraphenylmethane building blocks to construct the three-dimensional porous network. Since these tetrahedrons have very similar

dimensions, it is reasonable that linking them at corners to build an infinite framework can produce only certain pore diameters. The reduced pore size of **1FCOP** and **2FCOP** may be ascribable to an interpenetration phenomenon. Notably, **FPAF**, the material in which mesoporosity plays the bigger role, is the only one that does not have significant pore contributions below 12 Å.

BET and Langmuir models were applied to nitrogen isotherms at 77 K to calculate surface area values. **FPAF** has the highest surface area value among the four materials, 2054 m^2/g with BET model, one of the highest reported in the field of fluorinated covalent frameworks, as it can be observed in the comparison reported in **Table A5.3**. **1FCOP** and **2FCOP** show surface area values similar to those of other analogous fluorinated porous materials obtained through Sonogashira coupling reported in literature.

There is an open debate in porous materials community whether fluorinated porous frameworks are more efficient towards carbon dioxide and methane adsorption respect to the non-fluorinated analogues or not. Fluorination is expected to be beneficial towards adsorption of polarizable species because of the electrostatic interactions that the highly electronegative fluorine atoms should establish with the quadrupolar electric moment of CO_2 molecules. However, it is at the moment unclear to what extent fluorine plays a role. Some researchers hypothesize that the increased adsorption capacity of fluorinated material is attributable to the reduced pore dimensions and to the consequent *molecular sieve* effect[21]. Our series of fluorinated material could be compared with their non-fluorinated analogues to help shed light on the topic.

For these reasons, the new fluorinated matrices were tested for carbon dioxide and methane adsorption. CO_2 adsorption/desorption isotherms were collected at 195 K up to 1 bar of pressure (**Figure 5.3**) and at 273, 283, 298 K up to 10 bar (**Figure 5.4**). CH_4 isotherms were collected at 273, 283 and 298 K up to 10 bar to evaluate the low pressure methane adsorption of these materials. To calculate CO_2/N_2 selectivity applying the IAST theory, N_2 adsorption/desorption isotherms at 273, 283 and 298 K up to 10 bar were collected. In **Table 5.2** the main parameters derived from CO_2 and CH_4 isotherms are reported.

Due to its higher surface area, **FPAF** shows the highest CO_2 uptake at each temperature; its 195 K isotherm displays a significant increase in adsorbed compared, **1FCOP** and **2FCOP** curves. This is due to the higher mesoporous character of the former respect to the other three materials, which are more microporous. Notably, **FPAF** is able to adsorb more than its weight of CO_2 at 195 K, reaching 26.3 mmol/g, which corresponds to the 115% of its weight.

However, the maximum adsorption capacity of a material is directly dependent on its surface area and gives little information about its affinity towards a particular gas. In many applications, one is interested in the low-pressure adsorption capacity of the material; this depends on the strength of the interaction between the host matrix and the gaseous guest, which can be expressed as its isosteric heat of adsorption, Q_{st}. For this reason, isosteric heat of adsorption for CO_2 has been calculated for the four materials. High $Q_{st}(CO_2)$ values at low coverage value are very important in applications that require selective CO_2 uptake at ambient conditions. The detailed method adopted to calculate this value is reported in Appendix 5.

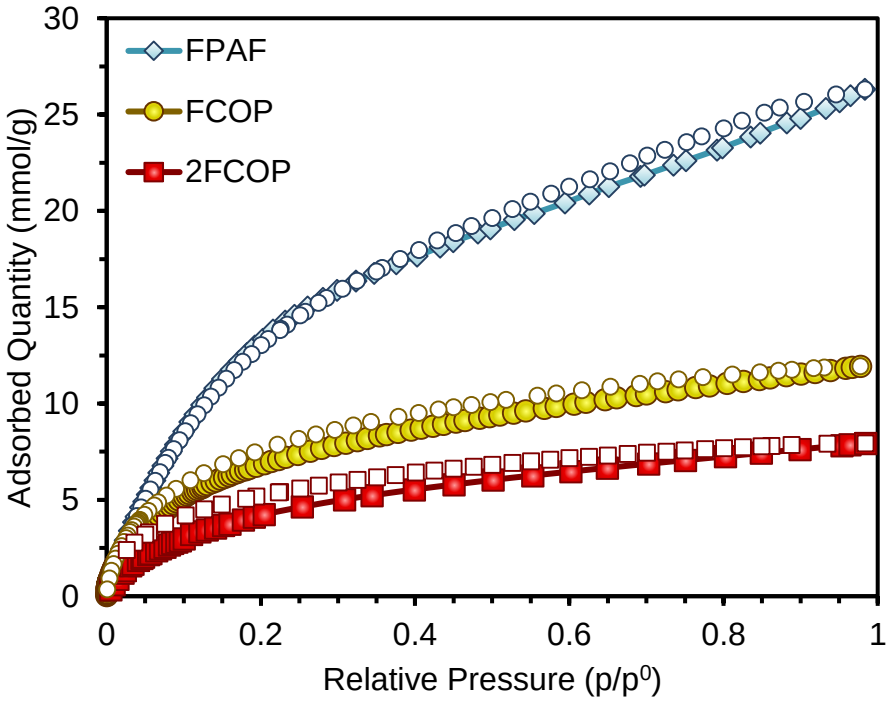

*Figure 5.3. CO_2 adsorption isotherms collected at 195 K up to 1 bar of pressure for **FPAF** (blue diamonds), **SS-FPAF** (green triangles), **1FCOP** (yellow circles) and **2FCOP** (red squares). Empty symbols represent desorption branches.*

1FCOP and **2FCOP** have good $Q_{st}(CO_2)$ values, about 28 kJ/mol, indicating favorable interactions with CO_2 molecules. These values are to be compared with the reported parameters of the unfluorinated (**MOP-1**) and the tetra-fluoro (**F-MOP-1**) analogue of **1FCOP** and **2FCOP** (see Appendix 5, **Table A5.3**). **MOP-1** heat of adsorption was calculated to be 26 kJ/mol, while 34 kJ/mol was found for **F-MOP-1**. Similarly, CO_2 uptake at 1 bar at 273 K and 298 K increases along the series **MOP-1** < **1FCOP** < **F-MOP-1**. According to these data, fluorination does have a positive role in CO_2 capture and an increase in the fluorine content of a material is correlated with an increase in $Q_{st}(CO_2)$ and uptake. However, these parameters are not linearly dependent. In fact, no significant difference can be found between CO_2 adsorption capacities of **1FCOP** and **2FCOP**: they have almost identical $Q_{st}(CO_2)$ values and the differences observed in CO_2 uptake can be related to the different total pore volume of the two materials. Hence, we might say that increasing the fluorine content of a porous material is generally beneficial towards its CO_2 adsorption capacities, although no simple predictions can be made about the extent of this improvement.

*Table 5.2. CO_2 adsorption capacities of **1FCOP**, **2FCOP**, **FPAF** and **SS-FPAF** at 195, 273, 283 and 298 K*

	T (K)	P (bar)	Q_{ads} (mmol/g)	Wt %	Q_{ads}(1 bar) (mmol/g)	Wt (1 bar) %	Q_{st} (CO_2)[a] (kJ/mol)	Selectivity[b] CO_2/N_2
1FCOP	195	1	11.9	52.0	/		28.4	/
	273	10	8.3	36.5	2.4	10.6	/	28
	283	10	7.0	30.4	1.8	7.9	/	/
	298	10	5.7	25.1	1.3	5.7	/	19
2FCOP	195	1	7.9	34.8	/	/	27.9	/
	273	10	5.7	25.1	1.8	7.9	/	40
	283	10	4.9	21.6	1.4	6.2	/	/
	298	10	3.9	17.2	1.0	4.4	/	23
FPAF	195	1	26.3	115	/		23.9	/
	273	10	14.4	63	2.7	11.9	/	14
	283	10	12.0	52.8	2.0	8.8	/	/
	298	10	8.6	37.6	1.4	6.2	/	11

[a] Calculated at 0.01 mmol applying the Clausius-Clapeyron

[b] Low pressure value (0.1 bar) calculated applying the IAST theory to a 15:85 CO_2/N_2 gas mixture

The calculated $Q_{st}(CO_2)$ value for **FPAF** is 23.9 kJ/mol, which is to be compared with the 15.6 kJ/mol reported for **PAF1**. Similarly, the reported CO_2 uptake of **PAF1** at 273 K and 1 bar is 9.1% which is significantly lower than the 11.9% measured for **FPAF**. These data support what we previously observed in the copolymers series: fluorination enhance CO_2 capture, although it is hard to predict to what extent.

For example, the fluorine content of **1FCOP** and **FPAF** is similar (6.24 %wt and 5.61 %wt, respectively), but $Q_{st}(CO_2)$ increase is 53% for **FPAF** and of only 9.2% for **1FCOP** respect to their non-fluorinated analogues (**PAF1** and **MOP-1**, respectively). This is most probably caused by the additional effect of pore size: it is known that micropores perform better towards CO_2 adsorption thanks to a *molecular sieve* effect. **MOP-1** possesses smaller pores compared to **PAF1**, hence its affinity towards CO_2 is already high thanks to well suited pore size and fluorination has a smaller influence compared to **PAF1**.

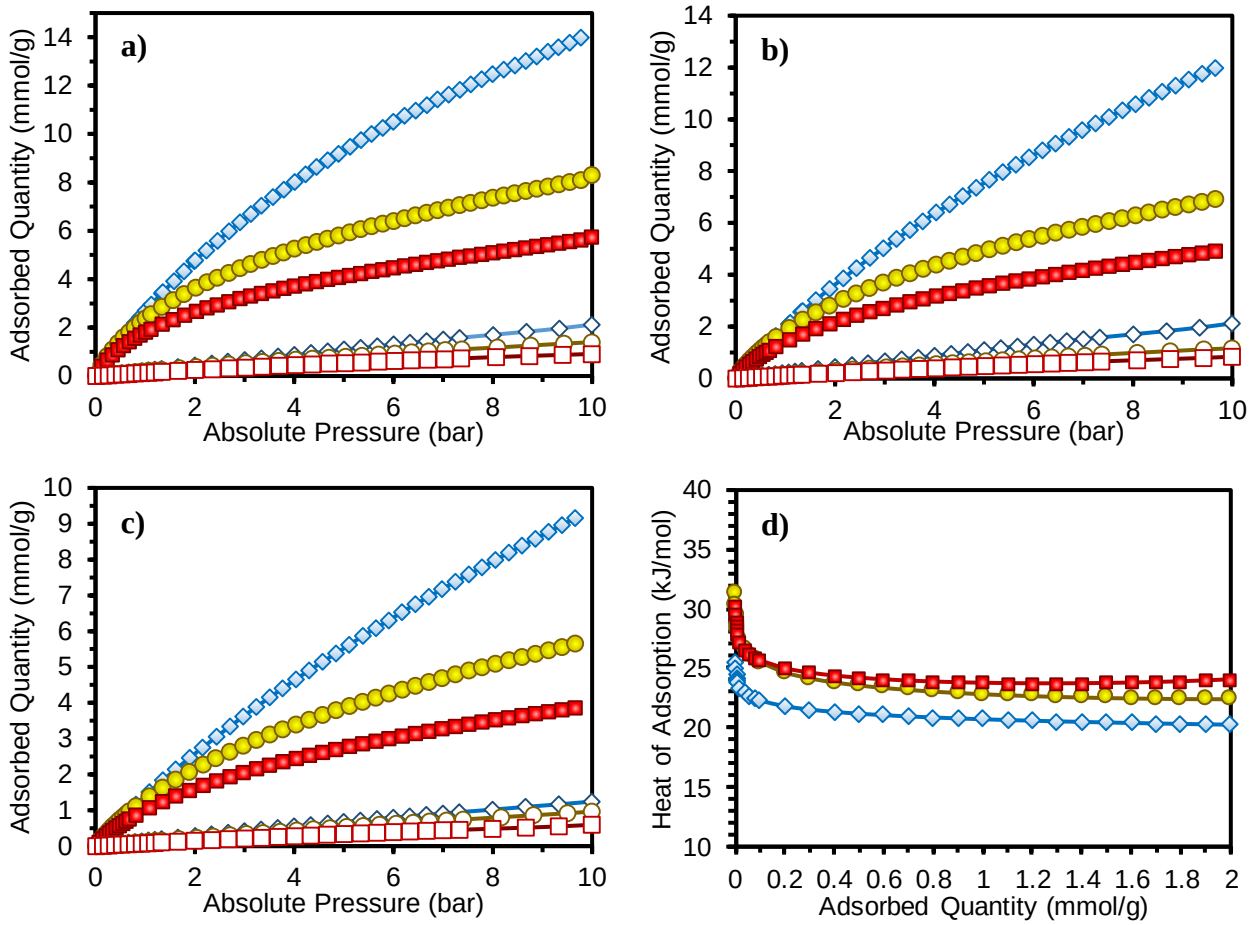

*Figure 5.4. CO_2 (full symbols) and N_2 (empty symbols) adsorption isotherms of **1FCOP** (yellow traces), **2FCOP** (red traces) and **FPAF** (blue traces) collected up to 10 bar at **a)** 273 K; **b)** 283K; **c)** 298 K. **d)** Isosteric heat of adsorption for CO_2 for **1FCOP** (yellow trace), **2FCOP** (red trace) and **FPAF** (blue trace) derived applying the van't Hoff equation to calculated isotherms obtained fitting the experimental curves with Langmuir-Freundlich model.*

Comparing CO_2 and N_2 isotherms in **Figure 5.4** it is clear that the fluorinated materials adsorb preferentially CO_2 over nitrogen. To quantify this behavior, the Ideal Adsorbed Solution Theory (IAST) was applied to calculate selectivity towards CO_2 adsorption from a 85:15 (mol:mol) N_2/CO_2 mixture from single-component adsorption isotherms (**Figure A5.6)**. At 0.1 bar and 273 K, the frameworks show the highest CO_2/N_2 selectivity, which is equal to 28, 40 and 14 for **1FCOP**, **2FCOP** and **FPAF**, respectively. Despite almost identical heat of adsorption values, **2FCOP** selectivity is higher than that of **1FCOP** at all temperatures.

Ultimately, the three new fluorinated materials were also tested for low-pressure methane adsorption with the aim of calculating the low-coverage $Q_{st}(CH_4)$. The results of CH_4 adsorption isotherms are reported in **Figure 5.5**, while **Table 5.3** summarize methane adsorption capacities. **FPAF** shows the highest uptake at all temperature thanks to its major surface area and available free volume.

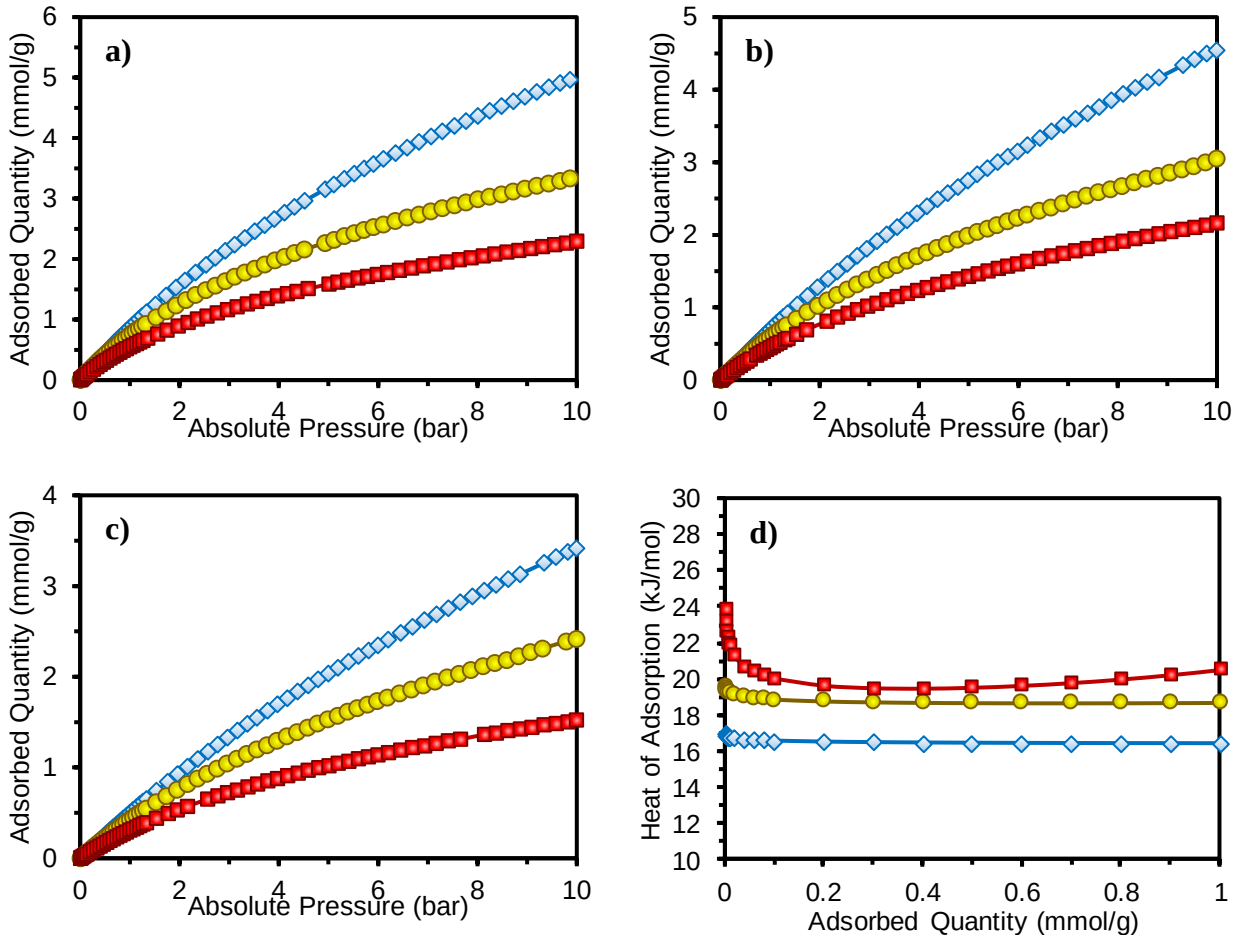

*Figure 5.5. CH_4 adsorption isotherms of **1FCOP** (yellow traces), **2FCOP** (red traces) and **FPAF** (blue traces) collected up to 10 bar at **a)** 273 K; **b)** 283K; **c)** 298 K. **d)** Isosteric heat of adsorption for CH_2 for **1FCOP** (yellow trace), **2FCOP** (red trace) and **FPAF** (blue trace) derived applying the van't Hoff equation to calculated isotherms obtained fitting the experimental curves with Langmuir-Freundlich model.*

All the new fluorinated covalent frameworks reported in this work show remarkable $Q_{st}(CH_4)$ values, higher than many reported MOFs and COFs (see **Table A5.3** in Appendix 5). In particular, **1FCOP** and **2FCOP** methane heats of adsorption are superior to the reported values for **H-KUST-1**, a Cu(II)-based MOF whose properties are considered the benchmark for methane storage in porous materials. The trend in $Q_{st}(CH_4)$ values is **FPAF** < **1FCOP2** < **2FCOP**. The two copolymers perform better thanks to the smaller pore size and the narrower pore size distribution, and **2FCOP** best **1FCOP** thanks to the higher fluorine content. The value for **FPAF** is to be compared with the reported value for **PAF1** (17 and 14 kJ/mol, respectively): once again our data suggest that the presence of fluorine in porous matrices increase their affinity towards polarizable guests. The beneficial fluorine effect on methane adsorption seems to be more pronounced compared to its role in CO_2 capture. It is worth pointing out that the calculated $Q_{st}(CH_4)$ value of **2FCOP**, reaching 22 kJ/mol, is higher than numerous reported values for organic porous materials MOF (see Appendix 5, **Table A5.3**). These results prompted us to calculate CO_2/CH_4 (50:50 mixture) and CH_4/N_2 (50:50 mixture) selectivity using IAST theory to assess frameworks performance towards methane purification (Appendix 5, **Figure A5.7 and A5.8**).

*Table 5.3. CH_4 adsorption capacities of **1FCOP**, **2FCOP**, **FPAF** and **SS-FPAF** at 273, 283 and 298 K up to 10 bar*

	T (K)	Q_{ads} (mmol/g)	Wt %	Q_{st} (CH_4)[a] (kJ/mol)	Selectivity[b] CH_4/N_2	Selectivity[c] CO_2/CH_4
1FCOP	273	3.3	5.3	19.2	5.3	5.1
	283	3.1	5.0	/	/	/
	298	2.4	3.8	/	3.8	5.3
2FCOP	273	2.3	3.7	21.9	7.9	5.4
	283	2.2	3.5	/	/	/
	298	1.5	2.4		5.6	4.2
FPAF	273	5.0	8.0	17.0	3.8	3.6
	283	4.5	7.2	/	/	/
	298	3.4	5.4		3.8	2.9

[a] Calculated at 0.01 mmol applying the Clausius-Clapeyron

[b] Low pressure value (0.1 bar) calculated applying the IAST theory to a 50:50 CH_4/N_2 gas mixture

[c] Low pressure value (0.1 bar) calculated applying the IAST theory to a 50:50 CO_2/CH_4 gas mixture

Thanks to their high $Q_{st}(CH_4)$, **1FCOP** and **2FCOP** show good selectivity for both CO_2/CH_4 and CH_4/N_2 binary mixtures. In particular, they are close to the selectivity value of **HKUST-1** for CO_2/CH_4 which is 4.8 kcal/mol. This is remarkable for fully organic materials with such a low fluorine content.

The data collected on methane adsorption strengthen the observation done on CO_2 adsorption performances of the three organic fluorinating materials: increasing the fluorine content of a porous matrix does increase its affinity towards CO_2 and CH_4, thus granting better adsorption capacities.

It was decided to present the characterization of **SS-FPAF** separated from the other materials since all the steps of its preparation have been characterized by IR spectrometry, solid-state NMR spectroscopy and N_2 adsorption-desorption isotherms and it is interesting to follow the evolution of the material with all these techniques. As mentioned in Section 5.2, preparation of **SS-FPAF** is a three-steps route, involving nitration of pristine PAF1 with nitric acid (**NO_2-PAF**), reduction of nitro-groups to amines with $SnCl_2$ (**NH_2-PAF**) and oxidation of the amino-groups with $NaNO_2$ to give diazo-groups having $(BF_4)^-$ as counteranion (**Diazo-PAF)** followed by thermal decomposition to give F-substituted aromatic rings.

NO_2-groups have characteristic IR signal and their appearance and disappearance could be followed by IR spectroscopy (**Figure 5.6**)

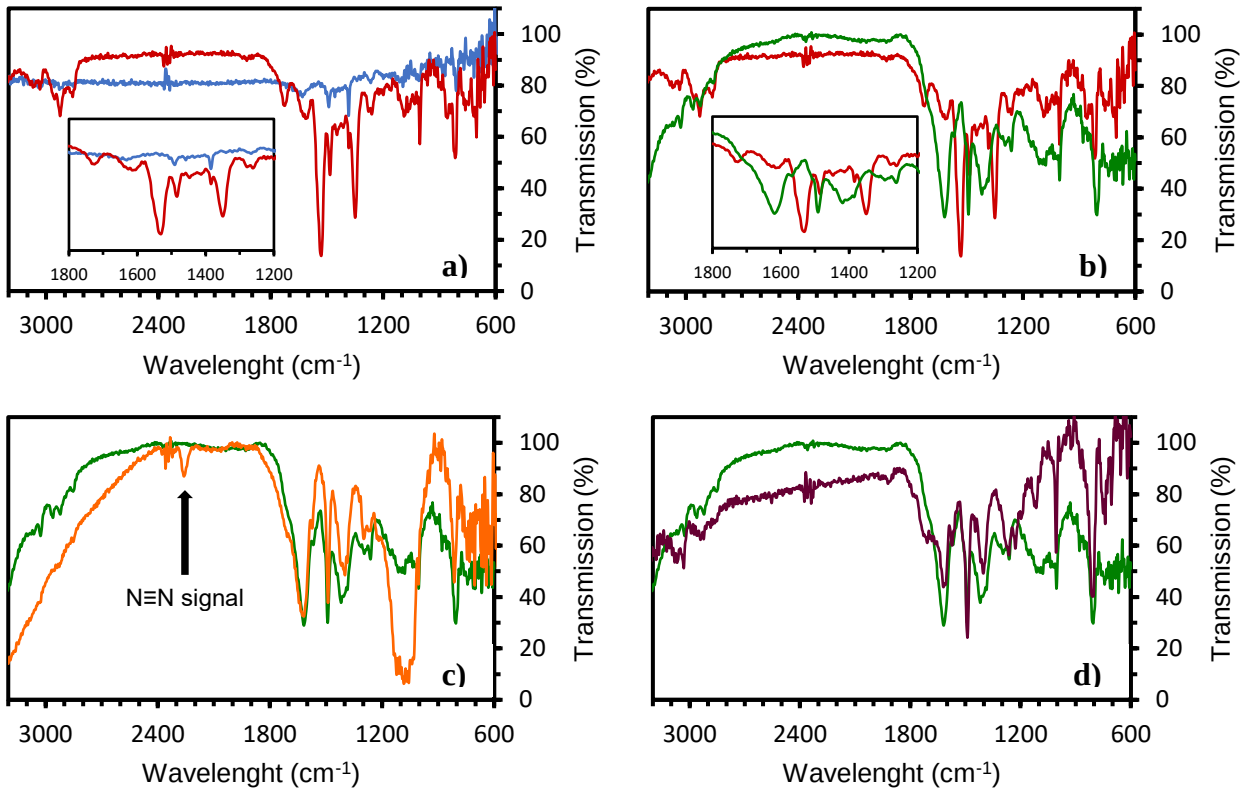

*Figure 5.6. IR spectroscopy of **SS-FPAF** and its intermediates. **a) PAF1** (blue trace) and **SS-NO₂PAF** (red trace); the inset shows the appearance of a signal at 1531 cm⁻¹ ascribable to NO_2-groups. **b) SS-NO₂PAF** (red trace) and **SS-NH₂PAF** (green trace); the inset shows the disappearance of the signal at 1531 cm⁻¹, indicating that all NO_2-groups have been reduced to amines. **c) Diazo-PAF** (orange trace) and **SS-NH₂PAF** (green trace); the presence of the characteristic signal of N≡N groups demonstrates the successful oxidation of amines. **d) SS-FPAF** (violet trace) and **SS-NH₂PAF** (green trace). Although fluorine has no easily recognizable IR signals, some differences between the two spectra suggest that NH_2-groups have been transformed in a different chemical species.*

The successful nitration of pristine **PAF1** is demonstrated by the appearance of an intense peak at 1531 cm^{-1} which is characteristic of NO_2 asymmetric stretching vibrations (**Figure 5.6a**). Similarly, the absence of this signal in **SS-NH₂PAF** spectrum (**Figure 5.6b**) is an indication of the successful reduction of all the nitro-groups to amines. Diazo-groups are another functional group which presence can be easily spotted by IR spectroscopy; the appearance of their characteristic signal at 2258 cm^{-1} in **Figure 5.6c** is a proof of the successful oxidation of aromatic amines with $NaNO_2$. Finally, thermal decomposition of **Diazo-PAF** gave a new species, as the absence of the peak at 2258 cm^{-1} in **Figure 5.6d** demonstrates. However, F-groups lack an easily recognizable IR signal, so IR spectroscopy is not sufficient to confirm the successful solid-state fluorination of **PAF1**.

For this reason, the series of **SS-FPAF** intermediates was also analyzed by solid state NMR spectroscopy and the results of the experiments are presented in **Figure 5.7**.

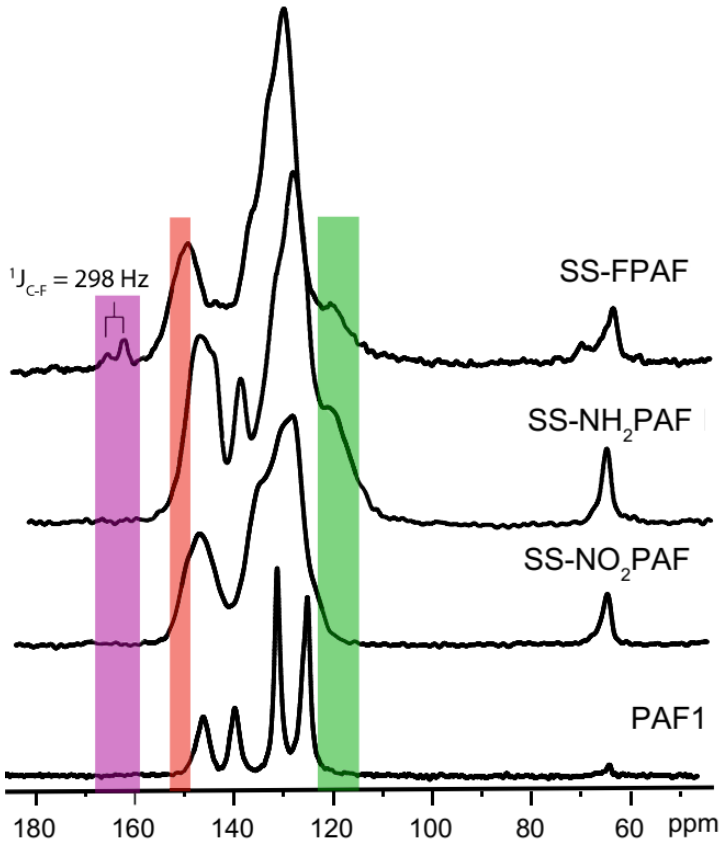

*Figure 5.7. Selected part of ^{13}C CP-MAS NMR spectra of **PAF1**, **SS-NO$_2$PAF**, **SS-NH$_2$PAF** and **SS-FPAF**. The coloured rectangles evidence the signals ascribable to aromatic carbons directly bonded to the following functional groups: NO$_2$-groups (red), NH$_2$-groups (green) and F-groups (violet).*

The most striking difference in the reported series of spectra is the considerable line broadening of all the functionalized PAF materials compared to pristine **PAF1**. This effect is a consequence of the lack of control over both the extent of reaction and on the attack position of nitro groups on each ring (*ortho* or *meta* respect to the central quaternary aliphatic carbon atom). It follows that short range chemical disorder is generated and thus an increase in chemical shift anisotropy is observed. Signal broadening cover most differences between spectra, but characteristic signals of functional groups can still be observed. In **SS-NO$_2$PAF** spectrum the last peak (146 ppm) has a clear shoulder at 149 ppm (red rectangle); this is the region where aromatic C-NO$_2$ are typically found. Moreover, in the following spectrum (**SS-NH$_2$PAF)**, the peak at 149 ppm disappears in favor of a new signal at 120 ppm, where typically fall aromatic C-NH$_2$ signals. Finally, the presence of C-F groups in **SS-FPAF** is undoubtedly proven by the doublet at 161-158 ppm generated by the coupling of ^{13}C nuclei and spin-active ^{19}F. These NMR spectra thus demonstrate the viability of the protocol for the post-synthetic fluorination of **PAF1** adopted in this work. However, uncomplete conversion of amino-groups is suggested by the presence of a residual signal at 120 ppm and improvements of the procedure are currently under investigation.

To verify that porosity was retained after each synthetic step and to evaluate the effect of the presence of functional groups over the surface area of the material, N_2 adsorption/desorption isotherms were collected at 77 K. The results are shown in **Figure 5.8**.

Table 5.4 summarizes the textural parameters of all the steps of the solid-state fluorination protocol derived from N_2 isotherms ad 77 K. Nitration of pristine PAF1 causes a considerable reduction in surface area and total pore volume. This is due to bulky NO_2 groups replacing hydrogen atoms, thus reducing the available free volume.

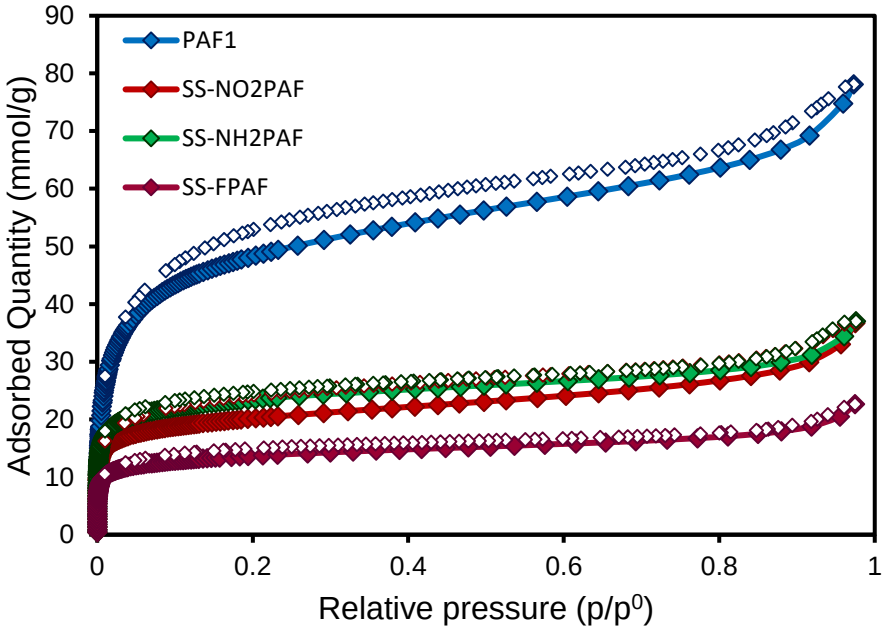

*Figure 5.8. Nitrogen adsorption/desorption isotherms collected at 77 K of the intermediates of **SS-FPAF**. Empty symbols represent desorption branches.*

A similar effect was observed by Zhang and coworkers[30] in their post-synthetic nitration reaction of **PAF1**. For analogous reasons, the reduction of nitro-groups to amines was predicted to increase specific surface area as NH_2 substituents are smaller than NO_2. Finally, the substitution of amino-groups with fluorine was expected to produce a further increase in surface area, as F atoms are smaller than NH_2 groups. Surprisingly, **SS-FPAF** has the lower surface area of the series. Solid-state NMR spectroscopy (**Figure 5.7**) seems to suggest incomplete reaction of amino-substituent, but this still does not explain the decrease in free volume. Even the presence of extremely bulky unreacted diazonium salts substituents cannot be taken into account to explain this, as **SS-FPAF** IR spectrum does not show any signal ascribable to the N≡N group (around 2200 cm^{1})

*Table 5.6. Textural parameters of **SS-FPAF** and its precursors as derived from N_2 adsorption isotherms*

	S_{BET} (m^2/g)	$S_{Langmuir}$ (m^2/g)	V_{total}[a] (cm^3/g)	V_{micro}[b] (cm^3/g)	V_{micro}/V_{total} (%)
PAF1	4080	4677	2.50	1.35	54.0
SS-NO_2PAF	1352	1524	0.80	0.47	58.8
SS-NH_2PAF	1982	2239	1.20	0.69	57.5
SS-FPAF	1151	1301	0.73	0.40	55.8

[a] calculated using Original Density Functional Theory and the N_2@carbon slit pore model

[b] calculated considering the cumulative pore volume up to pore 20 Å wide

Further investigations on the topic led us to consider the possible reactions of the highly reactive BF_3 molecules that are produced by the decomposition of the diazo-groups with $(BF_4)^-$ as counteranion. BF_3 is used to promote the polymerization of ethers. The formation of diazonium salts in our protocol is performed in water, but H_2O molecules are highly detrimental for the following thermal decomposition as they would react to form phenols instead of the desired aromatic fluorides. To remove water, we used dry THF as highly hygroscopic and volatile solvent. We soaked the sample with dry THF and removed it by cannula 5 times. Each time, one freeze-pump-thaw cycle was performed to remove water molecules trapped inside the pores. Then, before initiating thermal decomposition of diazonium salts, the sample was vacuum dried at room temperature for an hour, but small amounts of THF might have been remained trapped in the porous framework. After the decomposition of diazo-groups was started, BF_3 was formed and it promoted the polymerization of residual THF[32]. The presence of polytetrahydrofuran in pores of **SS-FPAF** would explain the very low surface area measured for this material. Moreover, it would also justify the presence of the small signal around 70 ppm in ^{13}C NMR of **SS-FPAF** (**Figure 5.7**) and of other minor signals observed in the 20-30 ppm region (see **Figure A5.10** for the full spectrum).

Even though the presence of polyTHF is highly detrimental for our scope, it would be interesting to prepare it on purpose and study the confined BF_3-promoted polymerization of THF in **PAF1**, since, with this methodology, monomers and initiators would meet inside the pores.

SS-FPAF $Q_{st}(CO_2)$ value was determined in any case and it was found to be very low (14 kJ/mol, see Appendix 5). This is actually reasonable taking into account the presence of polyTHF. Infact, due to the mechanism of reaction, the polymer was formed in proximity of the fluorine moieties. Consequently, CO_2 cannot interact with F atoms as they are covered by the polymer and the resulting heat of adsorption is low and comparable with unfunctionalized **PAF1** (15.6 kJ/mol)

5.4. Conclusions

Four new fluorinated organic porous materials where synthesized adopting different strategies. **1FCOP** and **2FCOP** were obtained by Sonogashira coupling reaction between tetrahedral aryl halogenide building blocks with four reacting bromine groups and linear 1,4-diethynylbenzene moieties bearing one or two fluorine substituents. **FPAF** was prepared from the Yamamoto-type homopolymerization reaction of a new derivative of tetrakis(4-bromophenylmethane) bearing a single fluorine on one phenyl ring atom on the meta position respect to the central aliphatic carbon atom. This molecule was specifically designed for this work. **SS-FPAF** was prepared by a post-synthetic functionalization approach involving a Sandmeyer reaction over -NH_2 groups to obtain the desired fluorine substituents. All the protocols were successfully employed to obtain porous materials with high surface area (ranging from 2050 to 850 m^2/g). The CO_2 and CH_4 adsorption performances of **1FCOP**, **2FCOP** and **FPAF** were evaluated. **2FCOP** is the material with the highest $Q_{st}(CO_2)$ and $Q_{st}(CH_4)$ values thanks to the higher fluorine content and highly microporous nature. The data presented in this work suggest an active role of fluorine moieties in the improvement of porous materials CO_2 and CH_4 capture performances. In particular, the introduction of fluorine groups in **FPAF** increased the $Q_{st}(CO_2)$ value of 53% compared to its non-fluorinated analogue.

Regarding the synthesis of **SS-FPAF**, it was discovered that the evolution of BF_3 as side product of the thermal decomposition reaction of the diazonium salt used to introduce the fluorine moieties promoted the polymerization of THF trapped inside the pores. This was revealed by solid-state ^{13}C-NMR and justify the low surface area of **SS-FPAF**. Although this unexpected event is detrimental for gas adsorption and molecular rotors, it is an interesting phenomenon that will be further investigated, as polymerization in nano-confined spaces is another research topic of Sozzani group.

In the future, the dynamics of the fluorinated *p*-phenyl rings of **1FCOP**, **2FCOP** and **FPAF** will be indagated by dielectric loss spectroscopy as all three materials were prepared in such a way that a net electric dipole moment is generated across the *p*-phenyl rings by the presence of the fluorine atoms.

5.4. Experimental section

^{1}H, ^{13}C and ^{19}F solution NMR spectra were recorded at 400, 100 and 377 MHz, respectively, on a Bruker Avance 400 Sectrometer. In the following, ^{1}H data are reported as follows: chemical shifts (in ppm and referenced to internal TMS), integration, multiplicity (s = singlet, d = doublet, t = triplet, q = quartet, m = multiplet), and coupling constants (in Hz). ^{13}C data are reported as follow: chemical shifts (in ppm and referenced to internal TMS), multiplicity (s = singlet, d = doublet), coupling constants (in Hz) ^{19}F data are reported as follows: chemical shifts (in ppm and referenced to internal $CFCl_3$).

^{13}C solid-state NMR experiments were carried out with a Bruker Avance 300 instrument operating at a static field of 7.04 T equipped with 4 mm double resonance MAS probe. The ramped-amplitude cross polarization experiments were performed at a spinning speed of 12.5 kHz using a recycle delay of 5 s and a contact time of 2 ms and 50 μs. The 90° pulse for proton was 2.9 μs. Crystalline polyethylene was taken as an external reference at 32.8 ppm from TMS.

IR spectra were acquired by ATR methods by means of a Nicolet iS10 instrument over the range 4000-600 cm^{-1}. In the following, signal intensities are denoted as br = broad, vs = very strong, s = strong, m = medium, and w = weak.

Differential Scanning Calorimetry (DSC) analyses were performed on a Mettler-Toledo StarE instrument from 0 to 450°C under an 80 ml/min flux of N_2.

Thermogravimetric Analyses (TGA) were performed on a Mettler-Toledo DSC/TGA 1 StarE System from 0 to 800 °C at a 10°C/min heating rate under a 50 ml/min flux of air.

N_2 adsorption/desorption isotherms were collected at liquid nitrogen temperature (77 K) and up to 1 bar of pressure by means of a Micromeritics ASAP 2020 HD analyzer. All samples were degassed by heating at 130°C for 5 hours under vacuum (approx. 10^{-3} mmHg) right before the analysis. Specific surface area values were calculated using the Brunauer, Emmett, and Teller (BET) model and the Langmuir model. Pore size distributions were calculated considering a slit pore geometry and the Non-Local Density Functional Theory (NLDFT). CO_2 adsorption/desorption isotherms were measured at 195 K up to 1 bar of pressure and at 273, 283, 298 K up to 10 bar using a Micromeritics ASAP 2050 analyzer. Samples were degassed at 130°C for 5 hours before each analysis.

Powder X-Ray Diffraction measurements were performed on Rigaku Miniflex 600 2θ-θ diffractometer equipped with a Cu-Kα tube (1.54059 Å). Acquisitions were performed in the 5-40 2θ angle range, with steps of 0.02° and speed of 1.5 s/step.

Chemicals and solvents were purchased by Sigma Aldrich or Alfa Aesar and used without further purification, unless otherwise specified.

5.4.1 Synthesis of tetrakis(4-bromophenyl)methane (**1**)

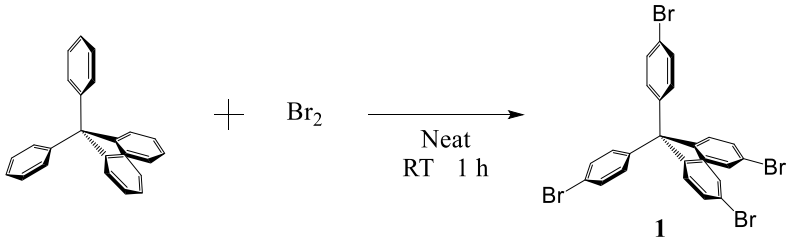

Tetrakis(4-bromophenyl)methane was synthesized according to the procedure published in J. Org. Chem., 69(5), 1524-1530, 2004.

Commercial tetraphenylmethane was further purified by sublimation at 180°C under vacuum before being used in this reaction. Br_2 (12.8 ml, 250 mmol) was transferred to a round-bottom 100 ml flask. Purified tetraphenylmethane (2 g, 6.25 mmol) was added in small portions under vigorous stirring. A white smoke (HBr) evolved from the flask. The mixture was left at room temperature under stirring until no more white smoke was produced (approx. 60 minutes). Then, the mixture was cooled with an ice bath and EtOH (50 ml) was slowly added. A white precipitate formed. The mixture was then stirred at RT for 2 hours; after that, the excess of bromine was quenched with a saturated aqueous sodium bisulfite solution. The white solid was recovered by filtration, washed with abundant water and EtOH. The crude product was crystallized from $CHCl_3$/EtOH to afford pure **1** as white crystalline needles (3.2 g, 80% yield).

5.4.2. Synthesis of 1,4-diethynyl-2-fluorobenzene (**2**)

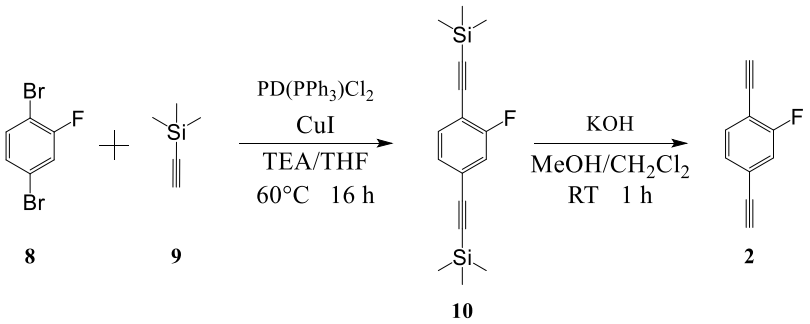

An oven-dried Schlenk was purged with N_2 and charged with N_2 purged triethylamine (TEA, 20 ml) by means of a syringe. Dry tetrahydrofuran (THF, 10 ml), previously distilled from sodium/benzophenone, was then added. Three freeze-pump-thaw cycles were performed on the solvents mixture. Then, 1,4-dibromo-2-fluoro-benzene (**8**) (1 g, 3.94 mmol), $PdCl_2(PPh_3)_2$ (70 mg, 0.1 mmol), CuI (20 mg, 0.1 mmol) and trimethylsilylacetylene (**9**) (TMSA, 1.50 ml, 10.6 mmol) were added. The resulting mixture was sealed under N_2 atmosphere, heated up to 60°C and kept at this temperature under stirring for 16 hours. After 16 hours, thin

layer chromatography (TLC) analysis (hexane) showed complete consumption of **8**. The reaction mixture was cooled down to room temperature and filtered over Celite. The solid residue was washed with ethyl acetate (EtOAc) and all the organic fractions were combined and passed over a silica pad to obtain a clear, brown solution. This solution was dried over Na_2SO_4 and the solvent was removed by rotary evaporation to give a brown solid. This solid was recrystallized from hexane/ethanol to afford ((2-fluoro-1,4-phenylene)bis(ethyne-2,1-diyl))bis(trimethylsilane) (**10**) as a highly crystalline white solid (940 mg, 82.5% yield). ^{1}H-NMR ($CDCl_3$, 400 MHz, ppm): 7.36 (1H, dd, J = 8.4, 7.2 Hz,), 7.16 (1H, dd, J = 7.2, 1.6 Hz), 7.14 (1H, dd, J = 10 Hz, 1.6 Hz), 0.26 (9H, s), 0.25 (9H, s). ^{13}C-NMR ($CDCl_3$, 100 MHz, ppm): 163.8, 161.3, 133.7, 127.69, 127.66, 125.1, 125.0, 119.0, 118.7, 112.4, 112.3, 103.4, 102.24, 102.20, 0.0 (6 C). ^{19}F-NMR ($CDCl_3$, 377 MHz, ppm): −110.3.

Intermediate (**10**) (500 mg, 1.74 mmol) was dissolved in CH_2Cl_2 (10 ml) in a 50-ml round-bottom flask and the obtained solution was cooled with an ice bath. In a beaker, KOH (2 g, 35.7 mmol) was dissolved in methanol (10 ml) and then added slowly to the reaction mixture. Then, the ice bath was removed and the mixture was left to react at room temperature. After 1 hour, TLC analysis (hexane/ethyl acetate, 8/2) showed complete consumption of (**10**). The product was extracted with CH_2Cl_2. The organic fractions were collected, dried with Na_2SO_4 and the solvent was removed under reduced pressure at 0°C. 1,4-diethynyl-2-fluorobenzene (**2**) was obtained as a white solid which was kept at -18 °C until needed (220 mg, 88% yield). IR (ATR, cm-1): 3265 (vs), 2115 (w, sharp), 1908 (w), 1750 (w), 1615 (m), 1546 (s), 1489 (s), 1418 (s), 1405 (s), 1279 (m), 1246 (s), 1143 (m), 1104 (s), 949 (s), 871 (vs), 826 (vs), 707 (m). ^{1}H-NMR (400 MHz, $CDCl_3$): δ 7.42 (t, J = 8 Hz, 1 H), 7.22 (dd, J = 8, 1.2 Hz, 1 H), 7.20 (dd, J = 10, 1.2 Hz, 1 H), 3.38 (s, 1 H), 3.20 (s, 1 H). ^{13}C-NMR ($CDCl_3$, ppm): 164.1 - 161.6 (d, C-F, $^{1}J_{C\text{-}F}$ = 250 Hz) 134.00 (s, CH), 128(s, CH), 124.6 - 124.5 (d, C, $^{3}J_{C\text{-}F}$ = 10 Hz), 119.3 - 119.1 (d, CH, $^{2}J_{C\text{-}F}$ = 20 Hz), 111.8 - 111.6 (d, C, $^{2}J_{C\text{-}F}$ = 20 Hz), 84.28 (C≡C), 82.00 (C≡C), 80.2 (C≡C), 76.7 (C≡C). ^{19}F NMR (377 MHz, $CDCl_3$, ppm): −110.31.

5.4.3. Synthesis of 1,4-diethynyl-2,3-difluorobenzene (**3**)

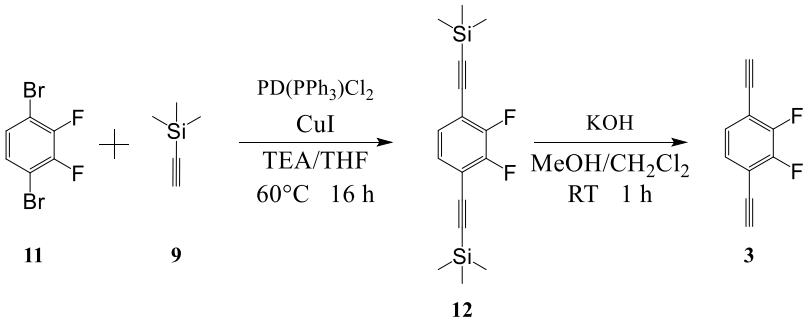

11 **9** **12** **3**

Intermediate (**12**) was obtained following a similar procedure to the one described for (**10**). In a typical synthesis, 1,4-dibromo-2,3-difluorobenzene (1 g, 3.78 mmol) was dissolved in N_2 purged TEA (20 ml) and dry THF (10 ml). TMSA (1.53 ml, 10.3 mmol), $PdCl_2(PPh_3)_2$ (70 mg, 0.1 mmol) and CuI (20 mg, 0.1 mmol) were used. After recrystallization, pure (**12**) was obtained as yellowish crystals (970 mg, 84 %). ^{1}H-NMR ($CDCl_3$, 400 MHz, ppm): 6.87 (m, 1H), 0.03 (s, 18H). ^{13}C-NMR ($CDCl_3$, 100 MHz, ppm): 152.39-149.85 (dd,

$^{1}J_{C-F}$ = 240 Hz, $^{2}J_{C-F}$ = 14.6 Hz, 2C), 127.71 (t, $^{3}J_{C-F}$ = 2.4 Hz, 2C), 114.05 (dd, $^{2}J_{C-F}$ = 9.2 Hz, $^{3}J_{C-F}$ = 5.4 Hz, 2C), 103.52 (s, 2C), 96.23 (d, $^{3}J_{C-F}$ = 2.1 Hz, 2C), -0.32 (s, 6C). ^{19}F NMR (377 MHz, $CDCl_3$, ppm): -134 (s, 2F).

Compound (**3**) was obtained from (**12**) following a similar procedure to the one described for (**2**). In a typical synthesis, (**12**) (500 mg, 1.63 mmol), KOH (2g, 35.7 mmol), CH_2Cl_2 (10 ml), MeOH (10 ml) were used. Pure (**3**) was obtained as a pale yellow solid (235 mg, 89% yield). ^{1}H-NMR (100 MHz, $CDCl_3$, ppm): 7.18 (m, 2H), 3.44 (s, 2H). ^{13}C-NMR (400 MHz, $CDCl_3$, ppm): 151.75-149.20 (dd, $^{1}J_{C-F}$ = 255 Hz, $^{2}J_{C-F}$ = 14.9 Hz, 2C), 127.01 (t, $^{3}J_{C-F}$ = 2.4 Hz, 2C), 112.46 (dd, $^{2}J_{C-F}$ = 9 Hz, $^{3}J_{C-F}$ = 5.1 Hz, 2C), 84.27 (s, 2C), 74.42 (s, 2C). ^{19}F NMR (377 MHz, $CDCl_3$, ppm): -134.05 (s, 2F)

5.4.4. Synthesis of 4,4',4''-((4-bromo-3-fluorofenil)methantryl)tris(bromobenzene) (**4**)

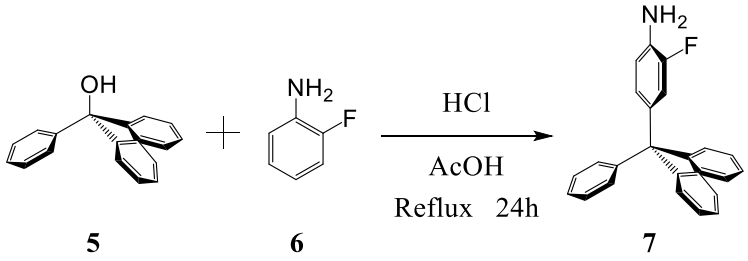

5 **6** **7**

A 50 ml round-bottom flask was loaded with triphenylmethanol (2 g, 8.15 mmol) (**5**) and acetic acid (AcOH, 10 ml). Next, 2-fluoroaniline (800 µl, 8.29 mmol) (**6**) and hydrochloric acid (37% wt/wt, 800 µl, 26.3 mmol) were added. The mixture was heated to reflux for 24 h. Full dissolution of solids only occurred after heating up. After 24 h, the heating was turned off and the mixture was allowed to slowly cool to room temperature. After a few hours, a white solid began to form. The resulting slurry was filtered on a Büchner funnel and washed with water. This intermediate is a mixture of the desired product and its chloride salt. To obtain pure 2-fluoro-4-tritylaniline, the crude product was suspended in ethanol (20 ml), and a solution of sodium hydroxide dissolved in a small amount of deionized water (approx. 2 g in 3 ml) was added. The mixture was heated, under stirring, to reflux for 12h. The mixture was then filtered on Büchner funnel and washed with water. The obtained solid was recrystallized from chloroform/hexane to give pure 2-fluoro-4-tritylaniline (**7**) as white crystals (885 mg, 33% yield). ^{1}H-NMR (DMSO-d_6, 400 MHz, ppm): 7.27 (6H, t, J =7.6; 7.2 Hz), 7.16 (3H, t, J =6.8; 6.8 Hz), 7.10 (6H, d, J=7.6 Hz), 6.65 (1H, t, J=8.8; 8.8 Hz), 6.60 (1H, s), 6.57 (1H, s); ^{13}C-NMR ($CDCl_3$, 100 MHz, ppm): 152.68-150.798 (C-F, d, $^{1}J_{C-F}$ = 263 Hz), 147.61 (3C, s), 138.96-138.92 (C, d, $^{3}J_{C-F}$ = 5 Hz), 132.85-132.74 (C, d, $^{2}J_{C-F}$ = 12 Hz), 131.92 (6C, s), 128.35 (6C,s), 128.11-128.09 (C, d, $^{4}J_{C-F}$ = 2 Hz), 126.82 (3C, s), 119.06-118.90 (C, d, $^{2}J_{C-F}$ = 16 Hz), 116.72-116.70 (C, d, $^{3}J_{C-F}$ = 3 Hz), 65.08 (C, s); ^{19}F-NMR (CDCl3, 377 MHz, ppm): -135.00 (dd, J = 8.9; 12.8 Hz). Melting point (DSC, ramp 10°C/min): 242 °C.

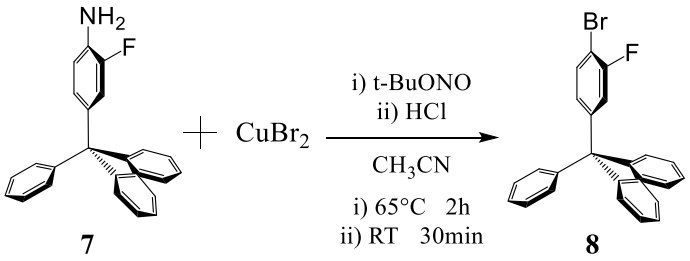

In a 100-ml round-bottom flask, intermediate **7** (670 mg, 1.97 mmol) was suspended in acetonitrile (30 ml). Next $CuBr_2$ (609 mg, 2.73 mmol) was added and the resulting green slurry was cooled with an ice bath. Then, tert-butylnitrite (t-BuONO) (0.5 ml, 4.3 mmol) was added dropwise. The mixture was then heated to 65°C and kept at this temperature under stirring overnight. Next, 5 ml of HCl 2N were added and the color changed from deep green to bright yellow. The organic phase was extracted with dichloromethane and washed with water (100 ml) and aqueous ammonia solution (33% wt, 2 x 80 ml). All the organic layers were combined, dried over Na_2SO_4 and the solvent was removed by rotary evaporation yielding a yellow solid. This solid was recrystallized from chloroform/ethanol to give pure (5) as a white crystalline solid (532 mg, 67% yield). ^{1}H-NMR ($CDCl_3$, 400 MHz, ppm): 7.40 (1H, dd, J = 8.0; 1.0 Hz), 7.28-7.16 (15H, m), 7.04 (1H, dd, J = 11; 2.5 Hz), 6.90 (1H, dd, J = 8.5; 2.5 Hz). ^{13}C-NMR ($CDCl_3$, ppm): 159.60-157.16 (C-F, d, $^{1}J_{C\text{-}F}$ = 244 Hz), 149.03-148.97 (C, d, $^{3}J_{C\text{-}F}$ = 6 Hz), 145.80 (3C, s), 132.18 (C, s), 130.90 (3C, s), 128.31-128.28 (C, d, $^{3}J_{C\text{-}F}$ = 7 Hz), 127.73 (3C, s) 126.31 (3C, s) 119.32-119.08 (C, d, $^{2}J_{C\text{-}F}$ = 24 Hz), 106.50-106.29 (C, d, $^{2}J_{C\text{-}F}$ = 21 Hz), 64.66 (C, s). ^{19}F-NMR ($CDCl_3$, ppm): -107.6 (s). Melting point (DSC, ramp 10°C/min): 243 °C.

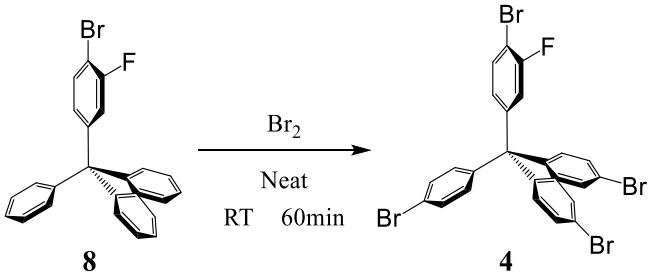

In a 20-ml round-bottom flask, Br_2 (2.1 ml, 40.1 mmol) was added; 340 mg of intermediate (**8**) (340 mg, 0.84 mmol) were added in small portions under vigorous stirring. The mixture was kept under stirring at room temperature until no more white smoke (HBr) evolved from the reaction mixture (approximatively 1 hour). Then, the mixture was cooled with an ice bath and ethanol (15 ml) was added. The mixture was then left under stirring at room temperature for 1 hour. Next, the mixture was poured in a saturated solution of sodium bisulfite in water (50 ml) and the precipitated solid was collected by filtration. This solid was purified by recrystallization from THF/hexane giving (**4**) as a white crystalline solid (270 mg, 50% yield). ^{1}H-NMR ($CDCl_3$, 400 MHz, ppm): 7.48-7.15 (7H, m), 7.04-7.01 (6H, m), 6.96 (1H, dd, J = 10.4; 2.4 Hz), 6.83 (1H, dd, J = 8.4; 2.0 Hz); ^{13}C-NMR ($CDCl_3$, 100 MHz, ppm): 159.87-157.41 (C-F, d, $^{1}J_{C\text{-}F}$ = 246 Hz), 147.36-147.31 (C, d, $^{3}J_{C\text{-}F}$ = 6 Hz), 143.98 (3C, s), 132.81 (C, s), 132.26 (6C, s), 131.24 (6C, s), 127.76-127.73 (C, d, $^{3}J_{C\text{-}F}$ =

3 Hz), 121.08 (3C, s), 118.92-118.68 (C, d, $^{2}J_{C-F}$ = 24 Hz), 107.44-107.23 (C, d, $^{2}J_{C-F}$ = 21 Hz), 63.69-63.68 (C, d, $^{4}J_{C-F}$ = 1.8 Hz); ^{19}F-NMR ($CDCl_3$, 377 MHz, ppm): -106.18 (dd, J = 7.3; 10.0 Hz). Melting point (DSC, ramp 10 °C/min): 284 °C

5.4.5. Synthesis of **1FCOP**

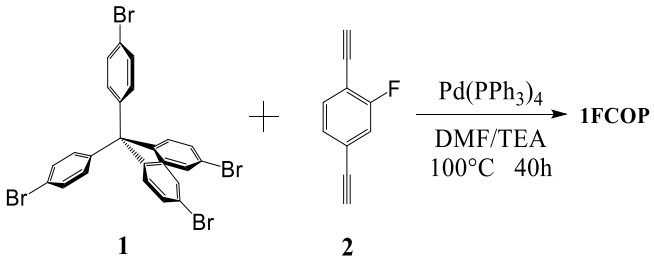

Anhydrous dimethylformamide (DMF, 100 ml) and anhydrous triethylamine (TEA, 40 ml) were poured into an oven-dried 250 ml two-neck round-bottom flask equipped with a nitrogen inlet and put under a flux of nitrogen. Two freeze-pump-thaw cycles were performed. Then (**2**) (181 mg, 1.26 mmol), (**1**) (400 mg, 0.63 mmol) and $Pd(PPh_3)_4$ (38.8 mg, 0.034 mmol) were added. Another freeze-pump-thaw cycle was performed before heating the mixture at 100°C under stirring. After a few hours, a voluminous solid formed from the reaction mixture. After 40 hours at 100°C, the mixture was slowly cooled to room temperature and the precipitate was collected by filtration and washed with methanol (2 X 30 ml), tetrahydrofuran (2 X 30 ml), water (2 X 50 ml) and chloroform (2 X 30 ml). A voluminous yellow powder was recovered from the filter. This product was further purified by soxhlet extraction with methanol for 24 h. Then the solid was dried under vacuum overnight at room temperature. A massive reduction of the powder's volume was observed after complete drying. Compound **1FCop** was finally recovered as a yellow-brown powder (340 mg, 89 %).IR (KBr pellet, cm-1): 3060(w, br), 2212(w), 1916(w), 1686(m), 1611(s), 1545(s), 1508(vs), 1414(s), 1270(w), 1209(s), 1191(s), 1113(m), 1015(m), 957(m), 871(m), 820(vs), 745(m), 717(m), 693(m), 621(w).

5.4.6. Synthesis of **2FCOP**

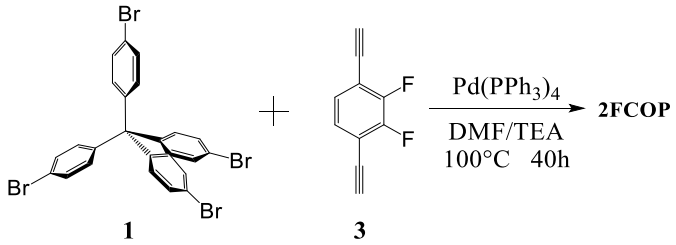

2FCop was synthesized following a similar procedure to the one described for the preparation of **1FCop**. In this case, the following reagents quantities were used: (**3**) (205 mg, 1.26 mmol), (**1**) (400 mg, 0.63 mmol), $Pd(PPh_3)_4$ (38.8 mg, 0.034 mmol). After purification and drying, **2FCop** was recovered as a red-brown powder (361 mg, 90 %). IR (KBr pellet, cm-1): 3029(w, br), 2214(w), 1917(w), 1715(m), 1621(m), 1617(m), 1562(w), 1506(s), 1486(s), 1459(vs), 1401(w), 1361(w), 1291(w), 1217(m), 1077(w), 1008(s), 955(w), 916(w), 817(vs), 734(w).

5.4.7. Synthesis of **FPAF**

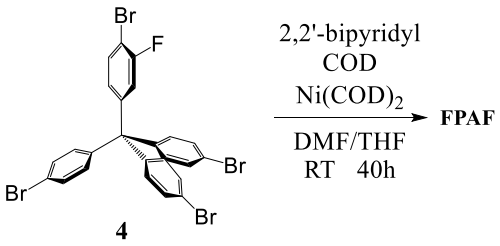

All the glassware used in this reaction was oven-dried overnight. Inside a glovebox, anhydrous DMF (100 ml) and anhydrous THF (20 ml) were transferred in a 250 ml two-neck round-bottom flask equipped with a nitrogen inlet. Then, 2,2'-bipyridyl (600 mg, 3.84 mmol) and cyclooctadiene (COD) (0.6 ml, 4.89 mmol) were added. A solution of (**4**) (450 mg, 0.703 mmol) in anhydrous THF (30 ml) was transferred in a dripping funnel and mounted over the round-bottom flask. Lastly, $Ni(COD)_2$ (1 g, 3.64 mmol) was added to the round-bottom flask. A deep violet solution formed. The apparatus was sealed under N_2, quickly brought outside the glovebox and immediately reconnected to fluxing nitrogen. The mixture was cooled to 0 °C with an ice bath and the monomer solution was slowly added over 20 minutes under vigorous stirring, while fluxing N_2 from the inlet. At the end of the addition, the dripping funnel was removed and the reaction mixture was sealed under nitrogen. The flask was left in the cooling bath for 60 minutes and then allowed to warm to room temperature. The reaction was left in these conditions for 48 hours. Then, 15 ml of concentrated HCl were added and the mixture was stirred at room temperature until the colour changed from violet to light blue. The mixture was filtered and the solid washed with methanol (2 X 30 ml), THF (2 X 30 ml), water (2 X 50 ml), and chloroform (2 X 30 ml). The solid was recovered and dried in vacuum overnight at room temperature. A massive reduction in the solid volume was observed after complete drying. **1FPAF** was recovered as a yellowish powder (192 mg, yield 85%). IR (ATR, cm^{-1}): 3033 (w, br), 1616 (w), 1489 (s), 1395 (m), 1259 (w), 1229 (w), 1190 (w), 803 (vs), 740 (s), 702 (s).

5.4.8. Synthesis of **SS-FPAF**

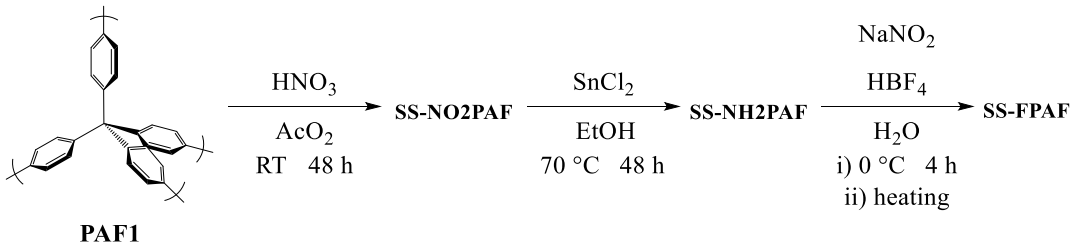

Pristine **PAF1** was synthesised following a similar procedure to the one described for **FPAF**. The following reagents quantities were employed: (1) (400 mg, 0.63 mmol), 2,2'-bipyridyl (600 mg, 3.84 mmol), COD (0.6 ml, 4.89 mmol), $Ni(COD)_2$ (1 g, 3.64 mmol), DMF (100 ml) and THF (50 ml). **PAF1** was obtained as a white powder (220 mg, yield 86%).

In a 100-ml round-bottom flask, **PAF1** (200 mg, 0.63 mmol) was suspended in acetic anhydride (30 ml). Two freeze-pump-thaw cycles were performed. The mixture was then kept at 0 °C with an ice bath and HNO_3 (65% wt, 6 g, 62 mmol) was slowly added under vigorous stirring. After the addiction, two more freeze-pump-thaw cycles were performed. After that, the reaction was warmed to room temperature and kept in these conditions under stirring for 48 h. The mixture gradually turned from gray to yellow. Finally, the solid was recovered by filtration and washed with water (300 ml). **SS-NO_2PAF1** was obtained as a pale-yellow powder (190 mg). IR (KBr pellet, cm^{-1}): 2919(w, br), 1724(w), 1623(w), 1533(vs), 1481(m), 1351(s), 1259(w), 1004(m), 813(m), 701(m).

Next, **SS-NO_2PAF1** (190 mg) was suspended in ethanol (25 ml) and $SnCl_2 \cdot 2H_2O$ (6.15 g, 27.5 mmol) was added. The mixture was stirred at room temperature for 15 minutes to allow the dissolution of the tin salt, then three freeze-pump-thaw cycles were performed. After that, the reaction was heated at 70°C under stirring for 7 hours. Finally, the mixture cooled to room temperature and kept in these conditions overnight under stirring. Next, concentrated HCl (30 ml) was added and the mixture was stirred at room temperature for 4 hours. After that, the solid was filtered and washed with abundant water (300 ml) and a 2M solution of NaOH (150 ml). **SS-NH_2PAF1** was recovered as a light gray powder (152 mg). IR (KBr pellet, cm^{-1}): 2964(w, br), 1621(vs), 1492(s), 1417(m, br), 1095(m, br), 1002(m), 808(s).

Next, **SS-NH_2PAF1** (152 mg) was suspended in water (15 ml) in a 100-ml Schlenk flask. Then, HBF_4 solution (48% wt/wt in water, 2.3 ml, 18.2 mmol) was added and two freeze-pump-thaw cycles were performed (be very careful while freezing water). Meanwhile, $NaNO_2$ (1.7 g, 24.5 mmol) was dissolved in water (3 ml) and the obtained solution was cooled to 0°C. Next, the Schlenk flask was immerged into an ice bath to keep the mixture temperature at 0°C and the cold sodium nitrite solution was slowly added. Two more freeze-pump-thaw cycles were performed before letting the mixture to react at 0°C for 4 hours. Next, the solution was filtered and washed with an aqueous solution of HBF_4 (5% wt/wt, 20 ml), methanol (50 ml) and diethyl ether (50 ml). All the solvents were used cold (0°C). The obtained yellow solid was quickly recovered, transferred

to an oven-dried Schlenk flask, cooled at 0°C and put under nitrogen. Then, cold, anhydrous THF (15 ml) was transferred in the Schlenk flask via cannula and the suspension was stirred at 0°C for 5 minutes. Next, one freeze-pump-thaw cycle was performed and then the solvent was removed via cannula and replaced with fresh dry THF. This procedure was repeated 5 times to ensure complete removal of water. After five cycles, the powder was dried in vacuum for 30 minutes. Finally, thermal decomposition of the diazonium salt was promoted by heating the flask with a heat gun. The gaseous N_2 and BF_3 formed during the decomposition were guided to a Drechsel bottle containing a 2M aqueous solution of NaOH. The heating was stopped as soon as the quenching basic solution started bubbling. The colour of the solid changed from yellow to black to grey. **SS-FPAF** was recovered as a grey powder (106 mg). IR (KBr pellet, cm^{-1}). 3029(w, br), 1714(w, br), 1621(s), 1486(vs), 1398(s), 1263(m), 1226(m), 1116(w), 1006(s), 806(vs), 750(s).

Bibliography for Chapter 5

1. Zhao, F., Liu, H., Mathe, S., Dong, A. & Zhang, J. Covalent Organic Frameworks: From Materials Design to Biomedical Application. *Nanomaterials* **8,** 15 (2017).
2. Wu, M. X. & Yang, Y. W. Metal–Organic Framework (MOF)-Based Drug/Cargo Delivery and Cancer Therapy. *Advanced Materials* **29,** 1606134 (2017).
3. Medina, D. D., Sick, T. & Bein, T. Photoactive and Conducting Covalent Organic Frameworks. *Adv. Energy Mater.* **7,** 1700387 (2017).
4. Doonan, C. J. & Sumby, C. J. Metal-organic framework catalysis. *CrystEngComm* **19,** 4045–4049 (2017).
5. IPCC - Intergovernmental Panel on Climate Change. (2010). Available at: http://www.ipcc.ch/. (Accessed: 12th October 2018)
6. Anderson, T. R., Hawkins, E. & Jones, P. D. CO2, the greenhouse effect and global warming: from the pioneering work of Arrhenius and Callendar to today's Earth System Models. *Endeavour* **40,** 178–187 (2016).
7. NOAA. What is Ocean Acidification? *PMEL* **2,** 1–7 (2018).
8. Lu, a.-H. & Hao, G.-P. *Porous materials for carbon dioxide capture*. *Annual Reports Section 'A'* **109,** (2013).
9. Oscurato, S. L., Salvatore, M., Maddalena, P. & Ambrosio, A. From nanoscopic to macroscopic photo-driven motion in azobenzene-containing materials. *Nanophotonics* **7,** 1387–1422 (2018).
10. Zhou, W. Methane storage in porous metal-organic frameworks: Current records and future perspectives. *Chem. Rec.* **10,** 200–204 (2010).
11. Furukawa, H. & Yaghi, O. M. Storage of Hydrogen, Methane, and Carbon Dioxide in Highly Porous Covalent Organic Frameworks for Clean Energy Applications. *J. Am. Chem. Soc.* **131,** 8875–8883 (2009).
12. Bracco, S. *et al.* Porous 3D polymers for high pressure methane storage and carbon dioxide capture. *J. Mater. Chem. A* **5,** 10328–10337 (2017).
13. Ben, T. *et al.* Gas storage in porous aromatic frameworks (PAFs). *Energy Environ. Sci.* **4,** 3991–3999 (2011).
14. Iupac. IUPAC Gold Book - Molecular sieve effect. (2014). doi:10.1351/goldbook.F02533
15. Eddaoudi, M. *et al.* Systematic Design of Pore Size and Functionality in Isoreticular MOFs and Their Application in Methane Storage Published by : American Association for the Advancement of Science Linked references are available on JSTOR for this article : Systematic Design. **295,** 469–472 (2016).
16. Yang, Z.-Z. *et al.* Fluorinated microporous organic polymers: design and applications in CO 2 adsorption and conversion. *Chem. Commun.* **50,** 13910–13913 (2014).
17. Noro, S. & Nakamura, T. Fluorine-functionalized metal–organic frameworks and porous coordination polymers. *NPG Asia Mater.* **9,** e433 (2017).
18. Hulvey, Z., Sava, D. A., Eckert, J. & Cheetham, A. K. Hydrogen storage in a highly interpenetrated

and partially fluorinated metal-organic framework. *Inorg. Chem.* **50,** 403–405 (2011).

19. Ozier, I. Ground-state electric dipole moment of methane. *Phys. Rev. Lett.* **27,** 1329–1332 (1971).
20. A. D. Buckingham and R. L. Disch. The Quadrupole Moment of the Carbon Dioxide Molecule. *Proc. R. Soc. Lond. A. Math. Phys. Sci.* **273,** 275–289 (1963).
21. Pachfule, P., Chen, Y., Jiang, J. & Banerjee, R. Fluorinated metal-organic frameworks: Advantageous for higher H2and CO2adsorption or not? *Chem. - A Eur. J.* **18,** 688–694 (2012).
22. Sonogashira, K. Development of Pd-Cu catalyzed cross-coupling of terminal acetylenes with sp2-carbon halides. *J. Organomet. Chem.* **653,** 46–49 (2002).
23. Stöckel, E. *et al.* High surface area amorphous microporous poly(aryleneethynylene) networks using tetrahedral carbon- and silicon-centred monomers. *Chem. Commun.* 212–214 (2009). doi:10.1039/b815044c
24. Bracco, S. *et al.* CO 2 regulates molecular rotor dynamics in porous materials. *Chem. Commun.* **53,** 7776–7779 (2017).
25. Comotti, A., Bracco, S. & Sozzani, P. Molecular Rotors Built in Porous Materials. *Acc. Chem. Res.* **49,** 1701–1710 (2016).
26. Yamamoto, T., Wakabayashi, S. & Osakada, K. Mechanism of C-C coupling reactions of aromatic halides, promoted by Ni(COD)2in the presence of 2,2′-bipyridine and PPh3, to give biaryls. *J. Organomet. Chem.* **428,** 223–237 (1992).
27. Ben, T. *et al.* Targeted synthesis of a porous aromatic framework with high stability and exceptionally high surface area. *Angew. Chemie - Int. Ed.* **48,** 9457–9460 (2009).
28. Yuan, D., Lu, W., Zhao, D. & Zhou, H. C. Highly stable porous polymer networks with exceptionally high gas-uptake capacities. *Adv. Mater.* **23,** 3723–3725 (2011).
29. Comotti, A., Bracco, S., Ben, T., Qiu, S. & Sozzani, P. Molecular rotors in porous organic frameworks. *Angew. Chemie - Int. Ed.* **53,** 1043–1047 (2014).
30. Zhang, Y., Li, B. & Ma, S. Dual functionalization of porous aromatic frameworks as a new platform for heterogeneous cascade catalysis. *Chem. Commun.* **50,** 8507–8510 (2014).
31. Garibay, S. J. *et al.* Accessing functionalized porous aromatic frameworks (PAFs) through a de novo approach. *CrystEngComm* **15,** 1515–1519 (2013).
32. Burrows, R. C. & Crowe, B. F. Polymerization of tetrahydrofuran. *J. Appl. Polym. Sci.* **6,** 465–473 (1962).

Appendix 1.

Brief theory of gas adsorption by porous solids

The aim of this appendix is to give to the reader a brief theoretical and mathematical background on gas adsorption on solid surfaces. In particular, mathematical methods that leads to specific surface areas, pore size distributions, enthalpies of adsorption and selectivities calculations used throughout this thesis are described in greater details. However, the reader should keep in mind that this is just a summary and that theory of adsorption is actually a much more complex and extended matter. For further reading, a few books on the topic are suggested in the references.

A1.1. The Langmuir model

Even though Langmuir proposed various mechanisms of adsorption, all based on the idea that a surface possesses only a limited number of adsorption sites, the one that is usually referred as "The Langmuir model" is the simplest of them and it is based on the assumption that adsorption on a plane surface only occurs on one kind of elementary space; each space can adsorb only one molecule. It is evident that Langmuir's original model did not allow for either porosity or physisorption. However, the Langmuir model provided a starting point for the development of the BET treatment and of other more refined physisorption isotherm equations. Moreover, since the Langmuir model fits very well type I adsorption isotherms from a purely mathematical point of view, it is still widely used in surface area calculations of microporous materials, despite it fails in the physical interpretation of adsorption in micropores.

Let us suppose that an adsorbent surface has a finite number N^s of equivalent and independent sites for localized adsorption (one molecule per site). The fraction of sites occupied by N^a is $\Theta = {N^a}/{N^s}$.

From the kinetic theory of gases, the rate of adsorption is dependent on the pressure and the fraction of the bare sites $(1 - \Theta)$. The rate of desorption is dependent on Θ and on the energy of activation E (i.e. equivalent to an energy of adsorption expressed as a positive quantity). The equilibrium is obtained for the values of Θ and p for which the rates of adsorption and desorption are equal. Thus, the net rate of adsorption is zero:

$$\frac{\mathrm{d}N^a}{\mathrm{d}t} = \alpha p(1 - \Theta) - \beta\Theta \exp\left(-\frac{E}{RT}\right) = 0 \qquad [A1.1]$$

where a and b are characteristic constants for the given gas–solid system. If, in an ideal case, the probability of desorption of an adsorbed molecule from the surface is independent of the surface coverage (i.e. there are no lateral interactions between the adsorbed molecules), the value of E is constant for a particular adsorption system. Then, Equation [A1.1] is applicable over the complete range of monolayer coverage. By rearrangement and simplification of Equation [A1.1], we arrive at the Langmuir isotherm equation:

$$\Theta = bp/(1 + bp) \qquad [A1.2]$$

where b, the 'adsorption coefficient', is exponentially related to the positive value of the energy of adsorption, E:

$$b = Kexp(E/RT) \qquad [A1.3]$$

the pre-exponential factor K being equal to the ratio of adsorption/desorption coefficient, α/β. It is evident that Equation [A1.2] is of a very general mathematical form (i.e. a hyperbolic function). At low Θ, it reduces to Henry's law (i.e. the quantity adsorbed is linearly dependent from the equilibrium pressure); at high surface coverage, a plateau is reached as Θ→1, which corresponds to the completion of the monolayer. Equation [A1.2] is usually applied in its linear form:

$$\frac{p}{q} = \left({}^{1}/_{\boldsymbol{q}_m b}\right) + {}^{p}/_{\boldsymbol{q}_m} \qquad [A1.4]$$

where $\boldsymbol{q}$ is the specific amount of gas adsorbed at the equilibrium pressure p and $\boldsymbol{n}_m$ is the monolayer capacity (so, $\Theta = \boldsymbol{q}/\boldsymbol{q}_m$). Although the Langmuir model is more strictly applicable to an ideal form of chemisorption, it can describe mathematically very well type I isotherms, despite its physical nature, as discussed before. Once, $\boldsymbol{n}_m$ is known, one can derive the surface area by the simple relation:

$$a\ (Langmuir) = \boldsymbol{q}_m \boldsymbol{\sigma} L \qquad [A1.5]$$

where σ is the average area occupied by each molecule in the completed monolayer and L is the Avogadro number. Emmet and Brunauer proposed that the molecular cross-sectional area, σ, can be calculated from the density of the liquid adsorptive in the bulk liquid state. Thus

$$\sigma = f\left(\frac{M}{\rho L}\right)^{2/3} \qquad [A1.6]$$

where *f* is a packing factor, which for hexagonal close-packing becomes 1.091, ρ is the absolute density of the liquid adsorptive at the operational temperature and M is the molar mass of the adsorptive.

A1.2. The BET model

In many real cases, physical adsorption of a vapor on a surface is not limited to monolayer surface coverage, especially at higher pressure. Multilayer adsorption readily happens in mesoporous materials and give birth to type II isotherms. Emmett and Brunauer came to the empirical conclusion that the beginning of the middle almost linear section of a Type II isotherm (point B in **Figure 1.5**) corresponds to monolayer completition. After that, multilayer adsorption begins. By introducing a number of simplifying assumptions, Brunauer et al. (1938) were able to extend the Langmuir mechanism to multilayer adsorption and obtain an isotherm equation (the BET equation), which has the Type II character. The original BET treatment involved an extension of the Langmuir kinetic theory of monomolecular adsorption to the formation of an infinite number of adsorbed layers at the saturation pressure, p^0. According to the BET model, the adsorbed molecules in one layer can act as adsorption sites for molecules in the next layer and, at any pressure below the saturation vapour pressure p^0, fractions of the surface ($\Theta_0, \Theta_1, \Theta_2, \ldots, \Theta_i$) are covered by 0, 1, 2, ... , *i* layers of adsorbed molecules (Θ_0 represents the fraction of bare surface). It follows that the adsorbed layer is envisaged not to be of uniform thickness, but instead to be made up of random stacks of molecules. If it is assumed that at equilibrium, characterized by the pressure p, the fractions of bare and covered surface, Θ_0 and Θ_1, remain constant, we can equate the rate of condensation on the bare surface to the rate of evaporation from the first layer:

$$a_1 p\Theta_0 = b_1\Theta_1 \exp\left(-\frac{E_1}{RT}\right) \qquad [A1.7]$$

where a_1 and b_1 are adsorption and desorption constants for the first layer and E_1 is the positive value of the so-called energy of adsorption in the first layer. It is assumed that a_1, b_1 and E_1 are independent of the quantity of adsorbed molecules already present in the first layer; that is, as in the Langmuir mechanism, no allowance is made for lateral adsorbate–adsorbate interactions. In the same way, at the equilibrium pressure *p*, the fractions of the surface $\Theta_2, \Theta_3, \ldots, \Theta_i$ must also remain constant and we may therefore write:

$$a_i p\Theta_{1-i} = b_i\Theta_i \exp\left(-\frac{E_i}{RT}\right) \qquad [A1.8]$$

where Θ_{1-i} and Θ_i represent, respectively, the fractions of surface covered by i-1 and i layers; a_i and b_i are adsorption and desorption constants and E_i is the energy of adsorption in the i-th layer. The sum of the fractions of surface equals unity:

$$\Theta_0 + \Theta_1 + \Theta_2 + \ldots + \Theta_i = 1 \qquad \text{[A1.9]}$$

Moreover, the adsorbed amount can be expressed as

$$n = n_m(1\Theta_1 + 2\Theta_2 + \cdots + i\Theta_i) \qquad \text{[A1.10]}$$

The derivation of the BET isotherm is based on two main assumptions:

- **a.** In the second and all higher layers, the energy of adsorption E_i has the same value as the liquefaction energy, E_L, of the adsorptive;
- **b.** The multilayer has infinite thickness at $p/p^0 = 1$ ($i = \infty$).

Let:

$$\frac{a_1}{b_1} = \frac{a_2}{b_2} = \cdots = \frac{a_i}{b_i} = g \qquad \text{[A1.11]}$$

where g is a constant since all the layers (except the first) have the same properties. We can now express Θ_1, Θ_2,..., Θ_i in terms of Θ_0:

$$\Theta_i = yx^{i-1}\Theta_0 \qquad \text{[A1.12]}$$

where

$$y = \frac{a_1}{b_1}\, p \exp\left(\frac{E_1}{RT}\right); x = \frac{p}{g}\exp\left(\frac{E_L}{RT}\right) \qquad \text{[A1.13]}$$

We may define a constant C:

$$C = \frac{y}{x} = \frac{a_1}{b_1}\, g\, \exp\left(\frac{E_1 - E_L}{RT}\right) \qquad \text{[A1.14]}$$

then

$$\Theta_i = C x^i \Theta_0 \qquad \text{[A1.15]}$$

So, we can write

$$\frac{\boldsymbol{q}}{\boldsymbol{q}_{\mathrm{m}}} = \sum_{i=1}^{\infty} i\Theta_i = C \sum_{i=1}^{\infty} i x^i \cdot \Theta_0 \qquad \text{[A1.16]}$$

Considering that

$$\sum_{i=1}^{\infty} i\, x^i = \frac{x}{(1-x)^2} \qquad \text{[A1.17]}$$

and since $\Theta = 1 - \sum_i^{\infty} \Theta_i$, we obtain from equation [A1.16] and [A1.17]:

$$\frac{\boldsymbol{q}}{\boldsymbol{q}_{\mathrm{m}}} = \frac{C\, x}{(1-x)(1-x+Cx)} \qquad \text{[A1.18]}$$

If at the saturation vapour pressure p^0 at constant, the adsorbed layer is assumed to be of infinite thickness, it follows that $x = 1$ and that $x = p/p^0$ so that:

$$\frac{\boldsymbol{q}}{\boldsymbol{q}_{\mathrm{m}}} = \frac{C\,(p/p^O)}{(1-p/p^O))(1-p/p^O+C(p/p^O))} \qquad \text{[A1.19]}$$

When q/q_m is plotted against p/p^0 at constant C, equation [A1.19] gives a curve of Type II shape provided that C >2. It is evident that the shape of the knee is dependent on the value of C, becoming sharper as C is increased. When C <2, but still positive, equation [A1.19] gives a curve with no inflexion point and having the general shape of a Type III isotherm. Equation [A.19] can be written in its linear form:

$$\frac{p}{q(p^0-p)} = \frac{1}{q_m C} + \frac{C-1}{q_m C} \cdot \frac{p}{p^O} \qquad [A1.20]$$

This 'linear transformed BET equation' provides the basis for the BET plot of experimental isotherm data in the form of $p/[q(p^0-p)]$ versus p/p^0.

As we have seen, the BET model is based on the following assumptions: (i) that adsorption takes place on an array of fixed sites, (ii) that the sites are energetically identical and (iii) that no allowance is made for lateral interactions between adsorbed molecules. These assumptions are very rigid and most real solid-gas systems do not behave accordingly. In spite of the weakness of the underlying theory, the BET equation remains the most widely used of all adsorption isotherm equations. It is extensively used for determining the surface area of porous and non-porous adsorbents. The reasons for the universal application of the BET *method* are discussed in the next paragraph.

A1.3. Assessment of surface area by gas adsorption: the BET method

Two stages are involved in the evaluation of the surface area from physisorption isotherm data by the BET method. First, it is necessary to construct the BET plot and from it to derive the value of the monolayer capacity, q_m. The second stage is the calculation of the specific surface area, a(BET), from q_m and this requires the knowledge of the average area, σ, occupied by each molecule in the completed monolayer (i.e. the molecular cross-sectional area).

The BET equation is conveniently expressed in its linear form as in [A1.20]. The plot of $(p/p^0)/[q(1-p/p^0)]$ versus p/p^0 should be a straight line with slope $s = (C-1)/q_m C$ and intercept $i = 1/q_m C$. By solving these two simultaneous equations, we obtain:

$$q_m = \frac{1}{s+i} \qquad [A1.21]$$

and

$$C = (s+i) + 1 \qquad [A1.22]$$

According to equation [A1.20], the relative pressure corresponding to monolayer completion is inversely dependent on the C value:

$$\left(\frac{p}{p_0}\right)_{q_m} = \frac{1}{\sqrt{C}+1} \qquad [A1.23]$$

It must be remembered that equation [A1.20] is obeyed over limited regions of the isotherm (i.e. the plot of $(p/p^0)/[q(1-p/p^0)]$ versus p/p^0 is not linear over the entire range of p/p^0). Moreover, the range of validity of the BET plot depends on the specific adsorbent/adsorptive system and oftentimes the selection of the appropriate pressure range often entails some degree of qualitative judgement and several narrow, adjacent, pressure ranges may seem to offer possible ranges of linearity. Because of that, it is difficult to give a predetermined p/p^0 range over which perform surface area calculations. However, a series of some simple criteria have been proposed and adopted to overcome this uncertainty:

- **a.** the quantity C should be positive (i.e. any negative intercept on the ordinate of the BET plot is an indication that one is outside the valid range of the BET equation);
- **b.** the application of the BET equation should be limited to the pressure range where the term $q(p^0-p)$ or alternatively $q(1-p/p^0)$ continuously increases with p/p^0; all data points above the maximum in the plot should be discarded;
- **c.** the pressure corresponding to q_m should be within the pressure range selected for the calculation and
- **d.** the calculated value of $(p/p^0)q_m$ (given by equation [A1.23]) should not differ, say, by more than 10%, from the value of p/p^0 corresponding to the BET $\mathbf{q}_m$ value obtained by application of equation [A1.20]. Otherwise, it is necessary to change the chosen range of relative pressures.

The specific surface area, *a*(BET), is obtained from the BET monolayer capacity, q_m, by the application of the simple relation [A1.5] utilizing [A1.6] to calculate the gas cross-sectional area.

Considerable caution must be exercised in the interpretation of type I isotherms with the BET model. In fact, BET model is not able to describe the micropore filling, much similarly as it was discussed for the Langmuir model. However, BET surface area of microporous materials is readily calculated and used in every published paper about microporous materials. This is done because BET calculations offer the possibility to simple relate parameters between different adsorbents, but it must be clear that those values are not the *effective area* of the materials, but rather a useful indication of their activity. In other words, the BET model is used to conveniently describe microporous adsorption from a mathematical point of view, despite the fact that the theoretical physical background of BET theory is not able to describe micropores filling.

A1.4. Pore size distribution by Non-Local Density Functional Theory

Density Functional Theory (DFT) is independent of capillary condensation and can be applied across the complete micropore–mesopore range. Non-Local DFT (NLDFT) is based on the well-established principles of classical and statistical thermodynamics and it is assumed that, under certain controlled conditions, the adsorbate is in thermodynamic equilibrium with the adsorptive in the gas phase. The distribution in density, $\rho(r)$, of the pore fluid is determined by minimizing the grand thermodynamic potential which is dependent on the fluid–fluid and fluid–solid interactions. Once $\rho(r)$ is known, the adsorption isotherm and other thermodynamic properties can be calculated. The parameters of the fluid–fluid interactions are crosschecked to ensure consistency with the bulk properties, and the fluid–solid interactions are obtained by adjusting the calculated isotherms to fit experimental data on non-porous reference adsorbents. It is generally assumed that the pores are of simple geometry (usually slits, cylinders or spheres). NLDFT considers the pore wall as smooth. Thus, a series of theoretical isotherms can be calculated for a particular gas–solid system and pores of a given shape. This series of theoretical isotherms is called the *kernel*. Calculation of the pore size distribution function, $f(w)$, is based on a solution of the generalized adsorption isotherm (GAI) equation as follows:

$$N_{exp}\left(\frac{p}{p^o}\right) = \int_{w_{min}}^{w_{max}} N_{theo}\left(\frac{p}{p^0}, w\right) f(w) dw \qquad [A1.24]$$

where w is the pore width, $N_{exp}(p/p^0)$ is the measured number of adsorbed molecules and $N_{theo}(p/p^0, w)$ is the kernel of theoretical isotherms in model pores. The integration is over a finite range of pore sizes.

A1.5. Isosteric heat of adsorption calculations

Thermodynamically, enthalpy of adsorption is the heat released or absorbed during the adsorption process. In the majority of cases, adsorption is an exothermic process, making it thermodynamically favourable. Despite not being formally correct, in porous materials' literature, enthalpy of adsorption is almost always called heat of adsorption, Q_{st}. It can be demonstrated that Q_{st} can be calculated as

$$Q_{st} = RT^2\left(\frac{\partial \ln p}{\partial T}\right) \qquad [A1.25]$$

Equation [A1.25] is analogous to the well-known Clausius-Clapeyron for one component gas-liquid system. Q_{st} can be obtained either directly from calorimetric measurements or indirectly from a series of isotherm collected at different method utilizing the *isosteric method.* This latter method is far more common in literature, hence the name *isosteric* heat of adsorption. According to this method, one must plot ln p versus $1/T$ for a given $\mathbf{q}$. Q_{st} will be obtained as the slope of the resulting straight line. However, one is often interested in Q_{st} values at extremely small loading and the experimental isotherms do not have experimental points at such low loading values; thus, the experimental isotherms cannot be directly used in Q_{st} calculations at very small loading. Is then necessary to derive an analytical expression of the experimental isotherm through a mathematical fitting of the curve. In principle, one can use many different mathematical equations to fit the experimental data. In chapter 4 of this thesis, it was decided to follow the work of Long et al. We used a dual-site Langmuir equation as the fitting equation. In a dual-site Langmuir model, one is supposing that adsorbent has two different and independent sets of adsorption sites, A and B; thus

$$\boldsymbol{q} = \boldsymbol{q}_A + \boldsymbol{q}_B = \frac{q_{sat,A} b_A p}{1+b_A p} + \frac{q_{sat,B} b_B p}{1+b_B p} \qquad [A1.26]$$

where $\mathbf{q}$ is the adsorbed quantity at the pressure p, $\mathbf{q}_A$ and $\mathbf{q}_B$ are the adsorbed quantities by sites A and B, respectively, at pressure p, $q_{sat,A}$ and $q_{sat,B}$ are the maximum adsorbed quantities by site A and B, respectively, at infinite pressure and b_A and b_B are defined as in equation [A1.3]. It follows that we can also define an energy E_A for adsorption on site A and an energy E_B for adsorption on site B. Equation [A1.26] must now be solved to find the corresponding p for a specific loading $\mathbf{q}$. We can rewrite [A1.26] as

$$(q_{sat,A} + q_{sat,B} - q) b_A b_B p^2 + [(q_{sat,a} - q) b_A + (q_{sat,B} - q) b_B] p - q = 0 \qquad [A1.27]$$

It is convenient to define the following parameters:

$$\alpha = (q_{sat,A} + q_{sat,B} - q) b_A b_B \qquad [A1.28]$$

$$\beta = (q_{sat,A} - q) b_A + (q_{sat,B} - q)\, b_B \qquad [A1.29]$$

For any specific loading $\mathbf{q}$, the corresponding pressure is obtained by solving the quadratic expression [A1.27].

Out of the two solution of [A1.27], only one is physically realizable and that is:

$$p = \frac{-\beta+\sqrt{\beta^2+4\alpha \boldsymbol{q}}}{2\alpha} \qquad \text{[A1.30]}$$

Now that we have an expression for p, we can calculate $\left(\frac{\partial \ln p}{\partial T}\right)_{\boldsymbol{q}}$ to get Q_{st} as a function of loading. In this thesis, the analytical function $\mathbf{q}(p)$ was obtained using Mathlab software to perform a non-linear fitting of three different isotherms collected at 273, 283 and 298 K and with [A1.26] as the fitting equation.

In chapter 3 and 5 we adopted a similar methodology, but we used a Langmuir-Freundlich model isotherm as it gave better fitting results. The Langmuir-Freundlich isotherm has the general form

$$\boldsymbol{q} = \frac{q_{max} b p^t}{1+bp^t} \qquad \text{[A1.31]}$$

where $\boldsymbol{q}$ is the adsorbed quantity at pressure p, q_{max} is the saturation loading and b and t are the Freundlich parameters. Parameter b can be written

$$b = b_0 e^{E/RT} \qquad \text{[A1.31]}$$

where b_0 is a pre-exponential factor related to the gas saturation pressure p^0 and E can be considered as the mean adsorbent-adsorptive interaction energy calculated from $p = 0$ to $p_{max.}$ In our fitting procedure, we used Langmuir-Freundlich model to fit simultaneously the three experimental curves. We allowed the saturation loading q_{max} and the Freundlich parameters t to vary independently for each experimental isotherm, while the pre-exponential factor b_0 and the energy E had to be the same for all the isotherms. We had then a total of eight fitting parameters: b_0, E, Q_{273}, t_{273}, Q_{283}, t_{283}, Q_{298} and t_{298}

Calculations were run using Mathlab software. We can reverse the Langmuir-Freundlich equation to obtain an analytical expression of p as a function of $\boldsymbol{q}$

$$p = \left(\frac{\boldsymbol{q}}{b(q_{max}-\boldsymbol{q})}\right)^{1/t} \qquad \text{[A1.32]}$$

and, thus, calculate Q_{st} via the van't Hoff equation.

Appendix 2

Supporting Information for Chapter 2

A2.1. Powder X-Ray Structural Analysis of α-[Zn(BPEB-d4)]

Microcrystalline batches of the MOFs were ground with agate mortar and pestle and deposited in the hollow of a zero-background silicon sample-holder. Diffraction data were collected at room temperature on a Bruker AXS D8 Advance θ:θ diffractometer, equipped a Cu-Kα tube (λ = 1.5418 Å), a Bruker Lynxeye linear position-sensitive detector, a filter of Ni in the diffracted beam, and the following optics: primary beam Soller slits (2.3°), fixed divergence slit (0.5°), receiving slit (8 mm). The generator was set at 40 kV and 40 mA. Acquisitions for qualitative analysis prior to functional characterization were performed in the 3–35° 2θ range, with steps of 0.02°, and speed of 1 s/step. Diffraction data for the refinement of the crystal structure of α-[Zn(BPEB-d_4)] were measured in the 3– 105° 2θ range, with steps of 0.02° and an overall scan time of approximately 12 h. A visual comparison (**Figure 2.1**) between the powder patterns of α-[Zn(BPEB-d_4)] and α-[Zn(BPEB)] suggested that the two materials are isostructural. Based on this evidence, the refinement of the crystal structure of α-[Zn(BPEB-d_4)] was carried out starting from the crystal structure of α-[Zn(BPEB)] by applying the Rietveld method, as implemented in TOPAS-R. The independent portion of the (BPEB-d_4)$^{2-}$ ligand was modelled as a rigid body, assigning average values to bond distances and angles (C-C of the hexa-atomic ring, 1.37-1.40 Å, refined; C-C, C-N, N-N of the penta-atomic ring, 1.36 Å; C-H/D, 0.95 Å; exocyclic C-C, 1.40-1.50 Å, refined; exocyclic C≡C, 1.24 Å; hexa-atomic ring internal bond angles, 120°; penta-atomic ring internal bond angles, 108°). The presence of orientational disorder, with respect to the main axis of the ligand, affecting the phenyl ring was verified in the final stages of the refinement and was found beneficial (as proved by a slight lowering of the figures of merit R_p and R_{wp}). The background was modeled by a polynomial function of the Chebyshev type, while peak profiles were described by the Fundamental Parameters Approach. One refined isotropic thermal factor (B_{iso}) was attributed to all atoms except the metal ion, to which the isotropic thermal factor $B_{iso}(M) = B_{iso}–2.0$ (Å^2) was assigned. The peak widths could not be satisfactorily modelled neither by employing the conventional Lorentzian or Gaussian functions (or a combination of them) alone, nor by combining them with spherical harmonics. A more sophisticated approach was necessary to take into account, concomitantly, of the sharpness of the [110] Bragg reflections and broadness of the other classes of reflections. In detail, we used two different Lorentzian descriptions (modulated by cos(θ)-dependent spherical harmonics of second and fourth order, respectively) for the [110] class and the other reflections. A tan(θ)-dependent Gaussian contribution was applied to all the Bragg reflections, irrespective of their *hkl* class. A more rigorous approach, not feasible through the Rietveld method, would take paracrystallinity into consideration. The final Rietveld refinement plot is shown in **Figure A2.1**

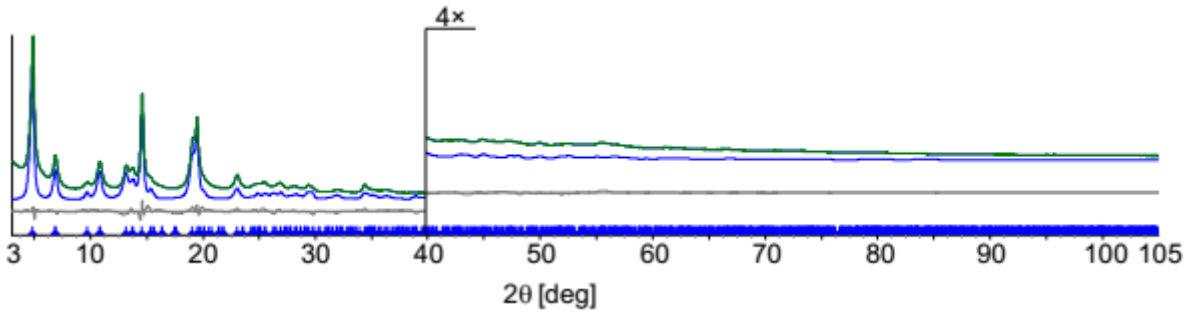

Figure A2.1 *Graphical result of the final Rietveld refinement carried out on α-[Zn(BPEB-d₄)] in terms of experimental, calculated and difference traces (green, blue and gray, respectively). The blue markers at the bottom indicate the positions of the Bragg reflections. Horizontal axis, 2θ [deg]; vertical axis, intensity [counts]. The portion above 40° has been magnified for the sake of clarity.*

A2.2. Variable Temperature Powder X-Ray Diffraction of α-[Zn(BPEB-d4)]

Variable-temperature powder X-ray diffraction (VT-PXRD) experiments were performed on α-[Zn(BPEB-d_4)] to highlight its structural response to temperature variation. Progressive heating from room temperature up to decomposition was performed in air, in the 3-23° 2θ range, using a custom-made sample heater (Officina Elettrotecnica di Tenno, Italy). A 20-mg batch of as-synthesize α-[Zn(BPEB-d_4)] was ground in an agate mortar and deposited in the hollow of an aluminum sample-holder. The thermal behavior was followed up to 490 °C heating the sample *in situ* and *operando* with steps of 20 °C. The parametric treatment of the data in the temperature range 30-330 °C with the Le Bail method, as implemented in TOPAS-R, allowed to depict the variation of the unit cell parameters as a function of the temperature. The experiment (**Figure A2.2a**) highlighted the remarkable thermal robustness of this material, which does not collapse and does not undergo phase transitions up to decomposition starting, in air, at ~400 °C. The parametric treatment of the VT-XRPD data acquired in the temperature range 30-330 °C (**Figure A2.2b**) highlighted that progressive heating brings about a moderate unit cell volume decrease (by about -1.8%), reasonably due to solvent release.

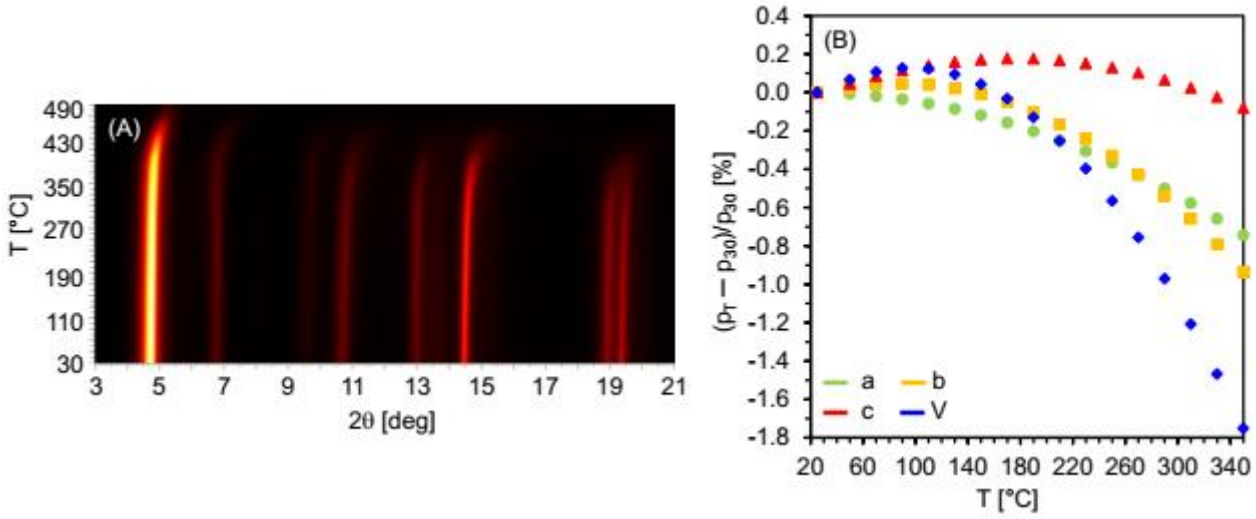

***Figure A2.2**. a) Plot of the powder X-ray diffraction patterns of α-[Zn(BPEB-d4)] acquired* in situ *and* operando *as a function of temperature by heating in air, with steps of 20 °C, from 30 °C up to 490 °C. b) Percentage variation of the unit cell parameters (p_T) α-[Zn(BPEB-d4)] as a function of temperature. At each temperature, the actual values (p_T) have been normalized with respect to those at 30 °C (p_{30}). a, green circles; b, orange squares; c, red triangles; V, blue diamonds*

A2.3. Differential Scanning Calorimetry of α-[Zn(BPEB-d4)]

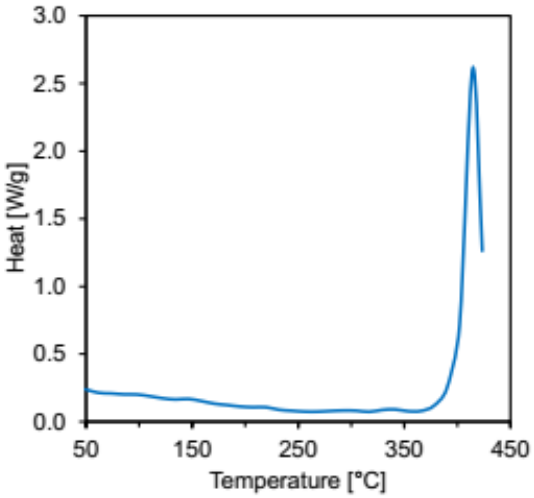

***Figure A2.3**. Trace of the differential scanning calorimetry carried out for α-[Zn(BPEB-d4)] in a flow of N_2 (80 mL/min) at a rate of 10 °C/min. The decomposition temperature of the compound (415 °C) is indicated by the maximum of the endothermic peak*

A2.4. Solid State NMR

^{13}C solid-state NMR experiments were carried out with a Bruker Avance 300 instrument operating at a static field of 7.04 T equipped with 4 mm double resonance MAS probe. The ramped-amplitude cross polarization experiments were performed at a spinning speed of 12.5 kHz using a recycle delay of 5 s and a contact time of 2 ms and 50 μs. The 90° pulse for proton was 2.9 μs. ^{13}C Single-pulse excitation (SPE) experiments were run using a 90° pulse of 4.6 μs and recycle delays of 10 and 20 s.

Crystalline polyethylene was taken as an external reference at 32.8 ppm from TMS. ^{1}H spin lattice relaxation experiments $T_1(^{1}H)$ were recorded using the inversion recovery pulse sequence at a spinning speed of 8 kHz in the range of 200 K - 298 K, with 32 scans for each recovery time. The 90° pulse for proton was 3.65 μs. The stability and accuracy of the temperature controller (Bruker B-VT2000) were approximately 0.1 K. The empty sample was sealed under vacuum before collecting ^{1}H T_1 relaxation times. The activation energy, the attempt frequency and C constant were calculated to be 0.5 kcal/mol, 2.2 10^{12} Hz and 2 10^{10} s^{-2}, respectively. The ^{1}H T_1 relaxation times for the α-[Zn(BPEB)] loaded with CO_2 range from 2.7 s and 1.9 s between 210 K and 260 K. The correlation between relaxation times and temperatures is described by Kubo and Tomita:

$$\frac{1}{T_1} = C\left[\frac{\tau_C}{1+\omega^2\tau_C^2} + \frac{4\tau_C}{1+4\omega^2\tau_C^2}\right]$$

$$\tau_C = \tau_0 e^{E_A/RT}$$

τ_0 represents the inverse of the attempt frequency, E_A is the activation energy of the motion, ω is the angular Larmor frequency of the nuclei and C is a constant. In the extreme narrowing limit, $\omega^2\tau_C^2 \ll 1$, and the equation is simplified to:

$$\frac{1}{T_1} = 5C\tau_0 e^{E_A/RT}$$

$$Ln\left(\frac{1}{T_1}\right) = Ln(5C\tau_0) + E_A/RT$$

The ^{2}H NMR experiments were carried out with a Bruker Avance 300 instrument operating at a static field of 7.04 T using a Bruker 5 mm wide-line probe. The quadrupolar spin-echo pulse sequence used a waiting time of 30 μs with a refocusing delay of 28 μs. The experiments were carried out with a pulse of 2.9 μs and a recycle delay of 15 s. The stability and accuracy of the temperature controller (Bruker B-VT2000) were approximately 1 K. All the experiments were performed on a sealed glass vial containing the deuterated sample under vacuum (39.7 mg) and CO_2 at 9 bar (at room temperature). In the α-[Zn(BPEB-d_4)]/CO2 sample, at low temperature there occurs high loading of 8.5 mmol g-1, corresponding to 95% of full loading. Above 200K there is a progressive decrease in loading reaching the value of 5.6 mmol g-1 at 290 K that corresponds to 62% of full loading.

Theoretical simulation of ^{2}H NMR spectra for a two-site 180° jump model was performed by the program Express 1.0 with a quadrupolar coupling constant of 180 kHz and an asymmetry parameter $\eta = 0.02$. Simulations are obtained for a log-Gaussian distribution of jump rates by superposition of 61 spectra for different jump rates. A single distribution width of $\sigma = 1.5$ was used. At high temperature a simple Gaussian distribution of amplitude librations with $\sigma = \pm 1.5° \div 5°$ was added to the two-site 180° jump model.

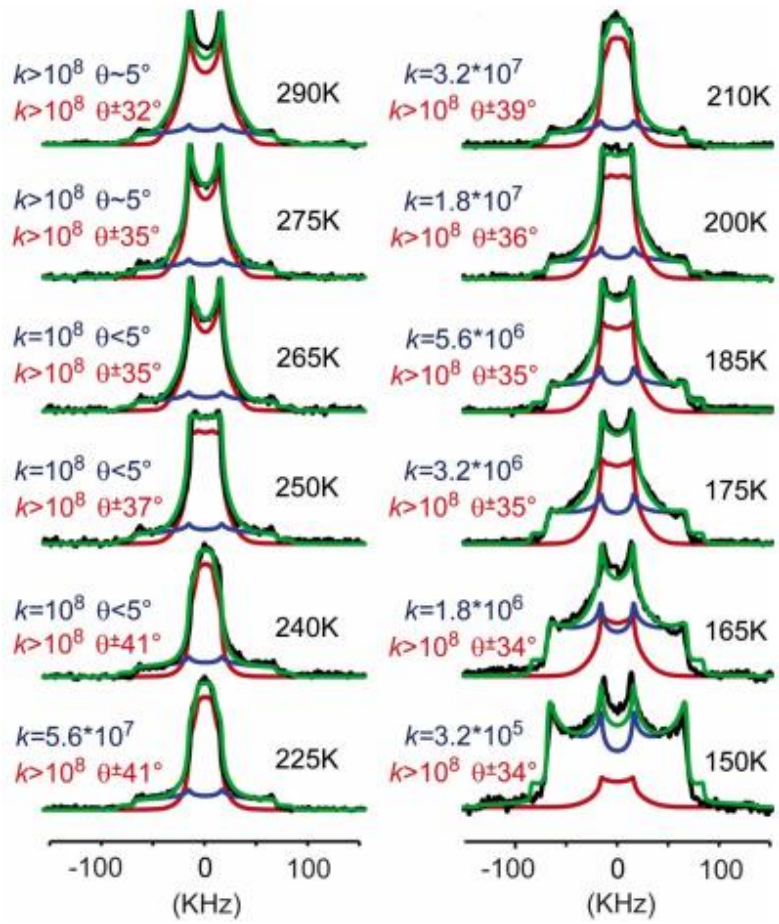

Figure A2.4. ^{2}H NMR spectra of α-[Zn(BPEB-d$_4$)]/CO2 at variable temperature. Experimental (black line) spectra, red and blue lines represent the components for I and II configurations, respectively. The simulated profile is highlighted in green. Rotational frequencies k and libration amplitudes θ are expressed in Hz and degrees, respectively.

Table A2.1. Comparison of rotational frequencies of a few molecular rotors in MOFs at room temperature.

	Temp	k	E_a	k_0 (τ_0)	
Zn-BPEB	298K	9.9 10^{11} Hz	0.5 Kcal mol^{-1}	2.2 10^{12} Hz 4.2 10^{-13} s	
CID-5/6 x=0.55	298K	3.2 10^{6} Hz ~ 5 10^{7} Hz	4.8 Kcal mol^{-1} 20 KJ mol^{-1} (4-site) 6.0 Kcal mol^{-1} 25 KJ mol^{-1} (2-site)	-	a)
{Fe(pyrazine)-[$Pt(CN)_4$]	290K 300K	2 10^{6} Hz 2 10^{7} Hz	7.8 Kcal mol^{-1} 32.6 KJ mol^{-1}	1.1 10^{12} Hz 9.1 10^{-13} s	b)
UiO66(Zr)	296K	2.3 MHz	7.2 Kcal mol^{-1} 30 KJ mol^{-1}	(0.5+0.8) 10^{12} Hz 1.67 10^{-12} s	c)
CdNa(2-stp)-d4-pyz)0.5 (H_2O)	293K	10^{5} Hz	-	-	d)
TPE-MOF 1a	300K	10^{4} Hz	10.3 Kcal mol^{-1} 43 KJ mol^{-1}	2.2 10^{11} Hz 4.5 10^{-12} s	e)
MOF-5	300K	10^{3} Hz	11.2 Kcal mol^{-1} 47 KJ mol^{-1}	2.4 10^{12} Hz 4.2 10^{-13} s	f)
MIL-47	300K	<1 KHz	10.8 Kcal mol^{-1} 45 KJmol^{-1}	0.88 10^{11} Hz 1.1 10^{-11} s	g)
MIL-53	300K	<1KHz	9.8 Kcal mol^{-1} 41 KJ mol^{-1}	1.26 10^{11} Hz 7.9 10^{-12} s	g)
IRMOF3-NH_2	-	-	5.0 Kcal mol^{-1} 20.9 KJ mol^{-1}	8.4 10^{8} Hz 1.19 10^{-9} s	h)
UiO-66 Zr	-	-	12.4 Kcal mol^{-1} 51.8 KJ mol^{-1}	1.3 10^{13} Hz $10^{-13.1}$ s	i)
UiO-66 Zr -Br	-	-	8.1 Kcal mol^{-1} 33.9 Kmol^{-1}	3.9 10^{14} Hz $10^{-13.6}$ s	i)
UiO-66 Zr –NH_2	-	-	12.4 Kcal mol^{-1} 51.8 KJ mol^{-1}	-	i)
IRMOF-Br	-	-.	7.3 Kcal mol^{-1} 30.5 KJ mol^{-1}	-	l)

Guillerm, E. de Souza Costa, F. Taulelle, C. Martineau, *Chem. Mater*. **2012**, *24*, 2168- 2177; l) E. B. Winston, P. J. Lowell, J. Vacek, J. Chocholousova, J. Michl, J. C. Price, *Phys. Chem. Chem. Phys.* **2008**, *10*, 5188–5191

a) M. Inukai, T. Fukushima, Y. Hijikata, N. Ogiwara, S. Horike, S. Kitagawa, *J. Am. Chem. Soc.* **2015**, 137, 12183-12186; b) J. A. Alberto Rodríguez-Velamazan, M. A. Gonzalez, J. A. Real, M. Castro, M. C. Muñoz, A. B. Gaspar, R. Ohtani, M. Ohba, K. Yoneda, Y. Hijikata, N. Yanai, M. Mizuno, H. Ando, S. Kitagawa, *J. Am. Chem. Soc.* **2012**, *134*, 5083-5089; c) D. I. Kolokolov, A. G. Stepanov, V. Guillerm, C. Serre, B. Frick, H. Jobic, *J. Phys. Chem. C* **2012**, *116*, 12131-12136; d) S. Horike, R. Matsuda,D. tanaka, S. Matsubara, M. Mizuno, K. Endo, S. Kitagawa, *Angew. Chem. Int. Ed.* **2006**, *45*, 7226-7230; e) N. B. Shustova, T.-C. Ong, A. F. Cozzolino, V. K. Michaelis, R. G. Griffin, M. Dinca, *J. Am. Chem. Soc.* **2012**, *134*, 15601-15070; f) S. L. Gould, D. Tranchemontagne, O. M. Yaghi, M. A. Garcia-Garibay, *J. Am. Chem. Soc.* **2008,** *130*, 3246-3247; g) D. I. Kolokolov, H. Jobic, A. G. Stepanov, V. Guillerm, T. Devic, C. Serre, G. Ferey, *Angew. Chem. Int. Ed.* **2010**, *49*, 4791-4794; h) W. Morris, R. E. Taylor, C. Dybowski, O. M. Yaghi, M. A. Garcia-Garibay, *J. Mol. Struct.* **2011**, *1004*, 94-101; i) S. Devautour-Vinot, G. Maurin, C. Serre, P. Horcajada, P. Paula da Cunha, V.

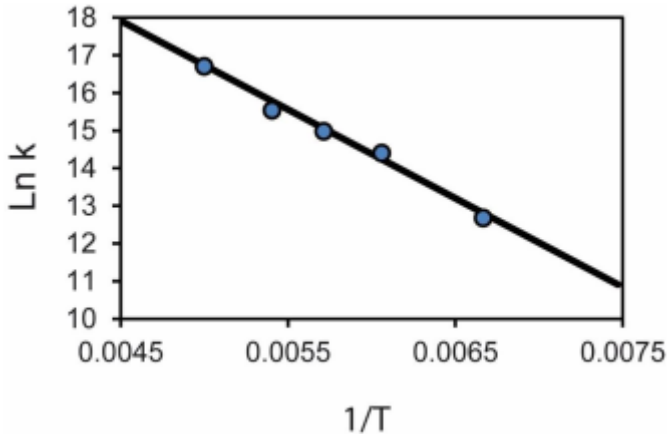

Figure A2.5. Arrhenius plot of reorientational rates versus the inverse of temperature (range 150-200K) of the blue profile (configuration II) in the α-[Zn(BPEB-d$_4$)]/CO2 sample. The reorentational rates are expressed in Hz and temperature in K.

Table A2 2. CO_2 loadings, expressed as CO_2 mmoles per gram, of the deuterated sample α-[Zn(BPEB-d$_4$)] sealed under CO2 pressure of 9 bar at room temperature.

T (K)	mmol/g
290	5.6
265	7.1
250	7.4
240	7.8
210	8.3
200	8.5

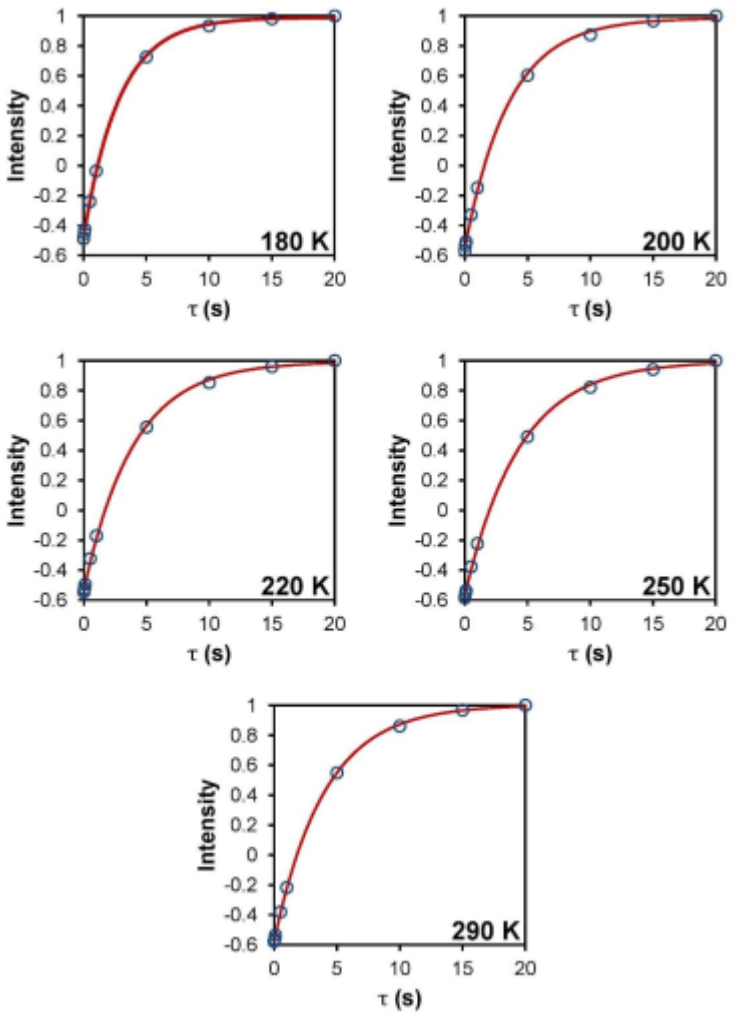

***Figure A2.6**. ^{1}H inversion recovery experiments for the measurement of ^{1}H T_1 relaxation times of α-[Zn(BPEB)]. The ^{1}H T_1 relaxation times are the following: 2.8 s (180 K), 3.5 (200 K), 3.9 s (220 K), 4.3 s (250 K) and 5.0 s (293 K).*

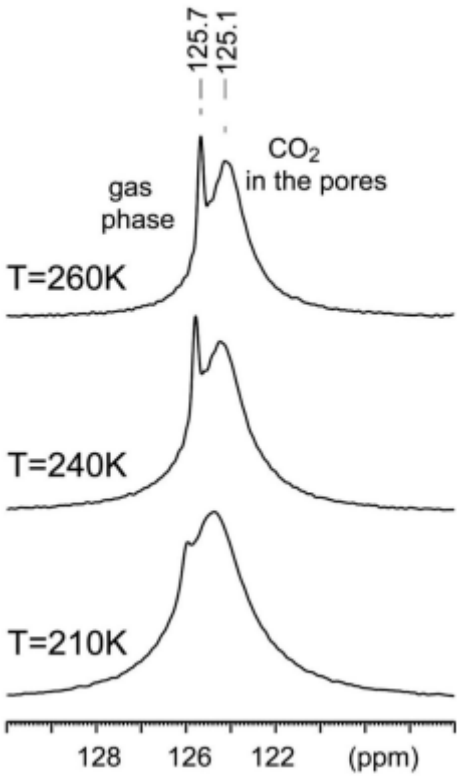

Figure A2.7. ^{13}C MAS collected on α-[Zn(BPEB)] loaded with ^{13}C enriched-CO_2. A recycle delay of 10 s was applied for collecting selectively CO2 signals.

A2.5. Gas adsorption measurements

Nitrogen adsorption-desorption isotherms were measured on α-[Zn(BPEB-d_4)] at liquid nitrogen temperature using a Micromeritics ASAP 2020 HD analyser (**Figure 2.4**). The samples were outgassed overnight at 120 °C under vacuum right before the analysis. Specific surface areas were calculated using the Brunauer, Emmett, and Teller (BET) model and the Langmuir model. The poresize distributions and the total pore volume were evaluated following non-local density functional theory (NLDFT) analysis for cylindrical pores and the Tarazona method. CO_2 adsorption isotherms were measured at 195 K up to 1 bar, and at 273, 283 and 298 K up to 10 bar using a Micromeritics ASAP 2050 analyser (**Figure 2.5**). The isosteric heat (ΔT) for CO_2 adsorption was calculated by applying the van't Hoff equation and considering the CO_2 isotherms at 195 K, 273 K, 283 K and 298 K. (**Figure A2 8 and Figure A2.9**):

$$\frac{d\ln(p)}{d\,(1/T)} = -\frac{\Delta H}{R}$$

where p is the pressure, T is the temperature and R the gas constant.

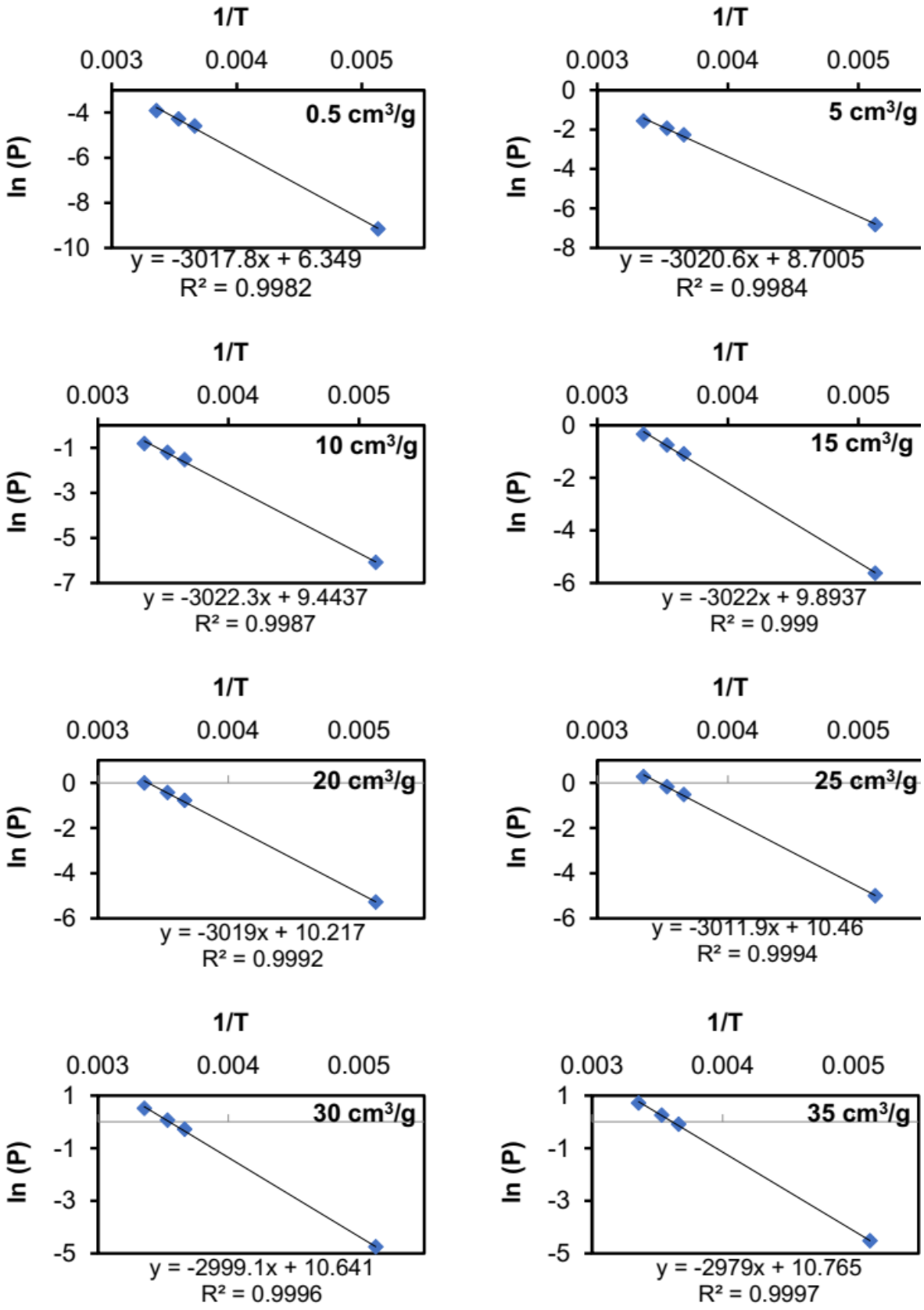

Figure A2.8. van't Hoff plots for the adsorption of CO_2 on α-[Zn(BPEB-d_4)] at distinct loading

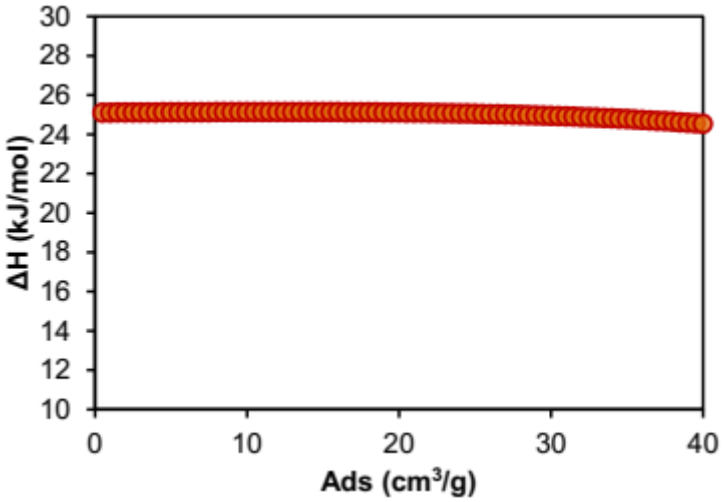

Figure A4.9. Calculated isosteric heat of adsorption at low loading of α-[Zn(BPEB-d4)]. The initial value is 25.1 kJ/mol and it decrease to 24.5 kJ/mol at 40 cm^3/g.

A2.6. Gas Adsorption Simulations

Grand Canonical Monte Carlo simulations were performed to estimate the adsorption behaviour of α-[Zn(BPEB-d_4)] (**Figure A2.10-14)**. The adsorptive was a geometry optimized CO_2 molecule. The Metropolis method and the Dreiding force field were used. The Lennard-Jones cut-off distance was set to 13 Å. The simulation box was a supercell of $1 \times 1 \times 3$ unit cells in which the atoms were fixed at the positions retrieved by PXRD Rietveld refinement. All the simulations includes 2×10^6 cycles equilibration period and 1×10^7 cycles of production for each pressure. The Ewald sum technique was used to compute the electrostatic interactions. CO_2 molecules within the crystal structure as obtained by applying a carbon dioxide density of 0.77 g/cm^3 and the optimization of the CO_2 coordinates using the Dreiding force field (500 cycles and convergence < 10^{-4} kcal/mol).

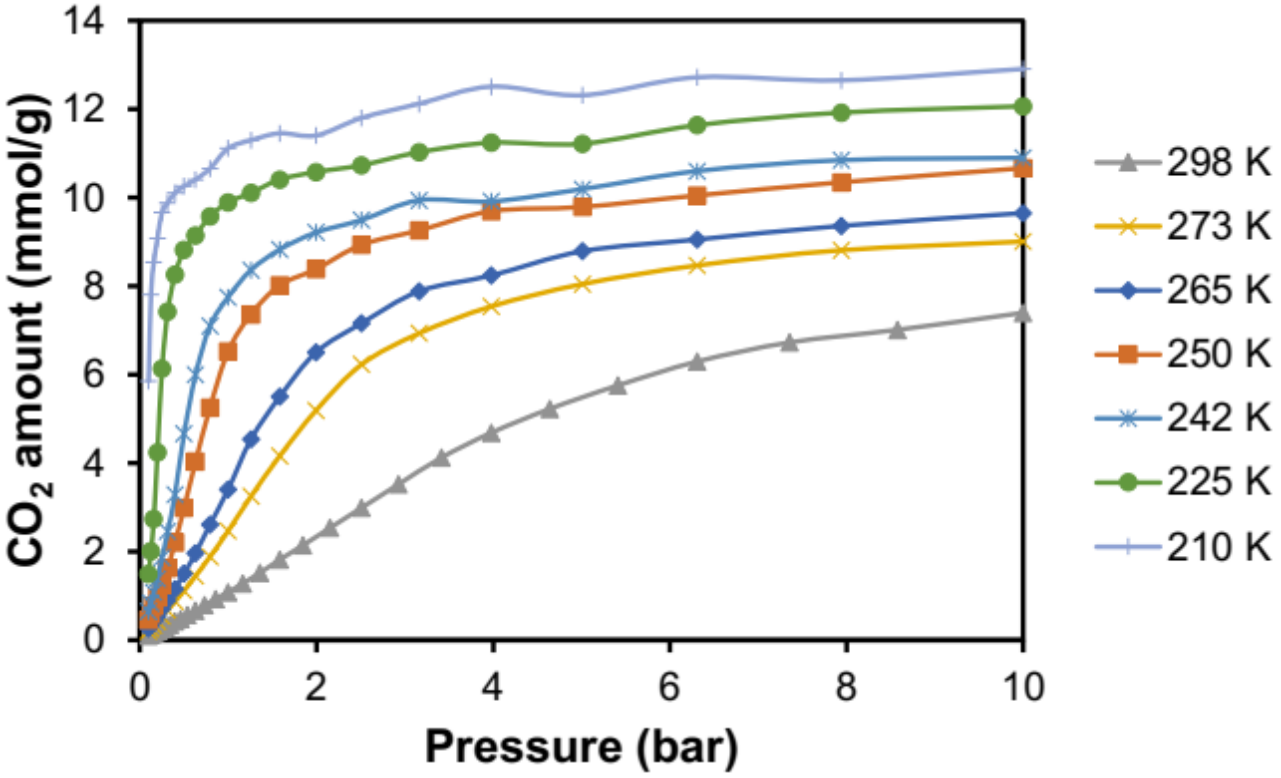

Figure A4.10. Simulated CO_2 adsorption isotherms of α-[Zn(BPEB)] at different temperatures.

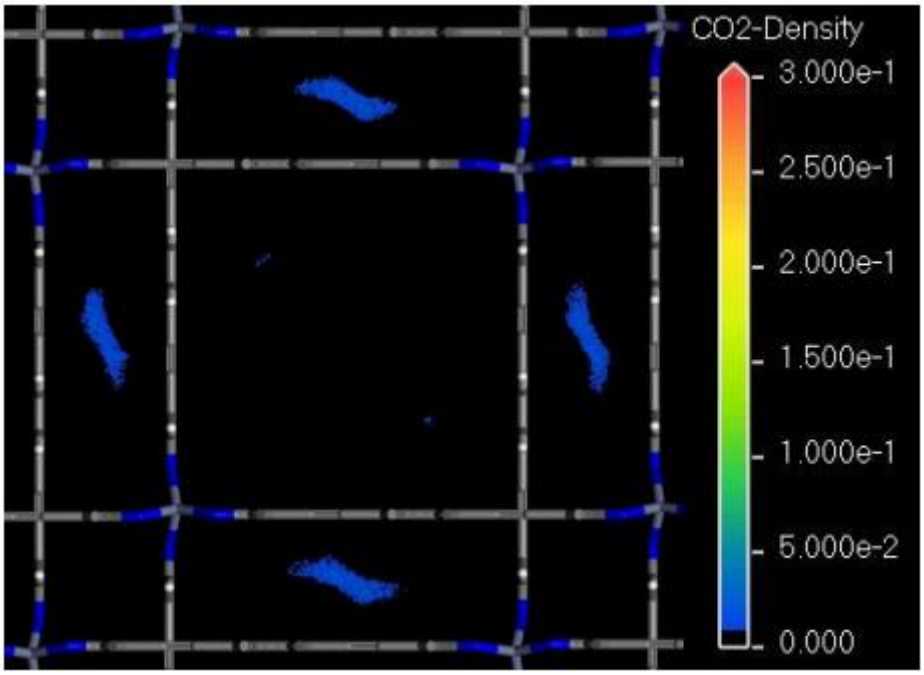

Figure A4.11. Distribution of center of mass of CO_2 molecules within the framework from the GCMC simulation of CO_2 adsorption at 298 K and 0.4 bar, as viewed perpendicular to the c-axis.

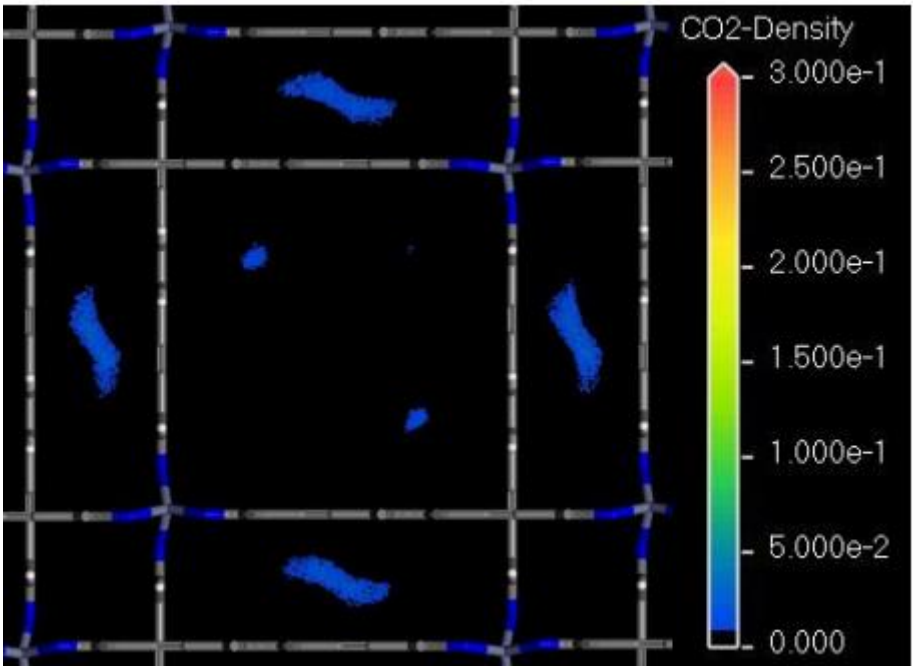

Figure A4.12. Distribution of center of mass of CO_2 molecules within the framework from the GCMC simulation of CO_2 adsorption at 298 K and 1 bar, as viewed perpendicular to the c-axis.

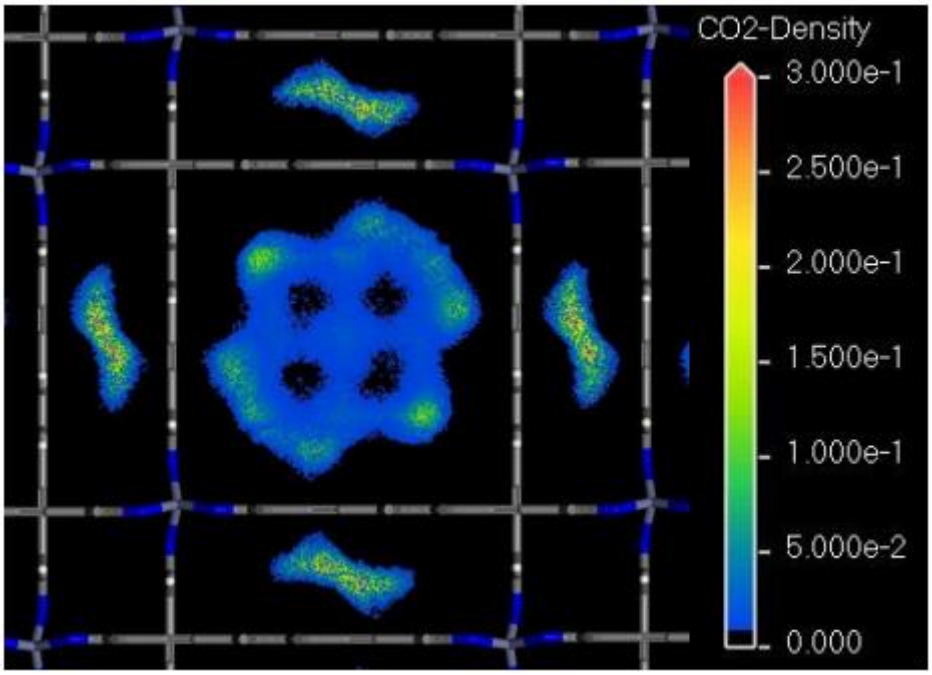

***Figure A4.13**. Distribution of center of mass of CO_2 molecules within the framework from the GCMC simulation of CO_2 adsorption work at 298 K and 10 bar, as viewed perpendicular to the c-axis.*

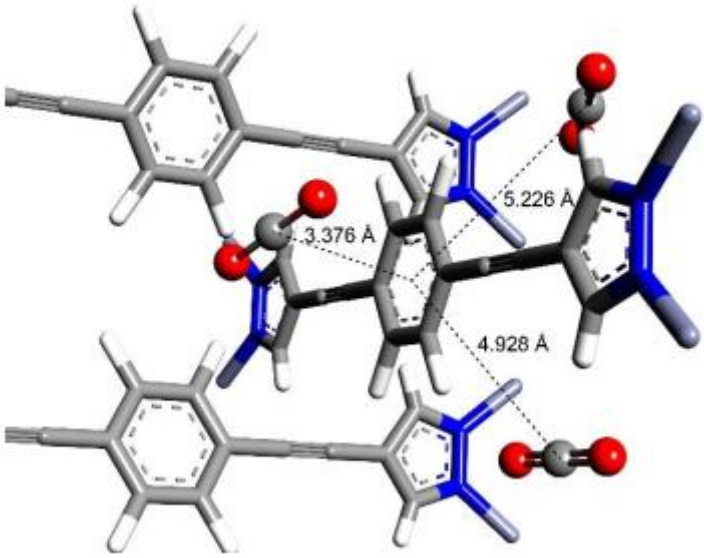

***Figure A4.14**. CO_2 molecules within the framework showing distances among CO_2 molecules and molecular rotor.*

Appendix 3

Supporting Information for Chapter 3

A3.1. Solution NMR of impure 4 and H_2BPEFB

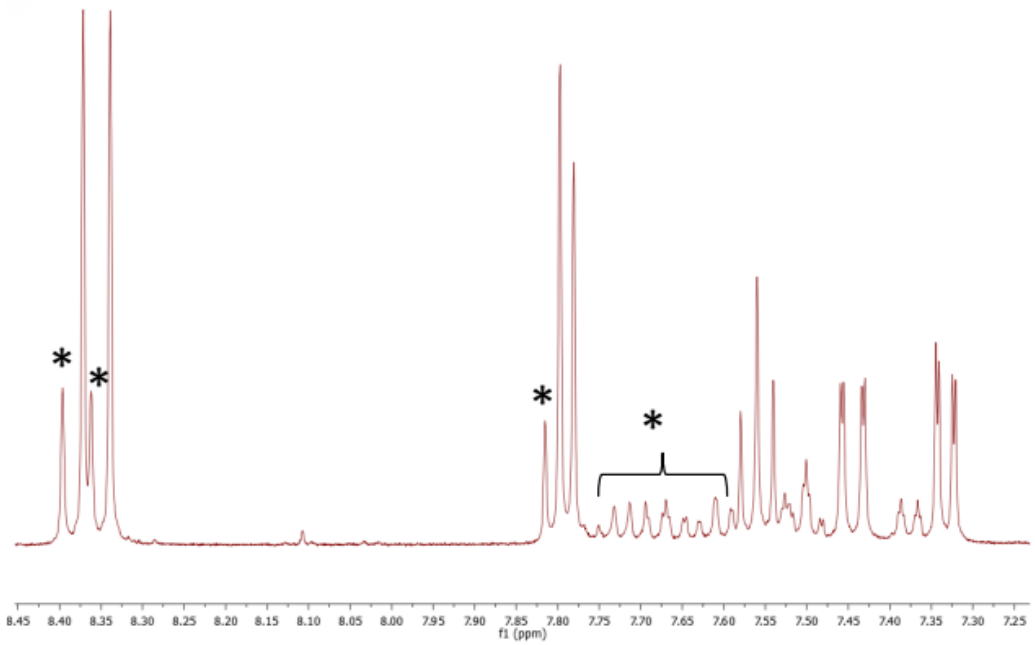

Figure A3.1. *Selected part of ^{1}H-NMR spectrum in $CDCl_3$ of* ***4*** *after column chromatography. Signals ascribed to the impurities cited in the main text are marked by asterisks (∗).*

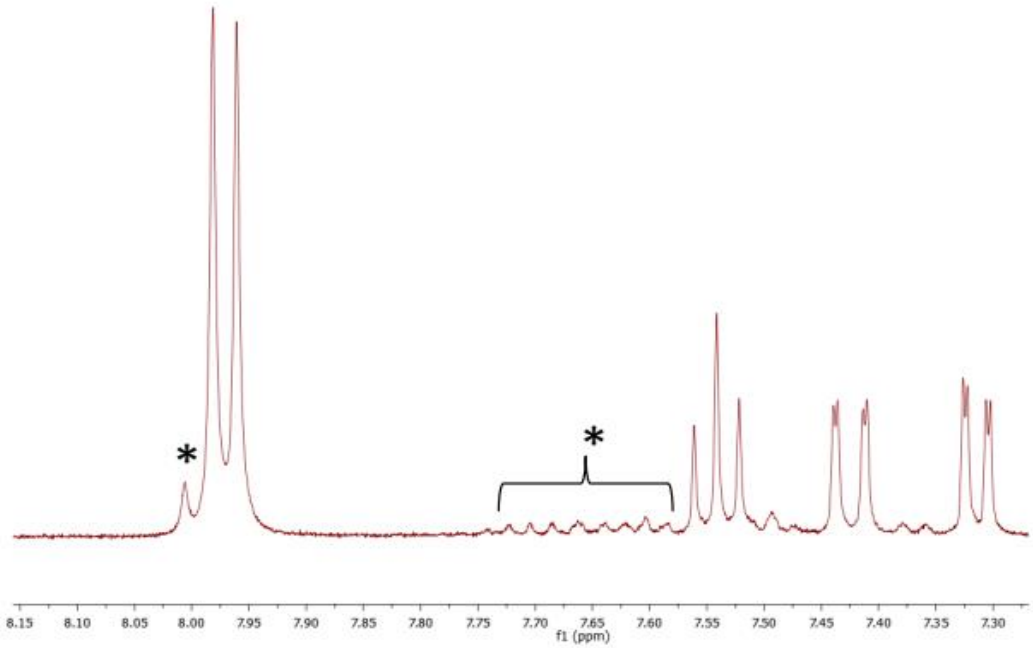

Figure A3.2. *Selected part of ^{1}H-NMR spectrum in $CDCl_3$ of H_2****BPEFB*** *obtained from impure* ***4***. *Signals ascribed to the impurities cited in the main text are marked by asterisks (∗). It is evident that simple deprotection of impure* ***4*** *did not remove the side products.*

A3.2. Powder X-Ray Diffractography

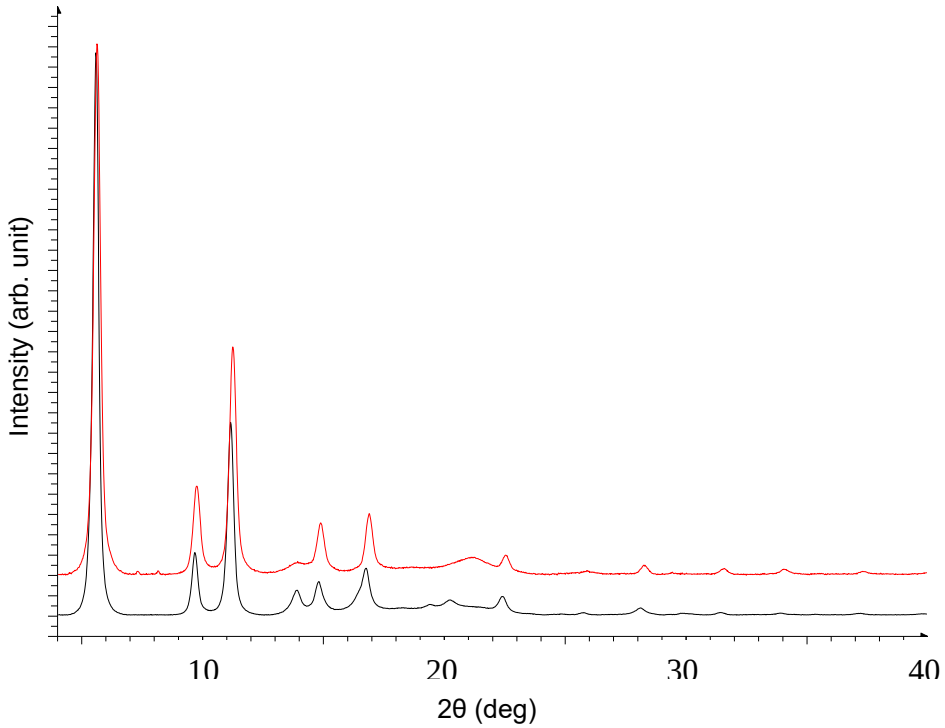

Figure A3.4. *Comparison of the PXRD patterns of [Ni(**BPEFB**)] (red trace) and [Ni(BPEB)] (black trace): the isomorphism of the two compounds is evident. When compared to α[-Zn(**BPEFB**)], the lower degree of crystallinity of the Ni-MOF is*

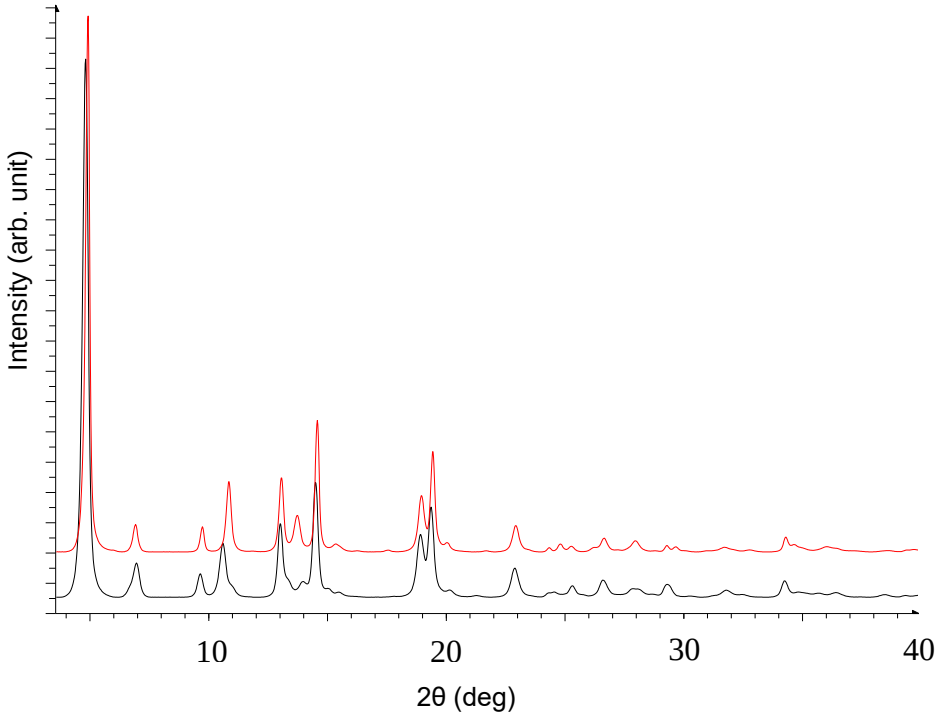

Figure A3.3. *Comparison between the PXRD patterns of α[-Zn(**BPEFB**)] (red trace) and α-[Zn(BPEB)] (black trace). The isomorphism between the two compounds is evident.*

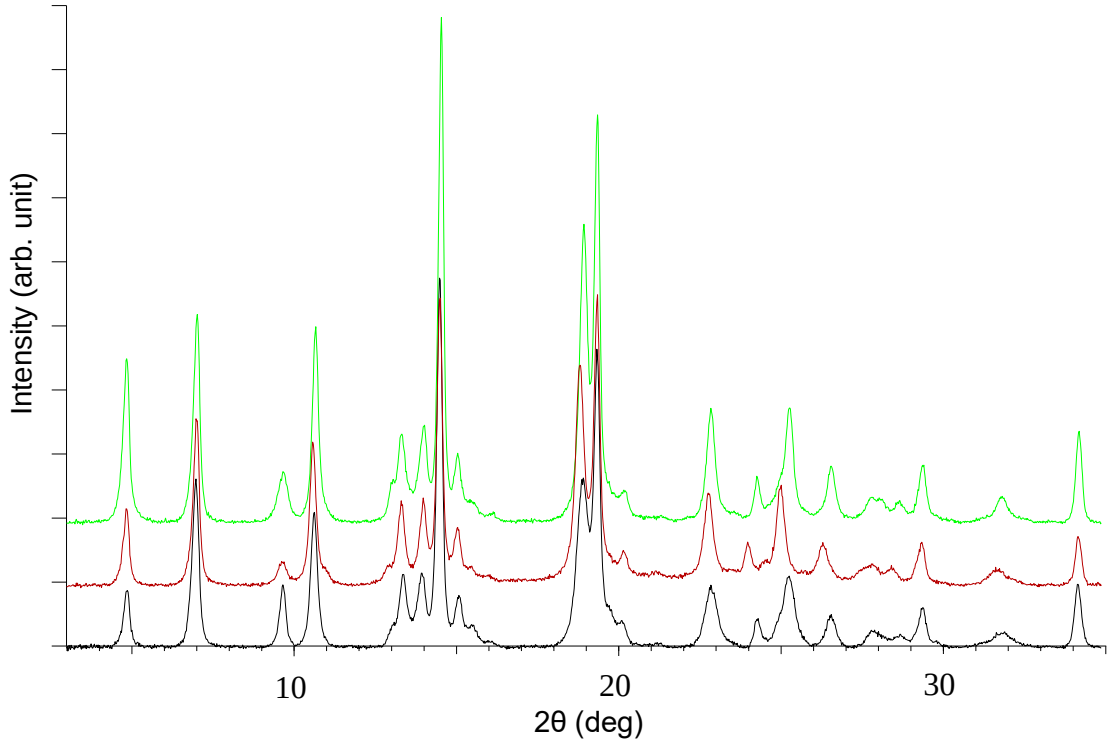

***Figure A3.5**. Comparison between three batches of [Zn(**BPEFB**)] synthetized using different reaction conditions. The variance of the relative intensities between the first two peaks can be appreciated, indicating a different ratio between α and β phases.*

A3.3. Differential Scanning Calorimetry Analysis

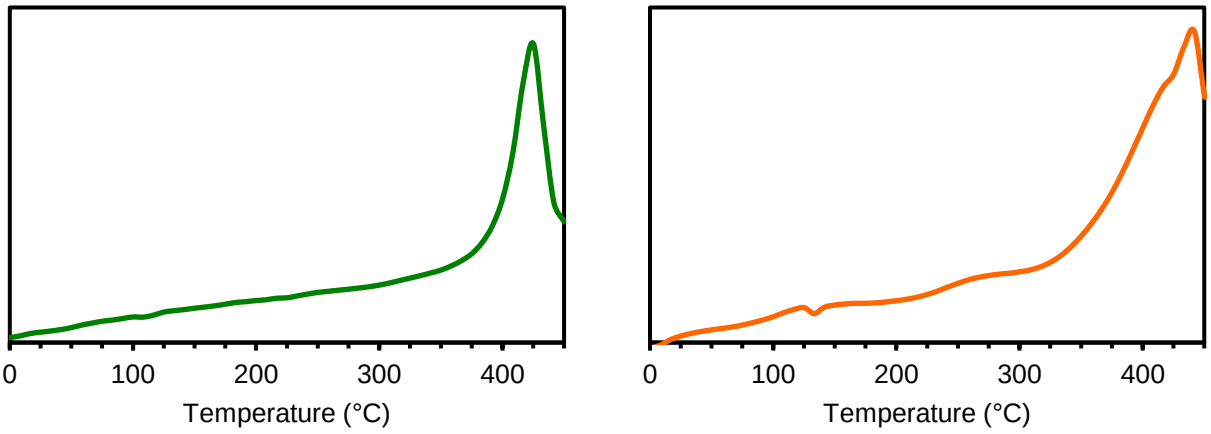

***Figure A3.6**. DSC analysis for α[-Zn(**BPEFB**)] (green trace) and [Ni(**BPEFB**)] (orange trace) collected from 0 to 450 °C with a heating rate of 10 °C/min under a 80 ml/min flux of nitrogen.*

A3.4. Isosteric heats of adsorption and IAST selectivity calculations

$Q_{st}(CO_2)$ for [Ni(**BPEFB**)] and α-[Zn(**BPEFB**)] was derived from CO_2 adsorption isotherms collected at 273, 283 and 298 K up to 10 bar of pressure using the van't Hoff equation:

$$Q_{st} = RT^2\left(\frac{\partial \ln p}{\partial T}\right)$$

First, the three isotherms were fitted adopting a Langmuir-Freundlich model, which has the general form

$$\boldsymbol{q} = \frac{q_{max} b p^t}{1 + b p^t}$$

where $\boldsymbol{q}$ is the adsorbed quantity at pressure p, q_{max} is the saturation loading and b and t are the Freundlich parameters. Parameter b can be written

$$b = b_0 e^{E/RT}$$

where b_0 is a pre-exponential factor related to the gas saturation pressure p^0 and E can be considered as the mean adsorbent-adsorptive interaction energy calculated from $p = 0$ to $p_{max.}$ In our fitting procedure, we used Langmuir-Freundlich model to fit simultaneously the three experimental curves. We allowed the saturation loading q_{max} and the Freundlich parameters t to vary independently for each experimental isotherm, while the pre-exponential factor b_0 and the energy E had to be the same for all the isotherms. We had then a total of eight fitting parameters: b_0, E, Q_{273}, t_{273}, Q_{283}, t_{283}, Q_{298} and t_{298}

Calculations were run using Mathlab software. The calculated fitting parameters are reported in **Table A3.1**, while **Figure A3.4a,b** shows the fitted curve over the experimental isotherms. We can reverse the Langmuir-Freundlich equation to obtain an analytical expression of p as a function of $\boldsymbol{q}$

$$p = \left(\frac{\boldsymbol{q}}{b(q_{max} - \boldsymbol{q})}\right)^{1/t}$$

And, thus, calculate Q_{st} via the van't Hoff equation. Since we were interested in calculating the low-loading Q_{st}, in the fitting procedure of experimental isotherms we only took in account experimental points up to 2 mmol/g of adsorbed quantity.

***Table A3.1**. Fitting parameters obtained for carbon dioxide adsorption for α-[Zn(**BPEFB**)] and [Ni(**BPEFB**)] using a Langmuir-Freundlich model considering experimental points up to Q(ads) = 2 mmol/g.*

	Q_{273} (mmol/g)	Q_{283} (mmol/g)	Q_{298} (mmol/g)	t_{273}	t_{283}	t_{298}	b_0 (bar^{-1})	E (kJ/mol)
α-[Zn(**1**)]	7.1191	6.5314	5.5996	0.9459	1	0.9925	$8.63 \cdot 10^{-4}$	13.8905
[Ni(**1**)]	8.7959	8.7959	7.1385	0.9054	0.8688	0.9393	$4.49 \cdot 10^{-3}$	9.6037

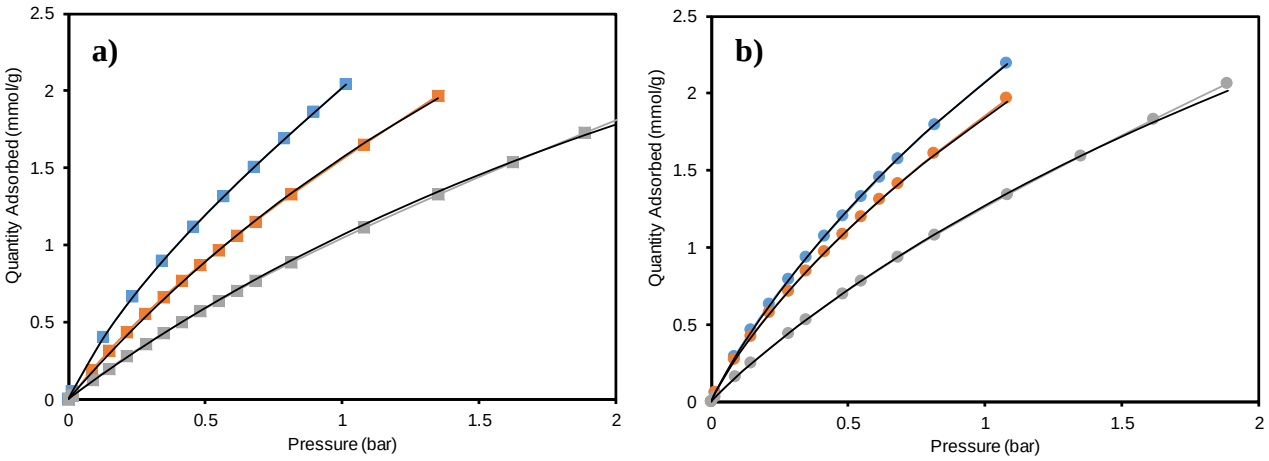

***Figure A3.7**. Results of the fitting procedure for **a)** α-[Zn(**BPEFB**)] (squares) and **b)** [Ni(**BPEFB**)] (dots) using the parameters reported in **Table A3.1** and the Langmuir-Freundlich model. CO_2 isotherms at 273 K (blue trace), 283 K (orange trace), 298 K (grey trace), and fitting (solid black trace).*

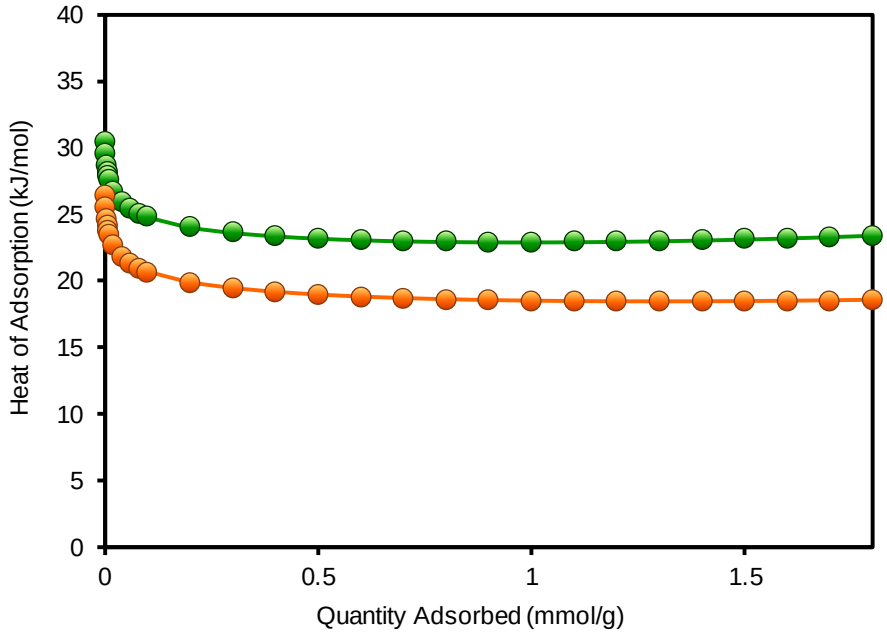

Figure A3.8. *$Q_{st}(CO_2)$ values calculated at increasing loading values for α-[Zn(**BPEFB**)] (green trace) and [Ni(**BPEFB**)] (orange*

For IAST calculations, N_2 isotherms were fitted up to 10 bar adopting the Langmuir-Freundlich model. We then calculated spreading pressures (integrals were solved using Wolfram Alpha) and we applied the standard equations for IAST.

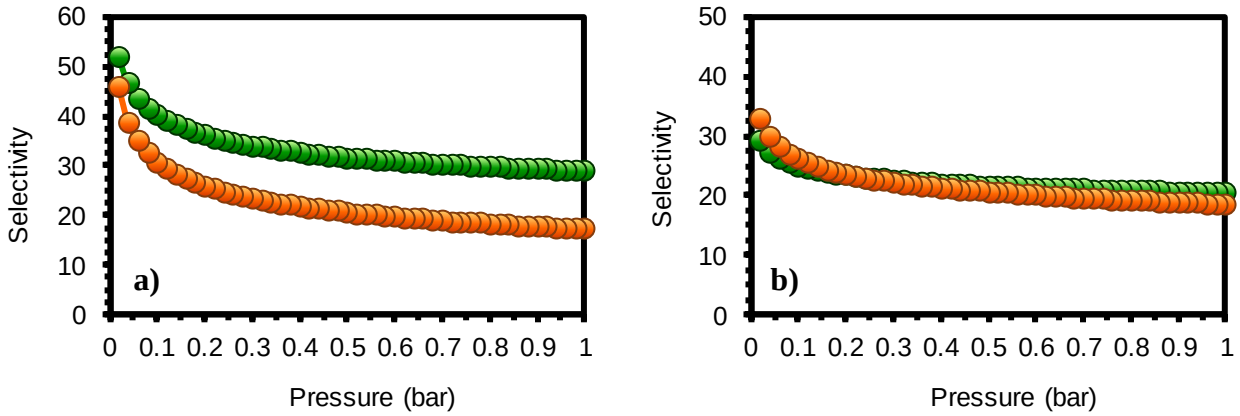

Figure A3.9. *IAST selectivity for the adsorption of CO_2 over N_2 from a 15:85 mixture calculated at **a)** 273 K and **b)** 298 K for α-[Zn(**BPEFB**)] (green trace) and [Ni(**BPEFB**)] (orange trace).*

A3.5. Pore Size Distributions

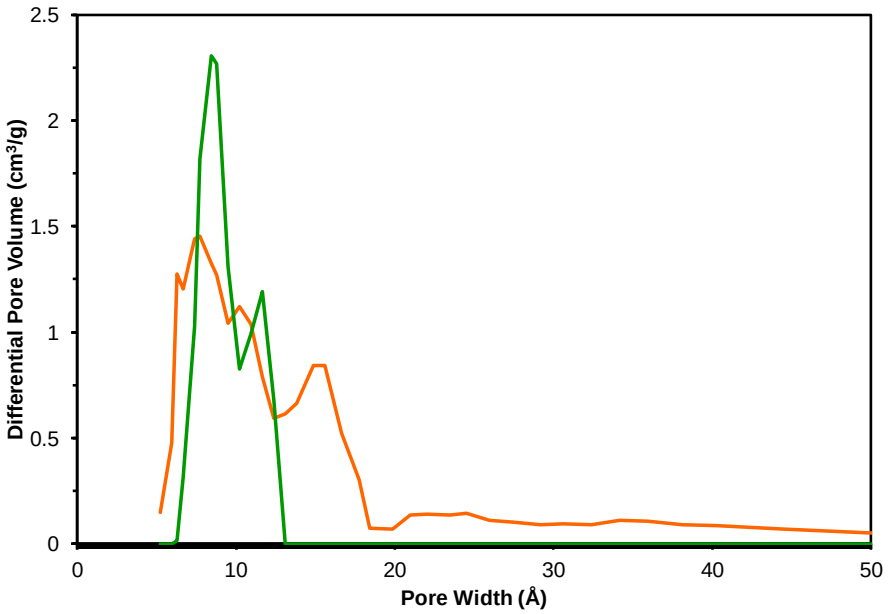

Figure A3.10. *Pore size distribution graphs for α-[Zn(**BPEFB**)] (green trace) and [Ni(**BPEFB**)] (orange trace) calculated by Non-Local DFT applying the Tarazona model for cylindrical pores.*

A3.6. ^{19}F MAS solid state NMR of α-[Zn(**BPEFB**)]

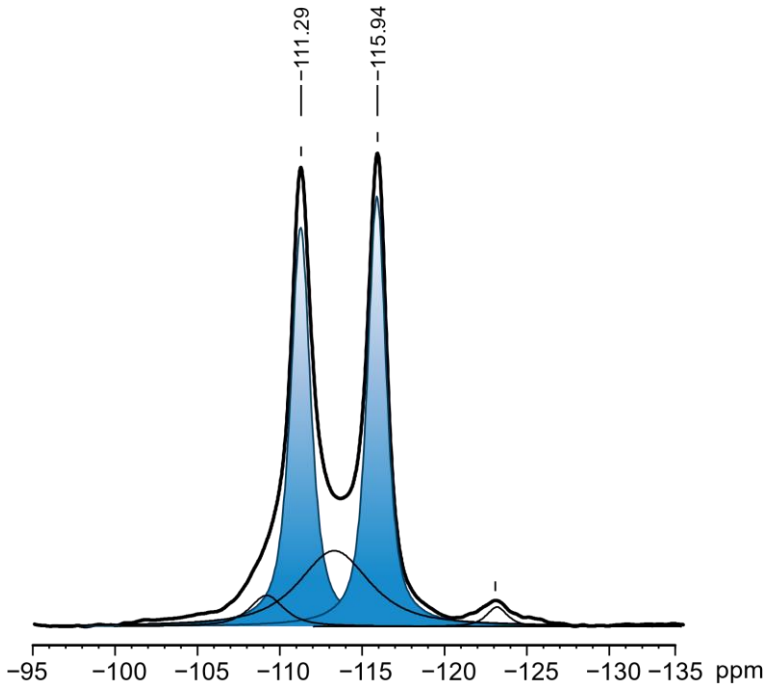

Figure A3.11. *^{19}F MAS solid state NMR of α-[Zn(**BPEFB**)] collected with a recycle delay of 20 s. The blue peaks represent the deconvolution of the two main signals deriving from fluorine atoms of α-[Zn(**BPEFB**)] structure. Smaller peaks indicate the presence of minor impurities.*

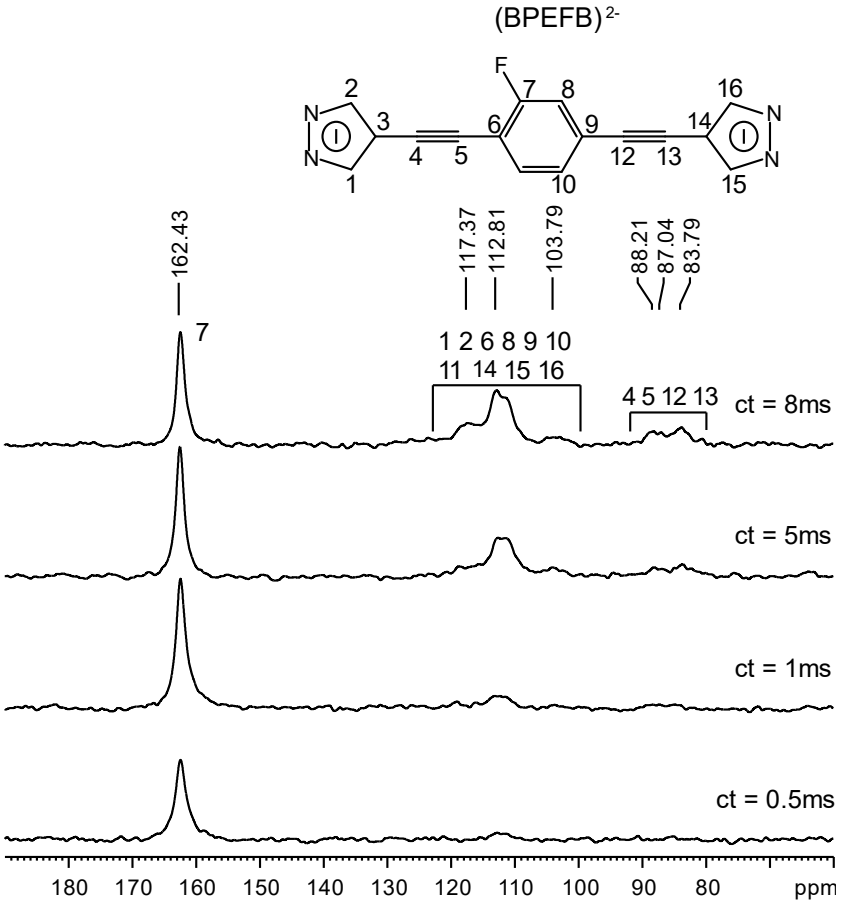

***Figure A3. 12**. ^{13}C CP/MAS NMR experiments cross-polarized with ^{19}F collected on α-[Zn(**BPEFB**)] with increasing contact times. It can be see that, as ct increases, carbon atoms further from the fluorine receive magnetization from it and give rise to new signals.*

*Table A3.2. Summary of [Zn(**BPEFB**)], [Ni(**BPEFB**)], [Zn(**BPEFB**)] and [Ni(**BPEFB**)] porosity parameters.*

	T (K)	P (bar)	Surface area (BET) (m^2/g)	Pore Volume (cm^3/g)	$Q_{max}(CO_2)$ (mmol/g)	$Wt(Q_{max})$ %	$Q_{1\ bar}(CO_2)$ (mmol/g)	Q_{st}[b] (kJ/mol)	Selectivity[c]
[Zn(**BPEFB**)]	/	/	1000	0.41	/	/	/	28	/
	195	1[a]			9.9	43.6	/	/	/
	273	10			8.3	36.5	2.04	/	36
	298	10			5.7	25.1	1.05	/	24
[Zn(**BPEB**)]	/	/	985	0.60					
	195	1			11.3	49.7		23	/
	273	10			8.2	36.1	1.76	/	21
	298	10			5.2	22.9		/	20
[Ni(**BPEFB**)]	/	/	1219	0.72	/	/	/	24	
	195	1[a]			12.6	55.4	/		/
	273	10			10.7	47.1	2.09	/	26
	298	10			7.7	33.9	1.26	/	24
[Ni(**BPEB**)]	/	/	1900	0.79					
	195	1[a]			11.6	51.0	/	23	/
	273	10			8.5	37.4	2.09	/	19
	298	10			5.9	26.0	1.26	/	19

Appendix 4.

Supporting Information for Chapter 4

A4.1. IR spectroscopy (ATR method) of **1**

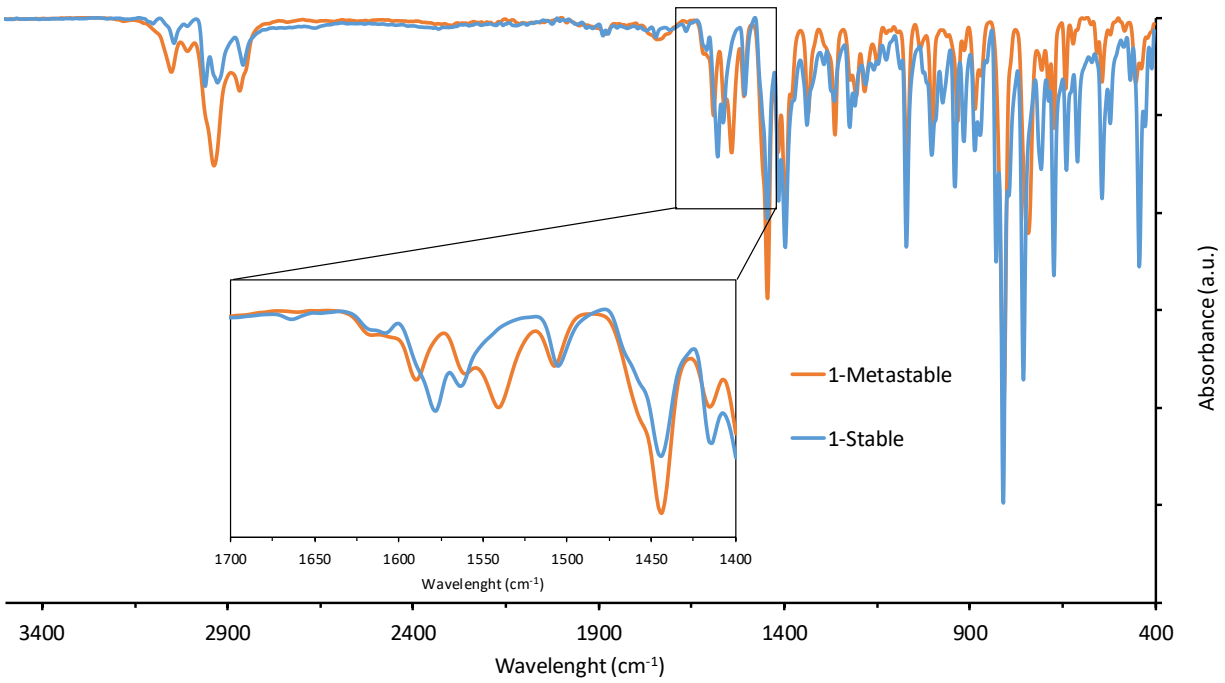

Figure A4.1. *IR spectra of **1**-stable (blue trace) and **1**-metastable (orange trace). The inset shows the C-C double-bond stretching region. The shift of the C-C double-bond stretching energy from 1578 to 1540 cm^{-1} is indicative of the formation of the metastable state at the expanses of the stable state.*

A4.2. Raman spectroscopy of **1**

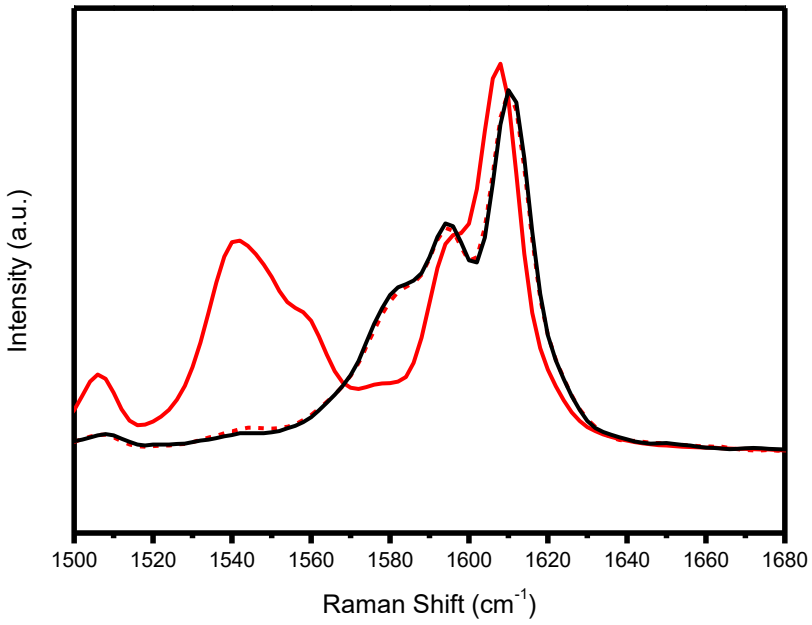

Figure A4.2. *Selected part of Raman spectra (785 nm, 50 mW) of **1**-stable (black trace), photostationary state mixture after irradiation with 365 nm light containing 94% of **1**-metastable (solid red line), and photostationary-state mixture after irradiation with 470 nm light showing complete recover of **1**-stable (dotted red line. Sample of **1**-stable was drop casted on quartz wafer from 1 mM (CH_2Cl_2) solution. A 1 mM solution of of **1**-stable in CH_2Cl_2 was irradiated with 365 nm until PSS was reached and drop casted on the quartz wafer. The same solution was irradiated with 470 nm light to promote the back-switch until PSS was reached. The observed signal is associated with C-C double-bond stretching mode and the shifting is indicative of the formation of **1**-metastable.*

A4.3. Solution UV/Vis spectroscopy of **1**

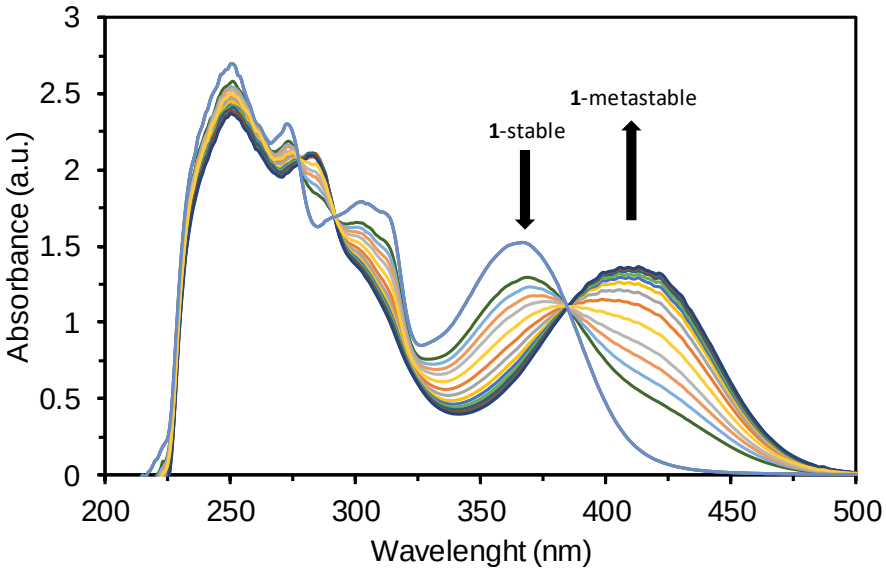

***Figure A4.3**. Collection of solution UV/Vis spectra of **1** collected on a 10^{-4} M solution in CH_2Cl_2. The spectra were collected at increasing irradiation time with 365 nm light. Total irradiation time: 33 minutes. PSS was reached after 21 minutes of irradiation. The disappearance of the peak at 368 nm in favour of the peak at 415 nm is indicative of the formation of **1**-metastable.*

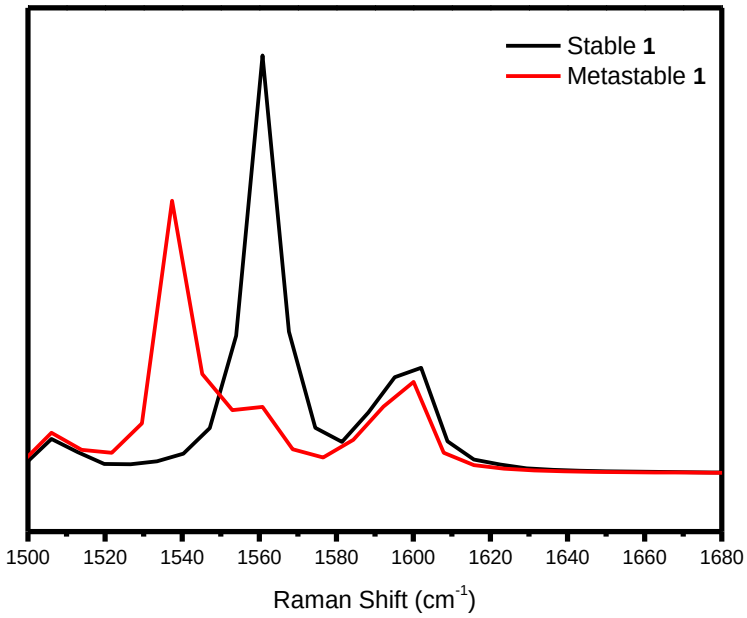

***Figure A4.4**. Comparison of selected part calculated (DFT, 631g-(d,p), scaling factor 0.978) raman spectra of 1-stable (black trace) and **1**-metastable (red trace). Gauss line broadening DFT (B3LYP 6-311++G(d.p) optimized structures of **1**-stable and **1**-metastable.*

A4.4. ^{1}H and ^{13}C solution NMR of **1**

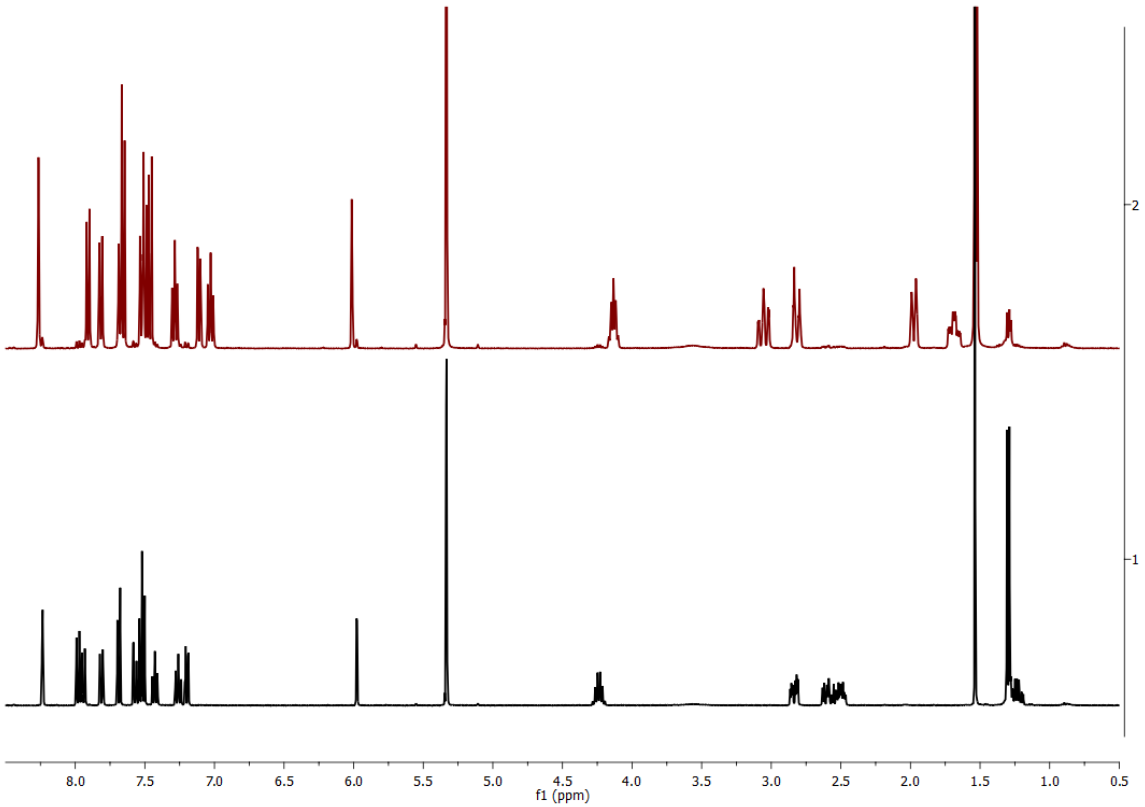

Figure A4.3. *Full ^{1}H-NMR solution spectra (CD_2Cl_2, 400 MHz, RT) of **1**-stable (black trace) and **1**-metastable (red trace) obtained irradiating a 10^{-2} M solution of **1**-stable with 365 nm light for 30 minutes.*

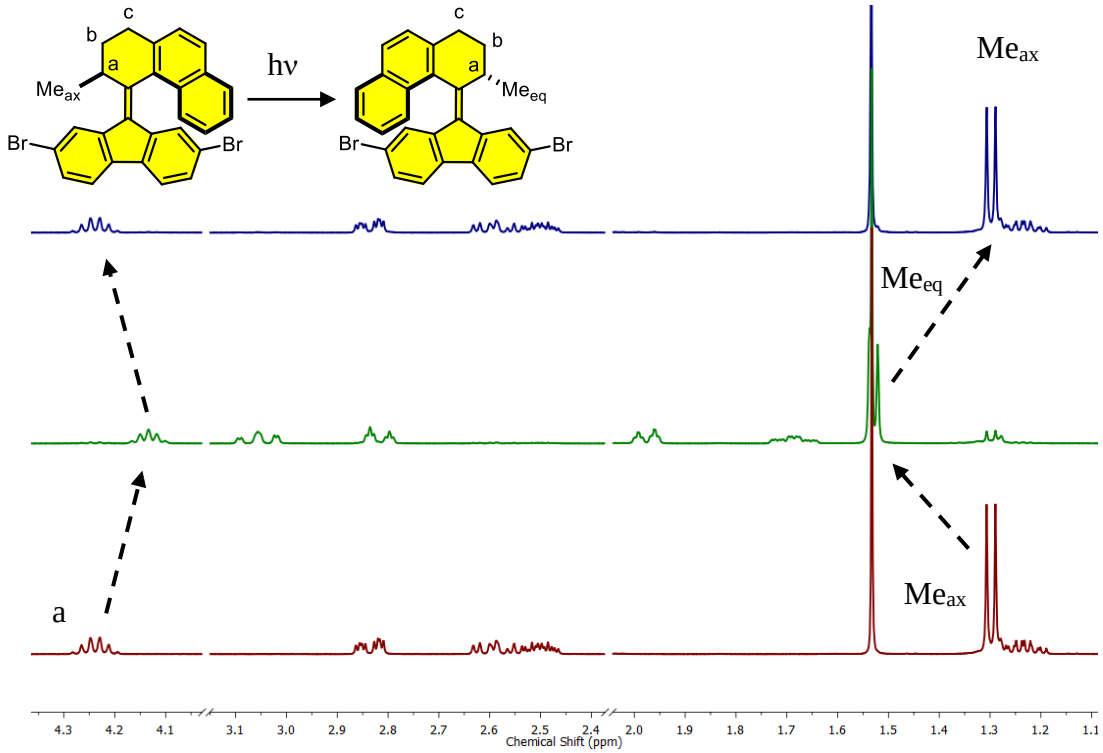

Figure A4.4. *Selected part of ^{1}H NMR (CD_2Cl_2, 400 MHz, RT) spectra showing changes upon irradiation with 365 nm and subsequent irradiation with 470 nm. Initial **1**-stable (red), photostationary state mixture (PSS_{365}) obtained upon irradiation with 365 nm for 30 min. (green) (**1**-stable:**1**-metastable 6:94), photostationary state mixture (PSS_{470}) mixture obtained upon irradiation of (PSS_{365}) mixture with 470 nm for 1 h (**1**-stable:**1**-metastable 97:3).*

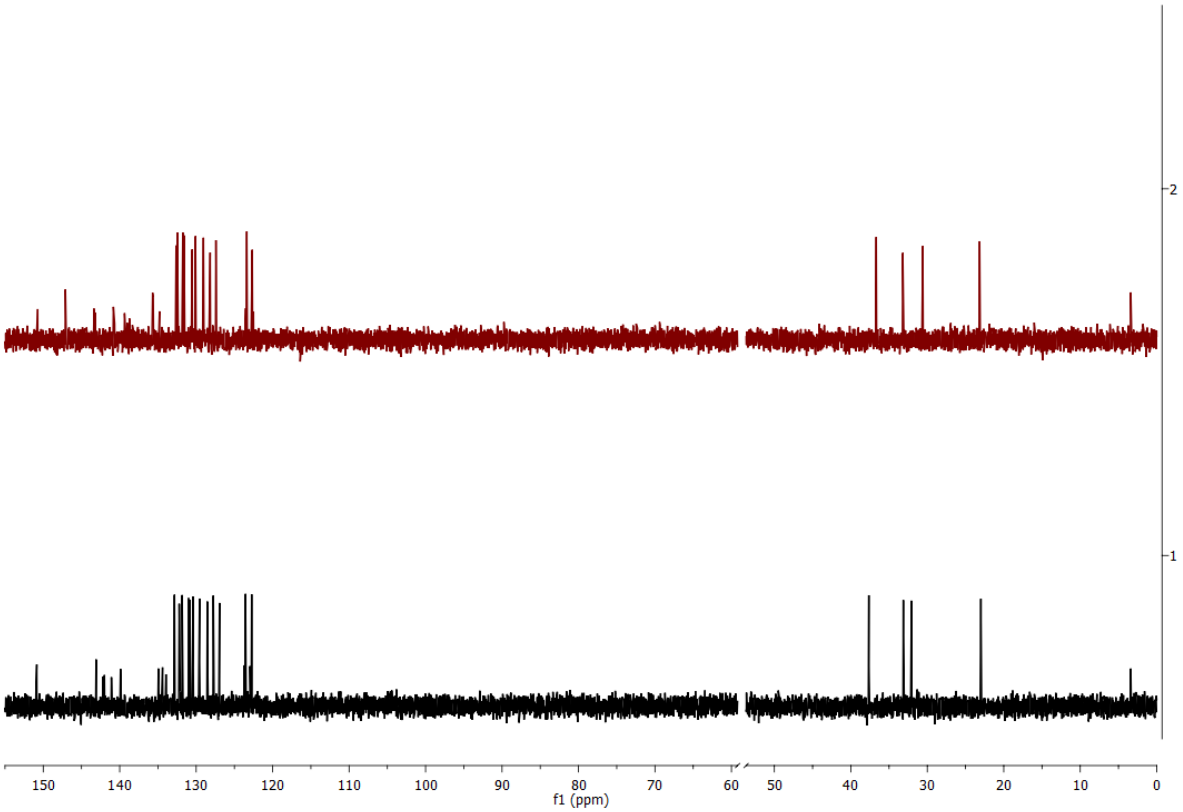

Figure A4.5. *Full ^{13}C-NMR solution spectra (CD_2Cl_2, 400 MHz, RT) of **1**-stable (black trace) and **1**-metastable (red trace) obtained irradiating a 10^{-2} M solution of **1**-stable with 365 nm light for 30 minutes. Solvent signal has been cut out for*

A4.5. Powder X-Ray Diffraction data of PSF1 and PSF2

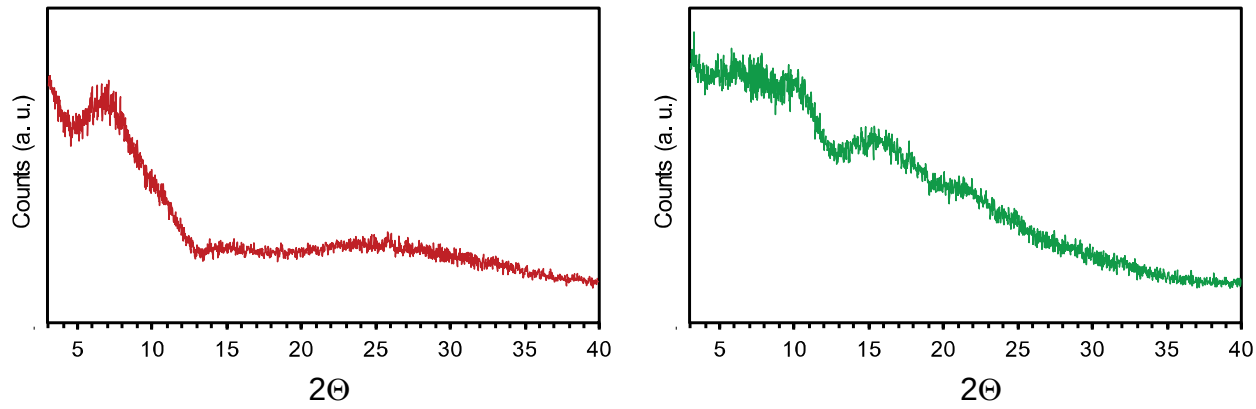

***Figure A4.6**. X-Ray Powder Diffraction analysis of **PSF1** (red trace) and **PSF2** (green trace). Both materials are amorphous, as expected.*

A4.6. Differential Scanning Calorimetry and Thermogravimetric Analysis of PSF1 and PSF2

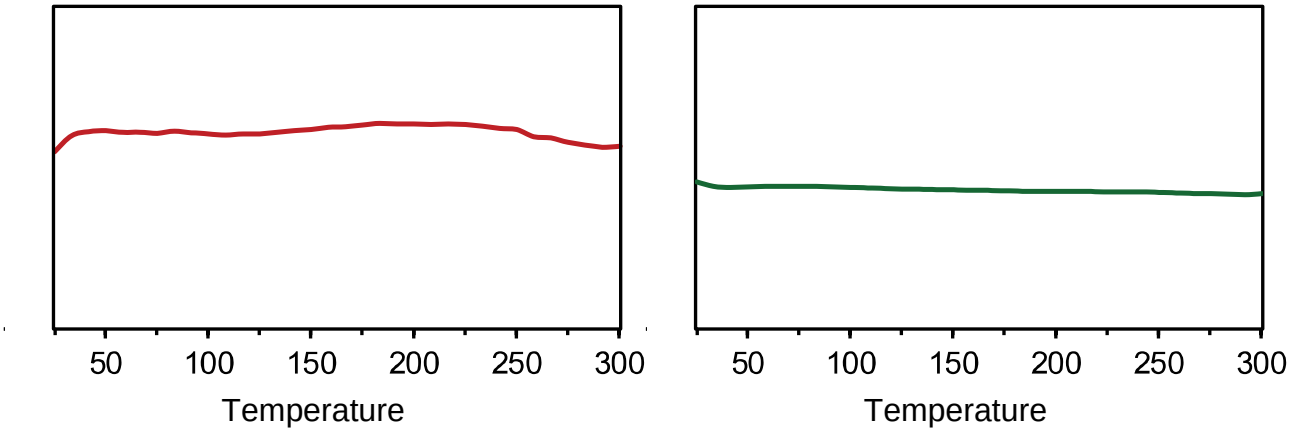

***Figure A4.7**. Differential Scanning Calorimetry analysis of **PSF1** (red trace) and **PSF2** (green trace) collected from 25 to 300 °C with a heating rate of 10 °C under 80 ml/min flux of nitrogen. The stability of both materials up to 300 °C is evident.*

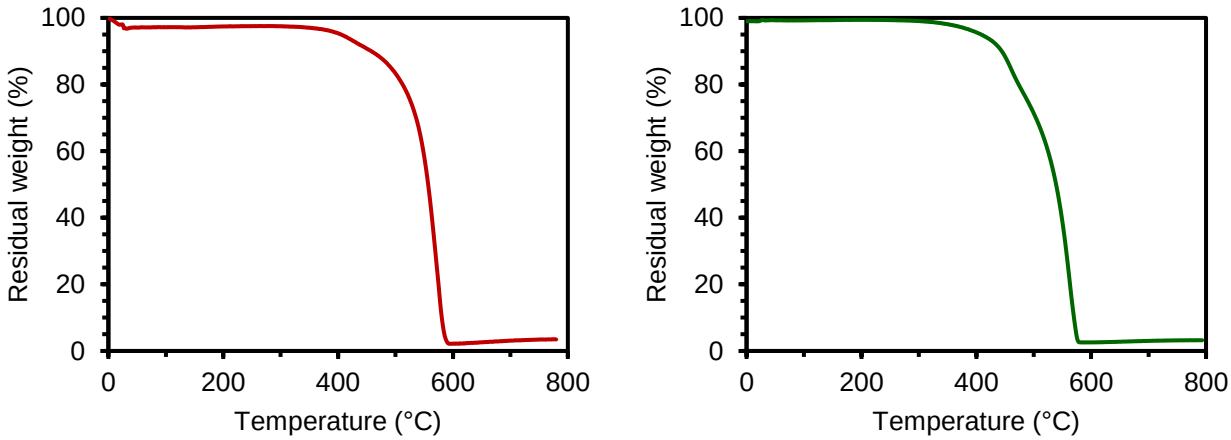

***Figure A4.10**. Thermogravimetric Analysis of **PSF1** (red trace) and **PSF2** (green trace) collected from 25 to 800 °C with a heating rate of 10 °C under 80 ml/min flux of air.*

A4.7. IR spectroscopy of **PSF1** and **PSF2**

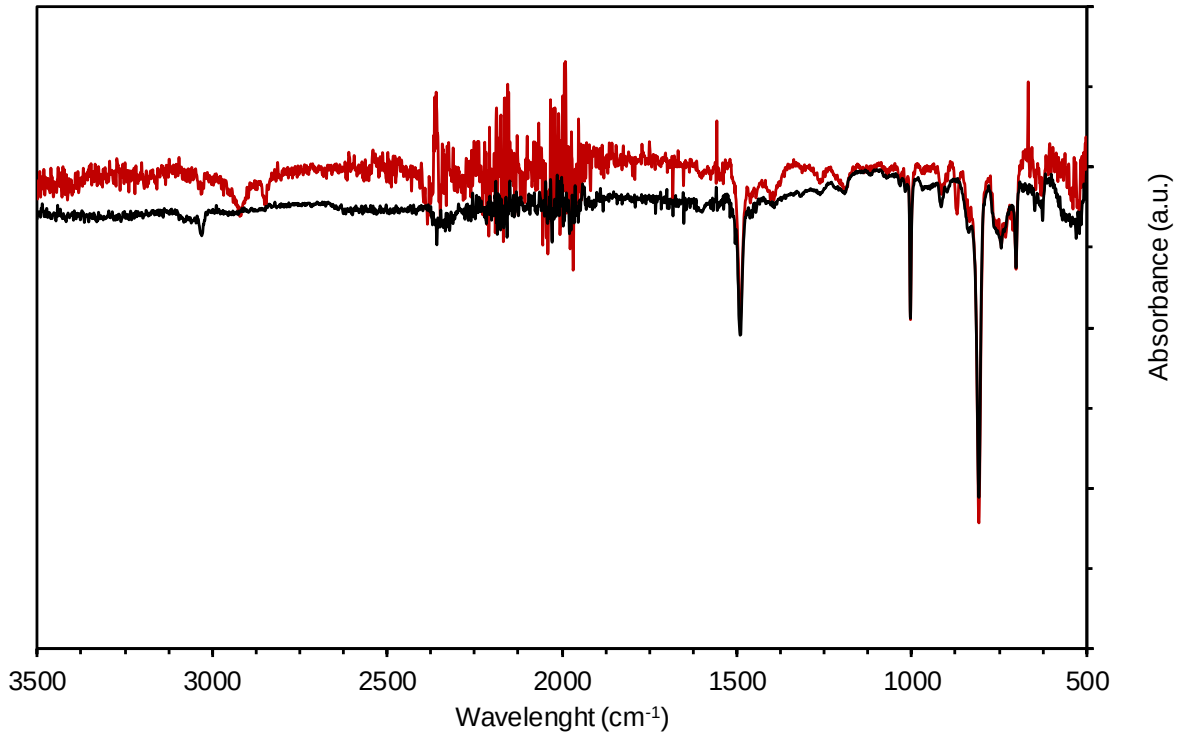

Figure A4.11. *IR spectroscopy (ATR method) of pristine **PSF1** (black trace) and irradiated **PSF1** (yellow trace, 365 nm, 20 minutes). Unfortunately, signal-to-noise ratio is too low to determine the occurrence of any difference before and after irradiation. This technique can't be used to prove the formation of switch metastable state in solid state for **PSF1**.*

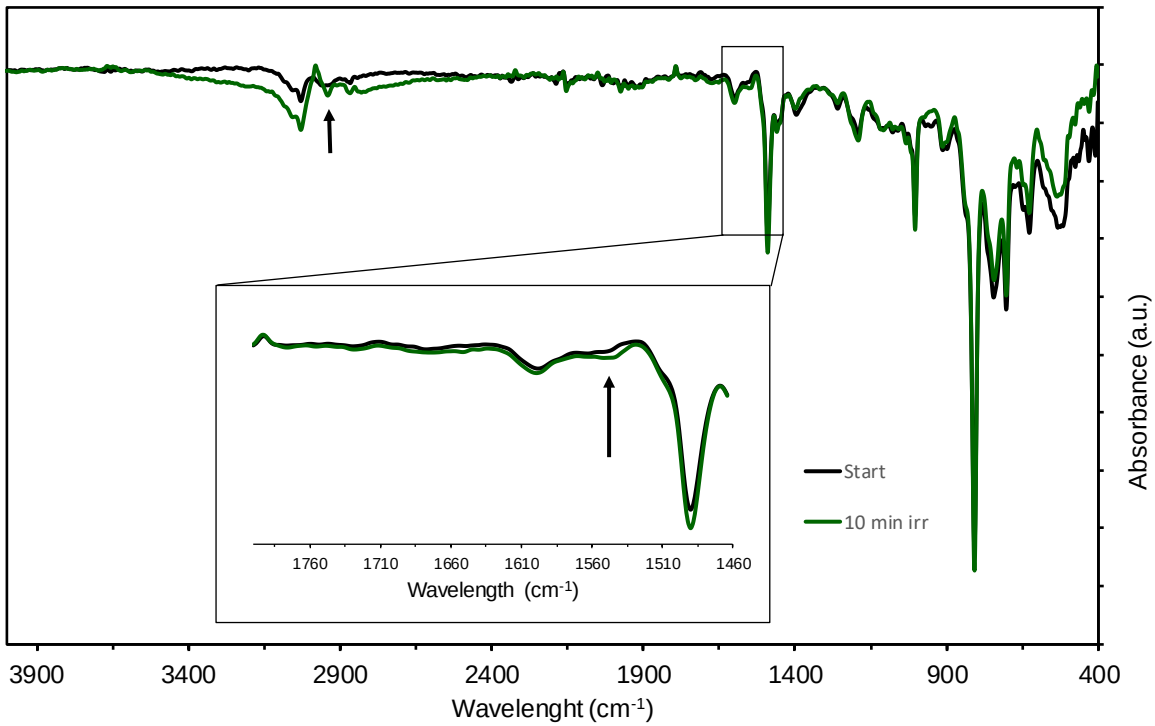

Figure A4.12. *IR spectroscopy (ATR method) of pristine **PSF2** (black trace) and irradiated **PSF2** (green trace, 365 nm, 10 minutes). The signal arising from switch C-C double bond is very weak, but a very small change in the 1560 cm^{1} region (see inset) is detectable, suggesting the formation of **1**-metastable in solid **PSF2**.*

A4.8. Gas adsorption analysis and heat of adsorption calculations

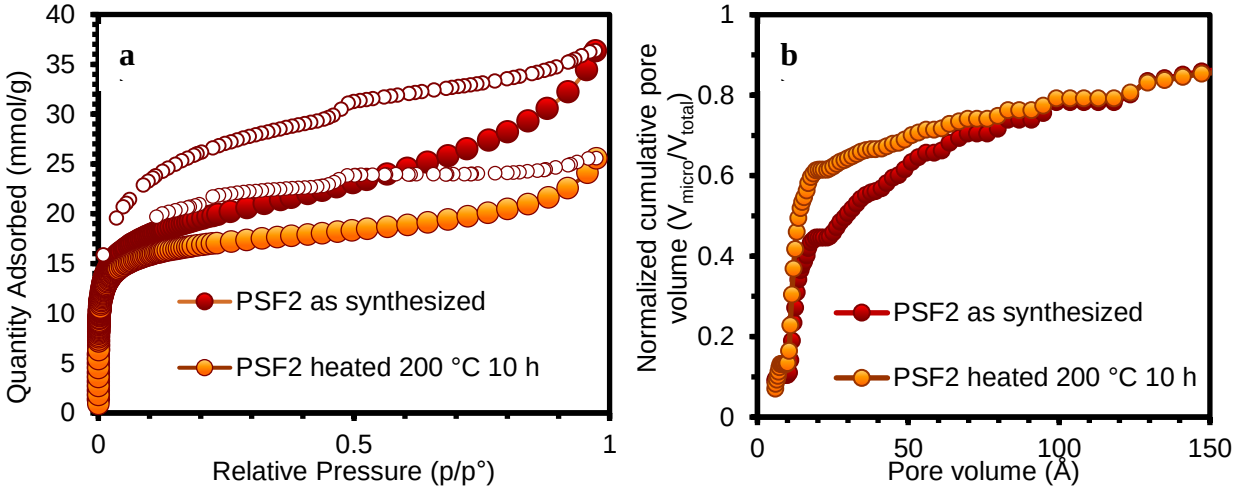

***Figure A4.13**. a) N_2 adsorption/desorption isotherms collected at 77 K and **b)** cumulative pore volume normalized over the total pore volume of pristine sample of **PSF2** and one thermally treated at 200 °C for 10 hours. The modifications on the isotherms shapes and on the overall porosity of the material can be appreciated.*

Table A4.3**. Textural parameters derived from the nitrogen isotherms collected at 77 K presented in **Figure A5.13

	S_{BET} (m^2/g)	$S_{Langmuir}$ (m^2/g)	Q_{ads} (p/p^o = 0.6) (mmol/g)	V_{total}[a] (cm^3/g)	V_{micro}[b] (cm^3/g)	V_{micro}/V_{total} (%)
PSF2 as synthesized	1615	1830	24.4	1.19	0.53	45
PSF2 heated 200 °C 10 h	1431	1618	18.5	0.82	0.51	61

[a] Calculated applying NLDFT adopting N_2@77K Carbon slit pore model

[b] Calculated considering pored up to 20 Å wide

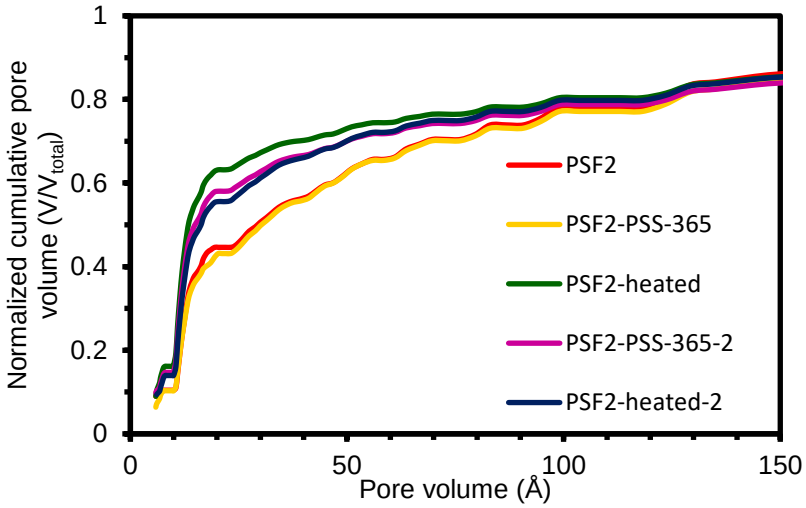

***Figure A4.14**. Cumulative Pore Volume of the various transformation of **PSF2** normalized over the total pore volume calculated by NLDFT and employing the N_2@carbon slit pore model. Note the increase in microporosity of the material after the first thermal treatment.*

Table A4.4. Textural parameters derived from N_2 adsorption isotherms collected at 77 K

	S_{BET} (m^2/g)	$S_{Langmuir}$ (m^2/g)	$Q_{ads}(p/p^o = 0.6)$ (mmol/g)	V_{total}[a] (cm^3/g)	V_{micro}[b] (cm^3/g)	V_{micro}/V_{total} (%)
PSF2	1615	1830	24.4	1.19	0.53	45
PSF2-PSS-365	1213	1374	19.3	0.94	0.41	44
PSF2-heated	1177	1335	15.7	0.66	0.42	64
PSF2-PSS-365-2	963	1090	13.2	0.58	0.34	59
PSF2-heated-2	1056	1199	15.0	0.66	0.37	56

[a] Calculated applying NLDFT adopting N_2@77K Carbon slit pore model

[b] Calculated considering pored up to 20 Å wide

*Table A4.3. Fitting parameters obtained for carbon dioxide adsorption for **PSF2** using a dual-site Langmuir model*

	$Q_{sat,a}$ (mmol/g)	$Q_{sat,b}$ (mmol/g)	$b_{0,a}$ (bar^{-1})	$b_{0,b}$ (bar^{-1})	E_a (kJ/mol)	E_b (kJ/mol)
PSF2	1.1897	16.3901	$5.47 \cdot 10^{-07}$	$3.92 \cdot 10^{-5}$	33.6236	18.2613

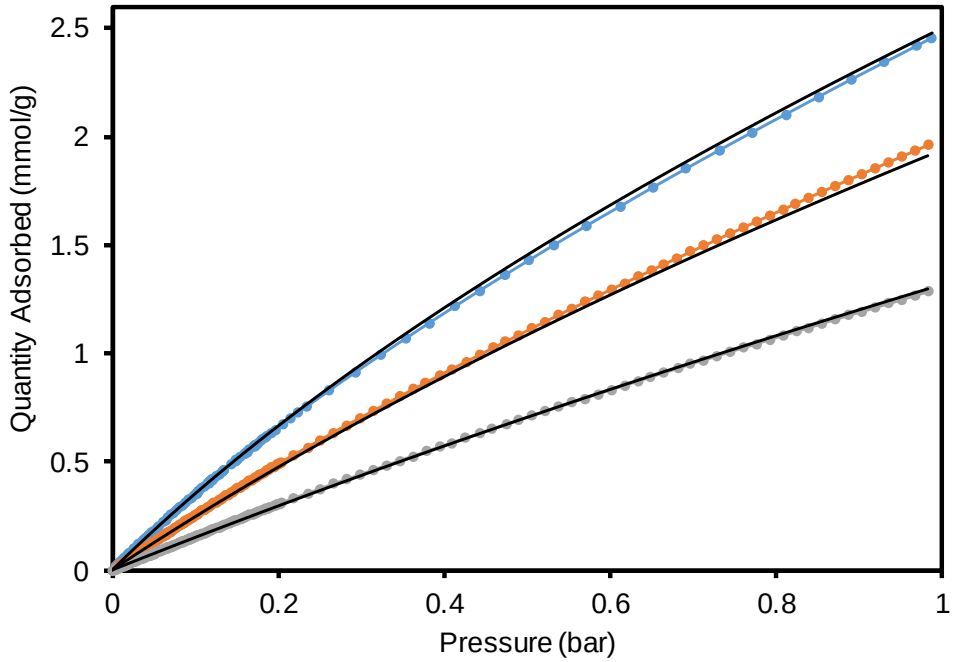

*Figure A4.15. Experimental (273 K, blue dots) (283 K, orange dots), (298K, grey dots) and fitted (solid black lines) CO_2 adsorption isotherms of **PSF2**. The fitting of the experimental isotherms was performed using the dual-site Langmuir equation. The fitted isotherms were used in heat of adsorption calculation.*

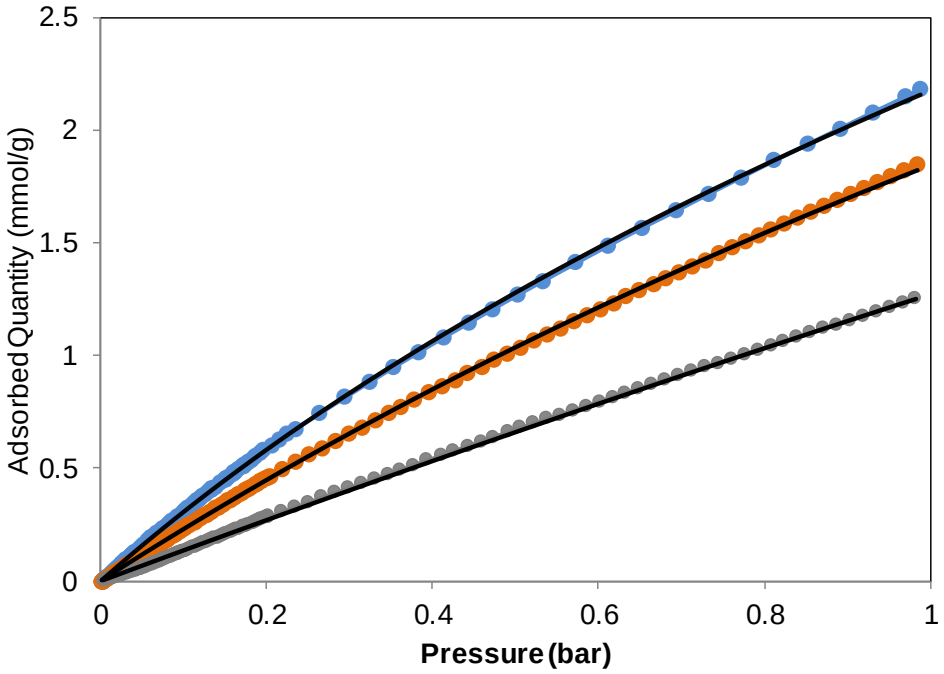

***Figure A4.16**. Experimental (273 K, blue dots) (283 K, orange dots), (298K, grey dots) and fitted (solid black lines) CO_2 adsorption isotherms of **PSF2-PSS-365**. The fitting of the experimental isotherms was performed using the dual-site Langmuir equation. The fitted isotherms were used in heat of adsorption calculation.*

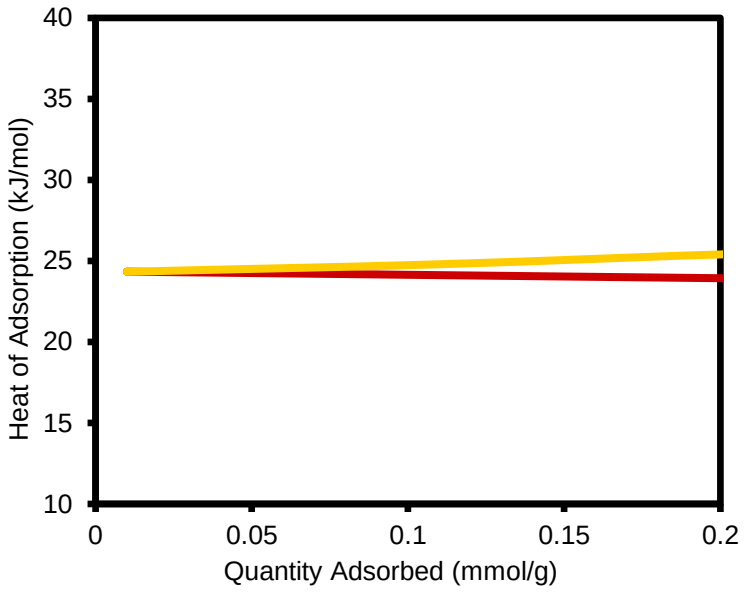

***Figure A4.17**. Isosteric heat of adsorption calculated for **PSF2** (red line) and **PSF2-PSS-365** (green line) applying the van't Hoff equation to the fitted isotherms. No significant changes are observed before and after irradiation with 365 nm light.*

A4.9. Solid state NMR

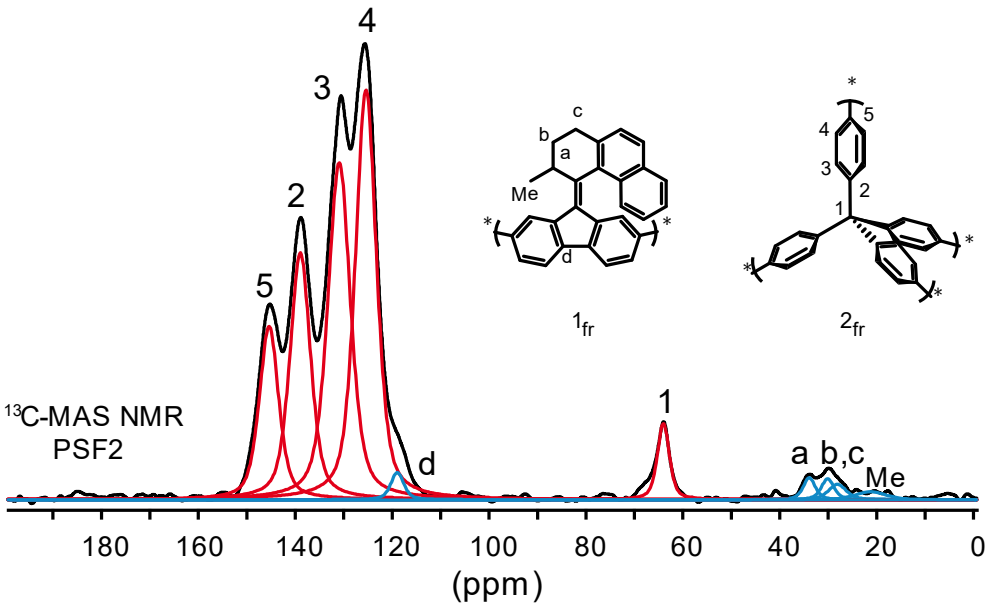

Figure A4.18. *^{13}C-MAS NMR of **PSF2** collected with a recycle delay of 100 s. This spectrum was used to quantify the switch moieties present in **PSF2** as described in the main text.*

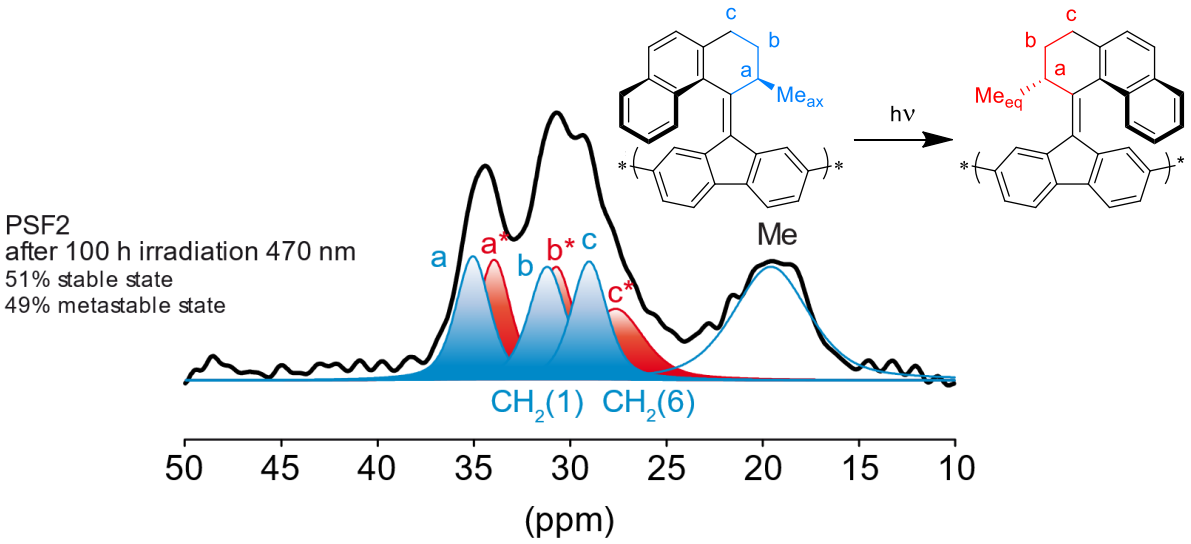

Figure A4.19. *Selected part of ^{13}C CP/MAS NMR spectrum of **PSF2-PSS-470** (solid black line). Coloured peaks represent the deconvoluted spectrum. Red peaks indicate signals coming from **1$_{fr}$**-metastable, blue peaks denote signals coming from **1$_{fr}$**-stable. The ratio between the total area of the blue and red peaks was used to determine the stable-to-metastable ratio.*

Appendix 5.

Supporting Information for Chapter 5

A5.1. Differential scanning calorimetry

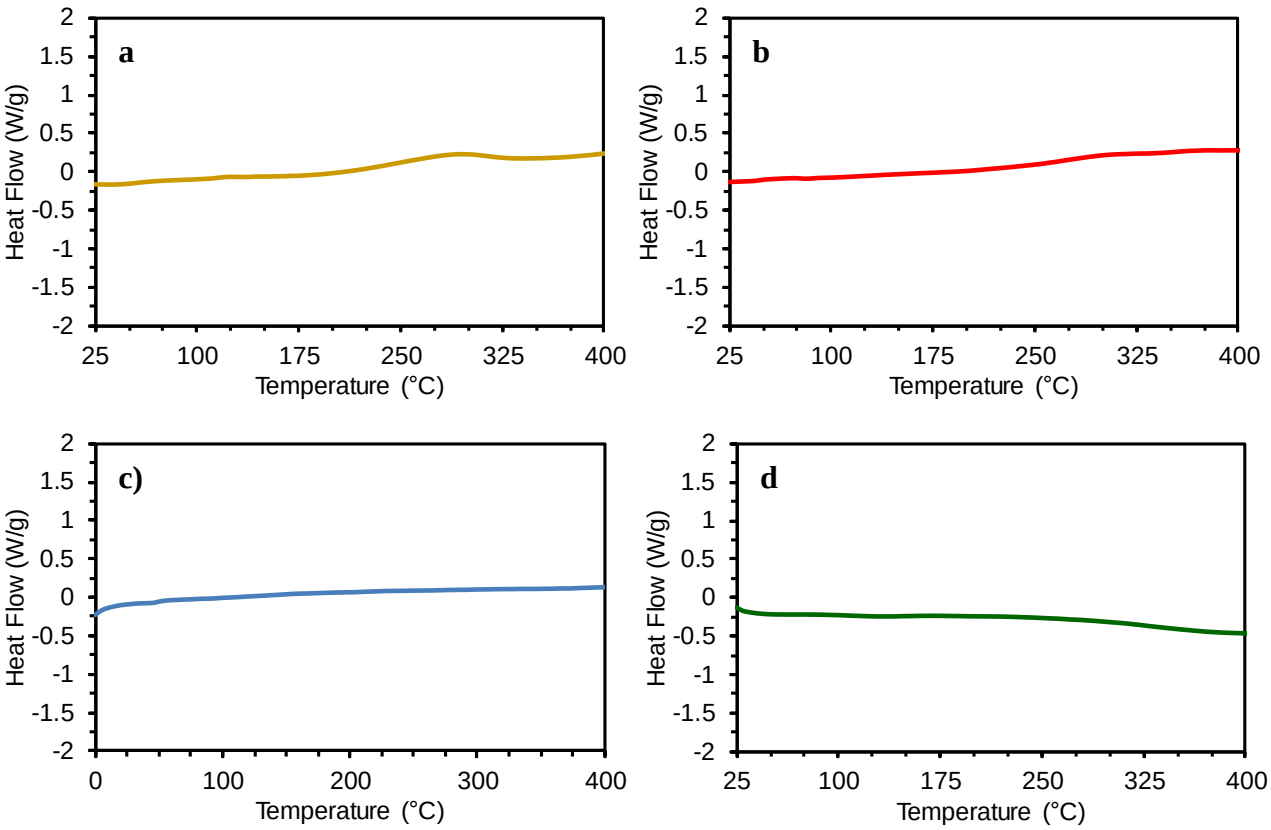

Figure A5.1. *DSC traces of* ***a) 1FCOP; b) 2FCOP; c) FPAF; d) SS-FPAF*** *collected from 25 to 400 °C with a heating rate of 10 °C/min under an 80 ml/min flux of* N_2

A5.2. Thermogravimetric Analysis

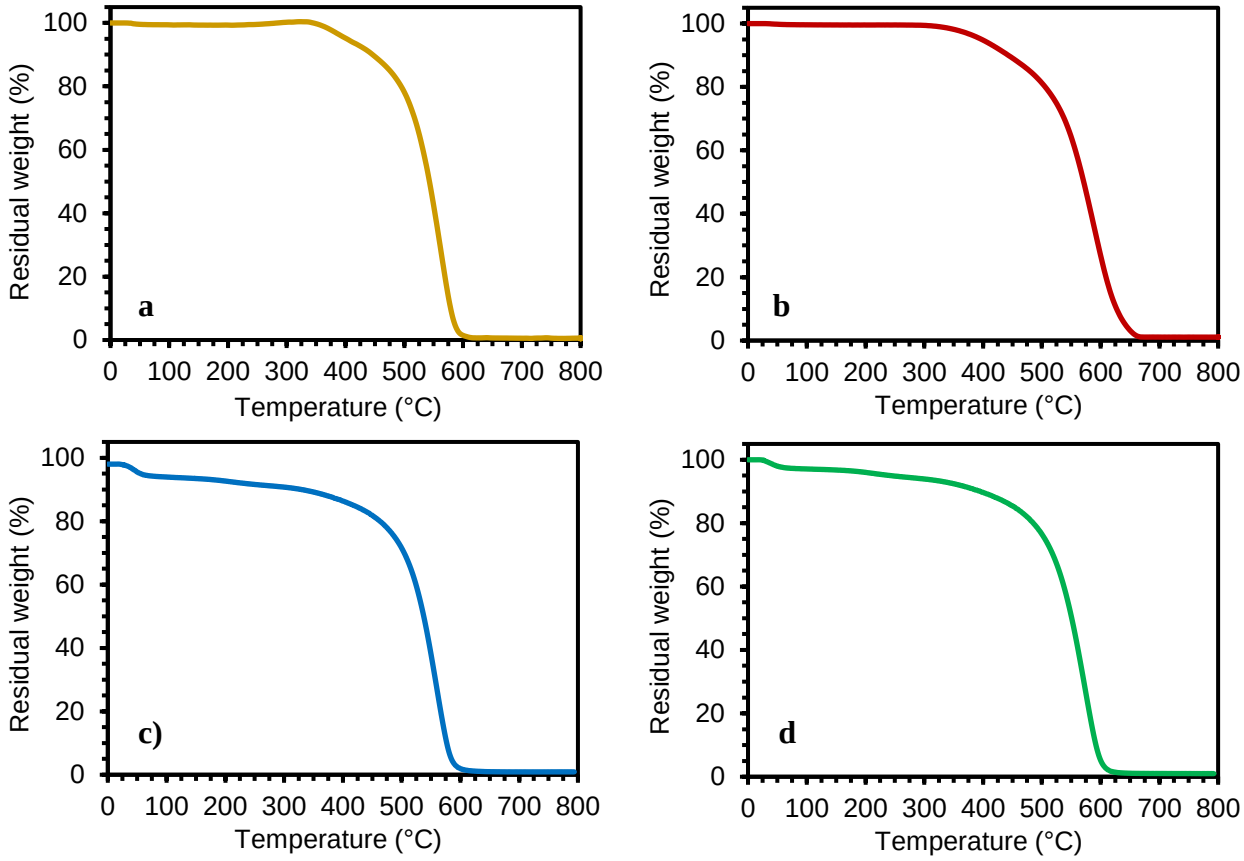

*Figure A5.2. TGA traces of **a) 1FCOP**; **b) 2FCOP**; **c) FPAF**; **d) SS-FPAF** collected from 0 to 800 °C with a heating rate of 20 °C/min.*

A5.3. Powder X-Ray Diffraction analysis

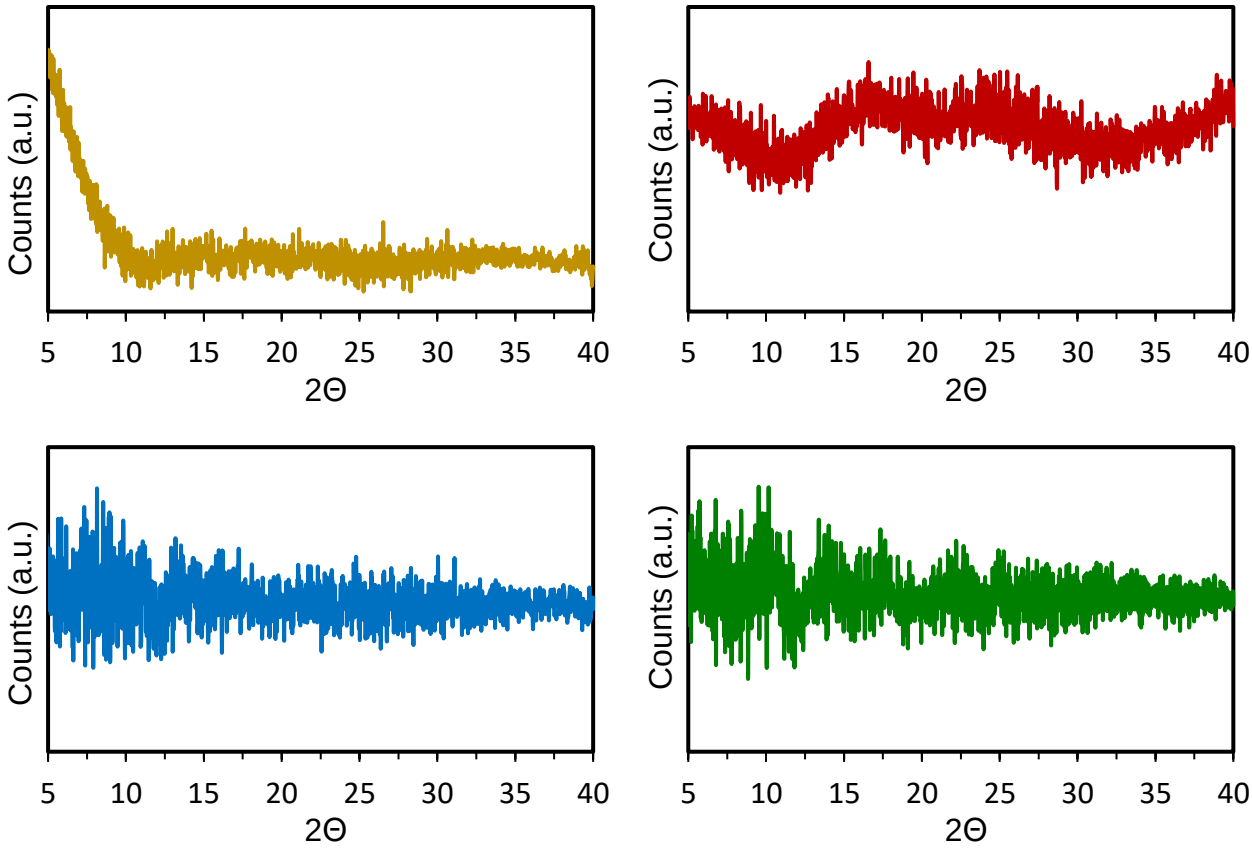

Figure A5.3*. XRPD traces of* ***1FCOP*** *(yellow trace),* ***2FCOP*** *(red trace),* ***FPAF*** *(blue trace) and* ***SS-FPAF*** *(green trace) collected from 5 to 40 2Θ°, with steps of 0.2°, and scanning speed of 1.5 s/step.*

A5.4. Isosteric heats of adsorption and IAST calculations

$Q_{st}(CO_2)$ and $Q_{st}(CH_4)$ were derived from CO_2 and CH_4 adsorption isotherms, respectively, collected at 273, 283 and 298 K up to 10 bar of pressure using the van't Hoff equation:

$$Q_{st} = RT^2\left(\frac{\partial \ln p}{\partial T}\right)$$

First, the three isotherms were fitted adopting a Langmuir-Freundlich model, which has the general form

$$\boldsymbol{q} = \frac{q_{max} b p^t}{1 + b p^t}$$

where $\boldsymbol{q}$ is the adsorbed quantity at pressure p, q_{max} is the saturation loading and b and t are the Freundlich parameters. Parameter b can be written

$$b = b_0 e^{E/RT}$$

where b_0 is a pre-exponential factor related to the gas saturation pressure p^0 and E can be considered as the mean adsorbent-adsorptive interaction energy calculated from $p = 0$ to $p_{max.}$ In our fitting procedure, we used Langmuir-Freundlich model to fit simultaneously the three experimental curves. We allowed the saturation loading q_{max} and the Freundlich parameters t to vary independently for each experimental isotherm, while the pre-exponential factor b_0 and the energy E had to be the same for all the isotherms. We had then a total of eight fitting parameters: b_0, E, Q_{273}, t_{273}, Q_{283}, t_{283}, Q_{298} and t_{298}

Calculations were run using Mathlab software. The calculated fitting parameters are reported in **Table A5.1** for CO_2 and **Table A5.2** for CH_4, while **Figures A5.X and A5.Y** shows the fitted curve over the experimental isotherms for CO_2 and CH_4, respectively. We can reverse the Langmuir-Freundlich equation to obtain an analytical expression of p as a function of $\boldsymbol{q}$

$$p = \left(\frac{\boldsymbol{q}}{b(q_{max} - \boldsymbol{q})}\right)^{1/t}$$

And, thus, calculate Q_{st} via the van't Hoff equation. In the case of CO_2 adsorption, we were interested in the low-loading behavior of the materials and thus, in the fitting procedure of experimental isotherms, we only took in account experimental points up to 2 mmol/g of adsorbed quantity. On the other hand, for methane adsorption the high-pressure behavior is important because of smaller adsorbed quantities, and so all experimental points up to 10 bar were included in the fitting calculations.

Table A5.1. *Fitting parameters obtained for carbon dioxide adsorption for* ***1FCOP, 2FCOP, FPAF*** *and* ***SS-FPAF*** *using a Langmuir-Freundlich model and considering experimental points up to Q(ads) = 2 mmol/g*

	Q_{273} (mmol/g)	Q_{283} (mmol/g)	Q_{298} (mmol/g)	t_{273}	t_{283}	t_{298}	b_0 (bar^{-1})	E (kJ/mol)
1FCOP	5.9076	5.7085	5.442	0.9555	0.9766	1	$1.65 \cdot 10^{-4}$	18.7676
2FCOP	4.4966	4.3197	4.1298	0.9416	0.9604	0.9761	$1.31 \cdot 10^{-4}$	19.3811
FPAF	25.3882	24.4427	24.4427	0.9743	0.9937	1	$2.83 \cdot 10^{-5}$	18.9671
SS-FPAF	8.9327	8.9327	6.9113	1	0.9642	1	$2.87 \cdot 10^{-2}$	5.765

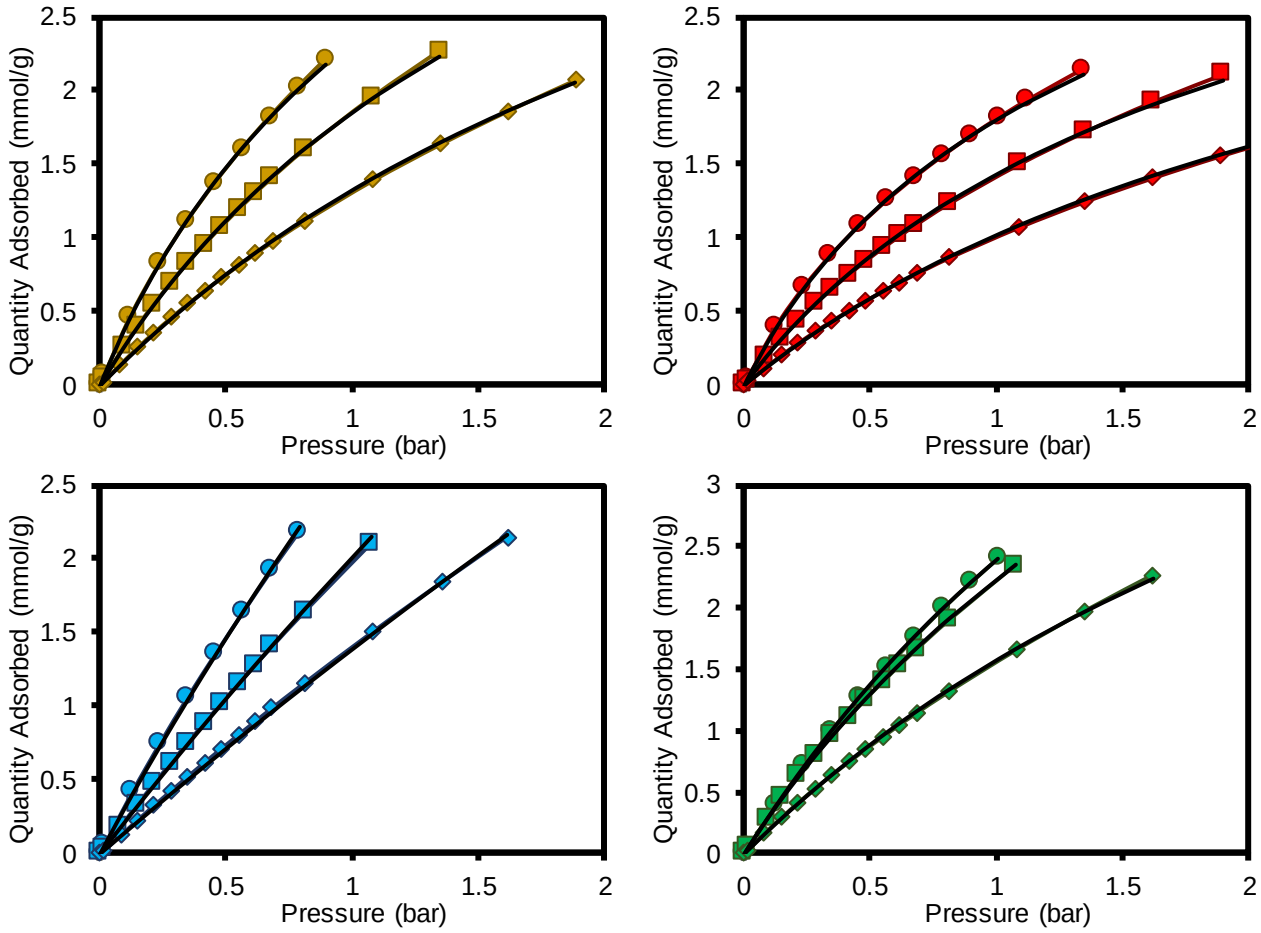

Figure A5.4*. Results of the carbon dioxide isotherms fitting procedure for* ***FCOP*** *(yellow traces),* ***2FCOP*** *(red traces),* ***FPAF*** *(blue traces) and* ***SS-FPAF*** *(green traces) using the parameters reported in* ***Table A5.1*** *and the Langmuir-Freundlich model.* CO_2 *isotherms at 273 K (dots), 283 K (squares), 298 K (diamonds) and fitting (solid black line).*

Table A5.2. *Fitting parameters obtained for methane adsorption for* ***1FCOP****,* ***2FCOP****,* ***FPAF*** *and* ***SS-FPAF*** *using a Langmuir-Freundlich model and considering experimental points up to p = 10 bar*

	Q_{273} (mmol/g)	Q_{283} (mmol/g)	Q_{298} (mmol/g)	t_{273}	t_{283}	t_{298}	b_0 (bar^{-1})	E (kJ/mol)
1FCOP	5.4189	5.4189	5.2003	0.9942	0.9921	1	$7.58 \cdot 10^{-5}$	17.3193
2FCOP	3.4618	3.3561	2.785	0.9674	1	1	$8.74 \cdot 10^{-4}$	12.2401
FPAF	25.3882	24.4427	24.4427	0.9743	0.9937	1	$2.83 \cdot 10^{-5}$	18.9671
SS-FPAF	8.9327	8.9327	6.9113	1	0.96416	1	$2.87 \cdot 10^{-2}$	5.765

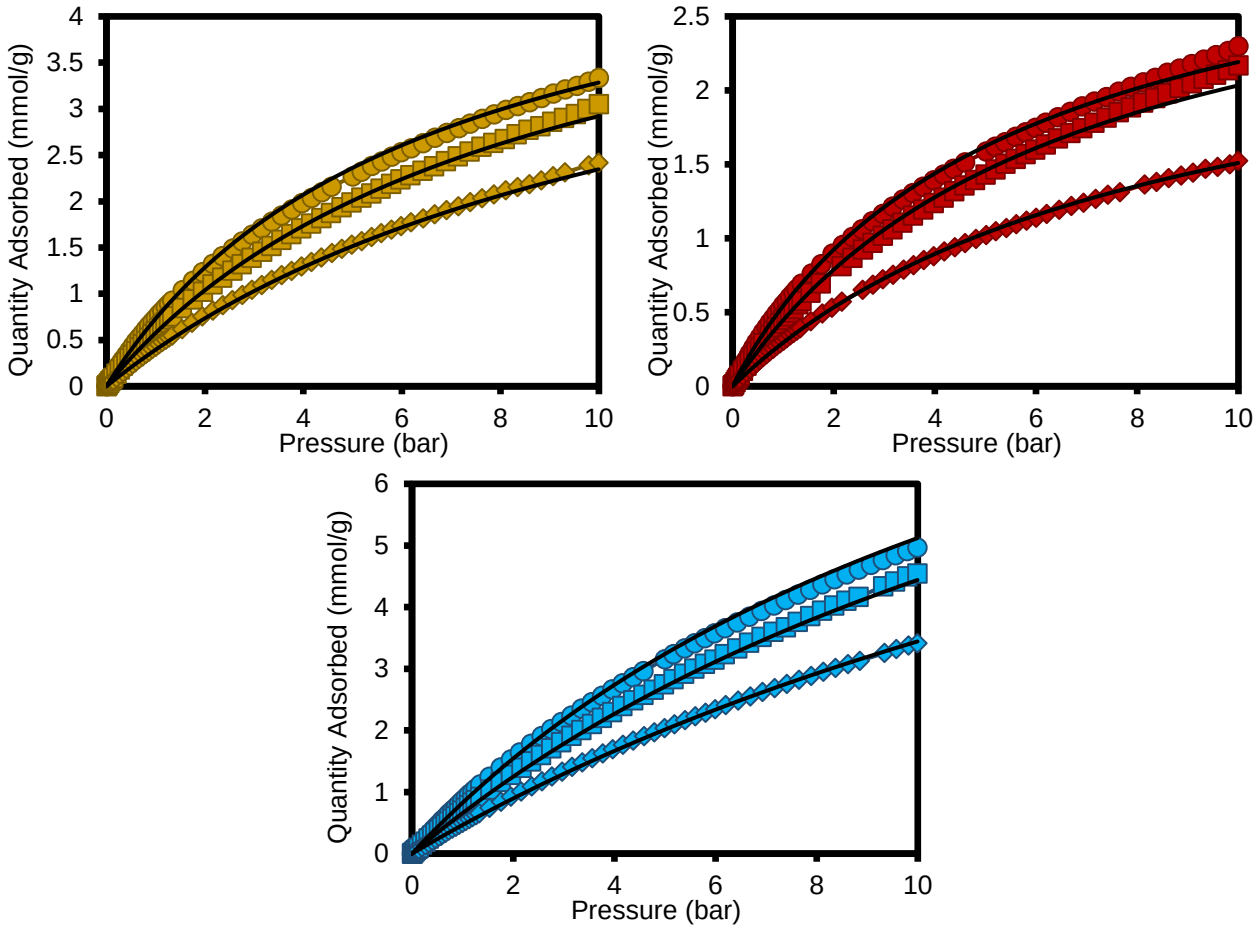

Figure A5.5. *Results of the methane isotherms fitting procedure for* ***FCOP*** *(yellow traces),* ***2FCOP*** *(red traces), and* ***FPAF*** *(blue traces) using the parameters reported in* ***Table A5.2*** *and the Langmuir-Freundlich model.* CH_4 *isotherms at 273 K (dots), 283 K (squares), 298 K (diamonds) and fitting (solid black line).*

For IAST calculations, N_2 isotherms were fitted up to 10 bar adopting the Langmuir-Freundlich model. We then calculated spreading pressures (integrals were solved using Wolfram Alpha) and we applied the standard equations for IAST.

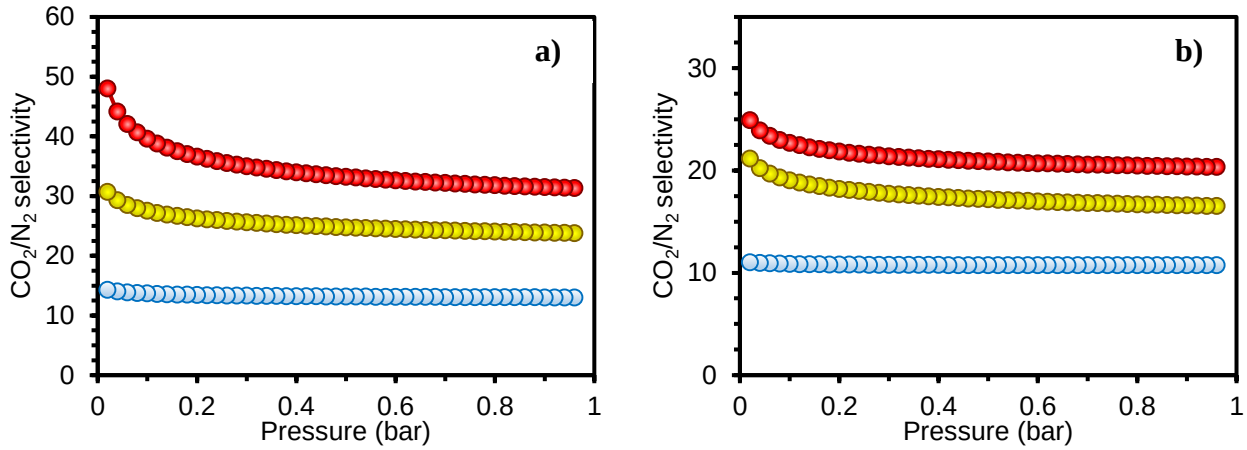

*Figure A5.6 IAST selectivity for the adsorption of CO_2 over N_2 from a 15:85 mixture calculated at **a)** 273 K and **b)** 298 K for **FCOP** (yellow trace), **2FCOP** (red trace), **FPAF** (blue trace).*

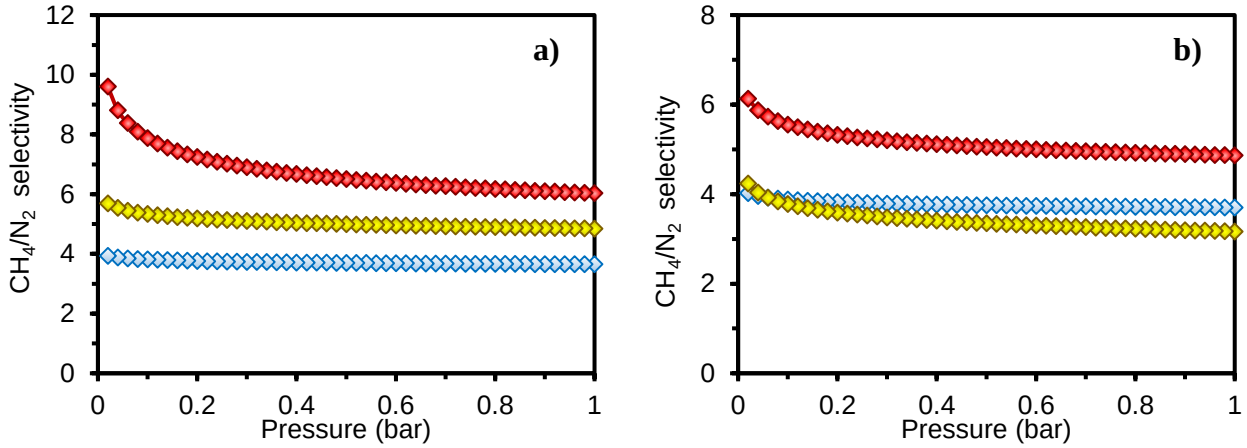

*Figure A5.7. IAST selectivity for the adsorption of CH_4 over N_2 from a 50:50 mixture calculated at **a)** 273 K and **b)** 298 K for **FCOP** (yellow trace), **2FCOP** (red trace), **FPAF** (blue trace).*

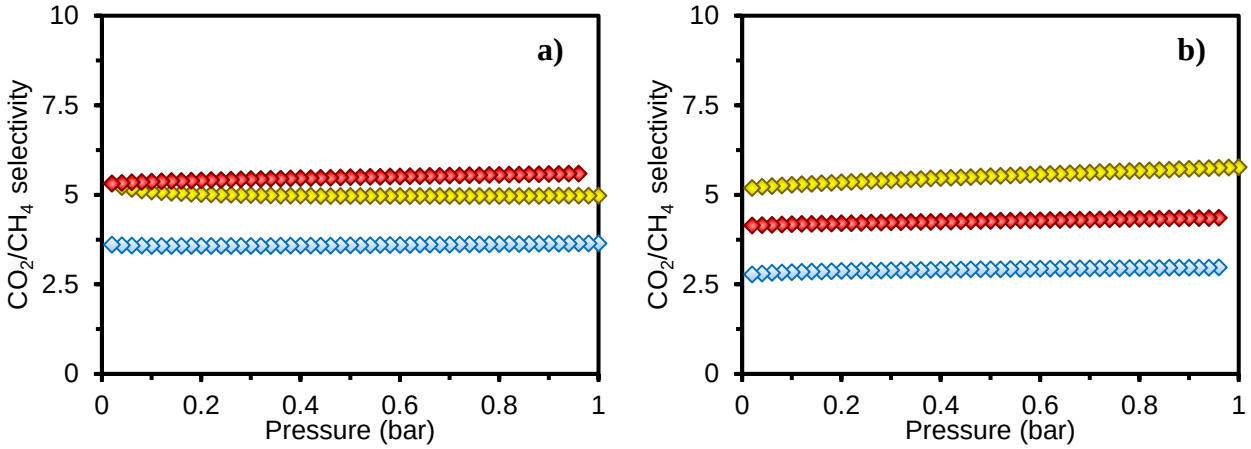

Figure A5.8. *IAST selectivity for the adsorption of CO_2 over CH_4 from a 50:50 mixture calculated at* ***a)*** *273 K and* ***b)*** *298 K for* ***FCOP*** *(yellow trace),* ***2FCOP*** *(red trace),* ***FPAF*** *(blue trace).*

A5.5. Pore size distribution

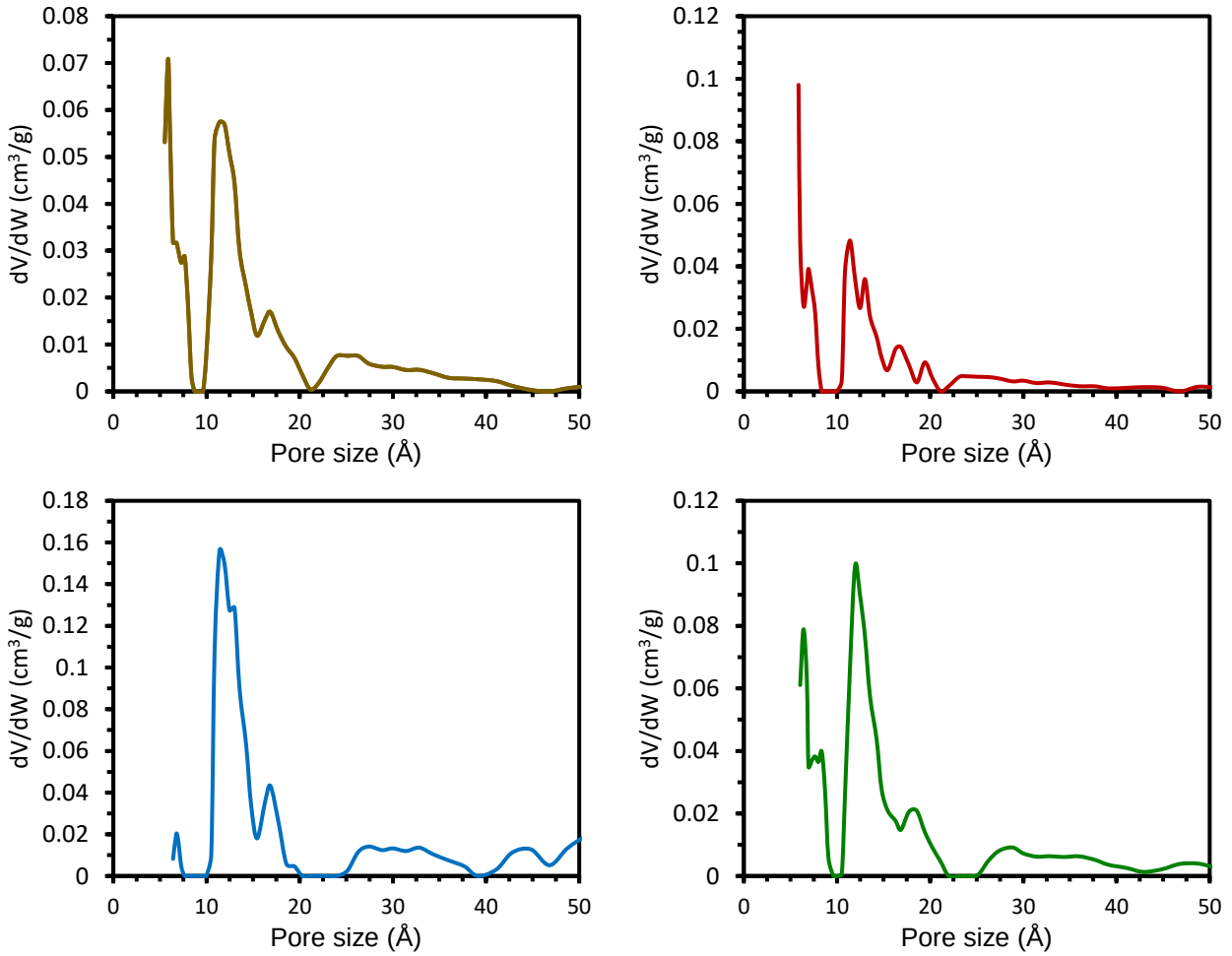

Figure A5.9. *Pore size distribution graphs of* ***1FCOP*** *(yellow trace),* ***2FCOP*** *(red trace),* ***FPAF*** *(blue trace) and* ***SS-FPAF*** *(green trace) calculated by NLDFT adopting the N_2@77K carbon slit pore model.*

A5.6. Solid-State NMR of SS-FPAF

As discussed in the main text, the full spectrum of **SS-FPAF** is reported to show the presence of minor signals in the aliphatic region (10-40 ppm) ascribable to the presence of polyTHF trapped in the pores of the material.

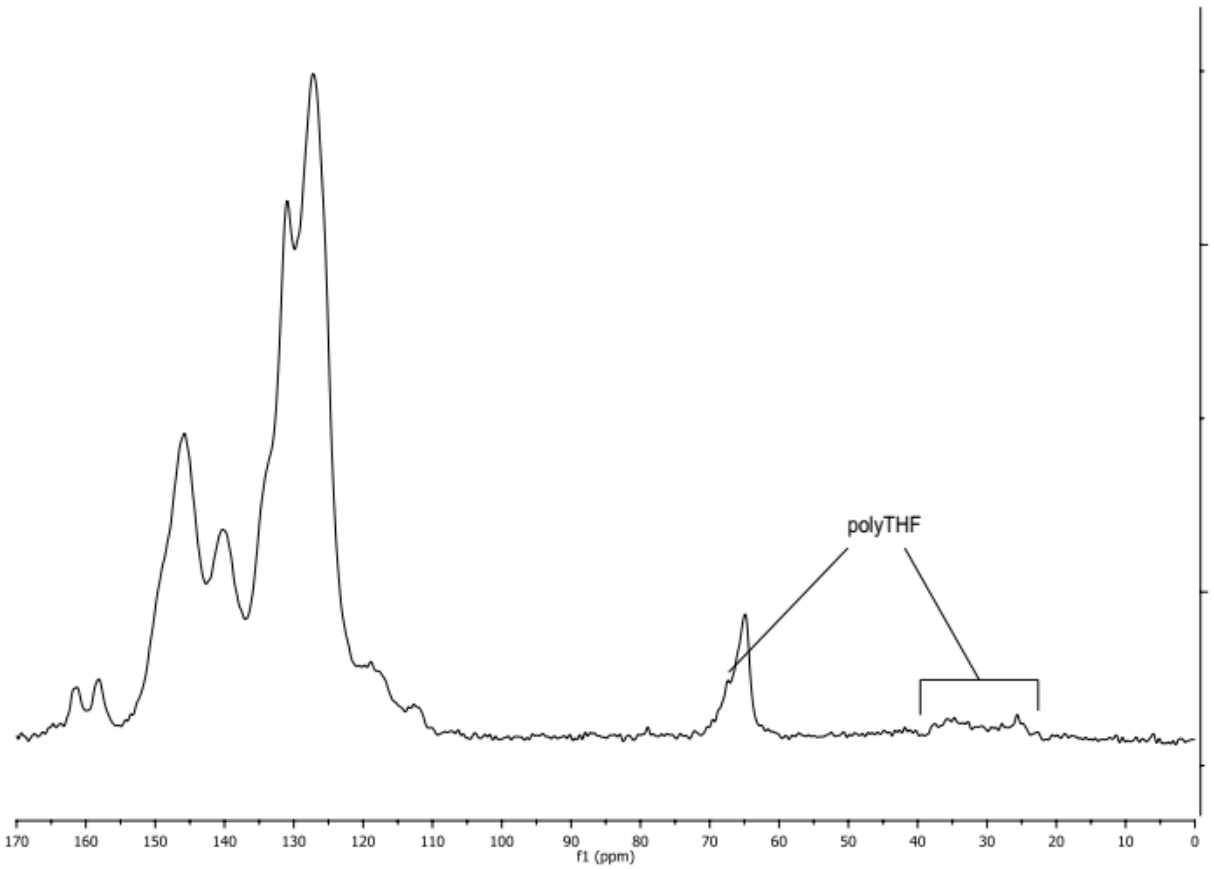

*Figure A5.10. Full ^{13}C-CP/MAS NMR spectrum of **SS-FPAF**. The presence of polyTHF is highlighted.*